

Evaluation of the potentials for optical coherence tomography (OCT) to detect early signs of retinal neurodegeneration

Mukhit Kulmaganbetov

A thesis submitted to Cardiff University in accordance with the requirements for the degree of Doctor of Philosophy in Vision sciences

School of Optometry and Vision Sciences
Cardiff University

Submitted June 2021

Acknowledgements

Firstly, I would like to express my sincere gratitude to my supervisors Professors James E. Morgan and Dr Julie Albon for all of their help and support, encouragement and enthusiasm, generosity in sharing their skills and knowledge throughout my PhD.

Secondly, I would like to thank all the staff and fellow PhD students of the School of Optometry and Vision sciences that I have had the pleasure of working with over the past three years. Particularly, Professors Jonathan Erichsen, Andrew Quantock and Tony Redmond who inspired and encouraged me to come to the UK, Dr's Nick White and Irina Erchova, who taught me many techniques that I have been using in my studies.

I am grateful to the past and present members of Morgan Lab. Many thanks must go to Dr James Tribble who helped to conduct chemical experiments in my first year, Dr's Ryan Bevan and Andrew Want, who helped me with the dissection of mice retina, and Ms Eirini Kokkali, who provided me with access to the Phoenix OCT at Redmond Building.

Huge thanks also to Dr's Ashley Wood and Ryan Bartlett, who provided me with the AMD and glaucoma OCT data. I wish to express my immeasurable appreciation to the collaborators at the University of Bristol – Professor Alin Achim and Dr Pui Anantrasirichai, who taught me the machine learning algorithms and kindly shared their codes.

My sincere thanks go to Cardiff Institute for Tissue Engineering and Repair (CITER) for the travel grant and extracurricular engagement opportunities. Special thanks to Mrs Sue Hobbs for her help and support, especially with all the administration of our studies. I am thankful for my housemates at Mischievous Miskins (Siamac Parker, Michael Howie and Guillermo Menendez) and Kazakh Society in Cardiff for friendship and joyful times.

Lastly, I am eternally grateful for the unconditional love, belief and support provided by my friends and family, in particular my mother Perizat Omirali and my sisters Aknur Sharipzhan and Moldir Kulmaganbetova.

And of course, it is my great honour to thank Vice-Chancellor for the International Scholarship for Research Excellence.

Abstract

Among neuroretinal degenerations, glaucoma and age-related macular degeneration (AMD) have become the most frequent reasons for irreversible blindness globally. Among the causes of the elderly and senile dementia, Alzheimer's disease (AD) has the leading position, the early ocular symptoms of which can potentially be a prognostic factor. The aim of this thesis was the early *in vivo* ligand-free detection of degenerative changes in the inner and outer retinal layers, which was possible using high-resolution optical coherence tomography (OCT) with the machine learning (ML) algorithms: support vector machine (SVM) and principal component analysis (PCA).

Prior to the application of SVM and PCA for the classification of human OCT images, evaluation of the classifiers was performed in the classification of optical phantoms, the accuracy of which was in the range of 82-100%. This was the first attempt to measure the textural properties of various polystyrene and silica beads optical phantoms.

To identify optical changes that characterise early apoptosis, OCT imaging of axotomised retinal ganglion cells (RGCs) in *ex vivo* retinal murine explants was performed. Substantial optical alterations in RGC dendrites in the early stages of apoptosis (up to 2 hours) were detected. ML algorithms correctly classified the retinal texture of the inner plexiform layer (IPL) of transgenic AD mice in all cases, indicating the potential for further investigation in *in vivo* animal and human studies. Not only the optical signature but also the transparency of the dissected murine retinal explants was investigated. Moreover, ML classification of 3xTg mice IPL layer was studied in terms of optical changes due to the RGD dendritic atrophy.

ML classifiers' accuracy in the detection of early and neovascular AMD was 93-100% for the texture of retinal pigment epithelium, 69-67% for the outer nuclear layer, 70% for the inner segment and 60-90% for the outer segment of photoreceptors. Classification of AMD stages and comparison with the age-matched healthy controls was carried out in the outer retina and RPE.

Grey-level co-occurrence, run-length matrices, local binary patterns features were extracted from the IPL of the macula to classify glaucoma OCT images. The accuracy of linear and non-linear SVMs, linear and quadratic discriminant analyses, decision tree and logistic regression was between 55-70%. Based on the classifiers' precision, recall and F_1 -score, Gaussian SVM

outperformed other ML techniques. In this study, the observation of early glaucomatous subtle optical changes of human IPL was conducted. Also, the significance of various supervised ML algorithms was investigated.

Understanding the optical signature of cumulative inherent speckle of OCT scans arising from apoptotic retinal ganglion cells and photoreceptors may provide vital information for the prevention of retinal neurodegeneration.

Abbreviations

AD – Alzheimer’s disease

AEL – axial eye length

AMD – age-related macular degeneration

ANOVA – analysis of variance

AO – adaptive optics

AOSLO – adaptive optics scanning light ophthalmoscopy

ARM – age-related maculopathy

ASE – amplified spontaneous emission

ASM – angular second moment

BMEIS – the boundary of myoid and ellipsoid of inner segments

CNS – central nervous system

CoR – coefficients of repeatability

COVID-19 – coronavirus disease

CSV – comma-separated values

CT – computed tomography

DARC – detection of apoptotic retinal cells method

DNA – deoxyribonucleic acid

DT – decision tree

ELM – external limiting membrane

ER – endoplasmic reticulum

ESF – edge spread function

ETDRS – Early Treatment Diabetic Retinopathy Study

FD-OCT – Fourier domain OCT

FERG – flash electroretinograms

F-FDG – fluorodeoxyglucose

FFT – fast Fourier transform

FWHM – full width at half maximum

G SVM – Gaussian SVM

GCC – ganglion cell complex
GCL – ganglion cell layer
GFAP – glial fibrillary acidic protein
GLCM – grey-level co-occurrence matrix
GLNU – grey-level non-uniformity
GLRM – grey-level run-length matrices
GS – gelatin solution
HBSS – Hank’s balanced salt solution
HFL – Henle fibre layer
HGRE – high grey-level run emphasis
ICON – in vivo confocal neuroimaging
IDM – inverse difference moment
ILM – internal limiting membrane
INL – inner nuclear layer
IOP – intraocular pressure
IPL – inner plexiform layer
IS PR – inner segments of the photoreceptor
IS PRL – inner segments of the photoreceptor layer
IS/OS PR – junction between the inner and outer segment of the photoreceptors
L SVM – linear SVM
LBP – local binary pattern
LC – lamina cribrosa
LDA – linear discriminant analysis
LGN – lateral geniculate nucleus
LGRE – low grey-level run emphasis
LR – logistic regression
LRE – long-run emphasis
LRHGE – long run high grey-level emphasis
LRLGE – long run low grey-level emphasis

LSF – line spread function

MCI – mild cognitive impairment

MnSOD – manganese superoxide dismutase

MRI – magnetic resonance imaging

MTF – modulation transfer function

NA – numerical aperture

nAMD – neovascular AMD

nD-PCA – n-dimensional PCA

NIA – National Institute on Aging

NIH – National Institute of Health

NIR – near-infrared

NND – nearest neighbour distance

NNI – nearest neighbour index

OCT – optical coherence tomography

ON – optic nerve

ONH – optic nerve head

ONL – outer nuclear layer

OPL – outer plexiform layer

OS PR – outer segments of the photoreceptor

OS PRL – outer segments of the photoreceptor layer

PACG – primary angle-closure glaucoma

PAT – patient

PBs – polystyrene beads

PC – personal computer

PCA – principal component analysis

PERG – pattern electroretinograms

PET – positron emission tomography

PiB – Pittsburgh substance

PitB – Pittsburgh Compound B

POAG – primary open-angle glaucoma

PR – photoreceptor

PSF – point spread function

PZD – piezoelectric transducer

Q SVM – quadratic SVM

QDA – quadratic discriminant analysis

RGC – retinal ganglion cell

RI – refractive index

RLNU – run-length non-uniformity

RNFL – retinal nerve fibre layer

ROI – a region of interest

RP – run percentage

RPD – reticular pseudodrusen

RPE – retinal pigment epithelium

SD – standard deviation

SD-OCT – spectral domain OCT

SLD – superluminescent diode

SRE – short-run emphasis

SRHGE – short run high grey-level emphasis

SRLGE – short run low grey-level emphasis

SS-OCT – swept source OCT

SVM – support vector machine

TA – texture analysis

TD-OCT – time-domain OCT

TUNEL – terminal deoxynucleotidyl transferase-mediated deoxyuridine triphosphate (UTP)-biotin nick end-labelling

UHR-OCT – ultra-high resolution-OCT

VEGF – vascular endothelial growth factor

VOI – a volume of interest

3xTg-AD – triple-transgenic AD mouse model

Table of Contents

Acknowledgements	ii
Abstract	iii
Abbreviations	v
Table of Contents	ix
List of Figures	xii
List of Tables	xiv
List of Equations	xv
Chapter 1. General Introduction	1
1.1. Optical coherence tomography	1
1.1.1. Basic principles	1
1.1.2. OCT resolution	2
1.2. OCT anatomy of the retina	5
1.2.1. Cellular scattering contribution to OCT signal	9
1.3. Inner retina neurodegeneration	11
1.3.1. RGC apoptosis	11
1.3.2. Glaucoma	12
1.3.3. Alzheimer's disease	14
1.4. Outer retina neurodegeneration	17
1.4.1. Photoreceptor and RPE apoptosis	17
1.4.2. Age-related macular degeneration	19
1.5. Texture and texture analysis of OCT scans	21
1.6. Hypothesis and Aims	24
Papers arising from this thesis (on submission)	26
Papers arising from this thesis (on draft)	26
Abstract arising from this thesis	26
Chapter 2. General Methods	27
2.1. Phantom preparation	27
2.2. Animal retina dissection	29
2.3. OCT imaging	30
2.4. Microscopy imaging	33
2.4.1. Phantom microscopy	33
2.4.2. Retinal explant microscopy	33
2.5. Refractometry	35
2.6. Image processing and analysis of textural features	37
2.6.1. Grey-level co-occurrence matrix	37

2.6.2.	Grey-level run-length matrices	40
2.6.3.	Local binary pattern.....	42
2.7.	Machine learning algorithms	44
2.7.1.	Support vector machine	45
2.7.2.	Discriminant analyses	47
2.7.3.	Logistic regression	48
2.7.4.	Decision tree	49
2.8.	Classifier performance evaluation	50
Chapter 3. Textural feature analysis of OCT phantoms.....		51
3.1.	Introduction	51
3.1.1.	Hypothesis	53
3.1.2.	Aims	53
3.2.	Methods	54
3.2.1.	Phantom preparation	54
3.2.2.	Particle dispersion calculation	55
3.2.3.	Phantom OCT imaging and image processing.....	55
3.2.4.	Texture analysis and classification	56
3.3.	Results	59
3.3.1.	Gelatin matrix.....	59
3.3.2.	Scattering particles.....	61
3.3.3.	Spatial distribution of scatterers	62
3.3.4.	Classification of phantoms	65
3.4.	Discussion	72
Chapter 4. Optical detection of neurodegeneration in mouse retinal explants.....		74
4.1.	Introduction.....	74
4.1.1.	Hypotheses	76
4.1.2.	Aims.....	76
4.2.	Experimental design.....	77
4.2.1.	Analysis of retinal explants post axotomy	77
4.2.2.	Retinal transparency post axotomy: analysis of the modulation transfer function	78
4.2.3.	Retinal atrophy post axotomy: texture analysis of RGC dendritic tree.....	80
4.2.4.	Analysis of RGC dendritic atrophy in Alzheimer's disease	80
4.3.	Results.....	81
4.3.1.	Transparency of the retinal explants	81
4.3.2.	Texture analysis of post axotomy RGC dendritic tree	85
4.3.3.	Optical detection of neurodegeneration of RGC dendrites in AD mice	91

4.4. Discussion.....	92
Chapter 5. Texture analysis of outer retinal layers in macular degeneration	95
5.1. Introduction.....	95
5.1.1. Hypothesis	97
5.1.2. Aims.....	97
5.2. Methods	98
5.2.1. OCT dataset	98
5.2.2. Texture analysis and machine learning	101
5.2.3. Greyscale histogram analysis.....	101
5.3. Results.....	104
5.4. Discussion.....	109
Chapter 6. Machine learning tools for the optical detection of glaucoma.....	111
6.1. Introduction.....	111
6.1.1. Hypothesis	113
6.1.2. Aims.....	113
6.2. Methods	114
6.2.1. OCT dataset, texture analysis and machine learning	114
6.2.2. Retinal layer segmentation.....	117
6.3. Results.....	119
6.4. Discussion	124
Chapter 7. General Discussion	126
7.1. OCT resolution and texture analysis	126
7.2. Phantom study: Feasibility of SVM and PCA to classify phantoms based on OCT-derived GLCM features.....	129
7.3. Explant study: Feasibility of using OCT image-derived texture features to detect early retinal neurodegeneration in models of retinal axotomy and Alzheimer’s disease	131
7.4. Human studies: Feasibility of machine learning classification tools for use in early detection of retinal neurodegeneration in AMD and Glaucoma	133
7.5. Other limitations.....	137
7.6. Conclusions and future work.....	139
References	141
Appendices.....	177
Appendix 1. Programming scripts and functions	177

List of Figures

Figure 1.1. Lab-based OCT system structure

Figure 1.2. OCT image acquired by OCT-1040nm with the corresponding fundus image

Figure 1.3. The schematic structure of the retina

Figure 1.4. OCT image and histologic micrograph of the normal human macula

Figure 1.5. Scattering contribution of a cell

Figure 1.6. Mitochondrial fission during RGC degeneration

Figure 1.7. Photoreceptors

Figure 2.1. The preparation procedure of the optical phantoms and OCT scanning

Figure 2.2. Schematic of the OCT-1040nm

Figure 2.3. The optical spectrum of the light source

Figure 2.4. OCT-1040nm system components

Figure 2.5. OCT-1040nm system components (top view)

Figure 2.6. Imaging scheme of the phantom

Figure 2.7. Abbe Refractometer Model 60/70

Figure 2.8. Example of image processing and VOI selection

Figure 2.9. Demonstration of the GLRM feature extraction

Figure 2.10. LBP histogram generation

Figure 2.11. Linear and non-linear SVMs

Figure 2.12. Difference between cost functions of the linear and logistic regressions

Figure 2.13. Decision tree scheme with 2 levels

Figure 3.1. Microscopy image of 2% GS + 1 μ m 10 μ l PBs phantom

Figure 3.2. Image processing and data preparation for the classifier

Figure 3.3. OCT images of various gelatin solution concentrations

Figure 3.4. Comparison of refractive indices of gelatin solutions and water

Figure 3.5. Micrographs of the phantoms

Figure 3.6. Monolayer PBs phantoms

Figure 3.7. Thresholded and colour-coded 3D OCT scans of 1 μ m PBs phantoms with different concentrations

Figure 3.8. Nearest neighbour index graph

Figure 3.9. Scatter plot of the phantoms with the size of PBs $\geq 1\mu\text{m}$

Figure 3.10. OCT B scans and their thresholded images

Figure 3.11. PCA of the different refractive index of scatterers

Figure 3.12. Different volumes of scatterers

Figure 4.1. Experimental design

Figure 4.2. Modulation transfer function measurement

Figure 4.3. Microscopy images of the calibration slide with and without retinal explant

Figure 4.4. Microscopy images of the calibration slide with the explants in the different time points

Figure 4.5. Edge and line spread functions and MTFs

Figure 4.6. 3D rendered OCT image of a mouse retinal explant

Figure 4.7. Time series of OCT images of the mice retinal explants

Figure 4.8. Texture analysis of early apoptosis in retinal explants

Figure 4.9. Texture analysis results of 3xTg-AD and C57BL/6 mice

Figure 5.1. OCT scan sample with retinal cells scheme

Figure 5.2. The study design

Figure 5.3. Example of macula OCT image stack with the grey-level histogram

Figure 5.4. OCT scan examples representing the classification groups ($k=3$)

Figure 5.5. Histograms of grey values

Figure 6.1. The order of morphological changes of the RGC apoptosis

Figure 6.2. Algorithm of the OCT scans analysis process

Figure 6.3. Algorithm of the OCT image processing

Figure 6.4. The screenshot of the cross-sectional OCT image

Figure 6.5. Macular thickness map using ETDRS circles

Figure 7.1. OCT system resolution scheme

Figure 7.2. Strategy scheme of the early detection of glaucoma and its potential prevention

Figure 7.3. Types of studies in this thesis

Figure 7.4. Evolution of the feature extraction

Figure 7.5. Evolution of the machine learning algorithms

List of Tables

Table 2.1. Grey-level co-occurrence matrix features

Table 3.1. Groups and types of phantoms

Table 3.2. NNI of 1 μ m PBs phantoms of various volumes of the scatterers

Table 4.1. Greyscales mean and range of intensities

Table 4.2. Summary of the modulation depth of the objects and MTF values

Table 4.3. Classification summary

Table 5.1. Diagnostic criteria for the classification of AMD

Table 5.2. Number of OCT scans and selected VOIs

Table 5.3. Classification summary on the level of different retinal layers

Table 5.4. SVM classification of GLCM and LBP features

Table 6.1. List of features used in the classification study

Table 6.2. Average thickness values of inner retinal layers

Table 6.3. Classification summary for all textural features and all classifiers

Table 6.4. Classification summary for Gaussian SVM

List of Equations

(1.1) Gladstone-Dale formula

(2.1) LBP calculation

(2.2) The discriminant function of LDA

(2.3) The discriminant function of QDA

(2.4) Logistic regression hypothesis

(2.5) Classification accuracy

(2.6) Precision formula

(2.7) Recall calculation

(2.8) F_1 score formula

(3.1) Nearest neighbour index

(4.1) Modulus of the line spread function Fourier transform

(4.2) MTF ratio calculation

(4.3) Modulation depths of the images

(7.1) OCT axial (longitudinal) resolution

(7.2) OCT transverse resolution

(7.3) Depth of focus

Chapter 1. General Introduction

1.1. Optical coherence tomography

Optical coherence tomography (OCT) is a biomedical and clinical cross-sectional 3-dimensional *in vivo* imaging method for materials and biological systems (Schuman et al. 1995; Drexler and Fujimoto 2008). The technology is based on low coherence interferometry and acquires the images by measuring the optical reflections from back scattered light (Huang et al. 1991; Drexler et al. 2001).

Fluorescein angiography (FA), magnetic resonance imaging (MRI) and ultrasound may serve as alternative imaging technologies of OCT. If FA is an invasive method, that requires intravenous injection of dye to visualise the microvasculature of the fundus, MRI and ultrasound are non-invasive. However, both techniques have a lower axial and lateral resolution in comparison to OCT.

OCT imaging has become one of the principal methods for imaging eye diseases in the last 30 years due to its capability for detailed visualisation of the structure of the anterior and posterior eye, including retina and choroid (Huang et al. 1991; Schuman et al. 1995; Tudor et al. 2014). The main advantages of OCT are that it is non-invasive, has a fast acquisition time (seconds), and confers high accuracy and diagnostic precision (Fujimoto et al. 1995; Fercher 1996; Drexler 2010; Tudor et al. 2014; Morgan et al. 2017).

1.1.1. Basic principles

The principle of OCT operation is similar to the performance of another medical imaging technology – ultrasonography (Culjat et al. 2010; Marchini et al. 2015). While ultrasound measures sound waves back-reflected from objects of various densities to produce images of the tissues (Chen et al. 2009; Culjat et al. 2010; Gazzard et al. 2015), OCT obtains directly time-encoded signals and determines the quantity of backscattered light (Krauss and Puliafito 1995; Drexler and Fujimoto 2008). This is the working procedure of the first clinical OCTs which analysed data in the time-domain (Time Domain, TD-OCT) (Pan et al. 1995; Drexler and

Fujimoto 2008) using a single photodetector and calculation of the time delay of echo back-scattered waves from the sample (Fujimoto et al. 1995).

By contrast, instead of using multiple reference beams from a moving mirror, spectral/Fourier domain OCT (SD-OCT/FD-OCT) acquires images by multiple detectors (Choma et al. 2003; Drexler and Fujimoto 2008). Therefore, the scanning speed is considerably increased to 27 000 A-scans per second (Gabriele et al. 2011), reaching 100 000 A-scans per second in laboratory-based SD-OCT, which is 200 times faster than TD-OCT (de Amorim Garcia Filho et al. 2013). Another advantage of SD-OCT over TD-OCT is an increase in sensitivity, which is 20-30dB higher in the spectral domain device (Choma et al. 2003).

Laser light from a solid-state or superluminescent diode (SLD) source travels to an interferometer and is divided into two high-bandwidth light beams: one directed at the object (sample tissue) with the other goes to the reference arm of the OCT (Figure 1.1) (Drexler and Fujimoto 2008). The back scattered light beams from both OCT arms are then combined and registered as an axial A-scan (de Amorim Garcia Filho et al. 2013). Light travelled along with the object is collected as A-scans for further reconstruction to a B-scan (Figure 1.2a) (Swanson et al. 1993). Figure 1.2b depicts the fundus photography of the same patient and the green arrow shows the projection of the B-scan along the fovea. OCT produces two and three-dimensional images with its averaging after a series of scans are accomplished by using the optical sectioning capability of OCT (Huang et al. 1991; Hee et al. 1995).

1.1.2. OCT resolution

OCT can provide images with an axial resolution in the range of 1 – 15 μ m (Drexler and Fujimoto 2008) with the coherence length of the light source in OCT determining the spatial resolution of the device (Morgner et al. 2000). Current commercially available OCT devices use a light source centred at a wavelength of approximately 840nm and their axial resolution is about 5 μ m (de Amorim Garcia Filho et al. 2013).

At the same time, laboratory-based OCT with broadband light sources has an axial resolution from 10 μ m to 2 μ m (Gabriele et al. 2011). Ultrahigh-resolution OCT allows imaging of the biological tissue structure with the axial resolution of 2–3 μ m (Drexler et al. 2001). One of the

limitations for the lateral resolution of OCT devices (about $20\mu\text{m}$) is the diffraction from the pupil (de Amorim Garcia Filho et al. 2013).

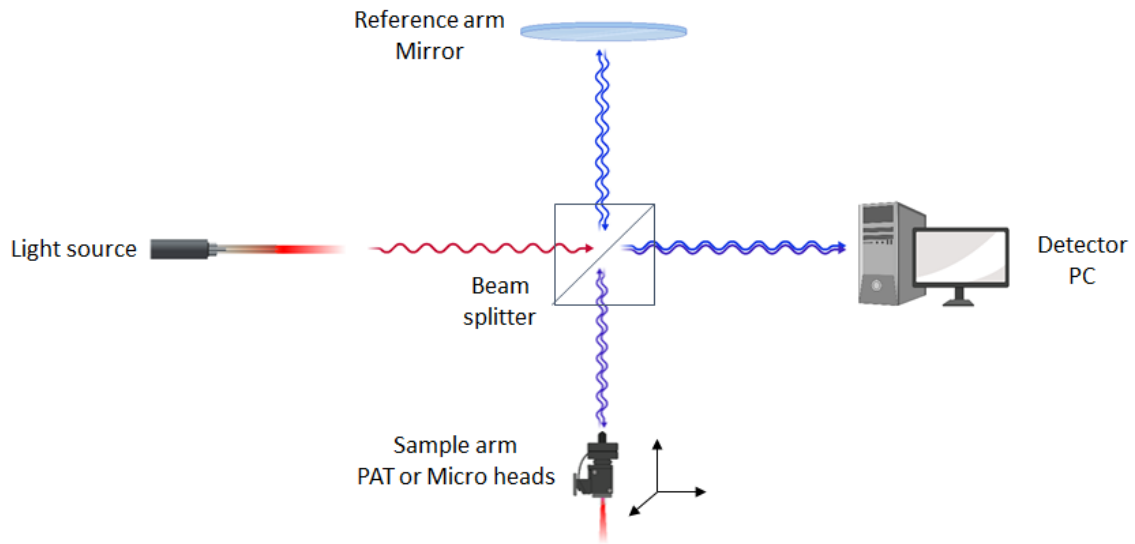


Figure 1.1. Lab-based OCT system structure. Coherent light from a laser source travels to the beam splitter (interferometer) and divided into two waves directing to both arms: 1. Moving mirror of reference arm; 2. Sample arm, which can be adjusted to scan in vivo human eye (PAT – patient) and ex vivo explants or in vitro samples (Micro – microscopy). Then reflected light is collected from both arms and directed to the detector. Created with BioRender.com

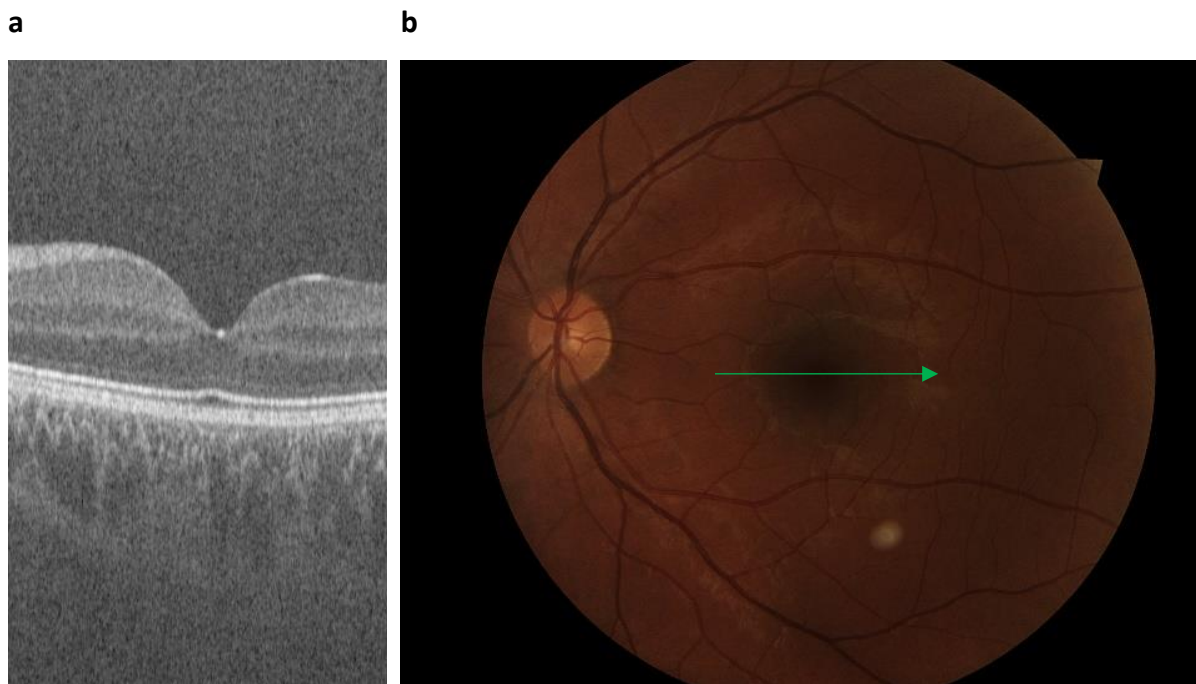


Figure 1.2. OCT image acquired by OCT-1040nm with the corresponding fundus image. a – OCT image through the macula of a healthy retina. b – fundus photo of the same patient's retina.

1.2. OCT anatomy of the retina

The retina comprises a complex multi-layered network of nerve cells with a combined thickness of 0.4 mm (Malhotra et al. 2011; Garhart and Lakshminarayanan 2016). Retinal neurons are the sensory part of the visual system that perceives the light and colour signals from the external world (Smerdon 2000; Westwood 2009). There are 3 cell layers in the retina represented by retinal ganglion cells (RGCs), bipolar cells and photoreceptors – rods and cones (Polyak 1949) (Pellegrino de Iraldi and Jaim Etcheverry 1967; Sung and Chuang 2010; Tian et al. 2017). The fovea is characterized by a high density of cones and the absence of rods (Schultze 1866). The plexiform layers of the retina consist of axons and dendrites of the corresponding retinal neurons and also amacrine and horizontal cells called interneurons (Figure 1.3) (Boycott et al. 1975; Pascale et al. 2012; Purnyn 2013).

The retinal ganglion cell complex (GCC) extends from the internal limiting membrane (ILM) to the inner nuclear layer (INL) (Kim et al. 2011). The inner plexiform layer (IPL) separates the INL from the retinal ganglion cells layer (GCL) and consists of a tangle of intricately branched and intertwining neuronal processes (Quigley et al. 1989; Tan et al. 2009). RGCs are located in the inner layers of the retina, the thickness of which decreases noticeably toward the periphery. The retinal nerve fibre layer (RNFL) consists of ganglion cell axons that exit the eye to form the optic nerve head (ONH) (Lee et al. 2015).

The sizes of RGC somas vary with retinal eccentricity. Moreover, the most prominent specialization of retinal topography and the majority of ganglion cells are located in the foveal area (Stone and Johnston 1981; Dowling 1987; Wässle and Boycott 1991). To the periphery, on the contrary, the number of RGCs drops sharply. This reflects the fact that in fovea there is an almost one-to-one correspondence between photoreceptors and ganglion cells, on the periphery, there is a strong convergence of photoreceptors to bipolar cells and bipolar cells to one ganglion cell (Perry and Cowey 1985; Curcio et al. 1990). Also, due to the projection of signals to the various layers of the lateral geniculate nucleus (LGN), there are two types of RGCs: parasol cells projects to magnocellular and midget cells – to parvocellular layers of LGN.

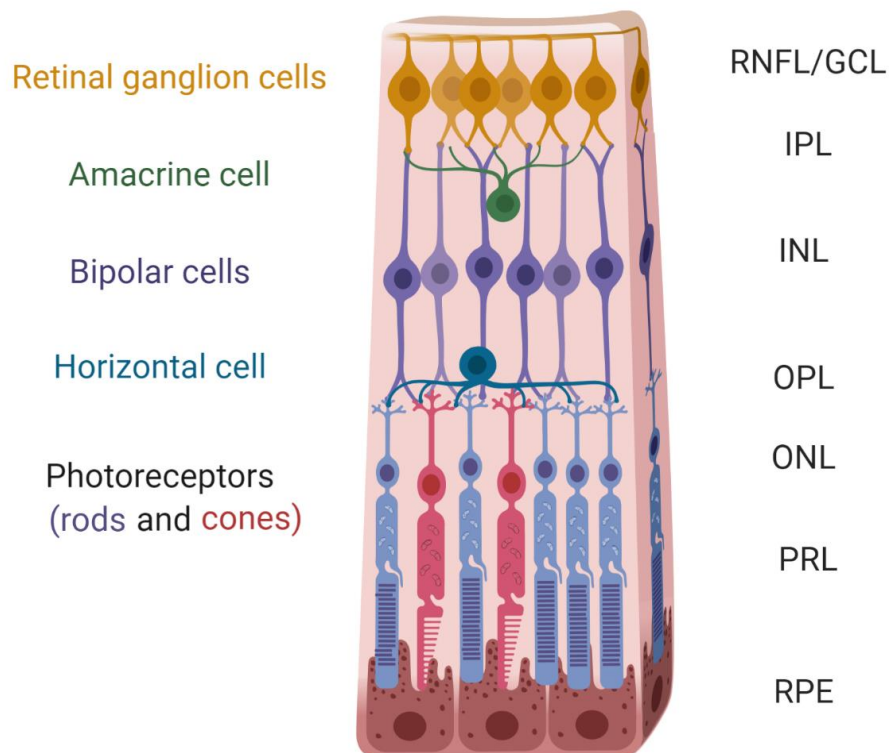


Figure 1.3. The schematic structure of the retina. 3 layers of neurons with amacrine and horizontal cells. Layers: RNFL – retinal nerve fibre layer; GCL –ganglion cell layer; IPL – inner plexiform layer; INL – inner nuclear layer; OPL – outer plexiform layer; ONL – outer nuclear layer; PRL – photoreceptor layer; RPE – retinal pigment epithelium. Created with BioRender.com

Axons of RGCs remain unmyelinated in the retina because of the need to maintain transparency (Yang et al. 2013). In the ONH, they form nerve fascicles that pass through the lamina cribrosa (LC) (Morgan 2004). As they emerge from the LC, these nerve fibres acquire a myelin sheath, which dramatically increases the diameter of the post laminar optic nerve (Elkington et al. 1990).

The LC is a sieve-like structure at the level of the sclera of the eye. In normal eyes, the LC is partly obscured by the axons of the retinal ganglion cells (RGCs) with only a small portion of LC visible using OCT (Morgan-Davies et al. 2004; Chauhan et al. 2013). Due to the pressure differences between the eye and the retrobulbar space, the LC provides structural and functional support to the axons of ganglion cells (Radius 1981; Zeimer and Ogura 1989). During glaucoma, the LC is the primary region of injury due to elevated IOP (Quigley et al. 1989; Quigley 1993; Tian et al. 2017).

The layered structure of the retina is visible in OCT images (Figure 1.4): RNFL and GCL are reflective and are seen as bright colours on a false-colour scale, whereas INL and ONL appear hypo-reflective, while IPL and OPL with axons and dendrites of retinal neurons are hyper-reflective (Drexler et al. 2001). As can be seen in Figure 1.4, the OCT morphology of the retina correlates well with the tissue microscopy images. The contrast in the reflectivity of biological structures affects the resolution of the retina and it can be used for the differentiation of the normal and pathologic states of the organ (Toth et al. 1997).

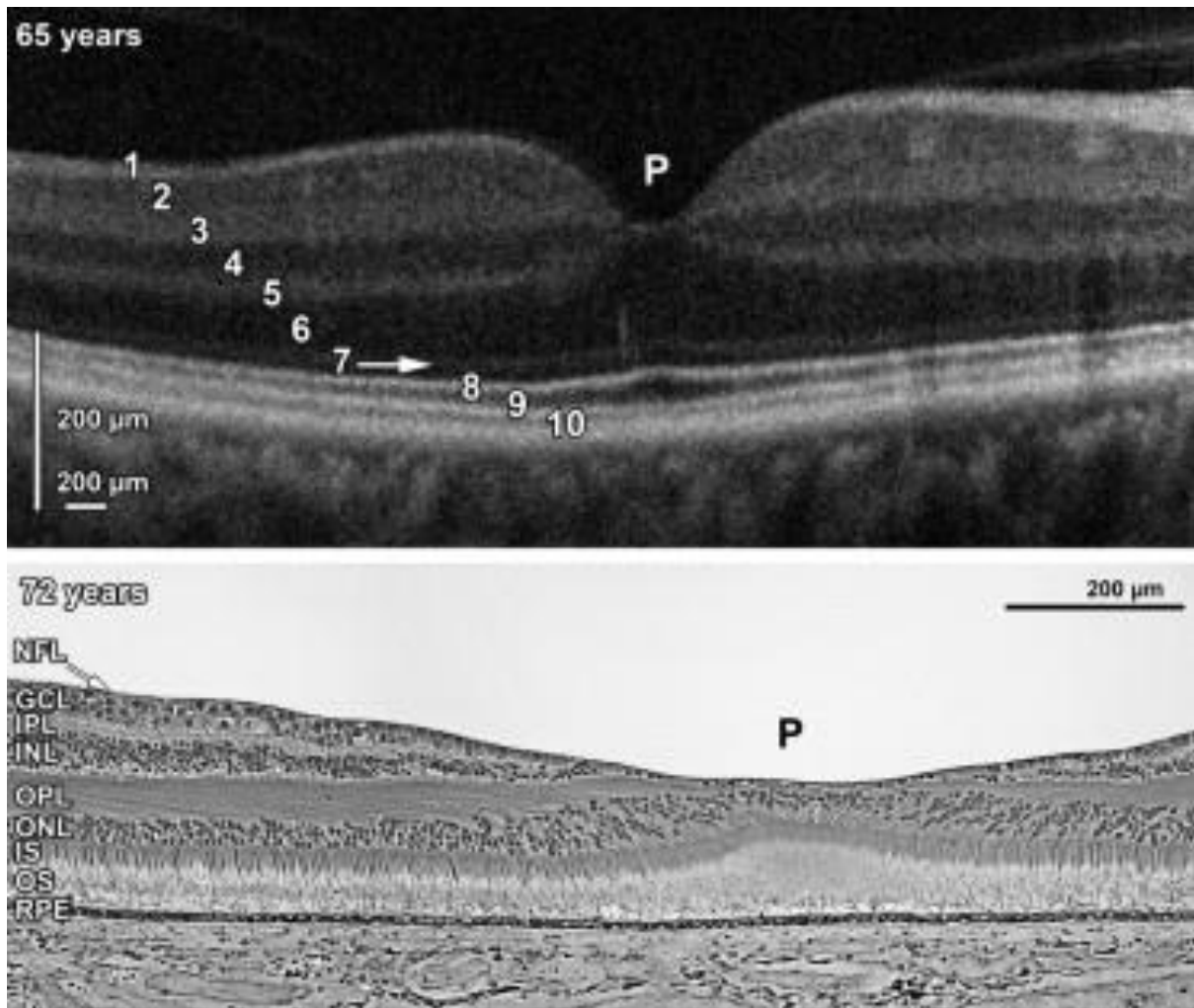


Figure 1.4. Top – OCT image of the normal human macula (65 years), bottom – histologic micrograph of the normal macula (72 years). 1–10 bands in the micrograph correspond to 1. NFL – nerve fibre layer; 2. GCL –ganglion cell layer; 3. IPL – inner plexiform layer; 4. INL – inner nuclear layer; 5. OPL – outer plexiform layer; 6. ONL – outer nuclear layer; 7. ELM – external limiting membrane; 8. IS PR – inner segments of the photoreceptors; 9. OS PR – outer segments of the photoreceptors; 10. RPE – retinal pigment epithelium; P – foveal pit. Images reproduced with permission from (Vajzovic et al. 2012).

1.2.1. Cellular scattering contribution to OCT signal

Scatterers of OCT light from the back-reflected retina can be multiple tissue components, including cell organelles, proteins, lipids and extracellular matrix constituents (Mourant et al. 1998; Wang and Tuchin 2013). Generally, the scattering may depend on the morphological and optical properties of the sample (Ejofodomi 2014; Sun et al. 2020). Light distribution and the spatial variation of the refractive index of the materials influence the scattering and absorption coefficients (Beuthan et al. 1996). While the refractive index of the whole cell equals 1.38, a significant contribution to light scattering belongs to the membranous organelles, the index of refraction of which amounts to 1.48 (Beuthan et al. 1996) (Figure 1.5). For instance, the regions with the mitochondria provide 90% of scattering reflection (Gourley et al. 2005). The membrane of the cell and organelles contains phospholipid polymers, which are the sources of scattering (Beuthan et al. 1996; Mourant et al. 2000; van der Meer et al. 2010).

According to the Gladstone-Dale equation, the cellular refractive index n is proportional to the local macromolecular mass density (1.1) (Barer and Tkaczyk 1954; Davies et al. 1954; Yi et al. 2016).

$$n = n_0 + \rho\alpha, (1.1)$$

where n_0 is the refractive index of water, ρ is the local mass density of macromolecules (g/ml), α is the refractive index increment (ml/g). For biological materials, this value is approximately 0.17 ml/g (Cherkezyan et al. 2012). Due to the varied distribution of mass density, the local differences in refractive index backscattered light is detectable due to elastic scattering (Beuthan et al. 1996).

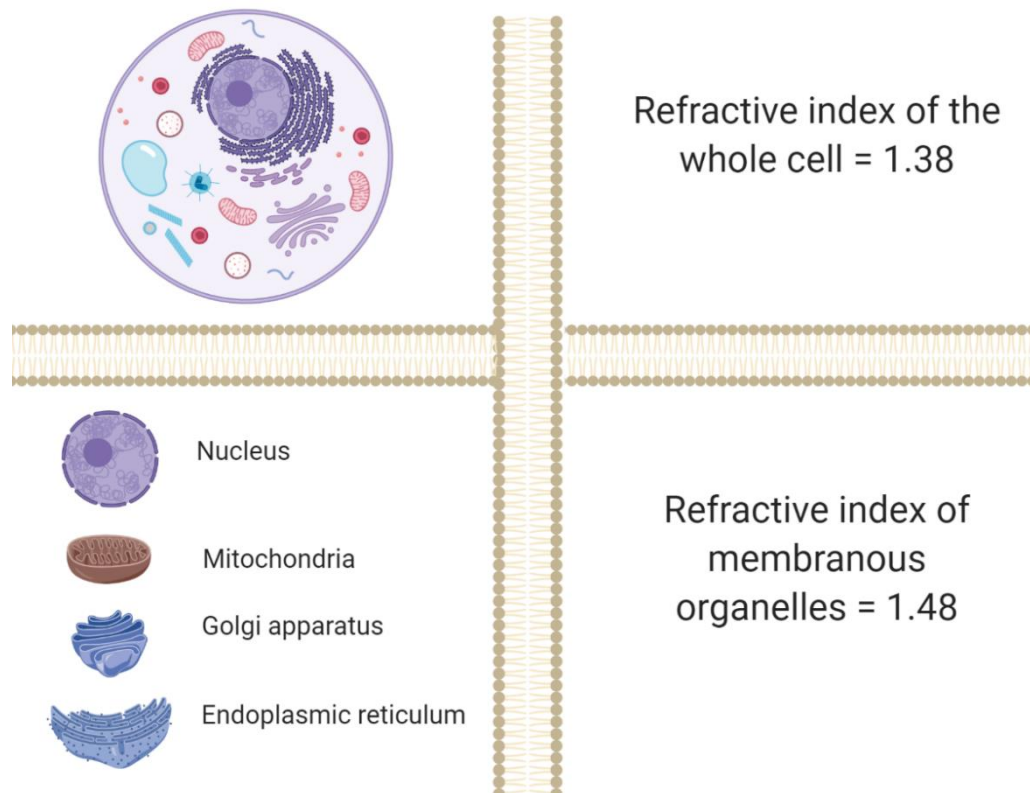


Figure 1.5. Scattering contribution of a cell. Individual organelles with phospholipid membrane have a higher refractive index than the overall index of refraction of the cell

1.3. Inner retina neurodegeneration

Neurodegeneration of the inner retina is one of the major causes of the pathogenesis of most diseases affecting the ocular fundus (Wert et al. 2014). Such ophthalmic and neuronal diseases as glaucoma, diabetic retinopathy, multiple sclerosis, Alzheimer's disease and Parkinson's disease often lead to vision impairment and loss of function of RGCs (Blanks et al. 1989; Kern and Barber 2008; Ozawa et al. 2011; Albrecht et al. 2012; van Dijk et al. 2012; Klistorner et al. 2017; La Morgia et al. 2017; Bevan et al. 2020; Catalani and Cervia 2020). In glaucoma, RGC apoptosis was reported by Kerrigan et al. (1997) after identifying TUNEL (terminal deoxynucleotidyl transferase-mediated deoxyuridine triphosphate (UTP)-biotin nick end-labelling) positive cells.

1.3.1. RGC apoptosis

Mitochondria are involved in multiple functions of the cell: generation of adenosine triphosphate, mineral homeostasis (especially Ca^{2+}), reactive oxygen production, specialisation and maturation of the cell (Giorgi et al. 2012; Zorov et al. 2014; Xavier et al. 2016). Due to the high energy-consuming nature of apoptosis, in the initiation of the cell death, mitochondrial fission is involved (Perfettini et al. 2005; Youle and Karbowski 2005) with associated changes in mitochondrial morphology (tiny spheres, reticular network) arising from the balance between fusion and fission (Chan 2006). This is a dynamic process that is mediated by mitochondrial proteins (Okamoto and Shaw 2005). Before caspase activation under the translocation of dynamin-related protein 1 (from the cytosol to mitochondria) the fragmentation of tubular mitochondria into numerous punctiform organelles begins in apoptotic cells (Figure 1.6) (Frank et al. 2001; Shim et al. 2016).

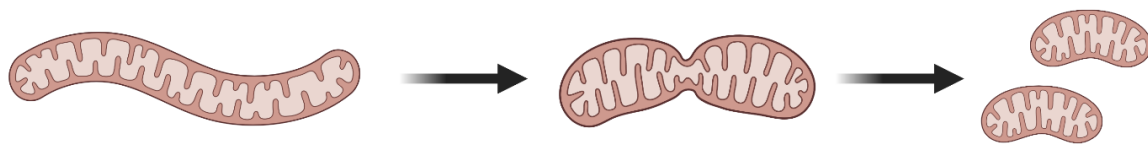


Figure 1.6. Mitochondrial fission during RGC degeneration. Created with BioRender.com

1.3.2. Glaucoma

Retinal neurodegeneration in glaucoma is often associated with a constant effect of increased intraocular pressure (IOP) (Frankfort et al. 2013). Multiple subcellular events of changing organelles' morphology and function at the onset of the disease may lead to large structural irreversible changes in a more progressive stage of glaucoma (Almasieh et al. 2012; Morgan et al. 2017).

Glaucoma is a group of diseases manifested by the excavation of the optic nerve head and deterioration of the visual field (Quigley and Broman 2006; Quigley 2011; Jonas et al. 2017), leading to irreversible blindness (Coleman 1999). An increase in the cup-to-disc ratio is a consequence of RGC axon damage (Quigley 2011). The common pathogenetic signs of the disease are a slow and imperceptibly progressive degeneration of the optic nerve (Foster et al. 2002), usually associated with a chronic increase of IOP (Armaly 1969; Sommer et al. 1991a), loss of RGCs, RNFL thinning (Jonas et al. 2017), initiated by the apoptosis of RGCs (Garcia-Valenzuela et al. 1994).

The currently available treatments of glaucoma are mainly focused on the reduction of elevated IOP (Heijl 2015). However, the relationship between increased IOP and the onset of glaucoma is complicated. Furthermore, the clinical manifestations occur after significant glaucomatous damage of the retina. For that reason, the early detection of retinal damage is essential (Morgan et al. 2017).

According to the state of the anterior chamber angle, there are two main morphological forms of glaucoma (Foster 2001; Quigley 2011): open-angle glaucoma and angle-closure glaucoma. Primary open-angle glaucoma (POAG) is a chronic, progressive irreversible optic neuropathy,

resulting in acquired atrophy of the optic nerve (loss of RGCs axons). The disease in the majority of cases is bilateral, usually asymmetric (Jonas et al. 1999). Even though the majority of patients with glaucoma have higher than normal intraocular pressures, some patients have normal or low IOP (Tanna 2015; Mallick et al. 2016). Other symptoms of POAG are halos around the sources of light, blurred vision, rarely eye pain and asymptomatic central vision loss in the later stages of the disease (Sommer et al. 1991a). In a gonioscopic observation, the angle of the anterior chamber is open (Prum et al. 2016b). The cupping of the optic nerve head is visualised by ophthalmoscopy; and a visual field test allows the detection of loss of visual sensitivity (Quigley 1993; Nilforushan et al. 2016).

Primary angle-closure glaucoma (PACG) is a type of glaucoma with an acute raised eye pressure due to disruption of aqueous humour outflow by appositional or synechial closure of the angle of the anterior chamber (Foster 2001; Foster et al. 2002; Prum et al. 2016a; Wright et al. 2016). Although PACG is generally an acute, painful disease associated with vision impairment, more than 75% of patients do not have an urgent attack (Yip and Foster 2006). Except for high intraocular pressure, mid-dilated pupil, red-eye, or nausea and vomiting, a non-specific headache, eye pain, or halos around lights are manifestations of the PACG (Coleman 1999; Prum et al. 2016a).

The diagnosis of PACG requires a slit-lamp and gonioscopy lens to evaluate the angle of the anterior chamber to observe the trabecular meshwork (Alsbirk 1976; Coleman 1999). Gonioscopy mirrors within the lens enable the assessment of the width of the angle between the iris and the cornea at their junction; this is the region of outflow of intraocular fluid. This method allows the classification of the type of glaucoma: POAG or PACG. (Quigley 1993). Moreover, OCT also can be used to measure the angle of the anterior chamber for further differentiation (Ni Ni et al. 2014).

Recently, glaucoma has become the most frequent cause of irreversible blindness throughout the world (Bourne et al. 2013; Tham et al. 2014), including developing countries (Cedrone et al. 2008). Both POAG and PACG are generally present in older people and these numbers are progressively increasing (Quigley and Broman 2006; Quigley 2011). POAG is seven times more prevalent than PACG in the United States, and worldwide (Sommer et al. 1991b). On the other hand, the number of angle-closure glaucoma is higher in Asia (Quigley 1996). IOP lowering

treatment decelerates the progression of both types of glaucoma (Heijl et al. 2002). However, there is a demand to stop the disease in the early stages.

1.3.3. Alzheimer's disease

Apoptosis of RGCs may also occur in the early stages of Alzheimer's disease (AD) (Obulesu and Lakshmi 2014; Bell et al. 2020). The pathogenesis of AD is based on the processes of accumulation and deposition of β -amyloid in the brain, which leads to dysfunction of synapses and death of neurons (Peña et al. 2006; Murphy and LeVine 2010). AD is one of the most common causes of dementia in the elderly and senile people (Prince 2015). The prevalence of AD is steadily increasing with age, and, according to "World Alzheimer Report 2015: The Global Impact of Dementia" the incidence of the disease will reach 131.5 million by 2050 (Prince 2015).

Recently, there has been significant progress in the development of diagnostic tools for the pathophysiological manifestations of AD. New laboratory and neuroimaging diagnostic methods are used, such as determining the level of β -amyloid, tau protein and phosphorylated tau protein in cerebrospinal fluid, Positron emission tomography (PET) with the radioactive analogue of thioflavin T – Pittsburgh substance or PiB, and fluorodeoxyglucose (^{18}F -FDG) (Blennow 2004; Mosconi et al. 2010; Jia et al. 2011). ^{18}F -FDG PET allows the assessment of the metabolic rate of various parts of the brain. Moreover, the degree of atrophy of the cerebral cortex brain can be assessed using Magnetic resonance imaging (MRI) (Johnson et al. 2012).

β -amyloid deposition and neurofibrillary tangles lead to the loss of synapses, progressive deficiency of neurotransmitters and neurons, which in turn may cause the atrophy of the affected areas of the brain (Serrano-Pozo et al. 2011). This complex cascade of events contributes to the development of clinical symptoms of dementia.

Polymorphous amyloid is deposited on the walls of cerebral vessels and in the parenchyma of the brain in the form of the so-called "Senile plaques" (Cras et al. 1991; Murphy and LeVine 2010). One of the hypotheses explaining the consequent death of neurons adjacent to these plaques is the activation of neuronal calcium channels (Shirwany et al. 2007). Hence, there might be an increase of intracellular calcium and the development of free radical oxidation of

neuronal membranes (Jadiya et al. 2019). Additionally, a direct toxic effect of β -amyloid on glial structures is also possible. For instance, microglia and macrophages are activated as a result of the direct toxic action of amyloid in the study of (Ling et al. 1992).

According to the National Institute on Aging (NIA) at the National Institute of Health (NIH) and the Alzheimer's Association, it was proposed to distinguish three stages of AD: preclinical Alzheimer's disease (asymptomatic), mild cognitive impairment (MCI) due to AD, and dementia due to AD (Jack et al. 2018). This classification improves the accuracy of diagnosis at all stages of the disease due to the focus on biomarkers of AD, that appear in an onset of the disease as a molecular neuropathological manifestation of the disease.

Pathological biomarkers of AD – β -amyloid plaques and hyper-phosphorylated tau – play a major role in the pathogenesis of the disease (Shirwany et al. 2007; Serrano-Pozo et al. 2011; Grimaldi et al. 2018). These protein deposits have a toxic effect and cumulate in the CNS and retina, which lead to the loss of RGC (Chiasseu et al. 2017). AD biomarkers can be found in cerebrospinal fluid (Blennow 2004; Buerger et al. 2006; Tapiola et al. 2009). Also, the detection of proteins is available through brain imaging or post-mortem retina (James et al. 2015; den Haan et al. 2018). Thus, there is a demand for effective and early diagnosis methods. Here, the eye as a window to the brain can be used for this purpose (Lim et al. 2016).

Three genes PS1M146 V, APPSwe and MAPTP301L are mutated in triple-transgenic (3xTg) AD mouse model, encoding presenilin 1, amyloid precursor protein and tau, respectively (Chiasseu et al. 2017). In the study of (Grimaldi et al. 2018), the neurotoxic proteins were detected in the retina of the 3xTg-AD mouse model at a pre-symptomatic early stage of the disease. In addition, an increase of early-phase RGC apoptosis and oxidative stress in the 3xTg-AD mouse were detected by *in vivo* cSLO with fluorescent cell death marker labelling (Cordeiro et al. 2010).

Moreover, microglial alterations in the 3xTg-AD retina were investigated in the study of (Edwards et al. 2014): Müller cells were positively reacted to glial fibrillary acidic protein (GFAP), whereas astrocytes were positive for S100. These glial markers showed the retinal glia activation in the retina of a mouse model of AD (Neves et al. 2017).

Along with the functional changes in AD, thinning of the retina, especially RNFL is observed (Hart et al. 2016; Neves et al. 2017). However, in the study of (Lim et al. 2015), the thicknesses of parafoveal RNFL, INL and IPL were increased. The thickening of these layers, according to the authors, is the result of the inflammatory process and aggregation of beta-amyloid drusen (Kayabasi and Sergott 2015; Lim et al. 2015).

There is a demand for the broader application of OCT in the diagnosis of early retinal alterations of AD. Ophthalmic manifestations of AD may precede irreversible changes in the brain (Hart et al. 2016; Lim et al. 2016; Czakó et al. 2020), which increases the need for non-invasive ligand-free detection of the disease. RGC apoptosis in the 3xTg-AD mouse model will be investigated in Chapter 4.

1.4. Outer retina neurodegeneration

Apoptosis of photoreceptors may also cause irreversible changes in the tissue morphology (Remé et al. 2000). Age-related macular degeneration (Dunaief et al. 2002; Ding et al. 2009; Telegina et al. 2017), pigment dystrophies (Tso et al. 1994; Travis 1998), retinal detachment (Lo et al. 2011; Murakami et al. 2013) and other diseases are the consequences of retinal and RPE cell death (Huang et al. 2014; Wert et al. 2014).

1.4.1. Photoreceptor and RPE apoptosis

The RPE plays a major role in the homeostasis of the neural retina and particularly photoreceptors (Fuhrmann et al. 2014). For instance, RPE cells absorb light photons that pass through the retina due to the presence of melanosomes (Herman and Steinberg 1982; Burgoyne et al. 2015). This absorption minimises the back scattering of light to the inner tissues (Prieto et al. 2005; Strauss 2005). While the products of photoreceptors' metabolism are ingested by RPE cells with further production of lipofuscin (Herman and Steinberg 1982; Katz et al. 1986; Kennedy et al. 1995) the accumulation of lipofuscin may lead to RPE dysfunction and contribute to age-related retinal degeneration (AMD) (Dorey et al. 1989), which recently was mathematically detected by using combined OCT and fundus autofluorescence in the study of (Nafar et al. 2020).

RPE cells envelop the distal tips of photoreceptors' outer segments (OS) (Lai et al. 1982), where the visual pigments are located (Young 1967). Through isthmus OS is connected with the inner segment (IS) of photoreceptor, that accommodates cell organelles: mitochondria, Golgi apparatus and endoplasmic reticulum. Nucleus and axonal synaptic terminals of photoreceptors are present in the cell body (De Robertis and Lasansky 1958).

Mitochondria in photoreceptors are mainly located in the IS (Figure 1.7) and mediate intercellular communication through mitochondria:plasma membrane tethers and factors regulating the cristae alignment (Meschede et al. 2020). According to Beuthan et al. (1996), membranous organelles have a great potential for the scattering of light due to the presence of the phospholipid bilayer. If mitochondria play the role of the scatterer in the IS of photoreceptors, nuclei may also contribute to the optical signature of the ONL of the retina.

Understanding the cellular and subcellular mechanisms of apoptosis may allow us to predict the changes in the OCT scans.

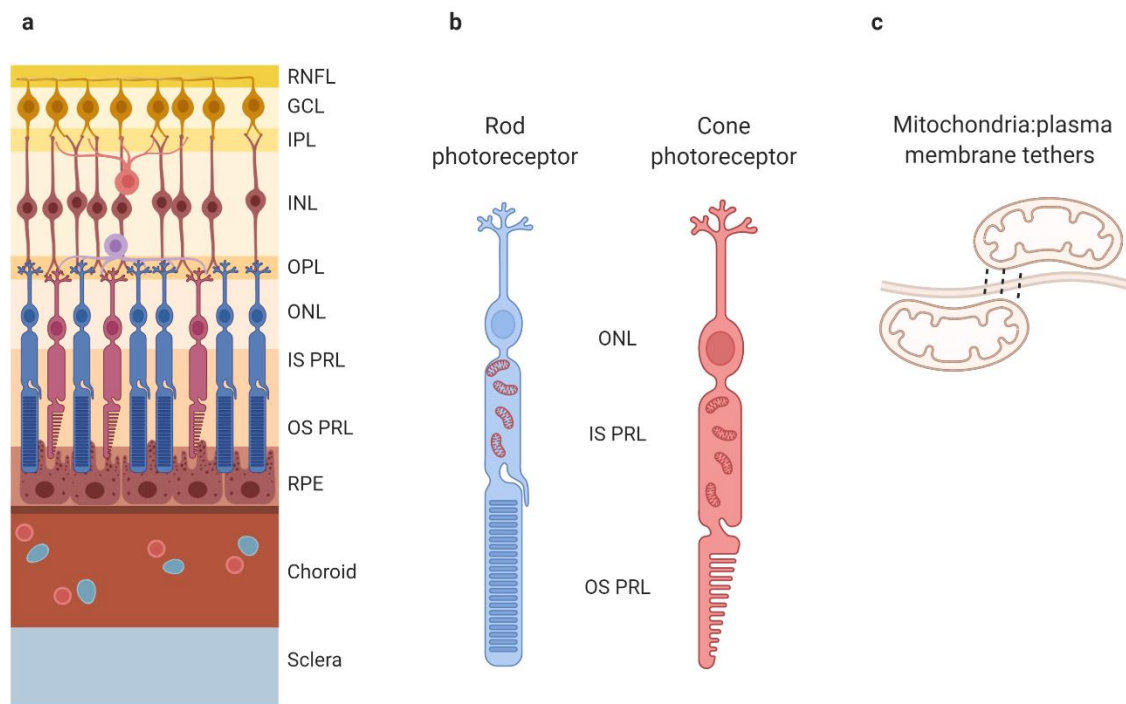


Figure 1.7. Photoreceptors: a – retinal structure scheme; b – rod and cone photoreceptors; c - mitochondria:plasma membrane tethers, which is the way of intercellular interaction. Created with BioRender.com

Other sources of light scatter include drusen and reticular pseudodrusen (Spaide and Curcio 2010; Greferath et al. 2016), usually located in the basal and apical sides of the RPE (Peng et al. 2003; Paavo et al. 2017). Formation of drusen in the subretinal or sub-RPE areas is the earliest sign of AMD (García-Layana et al. 2017). The genesis of drusen is complex and multiple constituent materials include lipid and other metabolic product depositions, inflammatory and proliferative immune cell proteins, and degenerated RPE cell debris (Velez-Montoya et al. 2014). Drusen can be detected using retinal colour photography (Kirkpatrick et al. 1995). Automated detection of the drusen was achieved by (Rapantzikos et al. 2003), however, classification of the drusen subtypes has not been performed.

1.4.2. Age-related macular degeneration

AMD is a chronic multifactorial progressive disease that affects the macula and leads to loss of central vision (Marshall 1987). The symptoms of AMD are complex and irregular (Bressler et al. 1988). In the early stages of the disease, patients are relatively asymptomatic (Milam et al. 2000). However, as the disease progresses, there may be manifestations such as sudden loss of vision, which cannot be corrected with glasses and the appearance of a grey or dark spot in front of the eye (positive scotoma) (Bressler et al. 1988; Klein 1991).

AMD occupies one of the leading positions among the causes of blindness and low vision worldwide (la Cour et al. 2002). Age, genetic and ethnic predispositions, smoking, excessive solar exposure, arterial hypertension, unbalanced diet and disorders in lipid metabolism can be considered as risk factors for the onset of AMD (Smith et al. 2001).

Despite the numerous studies devoted to AMD, the aetiology of the disease remains unclear. As an example of the ageing process, the incidence of AMD is directly dependent on age. An essential role in the pathogenesis of AMD has been attributed to oxidative stress (Beatty et al. 2000). The former consists of damage to the tissues of the eye due to the imbalance in the system of formation of free radicals and antioxidant protection (Tokarz et al. 2013; Lambert et al. 2016). The toxic effect of free radicals is realised through damage to the lipids and proteins of the cell membrane and transmembrane glycoproteins (Ding et al. 2009).

Multiple factors determine the retinal sensitivity to the products of oxidative stress and free radicals. Firstly, the combined action of constant light and oxygen exposure to the retina

creates ideal conditions for the synthesis of free radicals (Jarrett and Boulton 2012). Also, a considerable amount of polyunsaturated fatty acids contained here are highly sensitive to oxidation (Saccà et al. 2018).

Depending on symptoms and pathogenesis, there are 2 types of AMD, which can be also accepted as the stages of the disease: dry and wet (Bird et al. 1995; Adler et al. 1999; la Cour et al. 2002; Handa et al. 2019). In AMD, damage begins in the RPE and Bruch's membrane (Bonilha 2008; Bhutto and Lutty 2012). Due to ageing, products of ocular metabolism accumulate under the RPE and form drusen (Johnson et al. 2003; Ebrahimi and Handa 2011; Bowes Rickman et al. 2013; Brown et al. 2018).

As drusen accumulate, they can trigger inflammatory processes in the retina, with the production of vascular endothelial growth factor (VEGF) (Saint-Geniez et al. 2009; Stefánsson et al. 2011; Jiang et al. 2012; Kauppinen et al. 2016). VEGF promotes pathological neovascularisation from the choroid under the retina (Cabral et al. 2017; Yeo et al. 2019). At this stage, the dry form turns into the wet form of AMD (or neovascular AMD, n-AMD).

The endothelium of the newly formed choroidal vessels are weak and the plasma of the blood transfer to the intercellular space, causing retinal oedema (Julien et al. 2008; Campochiaro 2015; Daruich et al. 2018). These vessels can rupture at any time and cause haemorrhage under the retina or between layers, which have an additional damaging effect on the photoreceptors of the retina (Bhutto and Lutty 2012; Sun and Smith 2018). Furthermore, a haemorrhage can provoke the formation of scar tissue, which will lead to the irreversible loss of central vision (Coco and Sala-Puigdollers 2014).

1.5. Texture and texture analysis of OCT scans

Apoptosis of retinal cells induces a cascade of irreversible functional and morphological alterations in the early aetiopathogenesis of neurodegenerative diseases (Adler et al. 1999; Nickells 1999; Remé et al. 2000; Dunaief et al. 2002; Guo et al. 2005; Lo et al. 2011; Almasieh et al. 2012; Ahmad 2017; Bell et al. 2020). The role of membranous organelles, especially mitochondria is high in cell death and they have been shown to generate an optical signal in OCT images (Tso et al. 1994; Okamoto and Shaw 2005; Perfettini et al. 2005; Youle and Karbowski 2005; Zhang et al. 2019). Hence, these scatterers may help to detect retinal degeneration in pre-clinical stages of glaucoma, AD and AMD.

A number of optical techniques have been deployed to identify mitochondria-rich regions in the cells. These include a thresholding approach and texture-based segmentation (Pasternack et al. 2011; Mohammad et al. 2018). Threshold-based technology was used in the study of Pasternack et al., and they concluded that the mitochondria are the likeliest source of the changes in optical scatter in the first three hours of programmed cell death (Pasternack et al. 2010). The reason for these changes might be the structural and functional alterations in mitochondria.

For the purpose of detection of the earliest changes in RGC apoptosis, studies have included *in vivo* detection of apoptosis by Positron-emission tomography (PET) with marker ¹⁸F-labelled NST-732 (ApoTrace®) (Aloya et al. 2006), confocal scanning laser ophthalmoscopy (cSLO) using fluorescent annexin A5 (Ahmad 2017; Yap et al. 2018) and *in vivo* confocal neuroimaging (ICON), that allows monitoring the morphology and function of RGC (Prilloff et al. 2010). It has been suggested that programmed cell death can be quantified using the Detection of Apoptotic Retinal Cells (DARC) method in which fluorescently labelled protein Annexin-A5 binds to the apoptotic membrane phospholipid phosphatidylserine (Cordeiro 2007; Galvao et al. 2013; Yap et al. 2018). However, since this technique cannot quantify the number of remaining RGCs it is unclear how DARC can determine the proportion of dying cells. Moreover, DARC requires external ligands and intravenous injections at every patient visit, which may be impractical and unfavourable.

Labelling of externalised phosphatidylserine in apoptosis of photoreceptors was conducted in the study of Mazzoni et al. (2019). Here, they used Bis(zinc(II)-dipicolylamine (Zn-DPA) with

Texas-red (PSVue-550) to label the dying rods and cones. Also, the contribution of RPE apoptosis in the pathogenesis of AMD is significant (Wang et al. 2012), which was characterised by *in vivo* morphometry and multispectral autofluorescence (Granger et al. 2018).

All the named studies and other approaches of *in vivo* observation of retinal cell apoptosis, however, are dependent on using external ligands, which may be toxic or cause inflammatory reactions. Consequently, there is a great demand for diagnostic methods that can detect and quantify retinal neuron apoptosis on a subcellular level without exogenous ligands to label cells. For visualisation in clinical conditions of RGC, photoreceptors and RPE cell degeneration, it is necessary to use ultrahigh-resolution OCT imaging. However, OCT is used mainly for the assessment of the morphology of tissues, its thickness values and presence of signs and symptoms of diseases: oedema, neovascularization, drusen, tissue detachments and others (Toth et al. 1997; Unterhuber et al. 2005; Tan et al. 2009; Zweifel et al. 2010; Cheour et al. 2013; Leuschen et al. 2013).

The most common computational method of OCT scan analysis is the segmentation of the retinal layers and local anatomical pathological structures (Rapantzikos et al. 2003; Haeker et al. 2007; Garvin et al. 2009; Baumann et al. 2010; Kajić et al. 2010; Zhang et al. 2012; Lee et al. 2018). The measurement of retinal layer thickness and segmentation techniques relies on the detection of the boundary of layers, which is facilitated by the removal of image noise. The noise has little value with lower resolution forms of OCT. With high-resolution devices, however, it is likely that an increasing component of this signal is not noise but reflects the subcellular changes in optical scattering. These alterations can be investigated using texture analysis of OCT images (Gossage et al. 2003; Anantrasirichai et al. 2013; González-López et al. 2015).

Texture is a measure of regional variations in brightness, intensity and surface roughness of a small location of an image (Oberholzer et al. 1996; Gossage et al. 2003). The texture of an image demonstrates the spatial variation of pixel intensities (Nailon 2010) and each region in an image may have a constant unique texture. The former is true if a set of local statistics and other structural properties are constant, slightly varying, or approximately periodic (Chen, Pau and Wang, 1993).

Texture analysis is the characterisation of image properties by their features (Evennett et al. 1993). The aim of this analysis is the recognition of homogeneous regions of an image using textural properties (Davies 2005). This method is frequently used in classification (Bhattacharjee et al. 2011; Anantrasirichai et al. 2013), segmentation (Kajić et al. 2010; González-López et al. 2015) and synthesis (Costantini et al. 2008) of OCT images. The purpose of a classification method in image processing is to categorise different image regions into distinct groups or classes (Dong et al. 2017). The technique provides unique information on the spatial variation of pixels (texture) (Pietikainen 2000) and produces a classification map of the input image. Then each uniform textured region is identified with the texture group or class it belongs to.

Apart from that, texture analysis has been used to establish boundaries between different image regions (segmentation) and generate highly complex and realistic looking 2D and 3D surfaces of images (synthesis) (Pentland 1984; Mirmehdi et al. 2009).

Techniques of pixel variation analysis can be divided into 3 groups: statistical approaches, spectral technologies and structural technologies. The majority of statistical methods for texture analysis are based on histograms of image regions and their moments (Ramola et al. 2020). Examples of these features are coarseness and contrast. The goal of spectral techniques is to detect texture periodicity, orientation, etc., based on the power spectrum of a region (Humeau-Heurtier 2019). Spectral features extract the data of an image with more complete respect to texture characteristics in comparison to the statistical approach.

Pattern primitives and placement rules to describe the texture are used in structural technologies (Gossage et al. 2003). While in the first-order statistical texture analysis the frequency of a particular grey-level at a random image position is measured, co-occurrences between neighbouring pixels are calculated in the second-order statistics. Therefore, expanding the number of variables requires higher-order statistical texture analysis (Nailon 2010).

Although the current available OCT system may not provide cellular and subcellular resolution, analysis of textural parameters has a promising future to measure aspects of cellularity in biological tissues. In the experimental chapters of this thesis, examples of textural feature analysis of OCT scans acquired *in vitro*, *ex vivo* and *in vivo* are provided.

1.6. Hypothesis and Aims

This thesis aims to investigate the early subtle optical changes of retinal neurodegeneration that occur in the apoptotic retina, glaucoma, age-related macular degeneration and Alzheimer's disease (AD) using high-resolution optical coherence tomography.

Early retinal apoptosis and analysis of retinal degeneration in AD will primarily be conducted in an *ex vivo* model of retinal axotomy in mouse retinal explants and triple transgenic AD mouse models respectively. Additionally, the OCT image datasets of *in vivo* human macula will be utilised to assess texture associated with RGC dendropathy in glaucoma and also apoptosis of photoreceptors with RPE cells in early and advanced stages of AMD. Texture analysis of OCT images will be achieved using machine-learning tools.

The principal hypothesis of this thesis is that the combined use of OCT imaging and machine-learning algorithms will enable the detection of early subtle optical changes that can act as surrogates for biological processes in neuronal degeneration. This thesis will therefore address 4 key aims and hypotheses presented as separate experimental chapters.

1. Different types of phantoms with varying concentrations of matrix material and scatterers, size and refractive indices of the particles generate distinctive textures. Chapter 3 contains the results of the analysis of the textures of various types of OCT phantoms using principal component analysis and support vector machine (SVM). The phantom classification technique not only allows to detection of these optical differences in phantoms but also can be then used for the classification of the OCT scans in further experimental and clinical studies. This was the first attempt to measure the textural properties of various polystyrene and silica beads optical phantoms.

Aim: To prepare various types of phantoms and to evaluate the performance of machine learning classifications: support vector machine (SVM) and principal component analysis.

2. After the validation of the SVM classifier accuracy, texture analysis of *ex vivo* OCT scans was carried out to monitor the early optical alterations of retinal ganglion cell apoptosis. The texture of the inner plexiform layer (IPL) of retinal explants changes after the transection of the optic nerve due to cell death. Also, the texture of the IPL layer of the 3xTg Alzheimer's disease mouse model is different from the texture of the IPL layer of the control animals. The

results of these studies are stated in Chapter 4. Not only the optical signature but also the transparency of the dissected murine retinal explants was investigated. Moreover, ML classification of 3xTg mice IPL layer was studied in terms of optical changes due to the RGD dendritic atrophy.

Aim: To analyse the texture of the IPL layer of mice retinal explants and detect the alterations of RGC dendrites in the first hours after axotomy. Moreover, the second aim of the chapter is to detect the textural differences of AD-related RGC dendrites neurodegeneration.

3. In Chapter 5, the texture of outer retinal layers of *in vivo* OCT scans of early and neovascular age-related macular degeneration were analysed. The outer nuclear and photoreceptor layer can describe the condition, viability and health of photoreceptors, whereas RPE is responsible for the retinal pigment epithelium. Due to the multiple factors, but predominantly because of apoptosis of photoreceptors and RPE cells, the texture of the outer retinal layers may change in age-related macular degeneration. Classification of AMD stages and comparison with the age-matched healthy controls was carried out in the outer retina and RPE.

Aim: To analyse the texture of the soma and dendrites of the photoreceptors (outer nuclear layer, inner and outer segments of photoreceptors) and RPE cells of healthy and AMD patients (early and neovascular stages).

4. It is possible to detect the optical changes in the inner layers of the retina driven by apoptosis (at early stages) with alterations of mitochondria (number and morphology). These changes cause modifications in the light scattering properties of the tissue and they can be diagnosed by OCT. The most vulnerable retinal layer in the onset of glaucoma is the IPL, which corresponds to the dendritic tree of the retinal ganglion cell. As it was demonstrated previously in the murine explant study, the axotomy causes changes in the IPL of the tissue. Hence, the aim of Chapter 6 is to investigate the optical signature of glaucomatous IPL and compare it with healthy human participants. In this study, the observation of early glaucomatous subtle optical changes of human IPL was conducted. Also, the significance of various supervised ML algorithms was investigated.

Aim: To detect the optical changes of the IPL in glaucoma and to evaluate the performance of each machine learning classifier.

Papers arising from this thesis (on submission)

M. Kulmaganbetov, Ryan J. Bevan, N. Anantrasirichai, Alin Achim, Irina Erchova, Nick White, Julie Albon, James E Morgan (2021) Textural feature analysis of optical coherence tomography phantoms. Status: submitted to the Biomedical Optics Express journal

Papers arising from this thesis (on draft)

M. Kulmaganbetov, Nick White, Julie Albon, James E Morgan. Retinal phantom materials for the optical coherence tomography (review paper). Status: the first draft is under the revision of the Supervisory team. Contribution chapter: Chapter 3

M. Kulmaganbetov, Ryan J. Bevan, Andrew Want, Julie Albon, James E Morgan. OCT-microscopy and texture analysis of murine retinal explant degeneration. Status: the first draft is under the revision of the Supervisory team. Contribution chapter: Chapter 4

M. Kulmaganbetov, Ashley Wood, N. Anantrasirichai, Alin Achim, Julie Albon, James E Morgan. Analysis of LBP and GLCM features in the outer retinal layers for machine learning classification of AMD. Status: the first draft is under the revision of the Supervisory team. Contribution chapter: Chapter 5

M. Kulmaganbetov, Ryan Bartlett, N. Anantrasirichai, Alin Achim, Julie Albon, James E Morgan. Comparison of machine learning algorithms in the detection of glaucoma. Status: the first draft is under the revision of the Supervisory team. Contribution chapter: Chapter 6

Abstract arising from this thesis

Mukhit Kulmaganbetov, N. Anantrasirichai, Alin Achim, Julie Albon, Nick White, James E Morgan (2020) Texture analysis of OCT phantoms. Invest. Ophthalmol. Vis. Sci. 61(7):2038.

Chapter 2. General Methods

2.1. Phantom preparation

The matrix of the phantom is the artificial media that mimics the intracellular space and cytoplasm of tissues and cells, respectively. Hence, the physical and chemical features must be equivalent to the liquid biological structures. Furthermore, it stores other chemicals (scatterers) with higher than media refractive index, that fills the area as the cell and nuclei membranes, as well as the organelles.

For the preparation of the OCT phantoms, a range of polymer materials with refractive indices that were close to those seen in the retina was selected: gelatin solution with polystyrene beads (PBs) and silica microparticles (SiO_2). These combinations are the most frequently used mixtures for optical phantom fabrication purposes (Nivetha and Sujatha 2017). They not only provide favourable optical properties but also transparency of samples. The selection of particles has also had a purpose to mimic organelles in terms of size and refractive index.

Hydrogel polymer gelatin (Sigma-Aldrich) served as a mechanical support matrix, whereas microspheres based on polystyrene (Sigma-Aldrich) and silicon dioxide (Sigma-Aldrich) were the light scatterers in the transparent media. The size of microparticles ranged from $0.38\mu\text{m}$ to $5\mu\text{m}$.

Figure 2.1 illustrates the general procedure of phantom fabrication, the principle of fabrication of which was adopted for all agents. Preparation of a 2% gelatin solution by adding bovine gelatin to heated (60°) distilled water to a concentration of 2%. The solution was then agitated using a vortex mixer periodically 5 times (1 min of mixing after 5 min of break) before cooling to room temperature. After that various volumes and sizes of PBs or SiO_2 (see Chapter 3) was added to the medium with further vortex agitation to ensure the random dispersion of microparticles and to avoid the clumping of either gelatin or the microspheres/microparticles.

To ensure both OCT and microscopy imaging of phantoms in a hydrated state, prepared phantoms were placed on a 14 mm (diameter) glass-bottomed 35 mm petri dish with (MatTek

Corporation, USA) to enable imaging from the top and bottom of phantom samples (see Section 2.4.2 below), respectively.

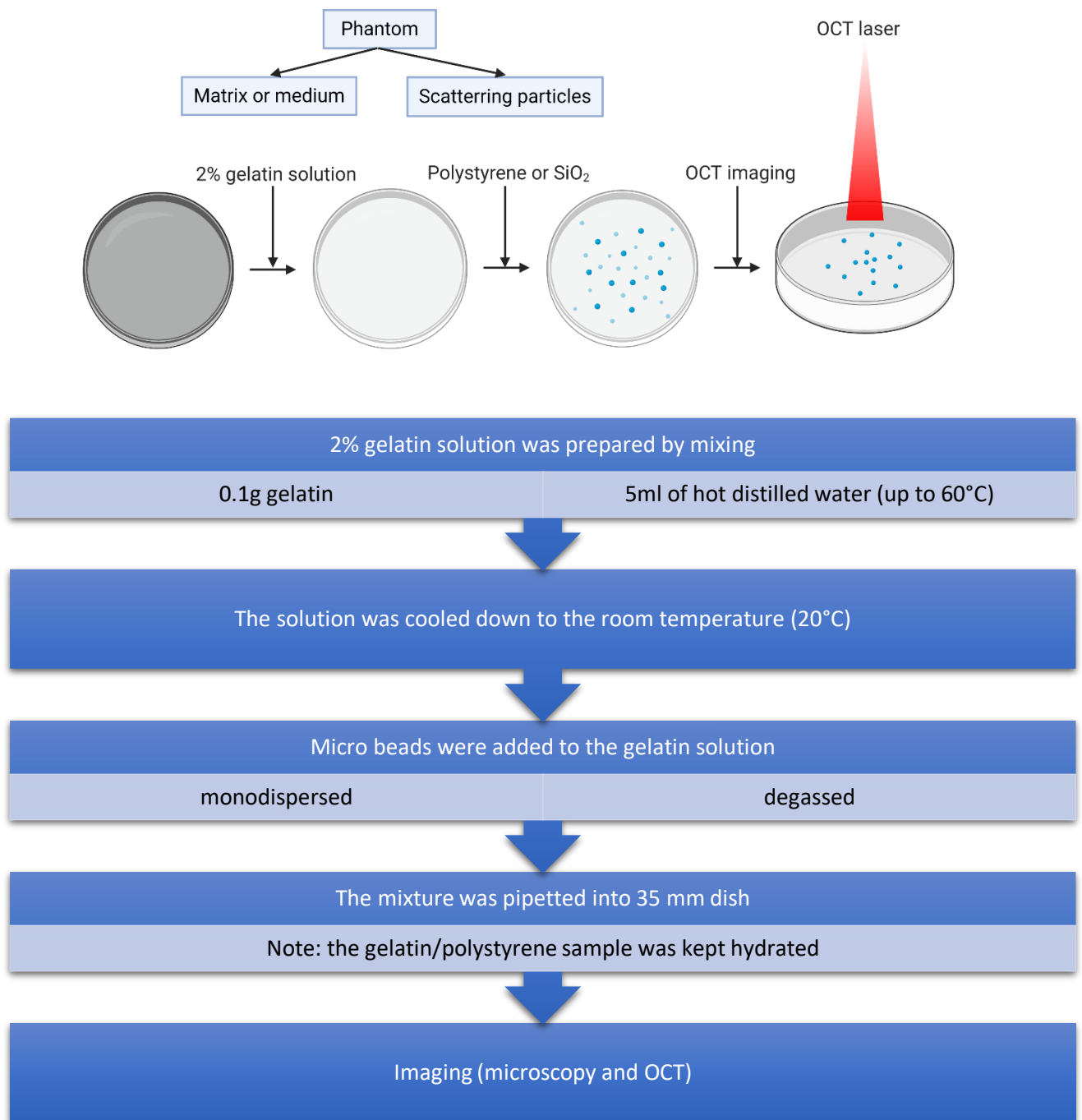


Figure 2.1. The preparation procedure of the optical phantoms and OCT scanning. Created with BioRender.com

2.2. Animal retina dissection

To study the main early pathogenetic pathway of most neurodegenerative diseases, enucleation and dissection of the murine eye were carried out. Transection of the optic nerve (i.e., axons of RGCs) may cause damage to the viability of RGCs, which starts from the dendrites (or else IPL in an OCT image). Thus, it allowed studying the earliest stages of apoptosis, which lies on the basis of glaucoma and AD.

All experiments conducted in this thesis were in accordance with Home Office regulations and the ARVO statement for use of Animals in Ophthalmic and Vision Research. 15 months old and older C57BL/6 mice and 3xTg mouse models were sacrificed by cervical dislocation (Schedule 1 Appropriate Methods of Humane Killing, United Kingdom Animal Scientific Procedures Act 1986).

After the enucleation, mice eyes were placed in Hank's balanced salt solution (HBSS, Life Technologies) for further dissection. A puncture of the limbus was performed to cut the outer eye layers, eliminate the lens, and dissect out the retina. The retina was transferred onto a petri-dish and 4 cuts were made in order to flatten the retina. The flat-mounted retina with ganglion cell layer up was visualized using OCT and the attached microscope module.

2.3. OCT imaging

The components of the spectral domain custom-developed research OCT device used for the acquisition of optical scans are shown in Figure 2.2. The light source 1-M-ASE-HPE-S (NP Photonics, Tucson, AZ, USA) had a central wavelength of 1040nm and a spectral bandwidth of 70nm (Figure 2.3). It was connected via 2x2 optical fibre coupler (FC; FOBC-2-64p/100-20-L-H64f-2; AFW Technologies, Hallam, Victoria, Australia) to sample and reference arms (Figure 2.4). Sample arm or imaging head included an achromatic off-axis parabolic reflector to collimate the fibre output beam to approximately 2mm diameter (RC02APC-P01; Thorlabs, Ely, UK), close-coupled 2D (XY) optical scanners (6210HBM60/6102103R; Cambridge Technology Division, GSI Group GmbH, Muenchner, Germany) and a broad-band near-infrared (NIR) telecentric scan lens (LSM02BB; Thorlabs). The reference arm comprised a polarization controller (PC; FPC560, Thorlabs), a second reflecting collimator (not shown; RC08APC-01; Thorlabs), an adjustable aperture (Ap), a precision NIR retroreflector (RR; 1 Arcsec Gold, Edmund Optics, York, UK) and a glass compensation block (CB; LSM02DC; Thorlabs) to correct for NIR dispersion in the scan lens. Reflected light from the sample and reference arm was combined in a spectrometer (Figure 2.5).

The sample and reference arms comprised fibres that were looped through a three-paddle polarization control to maximize fringe visibility. There are two inter-changeable sample arms: the patient module for imaging the human retina of a participant *in vivo* (OCT-PAT) and the microscopy stage module for tissue explants or chemical samples *ex vivo* or *in vitro* (OCT-M). OCT-PAT has achromatic doublet transfer optics and short pass dichroic mirror, whereas OCT-M consists of a 10x telecentric scan lens (Thorlabs LSM02-BB) giving a lateral resolution of $\sim 10\mu\text{m}$ in air and a field of view of 4.7mm.

The beams from the sample and reference arms were focused and spatially dispersed by 2 spherical dielectric coated mirrors and a grating (1200 lines per mm, 36° blaze angle). Then, the backscattered light was detected by a line scan camera Goodrich SU-LDH-1.7 (UTC Aerospace Systems, Arlington, VA, USA) (1024 pixel) operating at 47,000 acquisitions per second with a peak quantum efficiency of 70%.

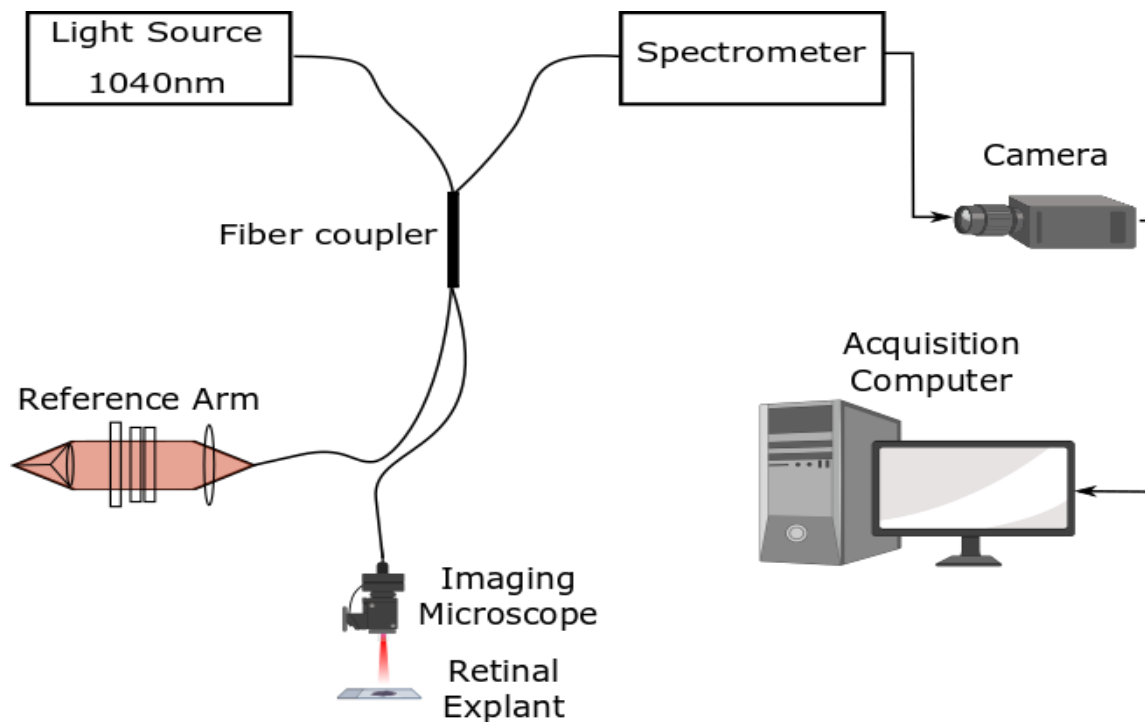


Figure 2.2. Schematic of the OCT-1040nm. Amplified Spontaneous Emission light source has the central wavelength of 1040nm with a spectrum range of 1000-1070nm. 2x2 fibre coupler divides the coherent light to the sample (Imaging microscope) and reference arms. Then reflected light is collected in a spectrometer for further transfer to the detector (camera and PC). Created with BioRender.com

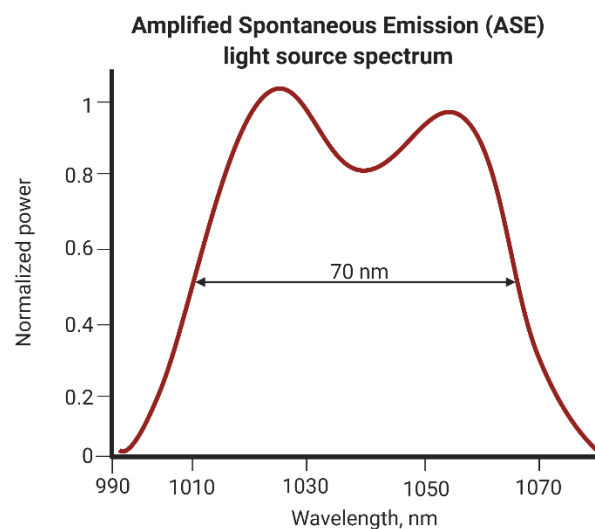


Figure 2.3. The optical spectrum of the light source with a central wavelength of 1040nm and a spectral bandwidth of 70nm.

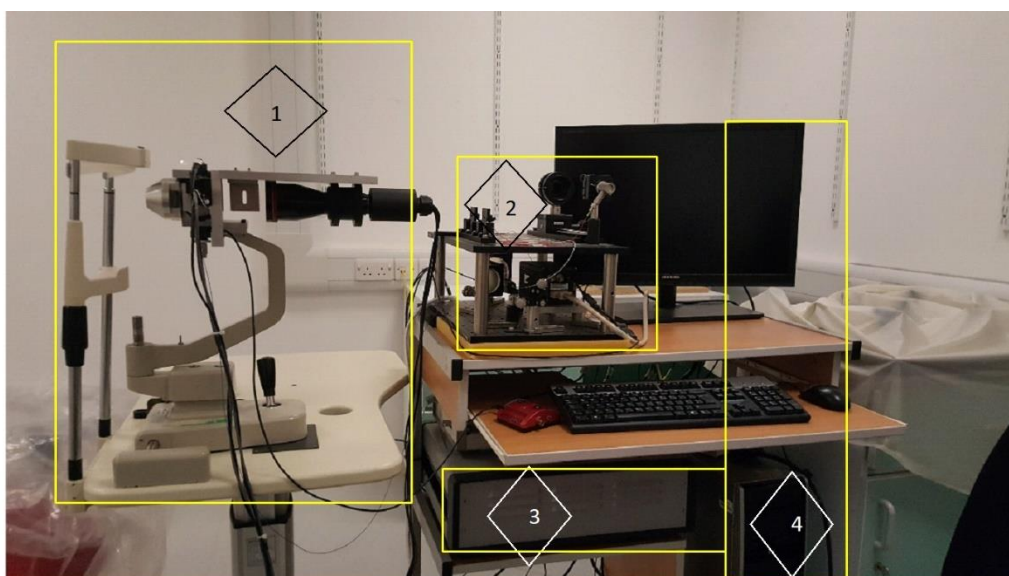


Figure 2.4. OCT-1040nm system components: 1 – Chin rest for a patient head; 2 – Spectrometer, polarisation control and reference arm; 3 – Galvanometer control box; 4 – The PC and monitor

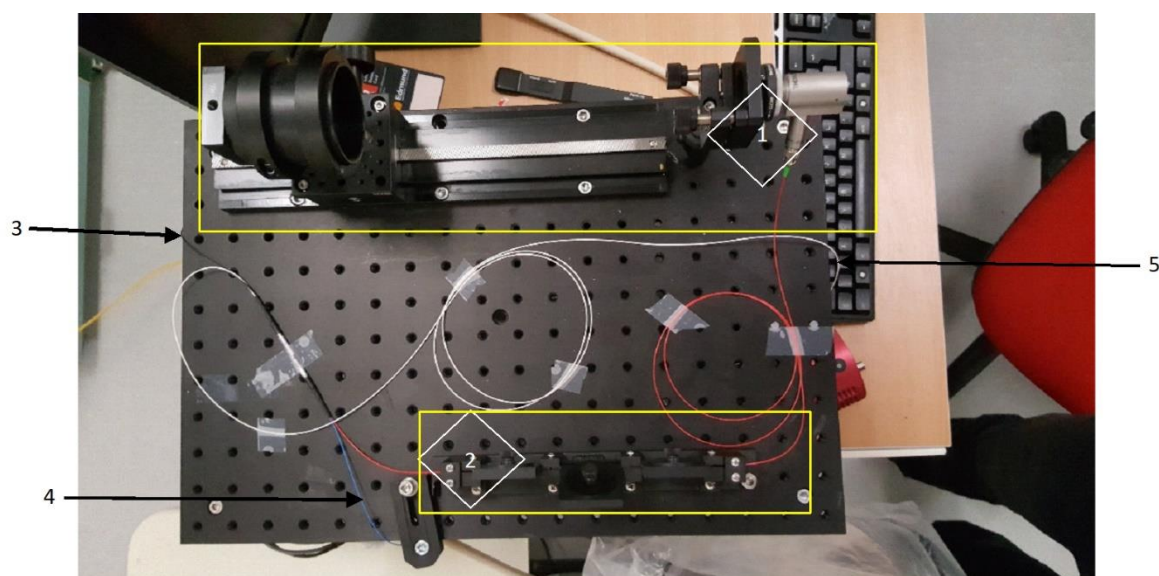


Figure 2.5. OCT-1040nm system components (top view): 1 – Reference arm (aperture power control lever, retroreflector and length control knob); 2 – three paddle polarisation control; 3 – fibre output from 1040nm ASE light source; 4 – fibre optics to the sample arm; 5 – fibre optics to the detectors

2.4. Microscopy imaging

Images of phantom preparations and mouse axotomised retinal explants were acquired using an inverted bright-field microscope (Olympus-IX71) with an x20 air objective (NA 0.7) with a DP70 digital camera (Olympus) and the SPOT Basic image capture software (version 5.5). Phantom micrographs were used to measure the dispersion of beads in the medium (see Section 3.2.2), whereas the retinal explants were imaged to assess the clarity and opacity of the tissues undergoing apoptosis (see Section 4.2.3).

2.4.1. Phantom microscopy

Once the samples were prepared, the phantoms (see Table 3.1) were transferred into the 35mm culture dishes. The images of the phantoms were acquired by an Olympus-IX71 (images at 15 fps) and were digitized by the camera, which can capture 1280x1024, 10-bit (1024 intensity/grayscale values) images. The glass-bottomed 35mm dish was used for the placement of the samples as it allowed visualization of the phantoms for both OCT and Olympus-IX71 (Figure 2.6: a, b, c and d).

2.4.2. Retinal explant microscopy

After the dissection, 2 flat-mounted mouse retinas were placed on the calibration slide with the grid lines (Figure 2.6e) to calculate the modulation transfer function (MTF) to monitor the clarity/opacity of the retinal tissue. The purpose of the latter is to ensure that the retinal explant remains clear and transparent throughout the session.

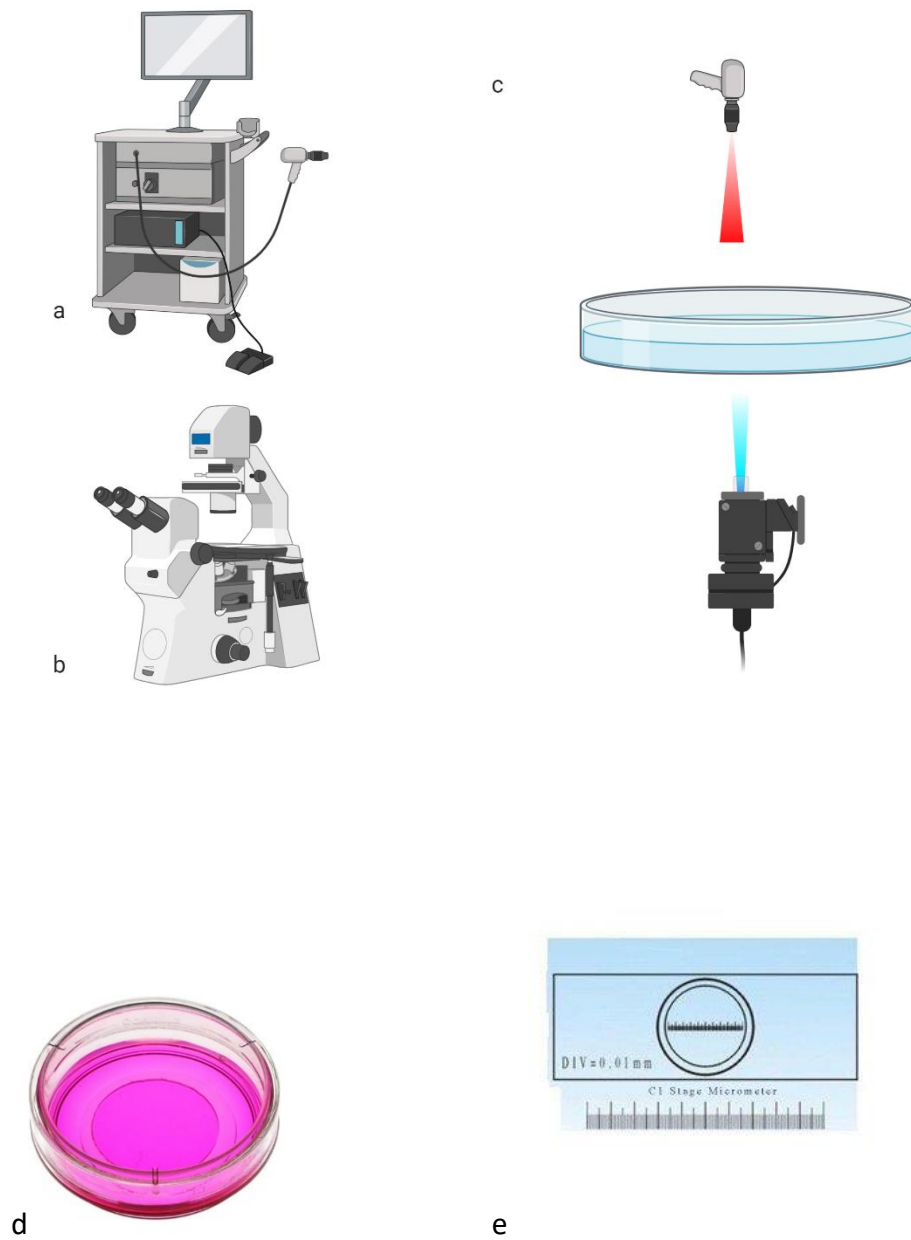


Figure 2.6. Imaging scheme of the phantom: a – optical coherence tomography; b – inverted research microscope; c – semi-transparent optical phantom in a dish can be imaged using OCT (red ray) and microscopy (blue ray); d – 35 mm dish (No. 1.5 Coverslip, 14 mm Glass Diameter, Uncoated to a thickness of 1-2 mm, MatTek); e – 0.01 mm stage micrometre microscope camera calibration slide.

2.5. Refractometry

The refractive indices (RIs) of phantom constituents were measured by the Direct Reading Abbe Refractometer Model 60/70 (Bellingham & Stanley Ltd) (Figure 2.7a). This consisted of a spectral lamp unit with a sodium bulb that provides a monochromatic light that passes through the samples.

Phantom gels were prepared, and their RIs were measured to assess their optical and physical properties. The refractive index of each sample was determined by recording a reading from the instrument's graduated scale graticule (Figure 2.7b) which was then converted to the Brix scale using conversion tables (Considine and Frankish 2014). The RI range of the equipment was 1.300 to 1.740.

.

a



b

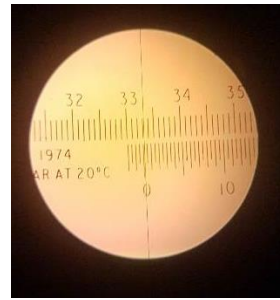


Figure 2.7. Abbe Refractometer Model 60/70 (a) and its graticule scale with the range of refractive index 1.300-1.740

2.6. Image processing and analysis of textural features

Back-reflected light from the sample and reference arms was acquired by the OCT device as spectral data in the 'FD1 file', which was then converted to TIFF image files by OCT1_FD1 software (Cardiff University, UK, version 2.3), which also performed dispersion compensation. Removal of anomalous B scans, image registration and alignment was achieved using ImageJ macro (version 1.51).

Then, random volumes of interests (VOIs) were selected using random number generator software (Diplodock, Russia, version 2.1) to maximize the randomness of the VOI selection. The software selected random numbers of x and y coordinates within the 3D OCT image. The z dimension corresponded to the thickness of the layer of interest (Figure 2.8: a, b), therefore depending on the investigated retinal layer (IPL in glaucoma and AD; outer layers in AMD) and its thickness, VOIs had various dimensions. In the example of mice IPL, the cuboidal VOI size was 30×30×30 pixels in x, y, z (Figure 2.8: c, d). The procedure was performed in ImageJ. VOI selection ensured a reduction of the time-cost of the analysis, rather than analysis of the whole OCT scan.

For the analysis of texture, grey-level co-occurrence matrix (GLCM), grey-level run-length matrices (GLRM), local binary pattern (LBP) and greyscale histogram parameters were extracted from the selected VOIs. Texture analysis scripts were adapted from Anantrasirichai et al. (2013). All computations were processed in MATLAB R2017b (MathWorks, USA) and code scripts are provided in Appendix 1.

2.6.1. Grey-level co-occurrence matrix

The grey-level co-occurrence matrix (GLCM) is the spatial histogram of the image, that shows the relationship between each intensity tone caused by alterations between grey levels i and j (Figure 2.8e). These levels are located at a particular distance d and are displaced by a particular angle ϑ . For quantification of the distributions of image grey-scale values probability density functions $s_{\vartheta}(i, j / d, \vartheta)$ (Rogowska et al 2003) were calculated using ImageJ. Here, in this study, the distance d was equal to 1 pixel, whereas the directions were taken from $\vartheta = (0^{\circ}, 45^{\circ}, 90^{\circ}, 135^{\circ})$.

Five textural features were then computed from each GLCM, including *energy* or *angular second moment (ASM)*, *inertia* (or *contrast*), *entropy*, *inverse difference moment* and *correlation* giving a total of 20 GLCM properties for each region (Table 2.1). The regularity of local greyscale distribution is measured by *energy* by summing the square of each value in the matrices of GLCM. *Inertia* provides higher weights to $s\vartheta(i, j | d, \vartheta)$ values that represent regions of high contrast (Gossage et al. 2006). The sum of each $s\vartheta(i, j | d, \vartheta)$ value multiplied by the log of the $s\vartheta(i, j | d, \vartheta)$ gives us *entropy*, where the randomness is evaluating. *Inverse difference moment* parameter measures the local minimal changes and *correlation* calculate the joint probability of occurrence. The latter is higher in regions with uniform grey-scale values.

Previously, GLCM has been applied for image classification of microscopy (Yogesana et al. 1996), ultrasound (Basset et al. 1993) and OCT images (Gossage et al. 2003) for the classification of normal and pathologic tissues.

Feature	Equation*	Higher in...
Angular second moment	$ASM = \sum_{i=0}^{L-1} \sum_{j=0}^{L-1} [S\theta(i, j d)]^2$	in homogeneous scenes because $s\vartheta(i, j d, \vartheta)$ contains only a few but relatively high values
Entropy	$Entropy = \sum_{i=0}^{L-1} \sum_{j=0}^{L-1} S\theta(i, j d) \log(S\theta(i, j d))$	in regions that contain a wide variety of intensity distributions
Correlation	$Correlation = \frac{\sum_{i=0}^{L-1} \sum_{j=0}^{L-1} (i - \mu_x)(j - \mu_y) S\theta(i, j d)}{\sigma_x \sigma_y}$	in images with uniform grey-scale values
Inverse difference moment	$IDM = \sum_{i=0}^{L-1} \sum_{j=0}^{L-1} \frac{1}{1 + (i - j)^2} S\theta(i, j d)$	in images with lower contrast values
Inertia	$Inertia = \sum_{i=0}^{L-1} \sum_{j=0}^{L-1} (i - j)^2 S\theta(i, j d)$	in regions of high contrast (with large intensity differences being in close proximity)
*where $S\theta(i, j d, \vartheta)$ is the i -th and j -th GLCM elements for the distance $d = 1$ and L is the number of grey levels in the image.		

Table 2.1. Grey-level co-occurrence matrix features

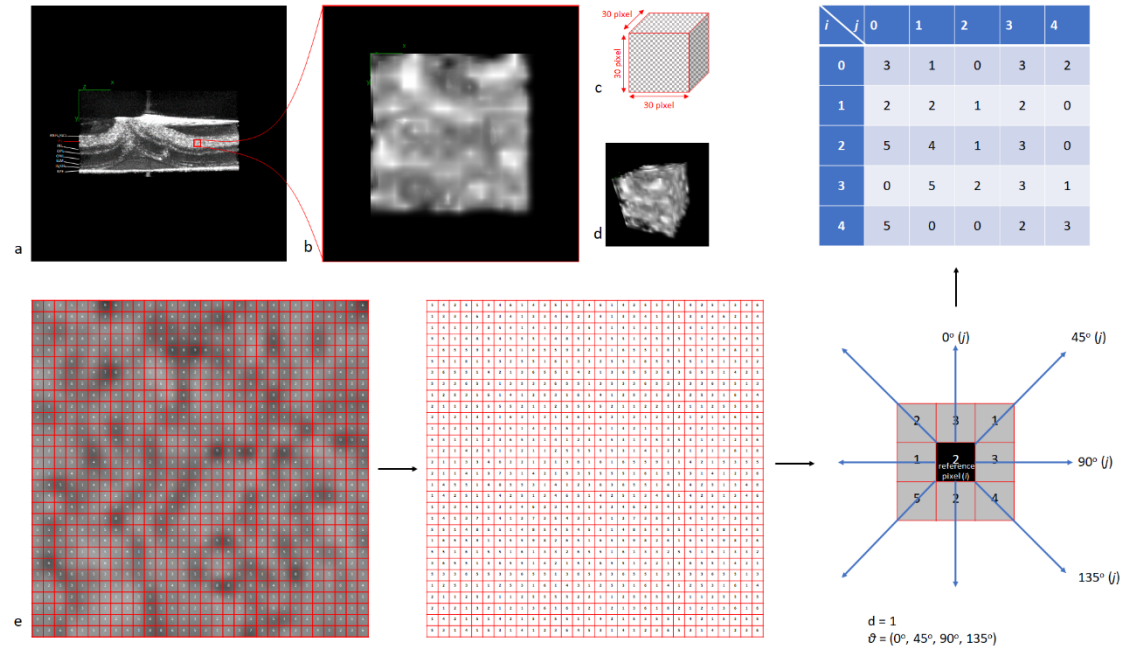


Figure 2.8. Example of image processing and VOI selection: a – OCT scan of mouse retinal explant; b – a volume of interest (VOI) cube image. c, d – schematic views of the 3D cube, voxel size is 30×30×30 pixels; e – extraction of grey level of each pixel for further GLCM texture analysis

2.6.2. Grey-level run-length matrices

Grey-level run-length matrices (GLRM) texture analysis has been applied in various studies to CT scans (Podda and Giachetti 2005) and MR images (Molina et al. 2016). GLRM compute the number of occurrences of a run with a particular length and grey level in a chosen direction. GLRM properties are calculated by subsampling grey levels in a coarser range of n values and computing the runs of equal levels with lengths from 1 to m along a given direction (Figure 2.9). Then these runs are stored in a run-length $m \times n$ matrix (Podda and Giachetti 2005).

Frequently used GLRM features, which were extracted from VOIs, include short-run emphasis (SRE), long-run emphasis (LRE), run-length non-uniformity (RLNU), grey-level non-uniformity (GLNU) and run percentage (RPC) (Galloway 1975; Anantrasirichai et al. 2013). SRE measures the fine texture, while LRE is used for the measurement of coarse texture. Also, GLRM measures the similarity of the grey level values (GNU) and the run lengths (RNU). The number of short runs is measured by RPC.

All five features were extracted from four axes: horizontal, vertical and two diagonals.

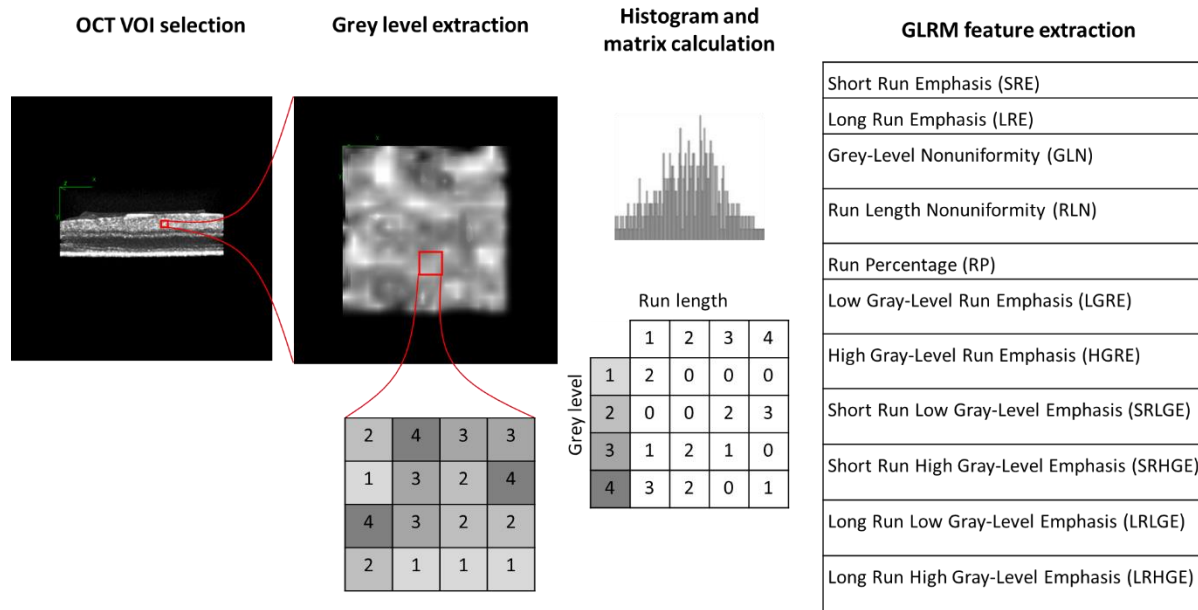


Figure 2.9. Demonstration of the GLRM feature extraction. After the VOI selection (column 1), extraction and normalization of voxel grey levels were performed (column 2), as demonstrated by a simplified matrix containing grey levels ranging from 1 to 4. Then, histogram, GLRM were calculated based on the grey level distribution of voxels (column 3) and GLRM features were derived from the matrix (column 4)

2.6.3. Local binary pattern

The data of texture orientation and coarseness can be derived from the local binary pattern (LBP) by labelling the pixels of a scan using a threshold of the local pixel neighbourhood (Ojala et al. 2002). In a study of Anantrasirichai et al. (2013), LBP properties demonstrated significant benefits for the classification performance with the addition of other textural features.

For the calculation of LBP features, the target window of an image was divided into several sub-regions. The grey value of the neighbourhood or reference pixels was then compared to the central or index pixel of a circle. Namely, if the reference pixel is greater or equal to the index pixel, then it is labelled as “1”, if less – then it labels as “0”. Thus, in LBP, the average sum of image intensity is computed for each local cell (2.1) (Dey et al. 2018). The results of the local spatial patterns were given in binary format.

$$\text{LBP}_{PR} = \sum_{p=0}^{P-1} s(g_p - g_c), \quad (2.1)$$

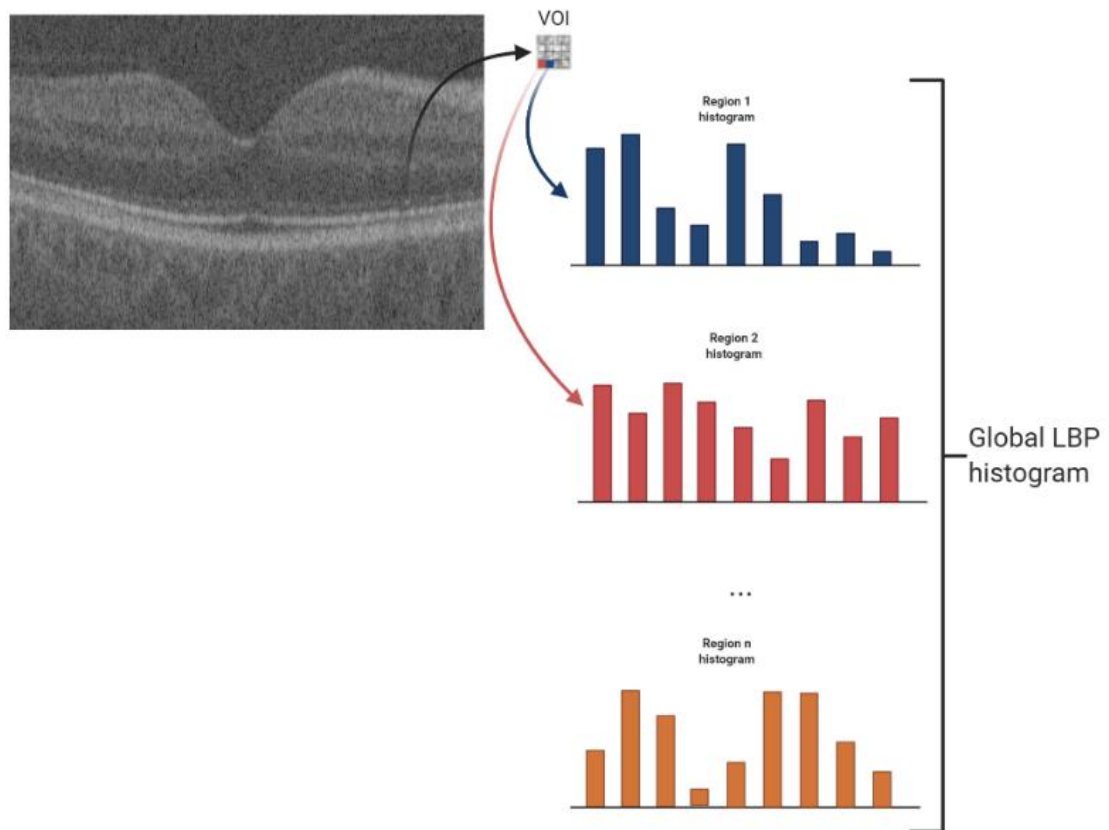
where g_c is the grey value of index pixel, g_p – the grey value of reference pixels and

$$s(x) = 1, \text{ if } x \geq 0$$

$$s(x) = 0, \text{ if } x < 0$$

Sampling points in the cell of this particular size ($R=1 \text{ pixel}$) equals eight ($P=8$). This process is followed by the calculation of the local and global (sum of local) histograms (Figure 2.10). 59 uniform patterns were extracted; each pattern is considered as a feature, therefore 59 LBP features were selected.

a



b

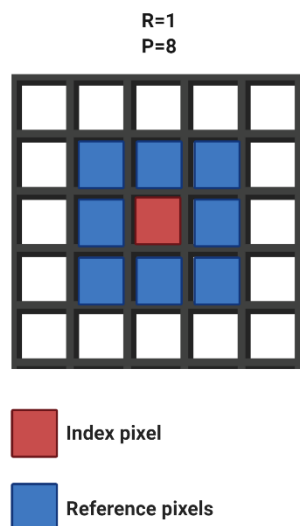


Figure 2.10. LBP histogram generation (a) and example of image greyscale matrix with values of $R=1$ and $P=8$ for a local descriptor (b). Created with BioRender.com

2.7. Machine learning algorithms

Extracted features were collected in comma-separated values (CSV) files as a multidimensional matrix, which was then imported to MATLAB Simulink (MathWorks) classification learner tool. The software enabled training and validation of the dataset for further classification of the test dataset.

Since the number of potential combinations of various features is large, it is a challenging decision to choose the optimal set of features for texture analysis (Bolón-Canedo and Remeseiro 2020). Moreover, due to the time-cost, the use of an extensive number of feature types is not needed (Blum and Langley 1997). One of the solutions to this issue is the application of feature selection, which is used in the training phase, as it will save the most relevant texture analysis variables (Blum and Langley 1997; Bolón-Canedo and Remeseiro 2020). There are many possible advantages of feature selection: improving the prediction, data understanding and visualization, cost-effectiveness, decreasing the number of measurements and saving time for segmentation of new images later after the training phase (Hira and Gillies 2015).

Data reduction

To reduce the dimensionality and select the most descriptive features, principal component analysis (PCA) was utilized in all experimental chapters. PCA is a vector space transform method, which has several functions. The main purposes of this technique are the reduction of the high-dimensional data sets for further analysis in lower dimensions and PCA-based representation (Abdi and Williams 2010). PCA computes the eigenvalue decomposition of the covariance matrix of the image without matrix-to-vector conversion (Qiao and Chen 2011). Then, a small number of eigenvectors, that have the largest eigenvalues, can represent the initial data set.

PCA operates by searching the axes that account for the largest number of variances in the dataset which are orthogonal to each other, whereas the neural network autoencoder is trained to copy its input to its output. In other words, the method maps the input information to a space of reduced dimension with further mapping the latent representation to the output. Thus, the compression of data is carried out by decreasing the reconstruction error.

So, in comparison to PCA, the properties of the latent vectors in the neural network autoencoder are different and the network itself might need to be tuned for the specific task to perform better in the hidden layers.

Bayesian dimensionality reduction technique compares simulated and observed summary statistics to overcome the problem of computationally intractable likelihood functions. Therefore, in order to minimize the loss of valuable information, the Bayesian method requires calculations based on vectors of summary statistics, rather than full data sets, which requires a high computational cost to determine Bayes optimal hypothesis in the general case. Also, another drawback of this method is that it requires initial knowledge of multiple probabilities.

For the purpose of analysis of multidimensional data, the n -dimensional PCA (nD-PCA) was suggested by (Hongchuan and Bennamoun 2006). Data with a great number of dimensions is evaluated as a higher-order tensor by Higher-Order Singular Value Decomposition. nD-PCA extends the PCA method to a higher dimensional data set. However, the data cannot be represented efficiently due to the compression of the latter on one mode subspace. Another drawback of PCA is that the method does not work well with non-linear or discontinuous data.

2.7.1. Support vector machine

A support vector machine (SVM) is a supervised learning technique that separates the data by composing a set of hyperplanes into various classes and constructs a maximal margin in the border of the classes (Noble 2006). The original multi-dimensional space can be mapped into a much higher-dimensional space, presumably making the separation easier in that space. This margin avoids misclassification in the multidimensional feature space of the training data set (Awad and Khanna 2015).

There are multiple similarities and differences between SVM and neural networks (NNs), which are the most applied classification tools. Both methods are parametric and can approximate non-linear decision functions. However, due to the dependency of NN on the number of observations, it can operate poorly if there is not processed the entire training dataset. In contrast, SVM identifies the decision boundary based on the sole support vectors.

Hence, in terms of time-cost, SVM is better and faster. In neural networks, the training is executed repeatedly to get a higher accuracy of the classification, which makes it hard to decide when to stop the procedure of training (Barzilai 2020). On the other hand, SVM trains the whole dataset simultaneously, which provides the best solution and reduces the cost of classification (Noble 2006; Awad and Khanna 2015). Also, the SVM method guarantees the convergence to a global minimum regardless of their initial configuration in comparison to NN.

In the cases of the higher-order polynomial order maps, non-linear kernels can be applied (Figure 2.11). For instance, in the study of Anantrasirichai et al. (2013), the examples of these kernels (polynomial, splines and radial basis) functions were tested and compared in the classification performance. Similarly, in the final experimental chapter of this thesis, Gaussian SVM and quadratic SVM were used and comparative results on their performances were provided.

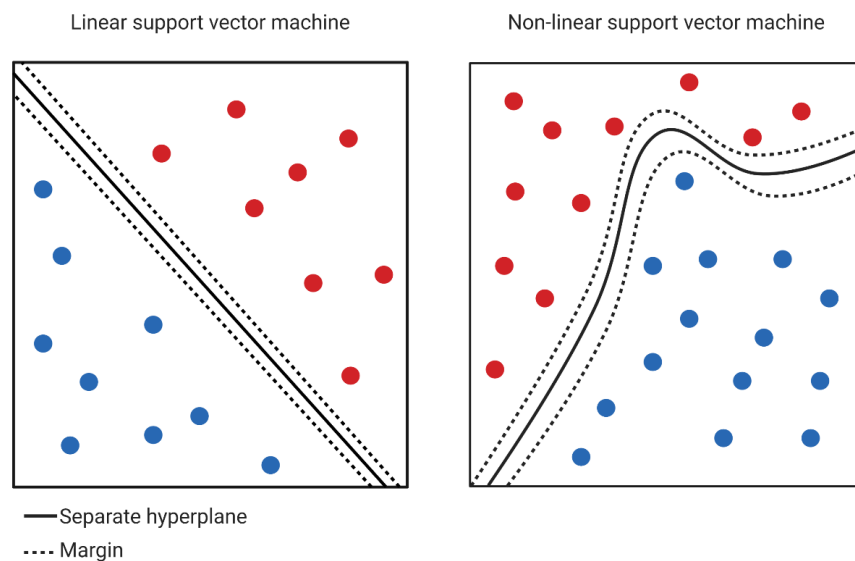


Figure 2.11. Linear and non-linear SVMs. Created with BioRender.com

2.7.2. Discriminant analyses

Discriminant analysis is a method to identify the linear combinations of observed variables that maximize the grouping of samples into separate classes. Measured variables play a role in the predictor variables to classify the response variable.

In general, linear discriminant analysis (LDA) is considered a tool for the dimensionality reduction of multidimensional data (Phinyomark et al. 2012). Moreover, this method is also used for data visualization (Jieping and Qi 2005). However, LDA has a strong potential and has already demonstrated robust classification results (Florian and Nicholas 2008; Pablo et al. 2010; Garcia-Martin et al. 2012).

If all the classes have the same covariance matrix, then the discriminant function can be divided by the linear decision boundary of the LDA (x). Otherwise, the covariance matrices are not equal, then we can consider using the quadratic discriminant analysis (QDA). Hence, QDA has the quadratic decision boundary (x).

$$\delta_k(x) = x^T \Sigma^{-1} \mu_k - \frac{1}{2} \mu_k^T \Sigma^{-1} \mu_k + \log \pi_k \quad (2.2)$$

$$\delta_k(x) = -\frac{1}{2} \log |\Sigma_k| - \frac{1}{2} (x - \mu_k)^T \Sigma_k^{-1} (x - \mu_k) + \log \pi_k, \quad (2.3)$$

where Σ^{-1} is the covariance matrix and μ_k is the mean vector.

Discriminant analysis technically is similar to principal component analysis with the main difference from PCA is the ability to predict unknown data based on the values of measured variables in that sample. Another difference is that PCA detects the linear combinations of the measurements that maximize variance when LDA aims to find the linear combinations of the measurements that best describe the separation between the groups. Thus, PCA does not require to know the groups of interest a priori after the segregation of groups, while in LDA, the groups of interest are known a priori.

2.7.3. Logistic regression

The similarity of logistic regression to linear regression is that the logistic regression finds an equation that predicts an outcome for a binary variable, Y , from one or more response variables, X . However, in logistic regression, the response variables can be categorical or continuous.

In the cases where the number of classes is two ($k=2$), logistic regression was applied. This machine learning tool works well for binary classification and differs from linear regression by its cost function (Figure 2.12). The latter is called a sigmoid function $\sigma(z) = \frac{1}{1+e^{-z}}$. Hence, the hypothesis for the logistic regression has the following equation 2.4.

$$h\theta(X) = \frac{1}{1 + e^{-(\beta_0 + \beta_1 X)}} \quad (2.4)$$

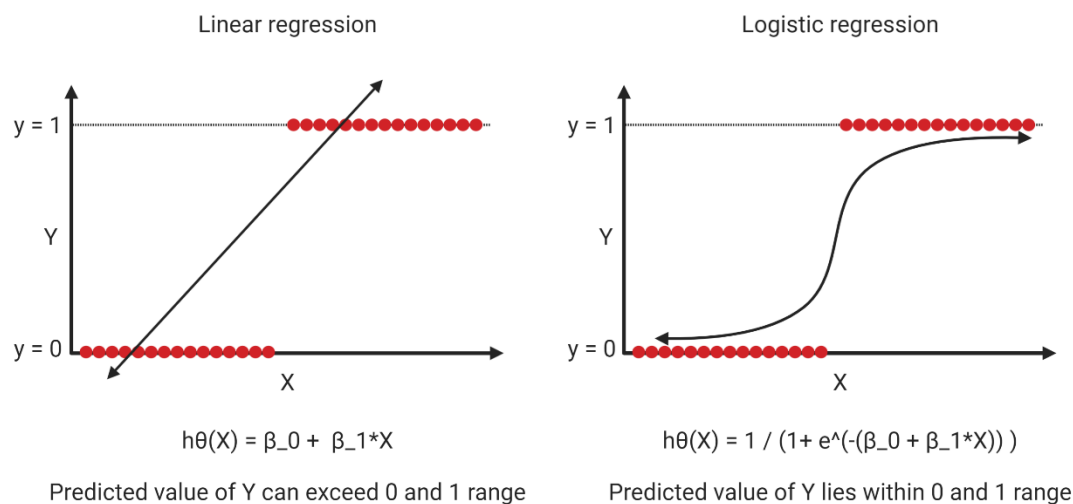


Figure 2.12. Difference between cost functions of the linear and logistic regressions. (Plots created with BioRender.com)

Although in comparison to SVM, logistic regression operates relatively faster, classification accuracy is lower to some degree. Moreover, logistic regression is built simpler for complicated relationships between variables. Hence, this method is not recommended to predict the decision boundary in nonlinear cases.

2.7.4. Decision tree

One of the most popular classification algorithms is the Decision tree (DT). The name of the classifier came from its structure: DT has root, internal and leaf nodes (Figure 2.13). If the root node is the input data, then the leaf node is the outcome, whereas each internal root is a feature.

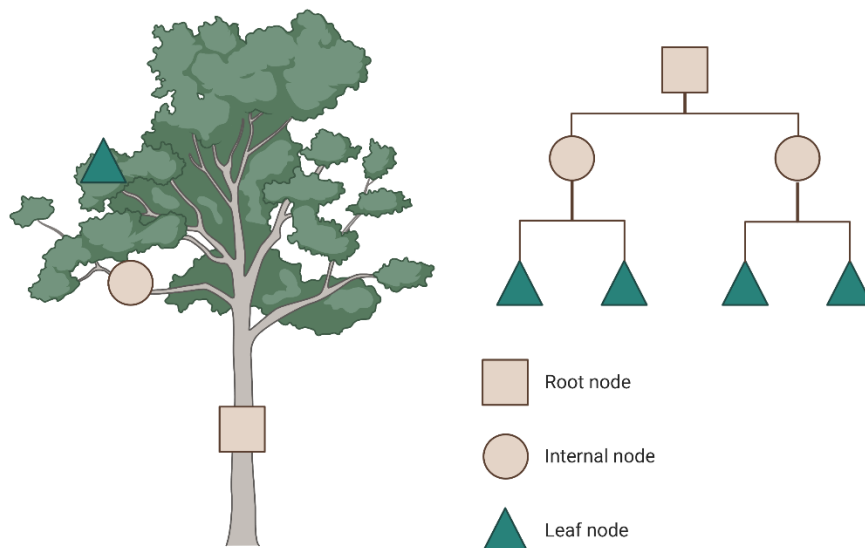


Figure 2.13. Decision tree scheme with 2 levels: Level one – Internal node; Level two – leaf node. The root node is the beginning of a tree and is considered as Level 0.

DT can be utilized to construct the automated prediction model and be used as a classification tree, where each internal node contains a set of attributes, or classification rules (i.e., decision rules). DTs with continuous, infinite possible outcomes are called regression trees.

Bagging, Random Forest and Boosted trees can be used for the improvement of classification accuracy of DT. Among the advantages of DT can be listed: the prediction cost declines with each additional data point; can be applied for both categorical and numerical data; can model problems with multiple outputs.

2.8. Classifier performance evaluation

Classification accuracy is the most common indicator of the machine learning algorithms' performance, which is the ratio of the number of correct predictions to the total number of input samples (2.5) (Jiao and Du 2016).

$$Accuracy = \frac{\text{Number of correct prediction}}{\text{Total number of predictions made}} \quad (2.5)$$

Additionally, other evaluation metrics were also applied to compare supervised machine learning tools: precision, recall and F_1 score in Chapter 6. Precision is the ratio between the true positive outcome to the total number of predicted as positive as shown in equation 2.6, whereas the recall computes the number of the actual positive sample (2.7). And the equilibrium between precision and recall can be calculated and it gives us F_1 score (2.8). The main advantage of this score over the accuracy is that it includes the values of false results as well as the confusion matrix of outcomes.

$$Precision = \frac{\text{True Positive}}{\text{True Positive} + \text{False Positive}} = \frac{\text{True Positive}}{\text{Total Predicted Positive}} \quad (2.6)$$

$$Recall = \frac{\text{True Positive}}{\text{True Positive} + \text{False Negative}} = \frac{\text{True Positive}}{\text{Total Actual Positive}} \quad (2.7)$$

$$F_1 = 2 \times \frac{\text{Precision} \times \text{Recall}}{\text{Precision} + \text{Recall}} \quad (2.8)$$

Among other evaluation tools for the classifier performance, can be listed confusion matrices (CMs), Receiver Operating Characteristic curve (ROC) and area under the ROC curve (AUC).

CM is a summary of predicted or classified results in a specific table layout. This table indicates the performance metrics of the ML algorithms for binary and multi-class classification cases. Detailed table layout results can be then used to calculate the accuracy, precision, recall and F_1 score.

ROC curve can be drawn by plotting the true positive (TP) against the false positive (FP). AUC is the single-valued metric used for evaluating the performance: the higher the AUC, the better the performance. ROC and AUC can be applied used to compare and evaluate different classification algorithms and when the dataset is imbalanced.

Chapter 3. Textural feature analysis of OCT phantoms

3.1. Introduction

Depending on the size, concentration and refractive index of the medium and scatterers, phantoms generate specific textures which can confer useful optical properties about a structure (Yasaka et al. 2017; Abadi et al. 2019). The texture of OCT images arises from a combination of signal, noise and speckle due to the use of the laser as a light source and interference with multiple forward and backward scattering photons (Schmitt et al. 1999). The relative contribution of speckle as a signal component has been a topic of debate (Schmitt et al. 1999; Dubose et al. 2018). Due to the influence of speckle on quality and the performance of earlier OCT devices, where the axial resolution was lower and motion artifacts more of a problem, it has routinely been considered as a type of noise with a little value, which is attenuated or removed using specifically designed filters (Ma et al. 2018). This approach has been strengthened by the view that OCTs can best function by providing information on the thickness of retinal layers (Kafieh et al. 2013).

Schmitt has identified two types of speckle: ‘chance’ speckle and ‘inherent’ speckle (Schmitt et al. 1999). ‘Chance’ speckle arises from multiple scattered photons, the width of which corresponds to one pixel. This type of speckle is random and can be removed by averaging during the OCT scan acquisitions. However, a larger ‘inherent’ speckle is consistent and located (on average) within the same region in multiple OCT images. This speckle originates from the wavefronts from multiple scatterers, located in the same focal volume (Schmitt et al. 1999). Cumulatively these speckle components may produce the specific optical texture of each tissue and have a characteristic pattern (Gossage et al. 2006).

Even though OCT provides a wide range of advantages, significant limitations arise from the spectral bandwidth of the source of a coherent light source (Fujimoto et al. 1995). Furthermore, the optical aberrations of the imaging system (which include those of the eye) are significant and prevent clinical imaging systems do not support isotropic resolutions (without resorting to adaptive optics to enhance lateral resolution). The axial resolution of the machine is determined by the full width at half maximum (FWHM) of the light source and not by the aberrations of the optic system; for a light source of our research-based OCT with

a 1040nm central wavelength and the FWHM of 70nm, the axial resolution is approximately 7 μ m in air (NP photonics 1-M-ASE-HPE-S). The lateral resolution for ocular imaging is aberration limited and is approximately 10-15 μ m (Jonnal et al. 2016).

Fourier-domain OCT measures the phase of the Fourier transform of the spectral interference between the back-reflected light from the sample and a reference arms (Leitgeb et al. 2003). The phase is an estimate of structural information about the sample refractive index within the implicit coherence gating enforced by the limited spectral bandwidth of the light source (Uttam and Liu 2015). Although current light sources do not permit consistent identification of subcellular structures with interference-based non-invasive optical imaging technologies, speckle components are likely derived from changes from back-reflected light that correlate with subcellular changes. To test this hypothesis, these changes can be modelled by the fabrication of phantoms comprising optical scattering agent with dimensions that approximate subcellular organelles mitochondria, apparatus Golgi, endoplasmic reticulum and lie in the range of 1-5 μ m.

Cellular events in apoptosis largely affect the morphological and optical properties of the cell (Frank et al. 2001; Almasieh et al. 2012). The main organelles that contribute to the scattering of OCT light are mitochondria, endoplasmic reticulum and Golgi apparatus, which have the higher RI ($n=1.48$) than the entire averaged RI of the cell ($n=1.38$) (Beuthan et al. 1996). The latter is lower due to the cytoplasm and extracellular matrix, in which RI is close to the water and 2% gelatin solution in this case.

3.1.1. Hypothesis

The application of PCA and SVM algorithms may allow the segregation of phantoms with varying optical textures derived from scatterers with these dimensions. These machine learning tools can be optimised using these phantoms as ground truths. In this study, texture analysis for the discrimination of optical phantoms with different concentrations, sizes and refractive indices of scatterers (polystyrene beads and silica microparticles) was applied.

In this chapter, the following hypothesis will therefore be tested:

Different types of phantoms with uniformly dispersed scatterers, with varying sizes and refractive indices of the particles, generate distinctive optical textures which can be detected by texture analysis of OCT derived images.

Texture analysis of OCT image datasets derived from phantoms of different types of phantoms, of a size similar to subcellular organelles (varying sizes and refractive indices), enables the detection of distinct optical scatter-derived signatures.

3.1.2. Aims

- To analyse the texture of various optical phantoms that are within the range of the optical properties of the human retina
- To develop phantom classification methods that can discriminate the phantoms using OCT images
- To validate the accuracy of SVM classification of phantoms based on texture analysis, with and without PCA

3.2. Methods

3.2.1. Phantom preparation

Phantom preparation was undertaken as described in Section 2.1. Four groups of phantom types were prepared (Table 3.1): various gelatin solution concentrations (2%, 5% and 10%); different sized polystyrene beads (PBs) i.e., $0.38\mu\text{m}$, $1\mu\text{m}$, $2\mu\text{m}$ and $5\mu\text{m}$; a different volume of $1\mu\text{m}$ PBs ($5\mu\text{l}$, $10\mu\text{l}$, $20\mu\text{l}$, $30\mu\text{l}$, $40\mu\text{l}$ and $50\mu\text{l}$) and phantoms with different refractive indices of scatterers (PBs=1.57; SiO_2 =1.43).

Phantom groups	No	Phantom types	Number of OCT scans
Phantoms without scatterers			
Different concentrations of gelatin solution	1	2% gelatin solution (2% GS)	10
	2	5% gelatin solution	10
	3	10% gelatin solution	10
Phantoms with scatterers			
Different size of scatterers: PBs	4	2% GS + $0.38\mu\text{m}$ $50\mu\text{l}$ PBs	10
	5	2% GS + $1\mu\text{m}$ $50\mu\text{l}$ PBs	10
	6	2% GS + $2\mu\text{m}$ $50\mu\text{l}$ PBs	10
	7	2% GS + $5\mu\text{m}$ $50\mu\text{l}$ PBs	10
Different volume of scatterers: PBs	8	2% GS + $1\mu\text{m}$ $5\mu\text{l}$ PBs	10
	9	2% GS + $1\mu\text{m}$ $10\mu\text{l}$ PBs	10
	10	2% GS + $1\mu\text{m}$ $20\mu\text{l}$ PBs	10
	11	2% GS + $1\mu\text{m}$ $30\mu\text{l}$ PBs	10
	12	2% GS + $1\mu\text{m}$ $40\mu\text{l}$ PBs	10
	13	2% GS + $1\mu\text{m}$ $50\mu\text{l}$ PBs	10
Different refractive index of scatterers	14	2% GS + $1\mu\text{m}$ $50\mu\text{l}$ PBs	10
	15	2% GS + $1\mu\text{m}$ $50\mu\text{l}$ SiO_2	10

Table 3.1. Groups and types of phantoms

The choice of the scattering particles was dictated by the refractive indices of membranous organelles. Moreover, the size of scatterers was also selected to correlate with the size of

these organelles. Since the size of isolated mitochondria ranges from 0.25 to 3 μ m (Bereiter-Hahn 1990; Beuthan et al. 1996; Rafelski and Marshall 2008; Wiemerslage and Lee 2016), depending on its state and participation in cellular events, the PBs size was in these dimensions. In the studies of Gourley, the diameter of the individual typical normal and diseased mitochondria differs and equals 600–700 nm (Gourley et al. 2005) and 750–830 nm (Gourley and Naviaux 2005), respectively. In abnormal mitochondria the diameter is enlarged, the protein concentration is decreased. Hence, the optical density also declines, which leads to the decrease of the optical properties of the organelle (Gourley et al. 2005).

3.2.2. Particle dispersion calculation

Even though OCT devices have a relatively high axial resolution, a microscopy investigation of the phantoms was performed to ensure the random monodispersion of the particles. The calculation of the microparticle distribution was quantified by computing the nearest neighbour index (NNI) using the R programming language (R Core Team version 3.5.0). To calculate the NNI (3.1), the nearest neighbour distance (NND), area of the pattern (a) and the number of particles (n) in this area were computed.

$$NNI = \frac{NND}{0.5 \sqrt{\frac{a}{n}}} \quad (3.1)$$

Phantoms of various PBs volumes (10 μ l, 20 μ l, 30 μ l, 40 μ l and 50 μ l) were prepared and microscopy images were acquired (example of 10 μ l PBs phantom in Figure 3.1a). Then, the cropping, colour-coding and threshold of the image were processed in ImageJ (Figure 3.1b) for the calculation of the pattern area and the number of PBs particles. NND and NNI were computed using (3.1) in R programming (Figure 3.1c).

3.2.3. Phantom OCT imaging and image processing

Ten OCT image datasets were acquired from each sample within the depth range of 1000 μ m, providing a total of 150 scans with the size of 512 \times 512 \times 1024 pixels in x, y, z, respectively. The air-gel interface on the top of the sample was located higher than the first Z0 scan (in z coordinate), thereby removing the effect of this large change in refractive index (Figure 3.2a). The scans were converted to an 8-bit resolution image with 0-255 greyscale levels. From each

OCT image dataset, five 3-dimensional volumes of interest (VOIs) with the size of 30×30×30 pixels were randomly selected (Figure 3.2b) for further feature extraction and image classification (Figure 3.2c).

3.2.4. Texture analysis and classification

For the purpose of texture analysis, the five most relevant GLCM texture features (see Table 2.1) were extracted using the ImageJ plugin, which has been used to calculate image texture parameters as described previously (Haralick et al. 1973). GLCM features were then imported into Simulink MATLAB R2017b (MathWorks) for classification using SVM with and without the utilization of PCA.

Application of PCA and SVM for phantom classification was chosen due to their high accuracy, ability to perform binary and multi-class classification and to operate with non-linear data. SVM outperformed other supervised machine learning tools in Chapter 6.

A 5-fold cross-validation was applied to estimate the skill of the model, avoid overfitting and evaluate the training dataset. The unseen test dataset was then evaluated with the generated codes. Data analysis were repeated 10 times and averaged values were accepted.

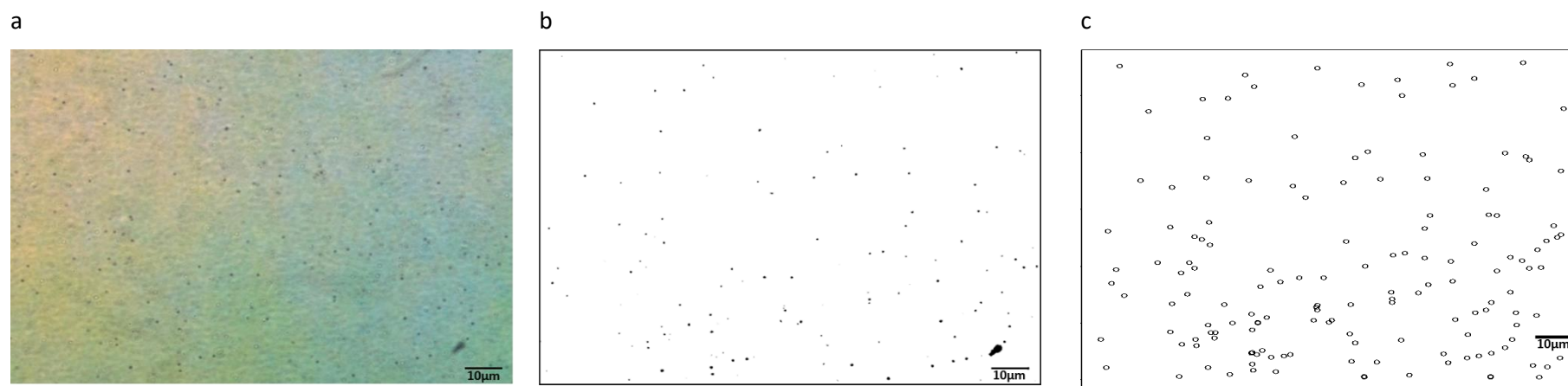


Figure 3.1. Image processing of microscopy image (a) captured of a 2% GS + 1μm 10μl PBs phantom, which underwent thresholding and was cropped using ImageJ (b); c – simulation of the distribution of the beads in R plot, from where NND, area of the pattern and the number of particles in this area were counted for the NNI calculation.

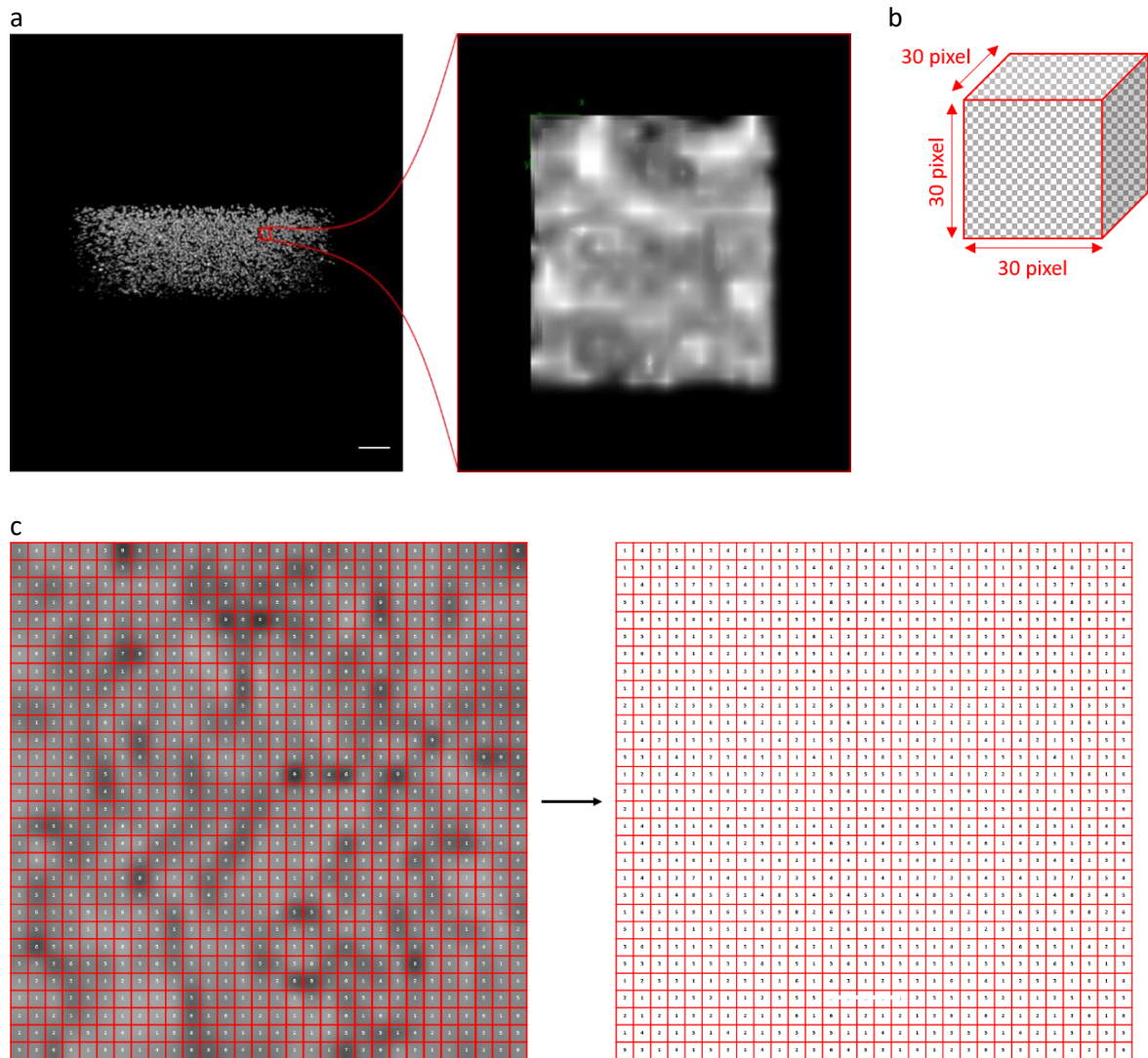


Figure 3.2. Image processing and data preparation for the classifier: a – OCT scan of phantom (scale bar – 10 μ m) and an extracted VOI cube (magnified); b – schematic view of the 3D cube, voxel dimensions 30 \times 30 \times 30 pixels; c – extraction of grey level of each pixel for further calculation of grey-level co-occurrence matrix features

3.3. Results

3.3.1. Gelatin matrix

Among various hydrogel-based chemicals, gelatin was selected as a suitable medium for scatterers. However, there was a debate concerning the correct concentration to use due to the varying characteristics of the gelatin solutions in different concentrations of solid states of chemicals. OCT scans were acquired to determine if there was clustering of gelatin powder in the solution, which may cause unwanted scattering and alterations to the optical properties of the phantom. “Clumping” image artefacts were higher with the increase of the solid hydrogel constituents in 5% and 10% *gelatin solutions* (Figure 3.3).

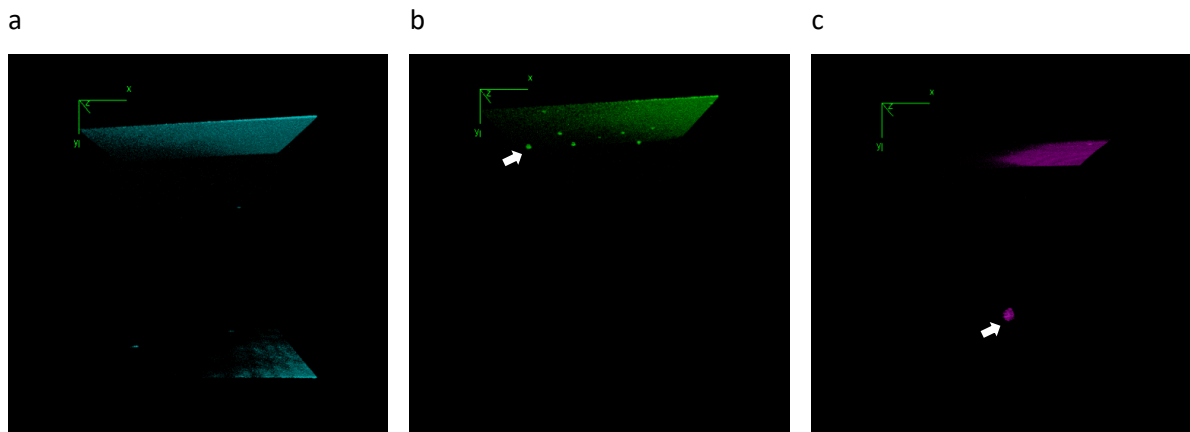


Figure 3.3. OCT images of various gelatin solution concentrations: a - 2% gelatin; b - 5% gelatin; c - 10% gelatin. Top plain layer – the surface of the phantom, bottom – the surface of the MatTek glass coverslipped bottom, these transitions of materials contribute to the back-reflected light due to a difference in RI. The clumping of gelatin powder in the solution is shown in the arrow. The axes correspond to the three dimensions x, y and z of 3D rendered OCT images

Not only the relative adhesion of molecules grows by the increase of the concentration of solid gelatin solution, but also the refractive index of the phantom medium (Vulprecht et al. 2020). Refractometry studies revealed that 2% *gelatin solution* has the closest RI to that of water (Figure 3.4), and hence the cytoplasm and intercellular matrix. Due to preferable mechanical and optical properties, 2% *gelatin solution* was therefore chosen as the standard medium for further preparations of phantoms.

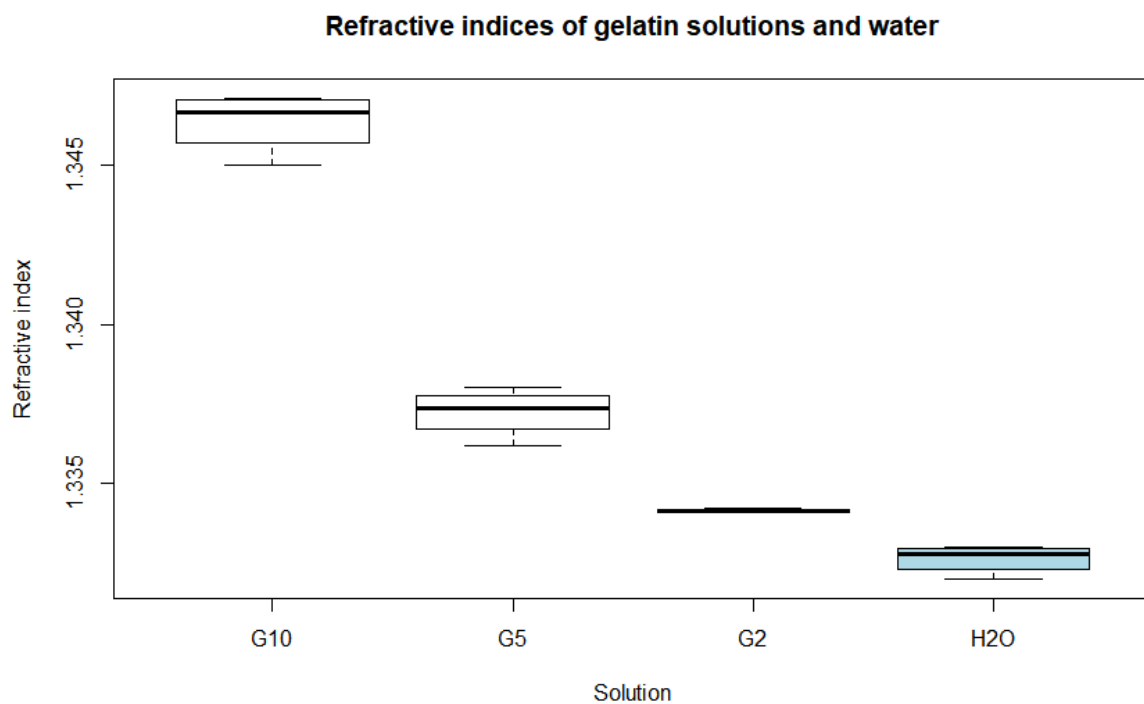


Figure 3.4. Comparison of refractive indices of gelatin solutions and water. Here: G10 – 10% gelatin solution (1.3464); G5 – 5% gelatin solution (1.3372); G2 – 2% gelatin solution (1.3341); H2O – water (1.3321), at $\lambda=589\text{nm}$

3.3.2. Scattering particles

After 2% gelatin was selected as a matrix medium, phantoms were prepared with scatterers of various sizes, concentrations and refractive indices. The quality of the preparation and the dispersion of the particle was inspected visually by microscopy. Examples of microscopy images of $2\mu\text{m}$ PBs are illustrated in Figure 3.5. Microscopic observations of all types of phantoms confirmed monodispersity and also the absence of air bubbles and the clumping of solid gelatin in the samples.

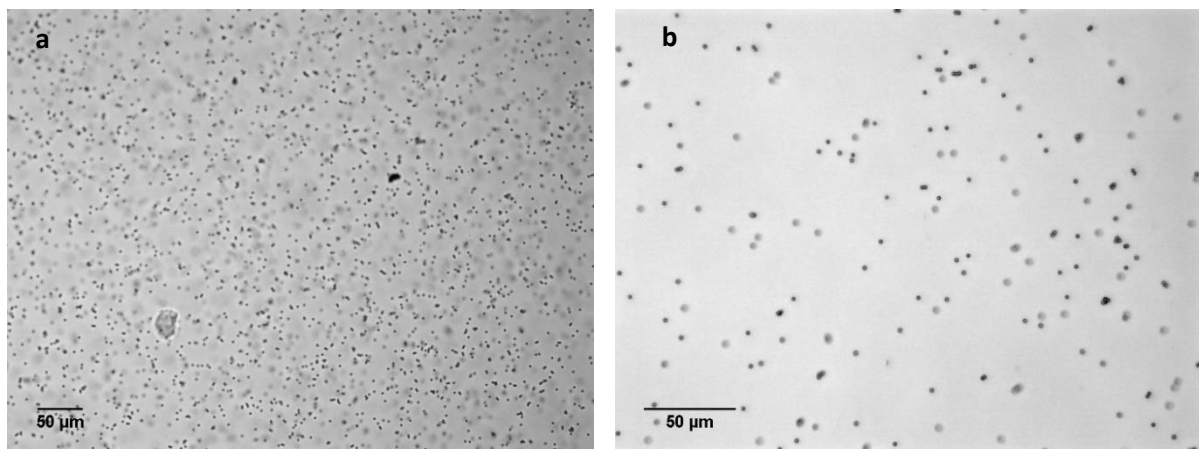


Figure 3.5. Micrographs of the phantoms: images (at different magnification) of samples containing $2\mu\text{m}$ polystyrene beads in 2% gelatin.

For further validation, the ability of OCT-1040 to detect scattering particles was tested. The examples of thresholded 3-D volumetric OCT images of the monolayered phantoms with $5\mu\text{m}$ and $1\mu\text{m}$ PBs beads are demonstrated in Figures 3.6 a and b, respectively. In comparison, the 2% gelatin phantom without any beads looks “empty” with a high backscattering of the phantom and coverslip surfaces (Figure 3.6c).

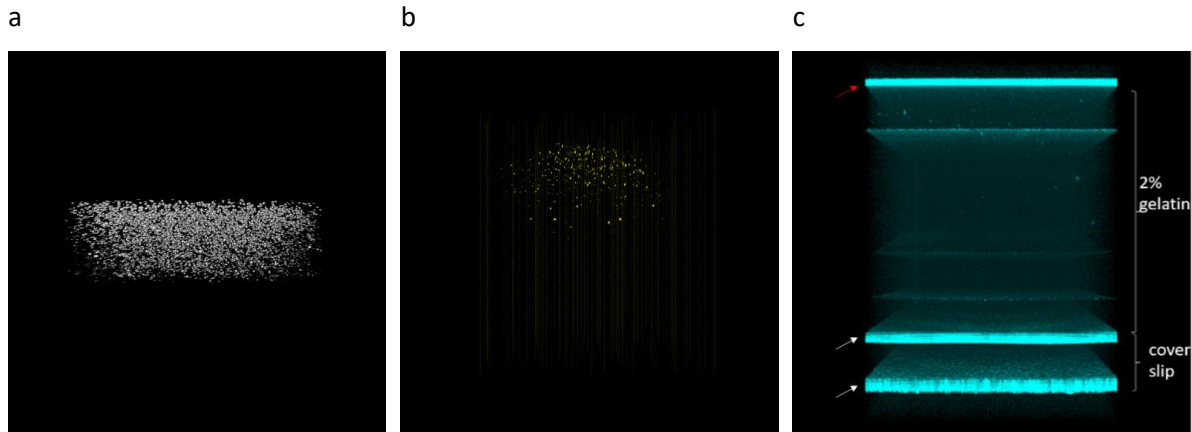
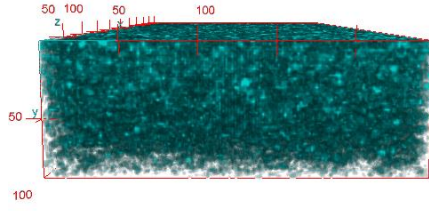


Figure 3.6. Monolayer PBs phantoms: a - 5µm PBs; b - 1µm PBs; c - test control phantom. In the test phantom without scatterers, three layers of light reflection are visible between the surfaces of the sample and the coverslip. The surface of the phantom is indicated with a red arrow; the top and bottom surfaces of the coverslip are shown with white arrows

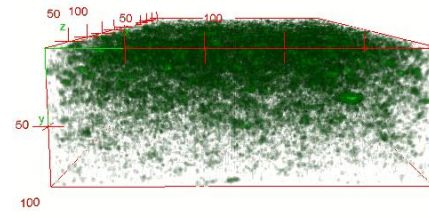
3.3.3. Spatial distribution of scatterers

While the visual inspection of particle distribution is useful for initial quality assurance, quantitative indices of particle dispersion were used following the nearest neighbour index. NNI is a tool to precisely measure the spatial distribution of particles and investigate the regularity of dispersion. Three main outcomes according to the NNI value: regular, random and clustered dispersion (Figure 3.7) were recorded. NNI measures the spatial distribution from 0 (clustered pattern) to 1 (randomly dispersed pattern) to 2.15 (regularly dispersed /uniform pattern). Table 3.2 summarises the NNI values of the phantoms of different volumes of 1µm PBs (Figure 3.8). The values in all samples were close to 1, which demonstrated the random allocation of scattering particles.

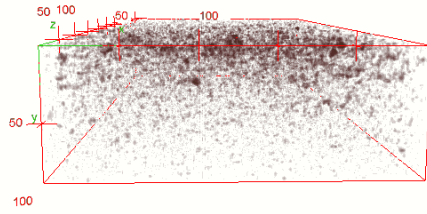
a



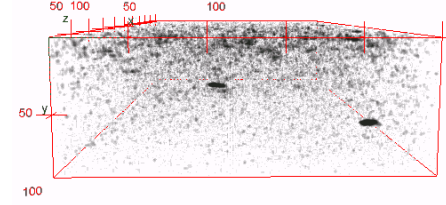
b



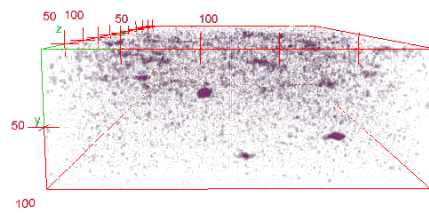
c



e



d



f

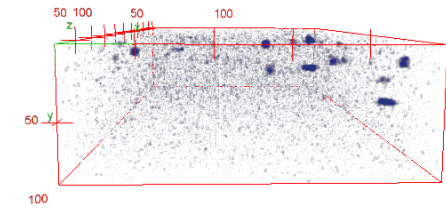


Figure 3.7. Thresholded and colour-coded 3D OCT scans of $1\mu\text{m}$ PBs phantoms with different concentrations: a - $50\mu\text{l}$ PBs; b - $40\mu\text{l}$ PBs; c - $30\mu\text{l}$ PBs; d - $20\mu\text{l}$ PBs; e - $10\mu\text{l}$ PBs; f - $5\mu\text{l}$ PBs. X, Y and Z scales correspond to the length, width and height of images in μm .

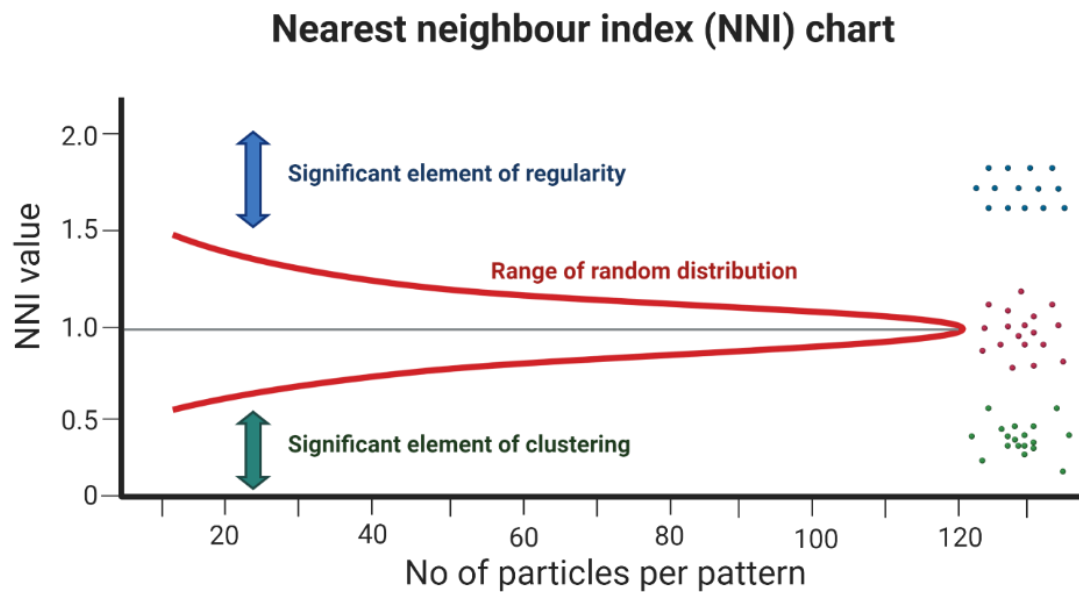


Figure 3.8. Nearest neighbour index graph. Created with BioRender.com

Sample	NND	Area	No of PBs per pattern	NNI
50 μ l PBs	50.65879	1792000	168	0.981003
40 μ l PBs	46.65486	1792000	174	0.919459
30 μ l PBs	37.53487	1792000	218	0.827988
20 μ l PBs	49.77891	1792000	139	0.878402
10 μ l PBs	55.97415	1792000	105	0.856925

Table 3.2. Nearest neighbour index of 1 μ m PBs phantoms of various volumes of the scatterers

3.3.4. Classification of phantoms

Different sizes of scatterers

OCT phantoms with $1\mu\text{m}$, $2\mu\text{m}$ and $5\mu\text{m}$ diameter of scatterers were classified correctly in almost all cases using SVM with and without PCA. Three clusters of scatters were separated in feature space when using the most discriminating features selected by PCA being contrast and entropy at 0 degrees as shown in Figure 3.9.

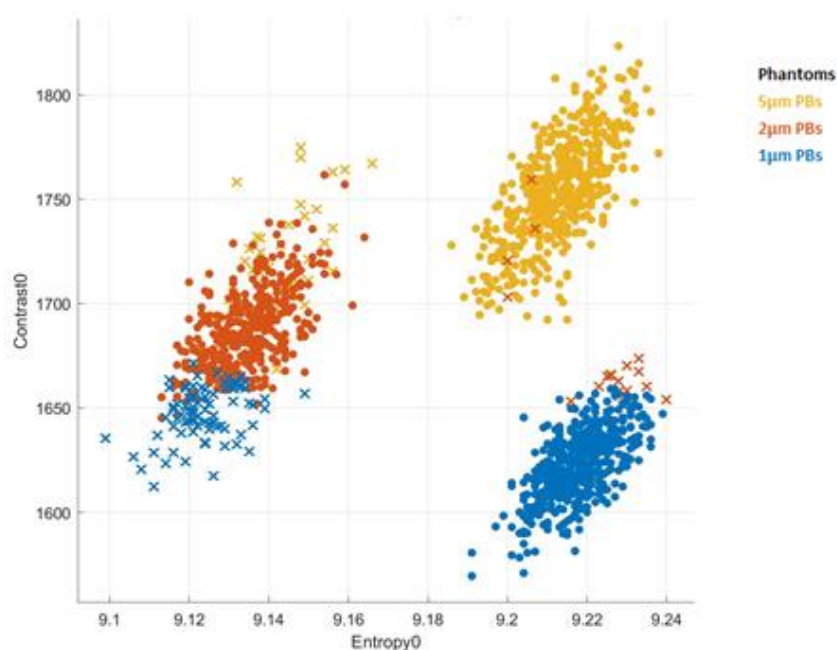


Figure 3.9. Three separable clusters in the scatter plot of the phantoms with the size of PBs $\geq 1\mu\text{m}$. The most descriptive GLCM features (Contrast0 and Entropy0 – features in 0 degrees between the index and reference pixels) were selected by PCA, forming a 2-dimensional feature space. Here: \cdot – correct and \times – incorrect classification

$5\mu\text{m}$ PBs could still be discerned as discrete entities although collectively they generated differences in the overall texture of the phantom. 93% of the phantoms were classified correctly, whereas the rest of the phantoms were categorised incorrectly as $2\mu\text{m}$ PBs (yellow \times in the left cluster, Figure 3.9). The incorrect classification was especially noted between phantoms of PBs of closer sizes, with only 87% of $1\mu\text{m}$ and 81% of $2\mu\text{m}$ PBs segregated properly, giving a total classification accuracy of 87%.

The level of discrimination was significantly reduced with submicron PBs ($0.38\mu\text{m}$) supporting lower levels of discrimination, where only 27% of $0.38\mu\text{m}$ PBs were detected correctly from the phantoms of the micron dimension. This demonstrated the resolution limit of the OCT device. Consequently, the sensitivity of the classifier was dropped from 87% and submicron ($0.38\mu\text{m}$) polystyrene beads had no discernible effect on the optical properties of the phantom. The scans from these phantoms were notably free of single-pixel speckle and random noise (Figure 3.10). OCT image thresholding was achieved using ImageJ automatic computing of a value cutoff.

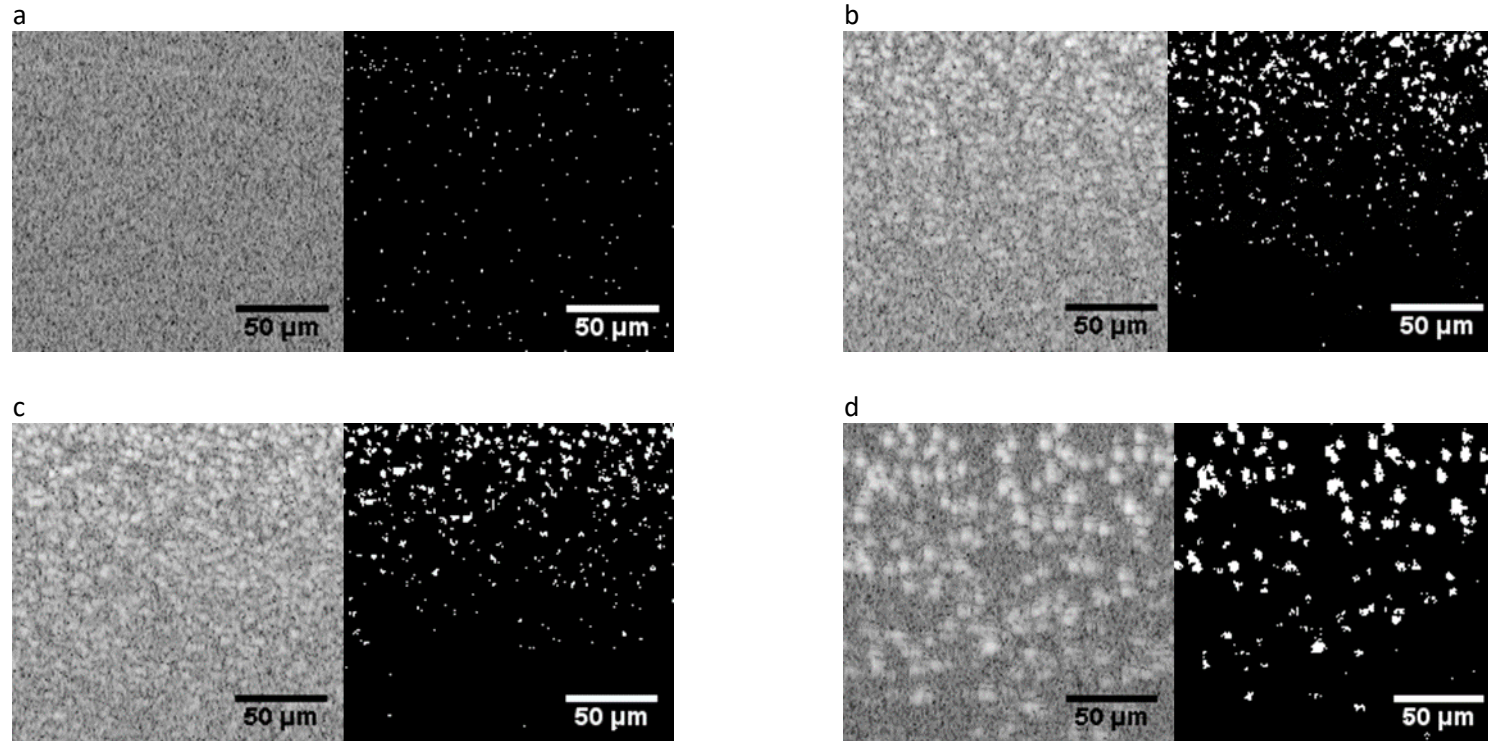


Figure 3.10. OCT B scans and their thresholded images of 0.38 μ m (a), 1 μ m (b), 2 μ m (c) and 5 μ m (d) PBs phantoms

Different refractive indices of scatterers

Due to the different refractive indices of PBs (1.57) (Jones et al. 2013) and SiO₂ (1.43) (Kischkat et al. 2012), the SVM classifier with and without PCA correctly detected the texture of PBs phantoms relative to silica samples in all cases. The principal component scores of each scattering particle type for the 3 components are plotted in X, Y and Z dimensions (Figure 3.11a). According to the type of scatterers (PBs=red, SiO₂=blue), segregation of the clusters into different types along the components can be detected. To illustrate the distribution of the groups along with individual components, plots I, II and III are projected in Figure 3.11b.

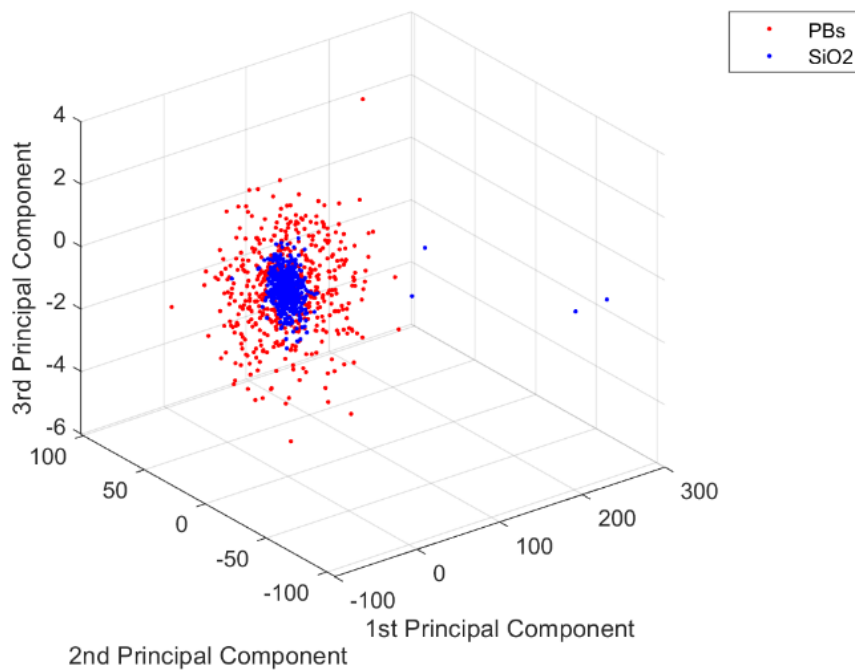
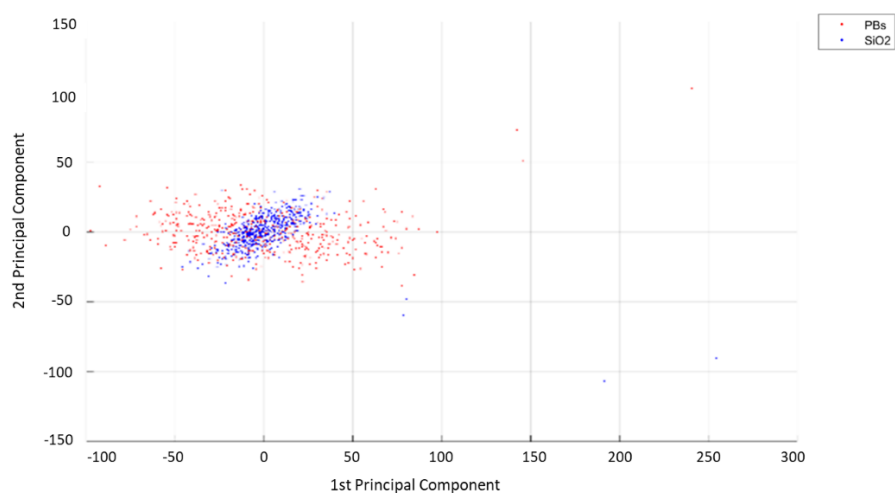
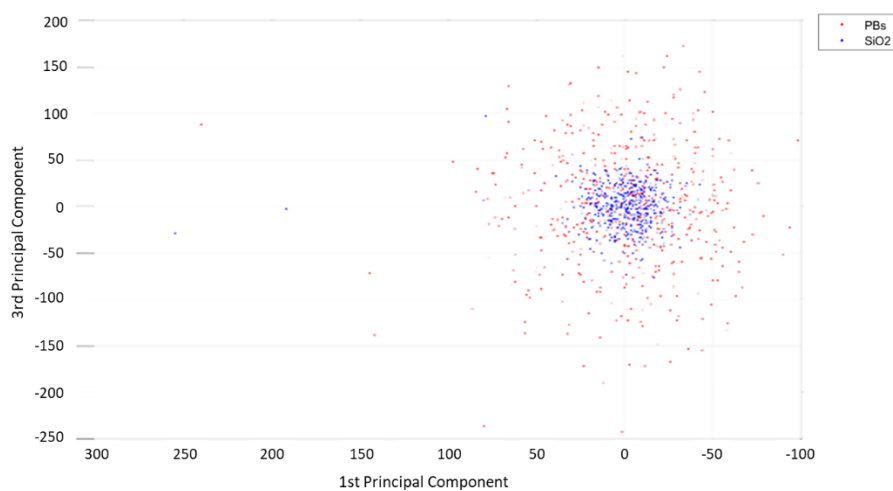


Figure 3.11a. Principal component analysis of the different refractive indices of scatterers. The 3-component solution that included 95% of the variance within the data

I



II



III

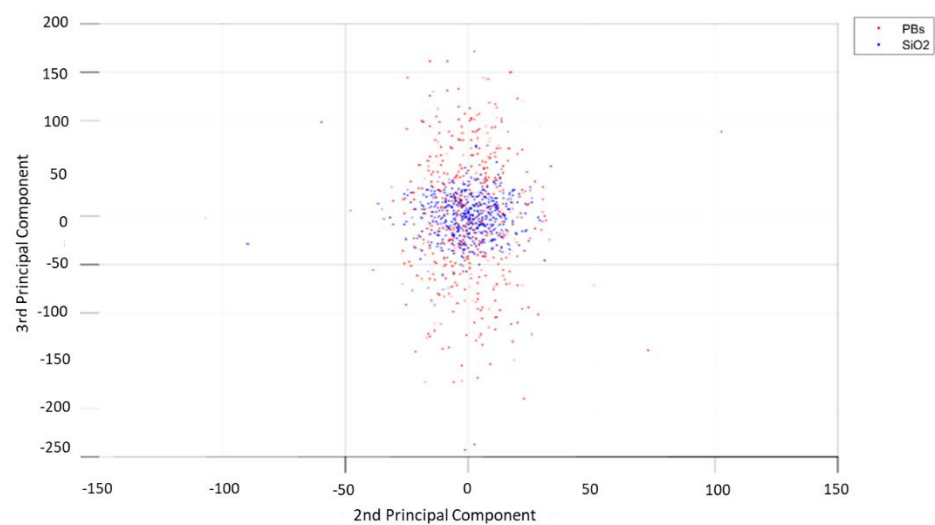


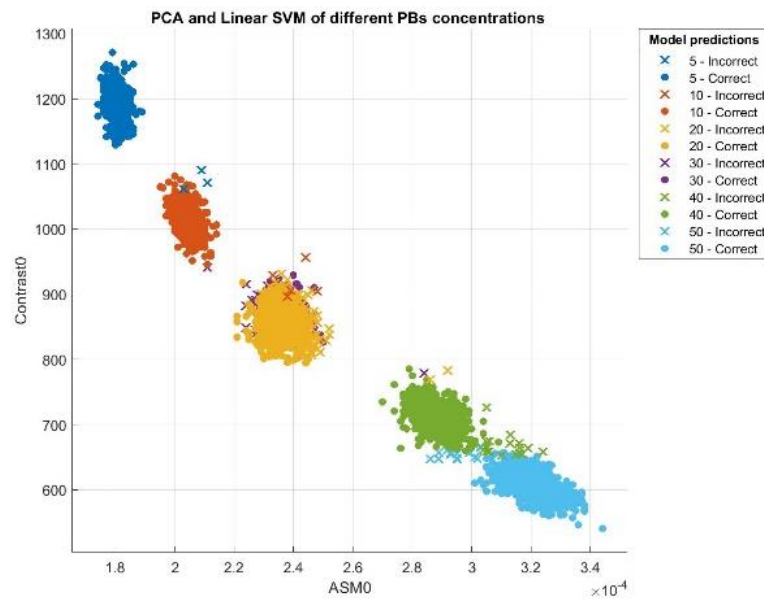
Figure 3.11b. The distribution of the groups along with individual components of PCA: I – the 2D plot of 1st and 2nd principal components; II – 1st and 3rd principal components; III – 2nd and 3rd principal components

Different volumes of PBs scatterers

The texture of different PBs volumes was detected accurately in 86.7% of cases with PCA and SVM, while 99.9% was achieved with SVM only. These are the overall classification accuracies in the detection of phantoms with various volumes of the PBs scatterers. In the classification of these types of phantoms, contrast and angular second moment (ASM) properties discriminated the most benefit to the classification performance during the feature selection process. An example of this is illustrated in Figure 3.12a: clusters of various phantom types were separable in the feature space, except for $20\mu\text{l}$ and $30\mu\text{l}$ of scatterers in 2% *gelatin solution*.

Figure 3.12b shows the similarity of textures generated by these two phantoms: 60% of $30\mu\text{l}$ PBs was classified as $20\mu\text{l}$ PBs sample, whereas 30% of $20\mu\text{l}$ PBs was selected as $30\mu\text{l}$ PBs phantoms. In contrast, 99-100% of phantoms with $5\mu\text{l}$ and $10\mu\text{l}$ PBs, 96-97% of $40\mu\text{l}$ and $50\mu\text{l}$ PBs were accurately detected by combined SVM+PCA classifier.

a



b

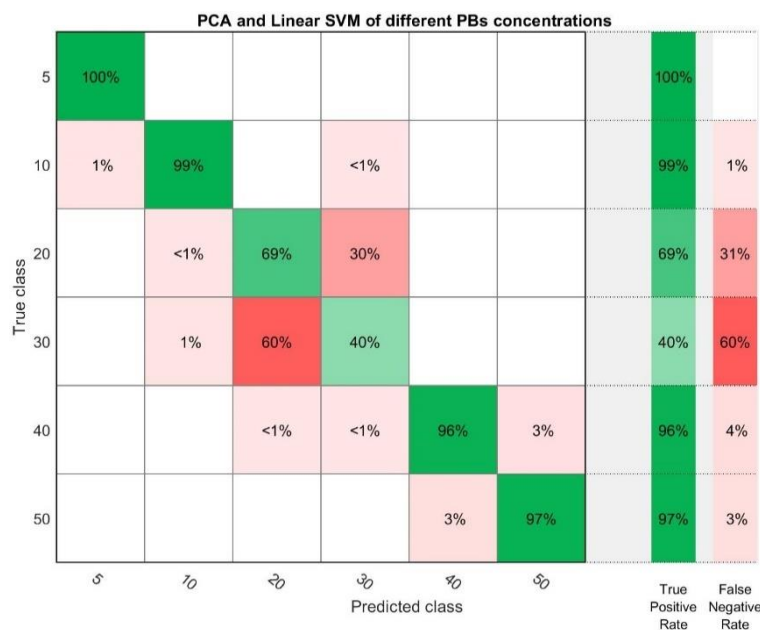


Figure 3.12. Different volumes of scatterers: a - clusters in the feature space: two most discriminating GLCM features – contrast and angular second moment (ASM) – demonstrated better classification performance. Here: • – correct and × – incorrect classification; (b) - confusion matrix. Here, 5, 10, 20, 30, 40 and 50 are the volumes of PBs in the gelatin solution in microlitre (μl).

3.4. Discussion

Due to the potential change of number and density of organelles in apoptosis, the evaluation of texture of varying volumes of PBs was carried out. The classification accuracy was about 87-99%, which indicates that the SVM classifier could detect the difference in the volume of scatterers in phantoms. No matter the concentration of PBs in gelatin, NNI calculation showed the uniform random distribution of particles in the medium, which is important due to the influence of mass density on the RI, according to the Gladstone-Dale equation (Chapter 1).

SVM classification showed that different types of scatterers and varying sizes of the same material can be discriminated against based on their optical textures. Classification accuracy of algorithms was between 81-93%. Nevertheless, the phantoms containing under resolution scatterers ($0.38\mu\text{m}$) changed the accuracy of SVM without PCA from 87% to 82.5%. Also, the classification of phantoms with $20\mu\text{l}$ and $30\mu\text{l}$ of PBs in 2% gelatin solution demonstrated interesting results. In the repeat experiments and analysis, it was clear, that the textures from these two types of phantoms were similar. The volume of the particulate mixtures in the standard medium is the other big issue of phantom preparation. The density of the scatterers and their distribution may give a specific textural picture. There should be conducted further studies on the density and volume of mitochondria and corresponding phantoms should be prepared.

Although gelatin has suitable mechanical and optical properties to act as an optical OCT phantom, these mixture solutions are not stable at room temperature. Also, it is important to ensure the random monodispersion of the particles. Otherwise, the clumped solid gelatin clusters or the scatterers may increase the regional refractive index and affect the power of back-reflected OCT light. These homogenous microbeads may not represent the exact delicate structure of elongated tubular or single punctiform mitochondria, and all these physical and optical parameters are a close estimate and approximate modelling of the main contributors of OCT scattering, especially in cellular degeneration. More robust studies with the use of biological phantoms are needed to demonstrate the changes during apoptosis.

The limitation of the OCT resolution cannot allow monitoring the cellular pathogenesis without the ultrahigh-resolution broadband light source, adaptive optics techniques, special complex image processing, analysis of texture and application of mathematic pixel computational learning algorithms. OCT image as a greyscale texture may consist of spectral and statistical information, that can be analysed and extracted as valuable information in the

early pathogenesis of various diseases. Nevertheless, with the available OCT with 70nm spectral band, non-isotropic resolution, extraction of only GLCM features, it was possible to achieve the high-accuracy classification of phantoms.

In summary, the study confirmed the utility of texture analysis in the discrimination of the phantoms of various sizes, concentrations and refractive indices of microparticles. Although the OCT device does not have cellular and subcellular resolution, speckle from backscattered light may show the characteristic texture of each phantom type. “Reading” of this speckle is possible by the application of texture analysis using machine learning classification tools.

Chapter 4. Optical detection of neurodegeneration in mouse retinal explants

4.1. Introduction

Lesion of RGC axons may cause the programmed cell death of neurons (Grafstein and Ingoglia 1982; Berkelaar et al. 1994). Intracranial and intraorbital transection of the optic nerve may cause the apoptosis of RGCs, which are likely the result of damaged axonal transport (Grafstein and Ingoglia 1982). Furthermore, impaired cell viability and homeostasis, as well as the dysfunction of the cellular trophic support system are also drivers of RGC degeneration (Nadal-Nicolás et al. 2015).

In axotomized RGC, nuclei are fragmented and clumped, making positive to peroxidase “apoptotic bodies”, which indicate the fragmentation of DNA and cytochemical alterations characteristic to apoptosis (Berkelaar et al. 1994). Besides, chromatin condensation was revealed along with internucleosomal fragmentation in a study by Quigley et al. (1995).

Despite the fact that the RGC cell death leads to the loss of control of the organelles (mitochondria, endoplasmic reticulum (ER), Golgi, etc.) and maintenance of the cellular environment (DePina and Langford 1999; Munemasa and Kitaoka 2013), the earliest stages of RGC degeneration is unclear. According to the study of Williams et al. (2013), the degeneration of RGC dendrites starts earlier than serious axon degeneration in DBA/2 J mice due to the influence of the complement cascade on dendritic atrophy. Hence, the RGC dies by a caspase-dependent mechanism, where caspases activate apoptosis through initiators (caspase-2, -8, -9 and -10) and executioners (caspase-3, -6 and -7) (Fan et al. 2005; Kumar 2006; Thomas et al. 2017)

Atrophy of RGC dendrites causes the loss of synapses with underlying bipolar cells (Lee et al. 2012). This leads to the dysfunction of RGC in the earliest stages of apoptosis, the action potential of which was tested on the pattern (PERGs) and flash (FERG) electroretinograms in DBA/2 J mice (Howell et al. 2007; Saleh et al. 2007).

Bevan et al. (2020) measured the RGC dendritic degeneration in amyloid overexpressing (3xTg-AD) and knock-in (APP^{NL-G-F}) mouse models, which corresponded with synaptic

dysfunction and deposition of beta-amyloid. These changes in RGC dendrites preceded irreversible cell loss (Williams et al. 2013).

Since the functional and morphological alterations in early apoptosis occur in the dendrites of RGC, evaluating the optical properties of the retinal IPL layer using OCT is proposed. The texture of this layer may change due to the events at the subcellular level, which have been proposed to be the source of OCT light scattering (Beuthan et al. 1996; Mourant et al. 2000; van der Meer et al. 2010). Even if OCT cannot allow visualizing the individual organelles, large multi-pixel speckle signals may carry information of the morphology, which can be described using texture analysis to extract and describe these events. The diagnosis of AD-related retinal symptoms, particularly the detection of the early signs, utilizing state-of-the-art high-resolution ligand-free imaging methods may allow the screening and monitoring of patients at high risk of AD development.

In this chapter, textural feature changes of RGC early neurodegeneration were monitored using high-resolution OCT and supervised machine learning algorithms (SVM and PCA+SVM). Also, for the first time, transparency of the murine retinal explants after the enucleation and dissection was investigated to exclude the optical changes due to the opacification of the tissue. Another novelty of this chapter is the observation of IPL optical differences of transgenic AD-mouse model from healthy controls (C57BL/6).

4.1.1. Hypotheses

- The texture of the inner plexiform layer (IPL) of retinal explants changes after transection of the optic nerve (ON) due to apoptosis. These texture-associated changes can be detected in the first hours after axotomy using machine learning classifiers: principal component analysis (PCA) and support vector machine (SVM).
- The texture of the IPL layer of the 3xTg Alzheimer's disease (AD) mice model is different from the texture of the IPL layer of the control (C57BL/6) mice.

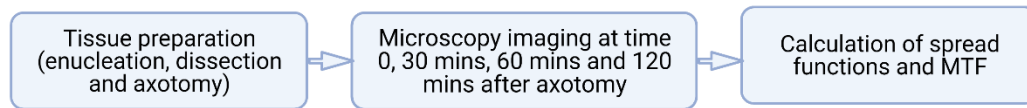
4.1.2. Aims

- To analyse the texture of the IPL layer of murine retinal explants
- To detect the optical alterations of RGC dendritic degeneration in the first hours after axotomy
- To detect the textural differences of AD-related dendritic neurodegeneration

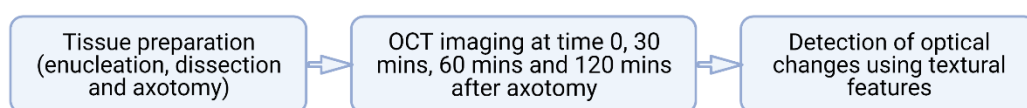
4.2. Experimental design

Figure 4.1 illustrates the stages of the experiments conducted using mice retinal explants.

Experiment 1. Evaluation of transparency/opacity of retinal explants after axotomy



Experiment 2. Monitoring of early RGC dendritic degeneration after axotomy



Experiment 3. OCT detection of RGC dendritic degeneration in Alzheimer's disease

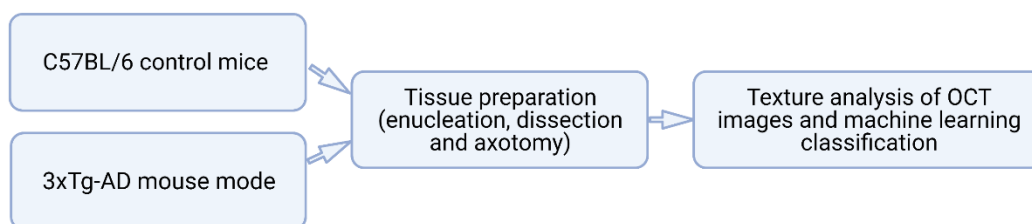


Figure 4.1. For the evaluation of retinal explants and ensuring the transparency of tissues, microscopy of samples was performed to quantify the modulation transfer function (MTF). Other retinal explants were imaged using OCT-1040 in four time-series (time 0 – immediately, 30 mins, 60 mins and 120) after axotomy. The texture of OCT scans was analysed using GLCM features. Texture analysis was also carried out on the IPL layer of transgenic AD mice. The scheme was created with BioRender.com

4.2.1. Analysis of retinal explants post axotomy

The retinal explants of C57BL/6 mice (age P15 and above) were dissected as described in Section 2.2. Five C57BL/6 retinal explants of 5 mice were used to model retinal axotomy: two of them were used to assess the transparency of tissues after axotomy (Experiment 1) and three explants were utilized to monitor RGC death over 2 hours (Experiment 2). In the post dissection and imaging periods, tissues were kept in HBSS (Life Technologies). The imaging of explants in OCT and microscopy was conducted as described in Sections 2.3 and 2.4.

4.2.2. Retinal transparency post axotomy: analysis of the modulation transfer function

Two retinal explants of C57BL/6 were visualized using the Olympus-IX71 microscope (Section 2.4.2) in order to inspect the tissues and measure the modulation transfer function (MTF). MTF detects the amount of contrast in the target object, maintained by the camera through identifying the transmitted spatial frequency ν content. MTF can be computed as the normalized modulus of the fast Fourier transform (FFT) of the point spread function (PSF) (Williams 2002). The summation of a line of overlapping PSFs forms the line spread function (LSF). Hence, MTF is inherently associated with the FFT of the LSF of the spatial distance x (equation 4.1).

$$MTF(\nu) = |FFT\{LSF(x)\}| = \frac{1}{\sqrt{2\pi}} \int_{-\infty}^{\infty} LSF(x) e^{-i2\pi\nu x} dx \quad (4.1)$$

LSF is the first derivative of the edge spread function (ESF). And ESF, in turn, is the profile of the image of an edge (Boreman 2001). In other words, ESF is built from a set of parallel LSFs, which end at the edge position.

Using the pixel intensity ranges from the microscopy images of the samples, the modulation transfer ratios and depth of images were calculated using equations 4.2 and 4.3, respectively. Hence, the MTF was defined as the ratio of the contrast of the image with the tissue to the contrast of the micrograph of the calibration slide.

$$MTF(f_x) = \frac{M_I(f_x)}{M_O(f_x)}, \quad (4.2)$$

where $M_I(f_x)$ and $M_O(f_x)$ are the modulation depths of the images of the grid lines with and without the retinal explant, respectively. Equation (4.2) was expanded as equation (4.3).

$$\begin{aligned} M_I(f_x) &= \frac{(I_{max-I} - I_{min-I})}{(I_{max-I} + I_{min-I})} \\ M_O(f_x) &= \frac{(I_{max-O} - I_{min-O})}{(I_{max-O} + I_{min-O})}, \end{aligned} \quad (4.3)$$

where I_{max-I} and I_{min-I} are the maximum and minimum intensity of the image with the retinal explant (I – image); I_{max-O} and I_{min-O} are the maximum and minimum intensity of the image without the retinal explant (O – object).

In order to measure the maximum and minimum intensity of the image with a retinal explant, dissected tissues were placed on the stage micrometre calibration slide (Muhwa Scientific, China). The slide plays the role of the calibration test target and consisted of a 1 mm scale

containing black and white line pairs (Figure 4.2a), marking 0.01mm divisions (Figure 4.2b). Also, the image of the slide without retinal explant was acquired to measure the I_{max-0} and I_{min-0} .

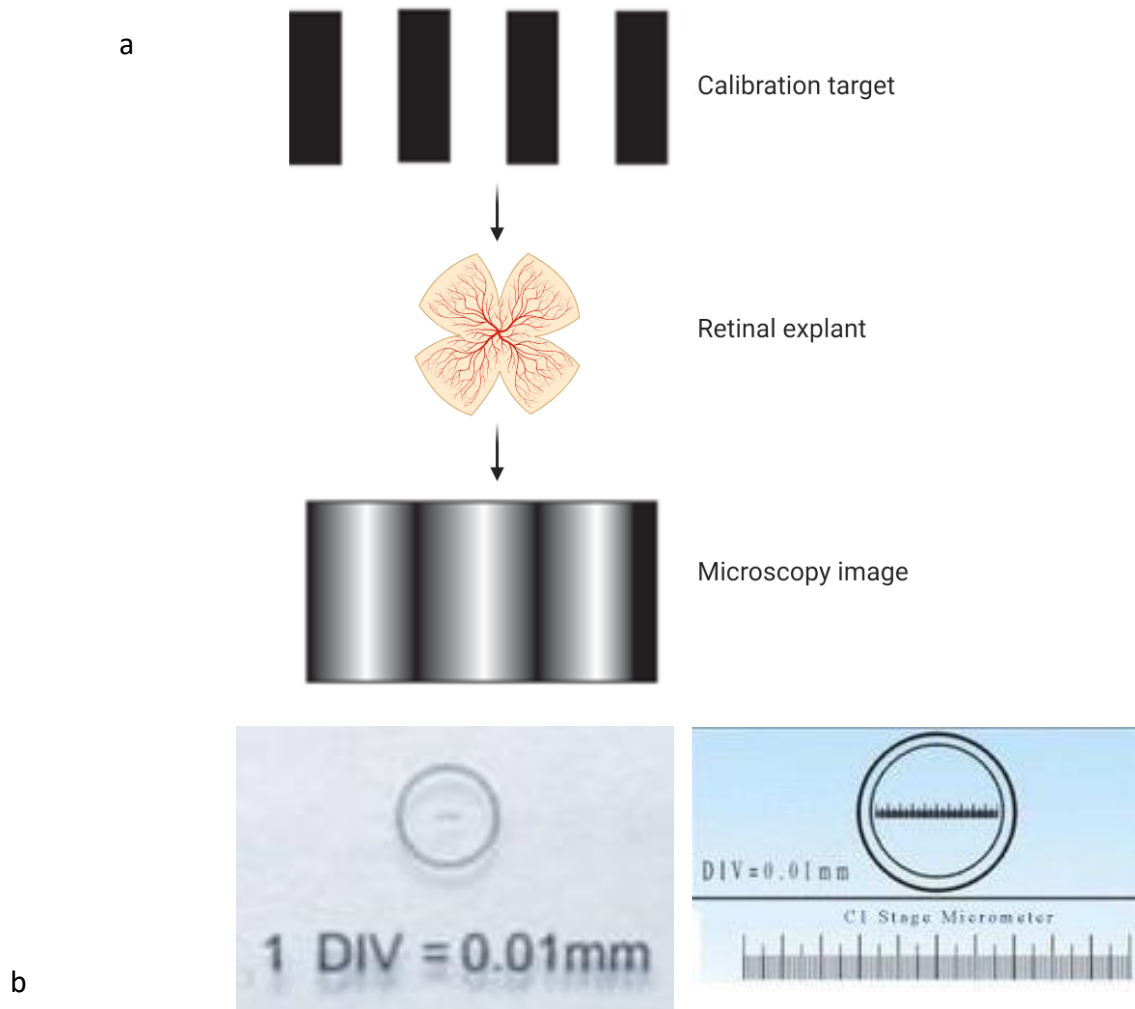


Figure 4.2. Modulation transfer function measurement: a – line edges before (top) and after addition of tissue sample (bottom); b – calibration slide and its schematic view. Created with BioRender.com

4.2.3. Retinal atrophy post axotomy: texture analysis of RGC dendritic tree

OCT acquisition from three C57BL/6 mice explants (2 images from each retina) was performed at four time points, giving a total number of scans 24 (Figure 4.1). All OCT scanning of C57BL/6 retinal explants for the time series was performed in the same location of the tissue without moving the sample and coverslip to ensure the consistency of data collected. 10 random VOIs within the IPL region were selected from each OCT scan, summing 240 VOIs in total. The dimensions of VOIs were 30×30×30 pixels in x, y and z scales. Then five GLCM features were extracted and imported to PCA and SVM classifiers. Texture analysis was performed in Simulink MATLAB R2017b (MathWorks) software. The details of image processing, feature extraction from the IPL and analysis are provided in Sections 2.6 and 2.7.

To assess whether data dimensionality reduction with PCA prior SVM or direct application of SVM works well with the monitoring of the textural changes in dying RGC, both were used. Linear SVM, as well as Gaussian SVM, had higher than LDA, QDA, DT and LR classifiers (Chapter 6).

4.2.4. Analysis of RGC dendritic atrophy in Alzheimer's disease

The 3xTg mice model was used for the analysis of the degeneration of the RGC dendritic tree in AD. For Experiment 3, 20 OCT images were acquired from seven 12 months old 3xTg-AD mice (The Jackson Laboratory, strain 34830-JAX: B6; 129-Tg (APP^{Swe}, tau^{P301L})1Lfa Psen1^{tm1^{Mpm}/Mmjax}) and three 15 months old C57BL/6J (B6/J Control, in house colony) and 200 VOIs in total (10 VOIs from each) were randomly divided into training (100), validation (50) and test (50) datasets. Similar procedures of VOI selection, feature extraction and image classification were applied as in the study of retinal atrophy post axotomy (Section 4.2.1.2).

4.3. Results

4.3.1. Transparency of the retinal explants

Since the transparency of retinal explants may change after dissection or during culture and thereby affect the results of texture analyses, the opacification of the tissues was assessed by computing the MTF. Generally, the MTF is used for the evaluation of the imaging performance of an optical system. However, here, the MTF was utilized to characterize the propagation of the modulated lights through the retinal explant.

Images taken by microscopy of the graticule, with and without the mice retinal tissue, are presented in Figure 4.3a. Also, the greyscale pixel value graph representations of the *en face* images are illustrated (Figure 4.3b).

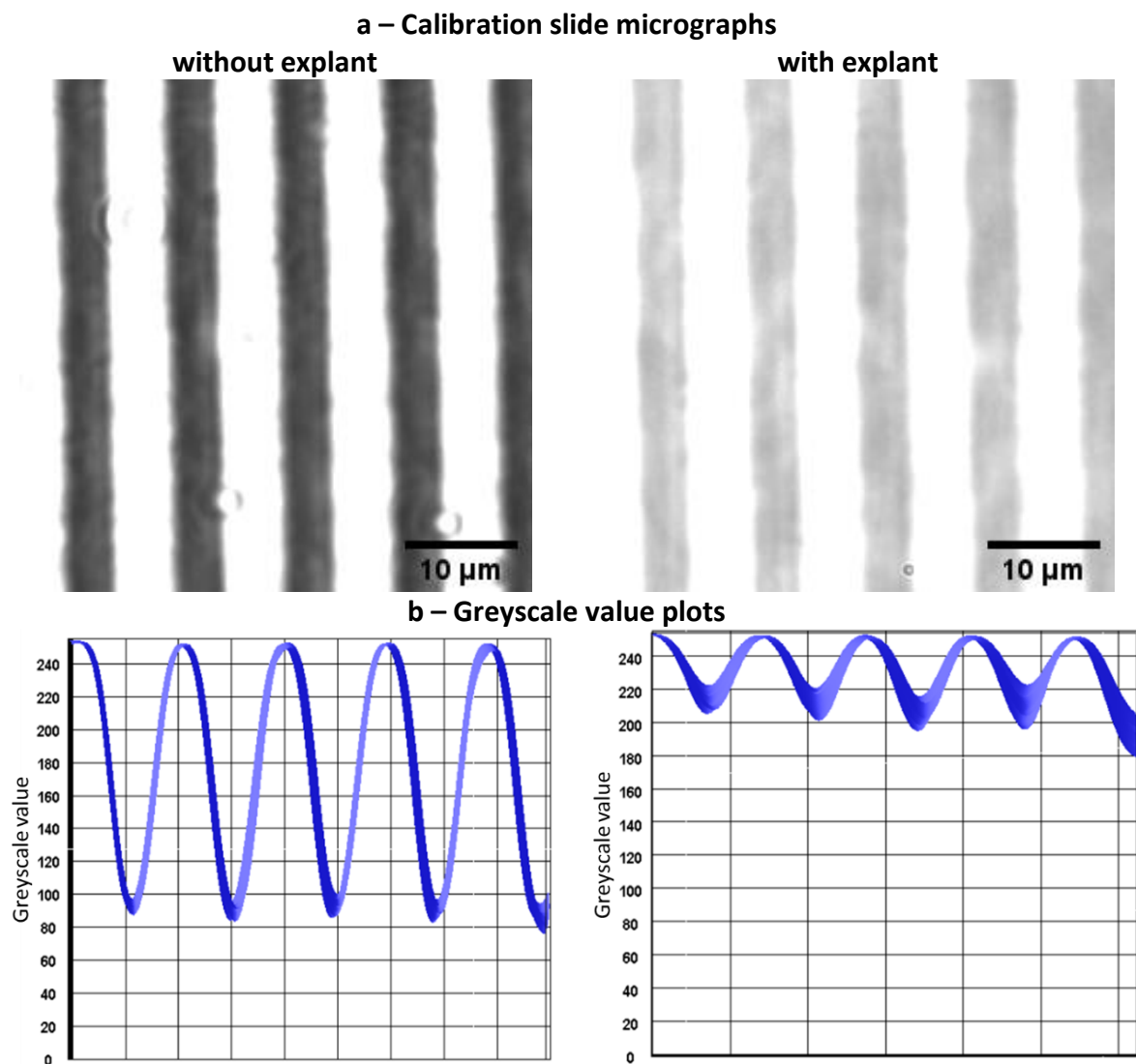


Figure 4.3. Microscopy images (a) and greyscale plots (b) of the calibration slide with and without mouse retinal explant

The greyscale plot has a sinusoidal shape with approximately the same modulation. The maximum intensity (I_{\max}) of both images with and without the retinal tissue is 255, whereas their minimum intensities (I_{\min}) differ: 57 for the image without explant and 138 for the image with explant.

Time series micrographs were also taken (Figure 4.4) and their mean, maximum and minimum intensity values were measured as well (Table 4.1). Using (4.1) and (4.2), modulation features were calculated and the summary of the modulation depth of the objects $M_o(f_x)$ and $MTF(f_x)$ the ratio is provided in Table 4.2, considering the modulation depth of the image $M_I(f_x) = 0.635$ (from Table 4.1).

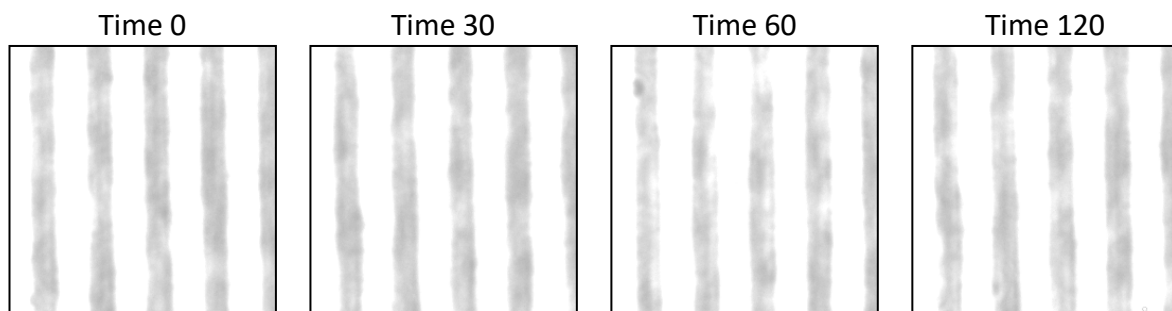


Figure 4.4. Microscopy images of the calibration slide with the tissue explants in the different time points

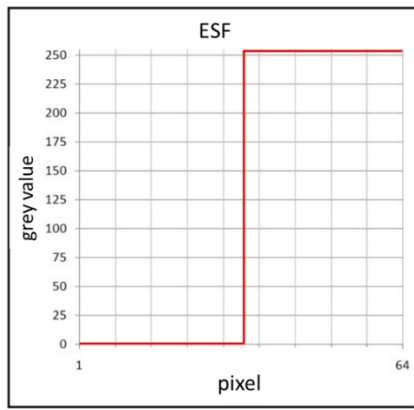
	Reference image (without tissue)	Time 0	Time 30	Time 60	Time 120
Mean grey-level	179.41	237.74	238.25	241.55	239.45
I_{\min}	57	181	184	179	186
I_{\max}	255	255	255	255	255

Table 4.1. Greyscales mean and range of intensities, computed from the images of Figure 4.3 for the reference image and Figure 4.4 – for the time points.

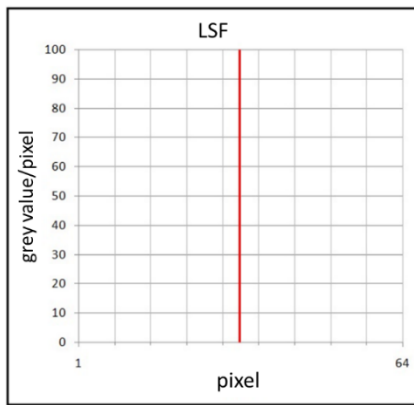
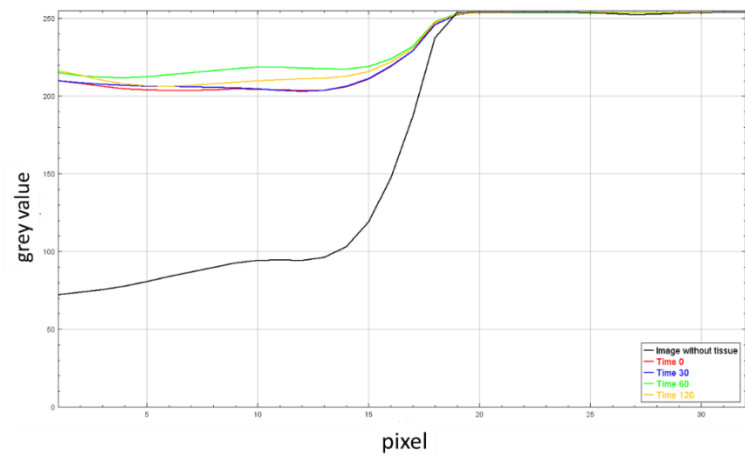
	Time 0	Time 30	Time 60	Time 120
$M_o(f_x)$	0.159	0.157	0.182	0.178
$MTF(f_x)$	0.250	0.247	0.287	0.281

Table 4.2. Summary of the modulation depth of the objects and MTF values, calculated using (4.1) and (4.2). Here, MTF values of Time 60 and 120 are higher than the MTF of Time 0 and 30

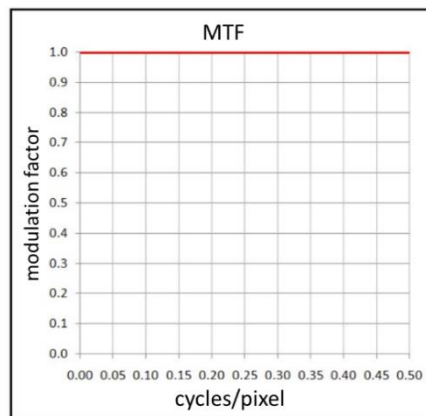
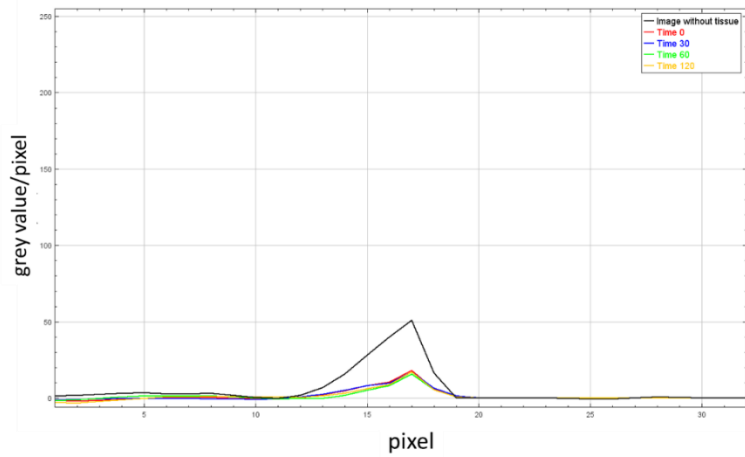
ESF, LSF and MTF relationships and the result of the computations are provided in Figure 4.5. the x-axis of the MTF plot is the normalized modulation factor against frequency input (cycles/pixel). Spread and modulation transfer functions values remained stable, and opacification of retinal explants did not occur after dissection. Transparency of post axotomy eyes was relatively constant over the 2-hour time period of analyses.



Edge spread functions



Line spread functions



Modulation transfer functions

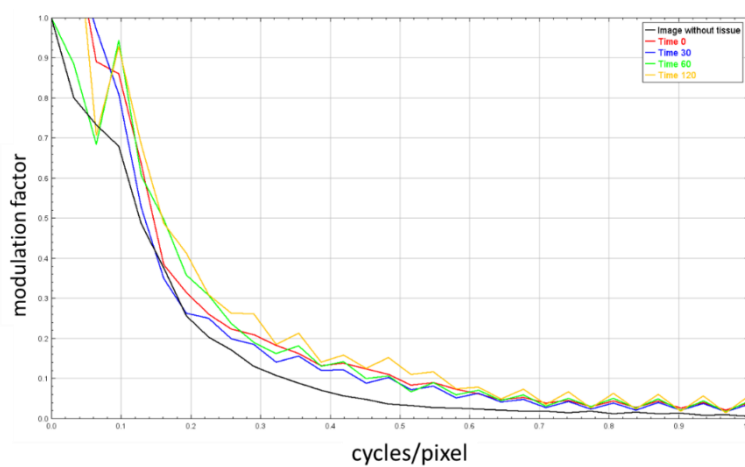


Figure 4.5. Edge and line spread functions and MTFs. Left: theoretically perfect system; right: same functions for images with and without the retinal explants. All functions were unchanged and there were no signs of secondary opacification of tissues during 2 hours of post dissection

4.3.2. Texture analysis of post axotomy RGC dendritic tree

OCT images of the retinal explants from C57BL/6 mice rats were inspected before feature extraction and texture analysis. A clear view of the morphology of the murine retina was observed (Figure 4.6). All layers of the retina were visible and the selection of random VOIs of the IPL was a straightforward process. The size of the volume of interest was small to avoid regions with prominent blood vessels.

OCT scans were acquired immediately after the transection of the ON (at time 0), and at 30 minutes, 60 minutes and 120 minutes following axotomy (Figure 4.7). Coverslip position was observed in the regions of abrupt pixel intensity transition.

Initially, GLCM-based texture analysis was performed at times 0 and 60 minutes after axotomy to test the classifier for the detection of the optical changes of apoptosis. A clear classification result was achieved with 2 distinct clusters (Figure 4.8a): the accuracy of the detection of time 0 explants from time 60 was 100% with and without PCA. Results suggest that the classifier operated correctly and that there could be detected changes associated with early retinal degeneration.

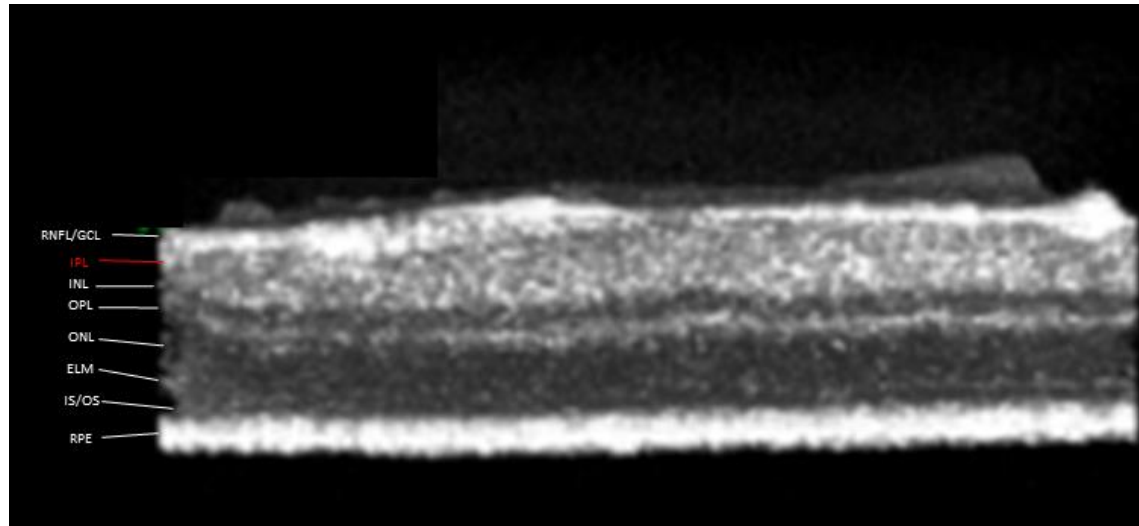
Then, the same analysis was applied for the detailed observation of the early and late stages of the RGC dendritic tree atrophy (data from 30 minutes and 120 minutes were added) together with the above-mentioned time points (time 0 and 60 minutes). Due to the interclass misclassification within time points of early stages (time 0 and 30 minutes) and similar in the time periods of late stages (1 and 2 hours). In Figure 4.8b, two groups of clusters in the feature space were formed. Potentially it indicates that the texture of these groups can be similar (Figure 4.8b) as we noted the similar MTF values in time 60 and time 120 in Table 4.4. The classification rate of SVM was 86.3%, SVM and PCA equals 81.9% (Table 4.3).

One of the explanations of the worse performance of SVM with PCA can be the result of the loss of some spatial information which is important for classification due to the dimensionality reduction. The confusion matrix in Table 4.3 depicts different accuracy of SVM with/without PCA: true positive rates are 75-96% with SVM only and 70-93% in the combinative application of both algorithms. Although, combining PCA with SVM intelligently can improve the SVM performance, in some cases it can degrade the SVM accuracy, which depends on whether the

SVM has had enough data in enough learning, test, and validation sets, to be sure it is not overtrained.

After the transection of the optic nerve, the cluster representing images in time 30 minutes shifted slightly right and top in Figure 4.8b. In contrast, in time 60 and 120, the clusters in 2D feature space shifted more to the same direction from the control position (time 0) and the border between early and late stages of apoptosis is clearly visible.

a



b

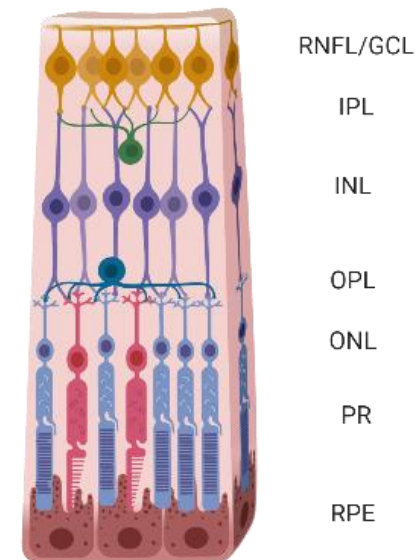


Figure 4.6. 3D rendered OCT image of a mouse retinal explant at time 0, RGC side up (a) with a schematic view of the retinal layers (b). RNFL – retinal nerve fibre layer; GCL – ganglion cell layer; IPL – inner plexiform layer; INL – inner nuclear layer; OPL – outer plexiform layer; ONL – outer nuclear layer; PR – photoreceptor layer; ELM – external limiting membrane; IS/OS – the junction between the photoreceptor outer and inner segments; RPE – retinal pigment epithelium.

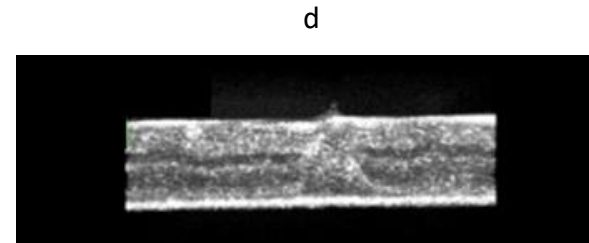
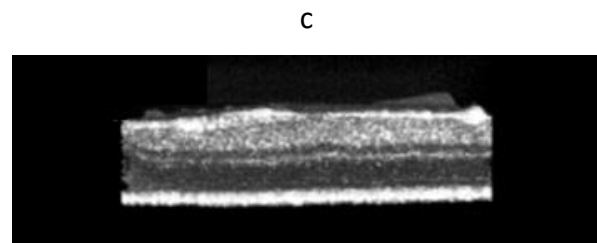
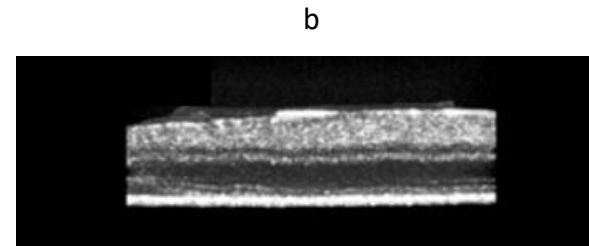
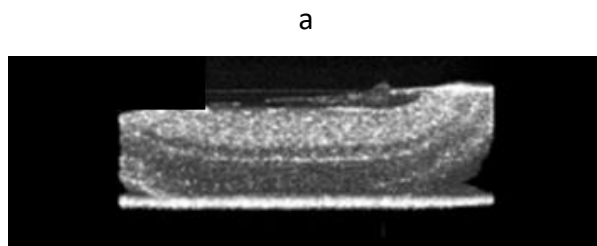
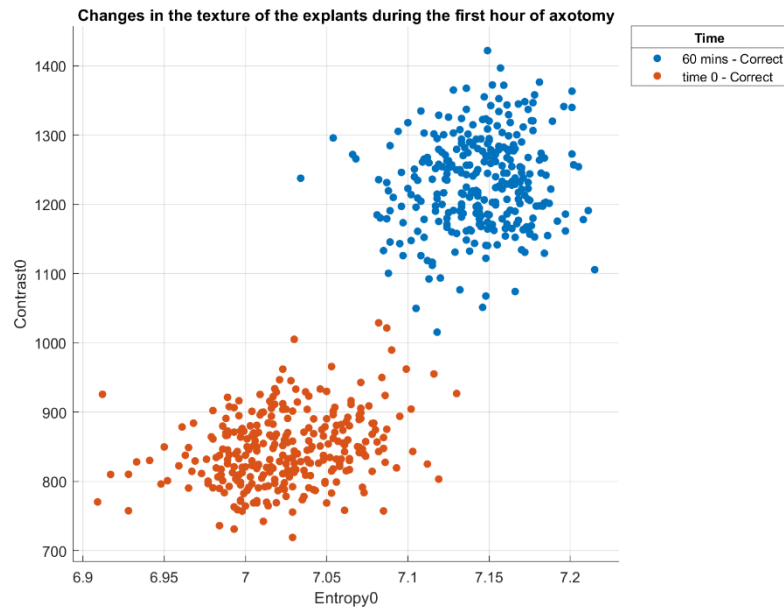


Figure 4.7. Time series of OCT images of the mice retinal explants: a – time 0 (after axotomy); b – 30 minutes after axotomy; c – 60 minutes after axotomy; d – 120 minutes after axotomy.

a



b

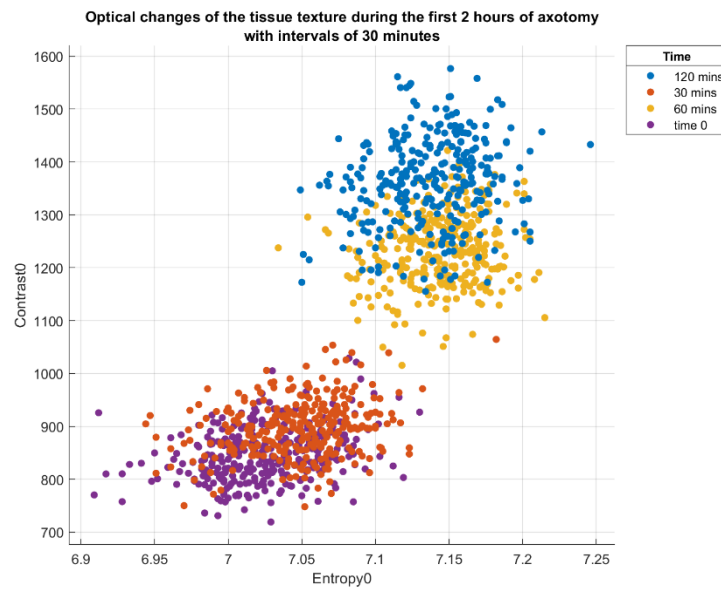


Figure 4.8. a – Texture analysis of early apoptosis in retinal explants, only time 0 and time 60 results shown. The accuracy of the classification was 100% with and without PCA. b – Texture analysis of apoptosis in retinal explants in time points: time 0, 30 minutes, 60 minutes and 120 minutes. Here: • – correct and × – incorrect classification

SVM classification							
	Timepoints	Predicted class (% correct)				True positive rate	False negative rate
		time 0	30 mins	60 mins	120 mins		
True class	time 0	75%	25%	0%	0%	75%	25%
	30 mins	23%	77%	0%	0%	77%	23%
	60 mins	0%	0%	97%	3%	97%	3%
	120 mins	0%	0%	4%	96%	96%	4%
PCA and SVM classification							
		Predicted class (% correct)					
True class	time 0	70%	30%	0%	0%	70%	30%
	30 mins	28%	72%	0%	0%	72%	28%
	60 mins	0%	0%	92%	8%	92%	8%
	120 mins	0%	0%	7%	93%	93%	7%

Table 4.3. Classification summary

4.3.3. Optical detection of neurodegeneration of RGC dendrites in AD mice

Next, this method was used to quantify neurodegeneration in the RGC dendrites of the 3xTg-AD mouse model retinal *ex-vivo* explants. To determine if neuronal degeneration occurring in retinal ganglion cells and their dendrites can also be detected following analysis of OCT images after processing of back-reflected light, the IPL layer in retinal explants of 3xTg-AD mouse and C57BL/6 (black6 or B6) were analysed immediately after ON transection.

Results acquired after the GLCM-based feature analysis indicated that the texture of the IPL layer of 3xTg-AD mice differed from that of the control C57BL/6 group mice. In Figure 4.9, the most descriptive GLCM features (Contrast0 and Entropy0 – features in 0 degrees between the index and reference pixels) were selected by PCA. The resultant 2-dimensional feature space classification resulted in 2 clusters (control and 3xTG) and demonstrated 100% accuracy of the classifier in both scenarios: with and without PCA.

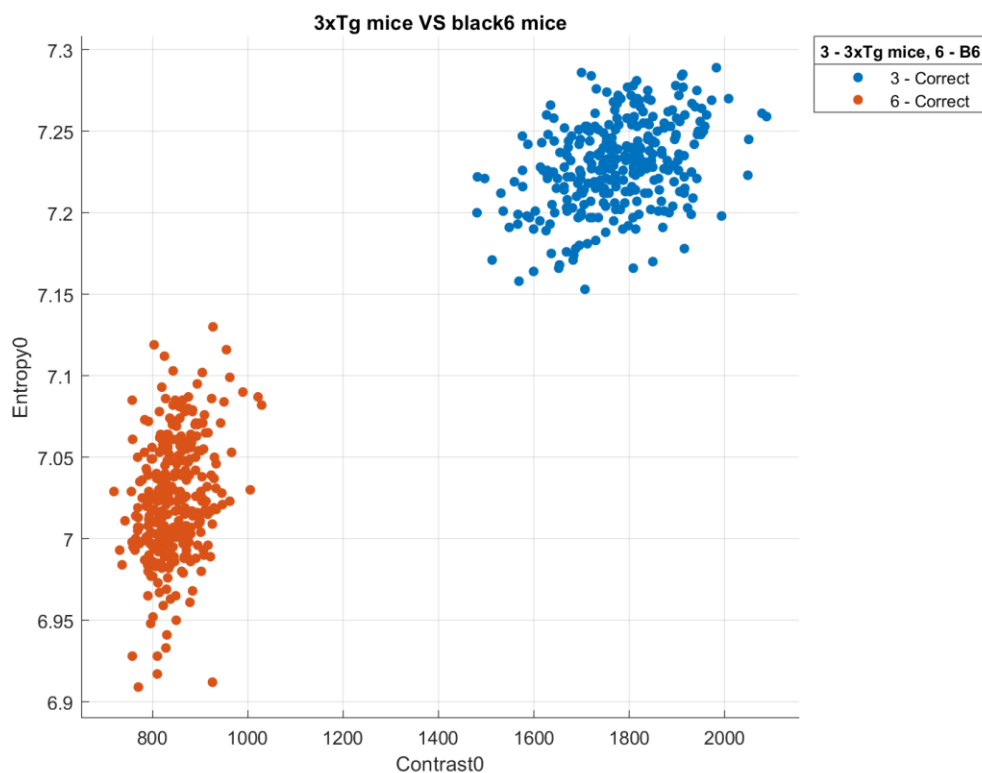


Figure 4.9. Texture analysis results of 3xTg-AD mice (n=7) and C57BL/6 (black6 or B6)(n=3) of IPL layer in retinal explants, OCT scans were acquired immediately after the transection of ON. The accuracy of the SVM classification was 100% with and without PCA. All VOIs were classified accurately, hence there are only sing “•” in the plot. Here: 3 – 3xTg; 6 – C57BL/6.

4.4. Discussion

Retinal explants in culture maintained their optical clarity for at least 2 hours after transection of the ON (i.e., the duration of the experiments in this chapter), indicating that any potential changes of the texture are unlikely to have arisen due to opacification of the samples. In general, the health and viability of RGC are dependent on the environmental conditions: pH, temperature, medium contents, sterility and oxygenation. OCT scanning may stimulate and/or accelerate RGC death (Bull et al. 2011). Although studies on the MTF support the theory of the optical changes of retinal neurodegeneration, these measurements should be performed in retinae for a longer time period post axotomy to show how and when opacification may happen which is presumably irreversible.

Potentially, the onset and early stages of retinal degenerative diseases are connected with the atypical function and abnormal morphology of the cell and its organelles. In Chapter 3, the benefits of using GLCM features and SVM as a machine learning tool to detect and discriminate subtle textural changes of OCT images were shown. Irregularities in OCT phantoms and biological tissues can be detected by texture analysis which attempts the recognition of homogeneous regions within the image using texture properties. Refractive indices, sizes and shapes of the various structures of the cell differ from each other and these contrasts are the subject for OCT light scattering.

This study showed that OCT imaging and analysis of textural features can be utilized to compute the early degeneration of neuronal tissue. Since the injury of the ON is reported to cause RGC death (Thanos 1988; Berkelaar et al. 1994; Garcia-Valenzuela et al. 1994; Quigley et al. 1995; Nadal-Nicolás et al. 2015), the axotomy model was used to monitor the optical changes in the IPL layer. This has been done based on the assumption, that the transection of the ON of C57BL/6 mice initiated apoptosis of the retinal ganglion cells, which usually starts in the dendritic terminals (Thanos 1988; Nadal-Nicolás et al. 2015). Hence, the optical changes of early apoptosis were first detected in the inner plexiform layer using OCT (Tudor et al. 2014). Further studies on the optical alterations of GCL and RNFL layers will be needed to understand the nature and pathogenesis of RGC apoptosis.

Optical alterations were subtle and only pixel differences in the backscattered light were measurable. As a tool for the mathematical quantification of biological changes, SVM and PCA

were utilised. Semi-automated texture analysis enabled the detection of the early cellular events preceding apoptosis, even if the identification of individual organelles was impossible. Therefore, the analysis of texture in the OCT image was the next step for measuring the integrity of the retina. Complex use of OCT and statistical texture analysis of the image enabled the classification of biological tissues of the same types (Gossage et al. 2003). Lab-based ultra-high-resolution OCT-1040 allowed us to acquire the scans of *ex vivo* murine explants without the removal of speckle.

It is challenging to detect the exact scattering source, and this was beyond the scope of this chapter. Nevertheless, it was demonstrated previously that the organelle network, particularly mitochondria, might be a possible source of OCT signal changes in the study of (Tudor et al. 2014). The shift of the cluster in the later stages of apoptosis (60 and 120 minutes) in 2-dimensional space (from 20D after PCA dimensionality reduction) demonstrated a change of the optical signature during the cell death process.

In addition, cellular nuclei and their components may also contribute to the backscattering of light in programmed cell death (Gavrieli et al. 1992). Similar apoptotic changes, initiated by the administration of staurosporine, were investigated in RGC-5 cell culture for *in vitro* detection of early apoptosis using ultra-high resolution OCT (Tudor et al. 2014).

Detection of apoptosis, particularly in its early stages, is a vital aim in many diseases. The non-invasive, ligand-free and non-toxic way of this procedure became clinically preferable (Tudor et al. 2014; Morgan et al. 2017). Ultrasound, X-ray, computed and MRI tomography allows the acquisition of high-quality images. These scans can be then processed and analysed using machine learning tools. The latter helps to calculate neuronal health, viability and death.

Therefore, it is possible and potentially useful to study further stages of apoptosis in 12 and 24 hours, and late cellular death in the first 7 days after axotomy. Also, the health of the other retinal layers (GCL, RNFL) corresponding to the RGC body and axons was not studied in this chapter. Moreover, the viability of bipolar and photoreceptor cells can be investigated for the subject of textural changes. In addition, among the other limitation of this study is the lack of histological and histochemical investigations of axotomized retinal explants in the first hours of apoptosis.

Application of the texture analysis in the detection of neurodegeneration of murine retinal OCT *in-vivo* can be studied. Furthermore, the diseases with cellular and subcellular alterations (glaucoma, AD, AMD and others) can be modelled in animal studies and the texture signature might be calculated using this semi-automated and other types of machine learning techniques.

The OCT-1040 system allowed the visualisation of all the retinal layers of the explants due to its high axial resolution, which is determined by the spectral bandwidth of the light source. For future work, the neurodegeneration of the retina can be computed for the other layers, including the compartments of retinal ganglion cells and photoreceptors.

For the purpose of *in vivo* studies in humans, the OCT device system should be modified: the numerical aperture of lenses would be decreased and the complex use of adaptive optics. The latter improves the transverse resolution. However, there are some limitations for the human eye: cataract, vitreal haemorrhage or other media opacities and movement artefacts. The next step for the application of the texture analysis of the neurodegeneration is *in vivo* detection of the optical signature in glaucoma and macular degenerations.

To conclude, optical changes of apoptosis and the mathematical description of biological changes in apoptosis and AD-related RGC neurodegeneration are described in this chapter. Detection of these changes without ligand was the aim of this study; OCT imaging and machine learning classifiers allowed us to observe the texture associated with optical alterations within the first hours of RGC death and dendrite degeneration in AD mice retina.

Chapter 5. Texture analysis of outer retinal layers in macular degeneration

5.1. Introduction

Age-related macular degeneration (AMD) is a complex disease with multiple pathogenetic factors and variable clinical symptoms (Holloway and Verhoeff 1929; Brown et al. 2019). AMD is the leading cause of irreversible vision loss in the industrialized world and disease with a substantial global economic burden (Velez-Montoya et al. 2014).

Degeneration of RPE leads to photoreceptor (PR) cell death. With apoptosis as the most likely driver, the number of TUNEL (transferase dUTP nick end labelling) positive cells have been shown to be higher in post-mortem human retinas with AMD compared with healthy controls (Dunaief et al. 2002). The close relationship between the homeostasis of photoreceptors and RPE cells, as supported by mitochondrial activity has elegantly been shown by studies demonstrating the changes in mitochondrial shape in AMD and a reduction in the levels of TOMM20 (translocase of outer mitochondrial membrane 20), and essential component of mitochondrial membrane transport (Brown et al. 2019). Mitochondrial DNA disorders in AMD have been reported (Karunadharma et al. 2010; Terluk et al. 2015) that are similar to those in Alzheimer's disease and Parkinson's disease (Giannoccaro et al. 2017; Tang et al. 2019; Theurey et al. 2019).

Although a broad range of imaging techniques have been developed to detect AMD, colour fundus photographs and OCT remain gold standard methods (Kanagasingam et al. 2014). The source of reflectivity changes in OCT images from eyes with AMD is a topic of active debate. Machine learning has emerged as a powerful method for the identification of subtle optical changes, drusen classification and the grading of disease severity when applied to OCT images. For instance, multi-scale textural features and shape parameters were extracted from OCT scans to train and segregate different macular conditions: macular hole, macular oedema and AMD (Liu et al. 2011).

Due to the location of the alterations in the outer retina, RPE and choroid, recent studies have been designed to detect the early changes *in vivo* and ligand-free. Ravenscroft et al. (2017) demonstrated the potential of the long-wavelength OCT to scan the choroid as a route to the

detection of early macular pathology. Their automated convolutional neural network method for the supervised machine learning classification generated a promising outcome for the detect choroidal signs of AMD (Ravenscroft et al. 2017).

In Chapter 4, the optical alterations of dying retinal cells of axotomized RGC and in transgenic rodent model were investigated, demonstrating that subtle changes in optical scatter likely driven by subcellular changes could be detected with OCT. In this chapter, the possibility that these techniques can be applied to the analysis of the photoreceptor/ RPE interface for the detection (ligand-free) of early and neovascular AMD was investigated.

Early AMD detection may change the treatment protocol and enhance the role of preventive measures. Also, correct management of modifiable risk factors can minimize the onset of the disease via increasing the viability and metabolism of the cells of the retina and RPE. The atrophic alterations of early AMD may generate the specific textural signature in the outer retina, which can be detected by high and ultrahigh-resolution OCT with combinative use of texture-based machine learning, which was achieved in this chapter and results of ML classification is provided.

5.1.1. Hypothesis

OCT texture of the outer retinal layers may change in age-related macular degeneration due to the multiple factors, but predominantly because of the apoptosis of photoreceptors and RPE cells. These changes can be detected using machine learning classifiers: principal component analysis (PCA) and support vector machine (SVM).

5.1.2. Aims

- To extract the grey-level co-occurrence matrix and local binary pattern textural features from the soma and dendrites of the photoreceptors and RPE cells.
- To analyse the texture of the outer nuclear layer (ONL), photoreceptor layer inner (IS PRL) and outer (OS PRL) segments, retinal pigment epithelium (RPE) in healthy and AMD patients.
- To obtain the optical signature of early and neovascular AMD.
- To assess the classification accuracy of the novel classifier.

5.2. Methods

5.2.1. OCT dataset

3D OCT image datasets acquired in 20-degree scans centred on the macula were kindly provided by Dr Ashley Wood and Dr Louise Terry, School of Optometry and Vision Sciences, Cardiff University. The same research-based OCT-1040 was used for the acquisition of scans. This OCT imaging system has been previously described in Section 2.3. These clinical images of patient eyes were obtained using the OCT sample arm adjusted to the PAT head, which stands for “patient”. The broadband spectrum of Amplified Spontaneous Emission 1-M-ASEHPE-S (NP Photonics, Tucson, AZ, USA) with long-wavelength light source allowed penetrating the deeper layers of neuronal retina and choroid (Ravenscroft et al. 2017).

The dataset consisted of 60 OCT retinal scans; 20 healthy controls and 40 acquired from patients with diagnosed AMD. The latter was categorized into two groups of 20 scans each: early AMD and neovascular AMD (nAMD). The classification of the disease was categorized using the diagnostic features of Table 5.1, which was adapted from the International Classification and Grading System for the classification of AMD (Bird et al. 1995).

The OCT images used in this chapter are 3D stacks of size $512 \times 512 \times 1024$ pixels in x, y and z, respectively. Due to the outer retinal localization of the pathology, ONL, IS PRL, OS PRL and RPE layers were studied in this investigation. From each layer, 5 volumes of interest (VOIs) were randomly selected (Table 5.2). VOI selection was achieved according to the normal retinal layers’ thicknesses. Therefore, the 3D volumetric dimensions of VOI of ONL and RPE layers were $30 \times 30 \times 30$ pixels (in x, y, z), whereas $15 \times 15 \times 15$ pixels were the sizes of VOI for inner and outer segments of PRL (Figure 5.1).

Condition		Diagnostic features
Early age-related maculopathy (ARM)		Drusen with or without associated pigment and/or focal hypopigmentation of the RPE
Late AMD	Dry AMD	Area of geographic atrophy $\geq 175\mu\text{m}$ in diameter
	Wet AMD	One or more of the following: <ul style="list-style-type: none"> • RPE detachment • SubRPE/Subretinal neovascular membrane • Disciform scar • Subretinal haemorrhage • Hard exudates

Table 5.1. Diagnostic criteria for the classification of AMD according to the International Classification and Grading System for the classification of AMD (Bird et al. 1995)

Group	Number of scans	Retinal layers of interest	Number of VOIs
nAMD or wet AMD	20 images	ONL	100 VOIs
		IS PRL	100 VOIs
		OS PRL	100 VOIs
		RPE	100 VOIs
early AMD	20 images	ONL	100 VOIs
		IS PRL	100 VOIs
		OS PRL	100 VOIs
		RPE	100 VOIs
control	20 images	ONL	100 VOIs
		IS PRL	100 VOIs
		OS PRL	100 VOIs
		RPE	100 VOIs
Total	60 images		1200 VOIs

Table 5.2. Number of OCT scans and selected volumes of interest (VOIs)

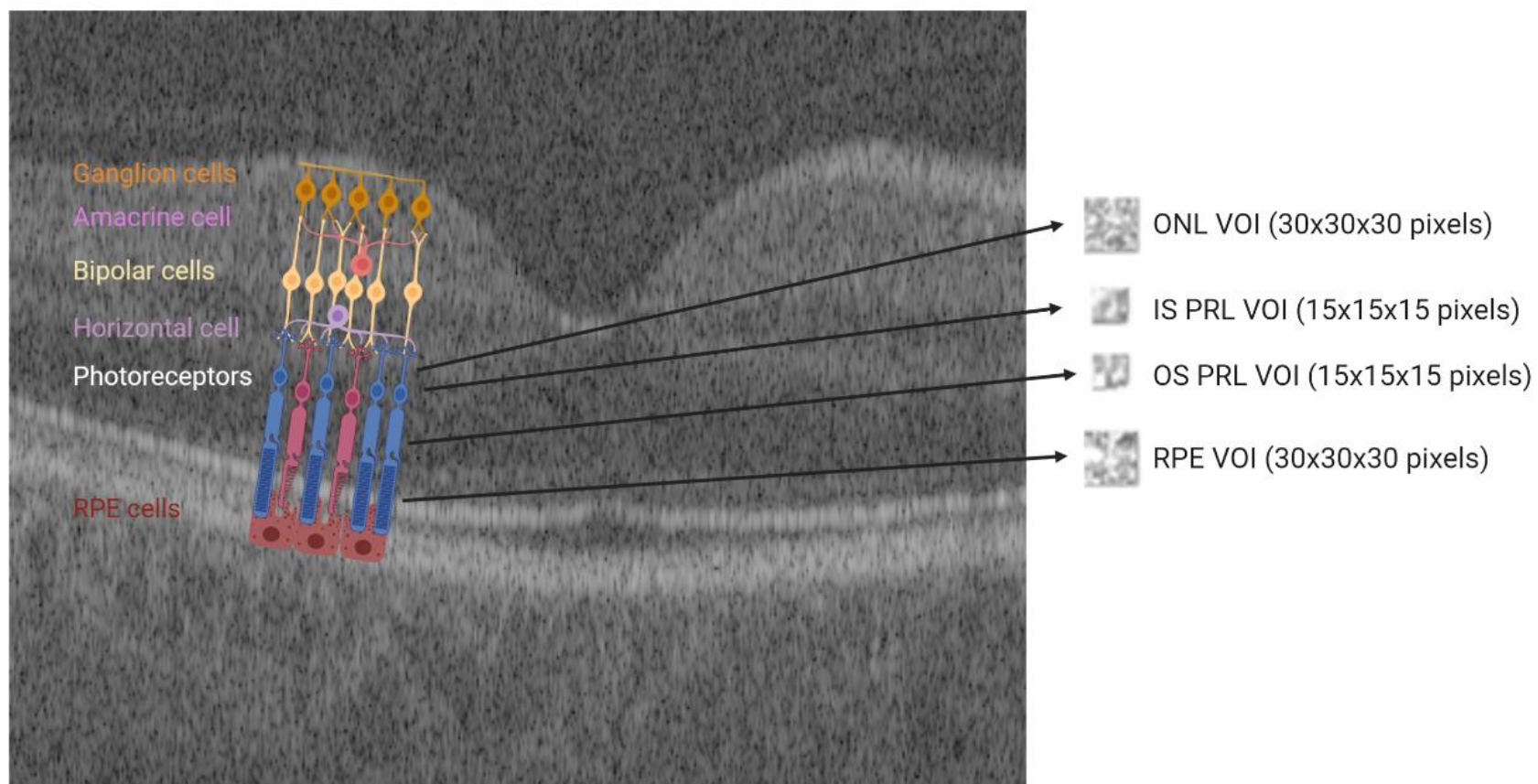


Figure 5.1. OCT scan sample with retinal cells scheme. VOIs were selected from the outer nuclear layer (ONL), retinal pigment epithelium (RPE), inner and outer segments of the photoreceptor layer (IS PRL and OS PRL).

5.2.2. Texture analysis and machine learning

Selected VOIs underwent texture analysis using grey-level co-occurrence matrix (GLCM) and local binary pattern (LBP) features (Figure 5.2), as described in detail in Sections 2.6.1 and 2.6.3. 20 GLCM and 59 LBP features were extracted from all VOIs and then imported into the classifiers (PCA+SVM and SVM only). Before the classification, all extracted VOIs were randomly divided into training (600), validation (300) and test (300) datasets. Results of previous chapters highlighted the diagnostic potential of the classifiers. The same tools were applied to human *in vivo* OCT images which supported a feature space with greater dimensions.

IPL texture analysis for human OCT was performed for glaucoma patients in Chapter 6 using PCA+SVM and only SVM. Also, in the study of Anantrasirichai (2013), high-accuracy SVM-based texture classification of glaucoma patients was achieved. Ternary (multi-class) classification of 2 stages AMD patients and age-matched healthy controls were also the subject of choice in favour of SVM.

The classifiers were run to test the datasets, consisting of all 1200 VOIs from 20 healthy control eyes, 20 eyes with early AMD and 20 eyes with neovascular AMD. 10 OCT images from each group (50%) were randomly selected for the training of the classifier, whereas the rest 30 images were included in the test dataset. Analysis with various random training and testing data was reiterated 10 times.

5.2.3. Greyscale histogram analysis

A separate analysis of the greyscale distribution calculation was carried out in the selected VOIs. A grey-level histogram maps each greyscale of a scan to its frequency. For 8- bits OCT B-scan the range of grey levels equals from 0 to 255 and the total number of pixels amounts to 512×1024 (Figure 5.3).

The two most descriptive statistical measures of greyscale histogram (mean and standard deviation) features were analysed and compared. For the comparison of mean values, the extension of independent two-samples t-test – one-way analysis of variance (ANOVA) – was performed with R Statistics 3.5.3. $P < 0.05$ was considered statistically significant.

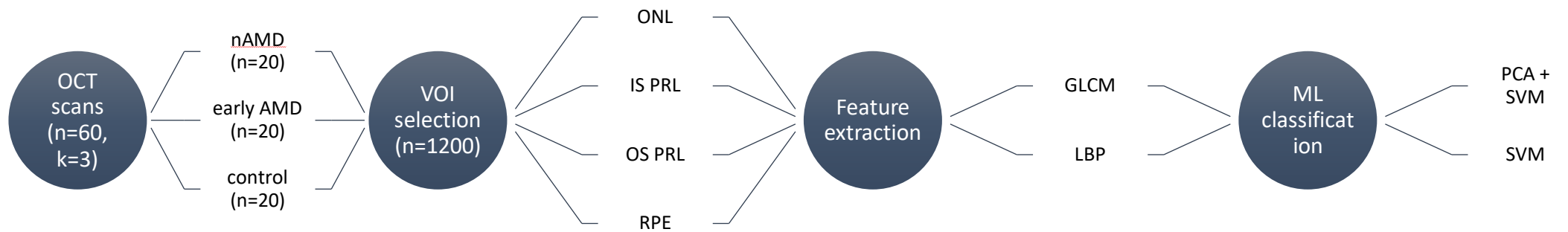


Figure 5.2. The study design: the volume of interest (VOI) selection, feature extraction, texture analysis and OCT image classification: n – number of scans/VOIs, k – number of classes; ONL – outer nuclear layer, IS PRL – the inner segment of photoreceptor layer, OS PRL – the outer segment of photoreceptor layer, RPE – retinal pigment epithelium; GLCM – grey-level co-occurrence matrix, LBP – local binary pattern, ML – machine learning, PCA – principal component analysis, SVM – support vector machine.

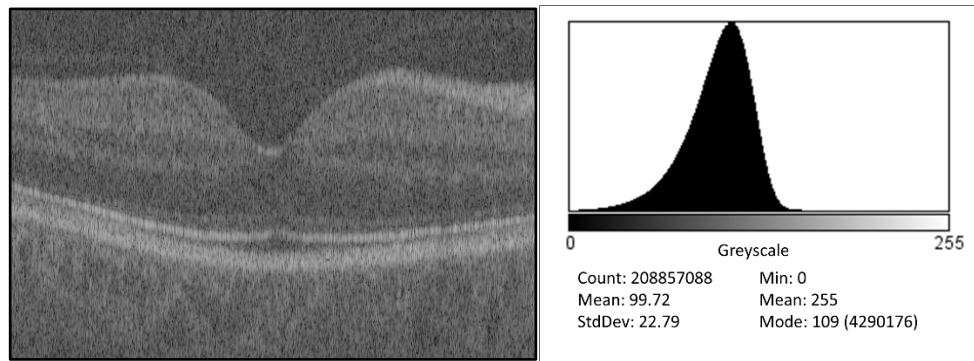


Figure 5.3. Example of macula OCT image stack with the grey-level histogram. Histogram analysis shows the distribution of the number of pixels (y-axis) according to the pixel intensity value (x-axis) in the volume of interest

5.3. Results

All scans were inspected for quality, and examples of OCT images of different classes are depicted in Figure 5.4. Neovascular membranes, hard exudates and other severe signs of AMD were present in patients with nAMD. By contrast, these were not apparent in patients with early AMD. The average age of patients with nAMD was 80 years (age range: 67-92 y.o.), compared with 74 years for early AMD (age range: 57-87 y.o.) and 73 years for healthy controls (age range: 59-88 y.o.). The mean axial eye length for all patients was 23.47 mm. Visual acuity was 0.34 for nAMD, 0.17 for the early AMD and 0.10 for healthy participants.

Table 5.3 demonstrates the average values of the classification summary as per cent agreement between classifier and ground truth. PCA eliminated the redundant data and eigenvectors with high values were selected for the reduction of the dimensionality. However, this did not always increase the accuracy of the classifier. In several cases, the SVM accuracy was higher with the inclusion of PCA than without.

It is notable that LBP features had a higher discriminative value than GLCM for the classification of AMD. Nevertheless, the combined use of GLCM and LBP textural properties increased the performance of both classifiers. Table 5.3 demonstrated that the classification accuracy increased for the detection of optical changes in the outer retinal layers. Thus, diagnostic accuracy was higher in RPE than OS PRL. Similarly, accuracy was greater for the OS PRL compared with the IS PRL and the IS PRL was greater than the ONL. This progression matches the known pathological sequence in AMD and confirms the RPE layer as the primary pathological site for AMD. Among all classes, nAMD had the highest accuracy for SVM and SVM+PCA classifiers – 94%, whereas the detection rate of the early AMD was 91% and for healthy participants, it averaged 92.5%. SVM classification of GLCM and LBP features of control vs early AMD vs nAMD is presented in Table 5.4.

According to the table, SVM with PCA was higher than the only SVM in one case, when LBP features were imported to compare the texture of the outer nuclear layer (66.3% versus 59%) and both classifiers' accuracy was equal (70%) in one case, when GLCM and LBP parameters were added in the texture analysis of IS PRL. All other models showed better performance of SVM without data dimensionality reduction. This may occur because the new feature space is a linear combination of original features, which may indicate that there is a loss of valuable

textural information. Also, it may depend on the way the pattern vector has been defined. One of the solutions to improve the PCA+SVM performance is to modify the elements of the pattern vector and monitor whether it affects the classification by either of the techniques.

Analysis of the greyscale histogram analysis did not identify any significant differences between the disease groups. A comparison of greyscale histograms of four retinal layers between groups is shown in Figure 5.5. The distribution curves shift to the left in Figure 5.5: A and B and nAMD curves were different in OS PRL and RPE in terms of intensities at peak (Figure 5.5: C and D), which may support the high SVM classification in this class of data.

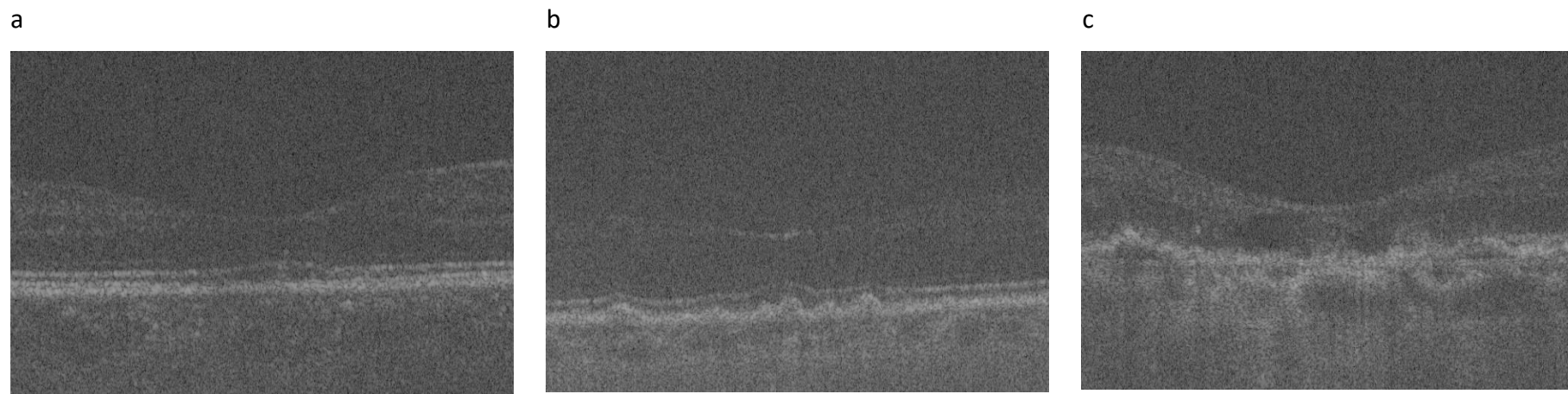


Figure 5.4. OCT scan examples representing the classification groups ($k=3$): a – healthy control; b – early AMD; c – neovascular AMD (nAMD)

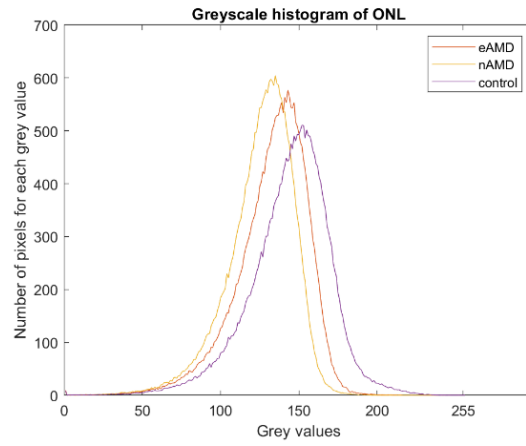
Retinal layer	Textural features	Classification accuracy	
		SVM	SVM+PCA
ONL	GLCM	48.6%	34.3%
	LBP	59.0%	66.3%
	GLCM+LBP	69.3%	67.6%
IS PRL	GLCM	57.9%	52.1%
	LBP	56.7%	53.3%
	GLCM+LBP	70%	70%
OS PRL	GLCM	63.5%	56.7%
	LBP	73.3%	56.7%
	GLCM+LBP	90%	60%
RPE	GLCM	72.2%	57.9%
	LBP	80%	73.3%
	GLCM+LBP	99%	93.3%

Table 5.3. Classification summary on the level of different retinal layers

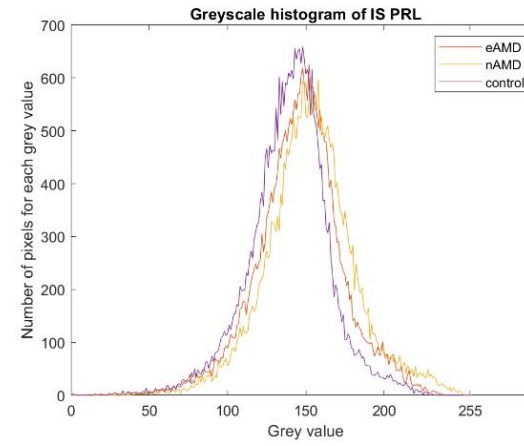
Groups	control	early AMD	nAMD
control	100%	73%	86%
early AMD	73%	100%	77%
nAMD	86%	77%	100%

Table 5.4. SVM classification of GLCM and LBP features

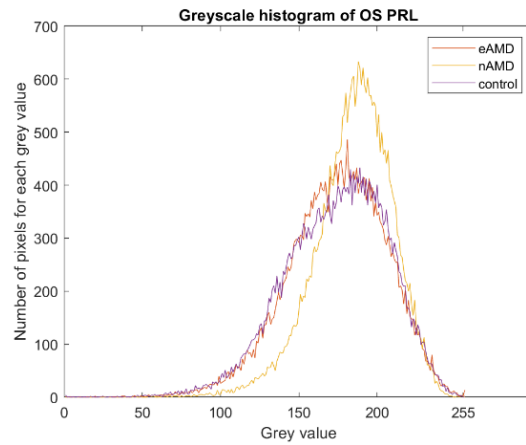
A



B



C



D

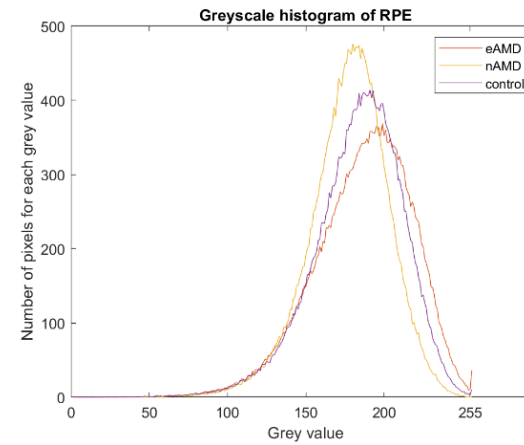


Figure 5.5. Histograms of grey values for comparison of greyscale histogram parameters between study groups.

5.4. Discussion

In this chapter, SVM and SVM+PCA classifiers provided high classification accuracy for the detection of AMD and the discrimination of early and late disease changes. The data confirm the feasibility of using these machine learning tools for the semi-automated classification of AMD disease stage, based on outer retinal layers' appearance. Discrimination accuracy was substantially lower for the ONL and IS PRL, consistent with our current knowledge of AMD pathogenesis in that it is initiated in the PR-RPE interface (Adler et al. 1999; Dunaief et al. 2002; la Cour et al. 2002).

Classification accuracy was higher for the detection of textural differences in OS PRL and RPE, corresponding to the outer segment of the photoreceptor and retinal pigment epithelium. Accuracy was greatest for patients with nAMD. Since the early and severe OCT changes usually appear in these layers and choroids, the analysis indicated that textural indices of damage can be detected using machine learning techniques.

Visual processing and the regeneration of photosensitive pigments requires an immense amount of energy, which is mainly contributed by mitochondria. Mitochondrial pathology has been reported in the outer retina in a number of inherited conditions. In experimental models, mitochondrial fragmentation has been observed in the inner segment of photoreceptor and RPE layers in the mice with knocked out mitochondrial antioxidant enzyme – manganese superoxide dismutase or MnSOD encoded by *Sod2* (Brown et al. 2019). The integrity of the outer retina is contingent on the regulation of metabolic demands and the ability of mitochondria to supply appropriate levels of ATP (Kanow et al. 2017). Metabolic stress will manifest as changes in mitochondrial migration and fragmentation in the RPE, choriocapillaris and other support retinal cells such as the Muller cells (Stone et al. 2008). All these changes are likely to contribute to the observed changes in the optical texture/contrast distribution in the outer retina.

Mitochondria along with the other membranous organelles play a major role in the scattering of light. Thus, the high accuracy of the classification in the mentioned layers can be attributed, in part, to pre-apoptotic or apoptotic processes, whereas the optical signature of the outer

segment of the PR layer can be generated mainly from the reticular pseudodrusen (RPD) (Rabiolo et al. 2017).

Feature extraction and selection is influenced by the quantity and quality of parameters. A limited feature set may not describe the entire texture, whereas more parameters may include redundant data and result in classifier overfitting. For AMD, both early and late, the local binary pattern features outperformed the parameters of the grey-level co-occurrence matrix; classification accuracy increased with the inclusion of more features.

In this chapter, 8 sampling points were used for the radius of 1 pixel for LBP analysis. However, the LBP descriptor can be extended to a wider circle with a longer radius (Ammar et al. 2018), which can be used in a further detailed study of textural features. LBP is broadly used for pattern detection and recognition techniques (Lemaître et al. 2016; Mishra and Bhatnagar 2020).

The study does not attempt to identify the source of OCT backscattering given the complexity of the change in AMD. Other groups have confirmed the value of texture analysis. For example Hierarchical Texton Mining techniques to classify the AMD stages using texture analysis of choroidal OCT scans has been proposed in the study of (Ravenscroft et al. 2017). Alterations in the morphology of choroidal vasculature due to the severity of AMD may cause changes in the shape and texture of the choroidal region of OCT images. These pathological signs were detected by texture recognition using learnable feature extractors.

The present study is limited by a relatively small dataset. Although the results of the chapter have promising performance, it is critical that the algorithms are trained using substantially larger datasets, which would limit the risk that ML approaches would behave unpredictably.

Even with the limited dataset, my analysis demonstrated the potential for texture-based analysis of the outer retinal layers for the detection of subtle retinal degeneration. The early detection AMD will support timely intervention on and reduce the risk of permanent vision-threatening damage.

Chapter 6. Machine learning tools for the optical detection of glaucoma

6.1. Introduction

RGC death caused by apoptosis is the main reason for vision loss in glaucoma, which is characterized by disruption of cell organelle (Figure 6.1) (Kerrigan et al. 1997; Okisaka et al. 1997). Numerous studies demonstrated the vital role of mitochondria in programmed cell death and its morphological changes (Nickells 1999; Okamoto and Shaw 2005; Chan 2006; Xavier et al. 2016; Williams et al. 2017; Tribble et al. 2019), which may affect the optical alterations of the tissue (Beuthan et al. 1996; Mourant et al. 1998; Gourley et al. 2005; Pasternack et al. 2010; Haseda et al. 2015).

Experimental glaucoma models demonstrated an early dendritic degeneration of RGC apoptosis, where the distal dendrites suffer more than primary and secondary processes (Williams et al. 2013; Williams et al. 2016; Della Santina and Ou 2017). This leads to the loss of synapses with interneurons: bipolar and amacrine cells. Only then during or after the loss of RGC axons, the clinical manifestation of glaucoma may occur. At this stage, morphological changes are irreversible.

In Chapter 3, the complex use of OCT-1040 and texture analysis was shown in detecting the subtle optical differences in OCT phantom with particle size and refractive index that was close to mitochondrial. Then, Chapter 4 illustrated the *ex vivo* monitoring of RGC dendritic degeneration in axotomized retinal explants. Also, in the same chapter, textural differences of IPL of healthy and transgenic Alzheimer's disease mice models were shown.

Machine learning classification of *in vivo* human OCT dataset was conducted in Chapter 5 for AMD patients. Thus, all these studies lead to the aim of this study which is to detect the optical changes of glaucoma in RGC dendrites using OCT and texture analysis. Various types of supervised texture-based machine learning tools were applied to compare their performances in the classification of glaucoma. Also, the impact of PCA on ML algorithms in terms of classification improvement was evaluated. It was also shown that the combinative extraction of GLCM, GLRM and LBP provides better determination of the textural differences of glaucomatous and healthy IPL.

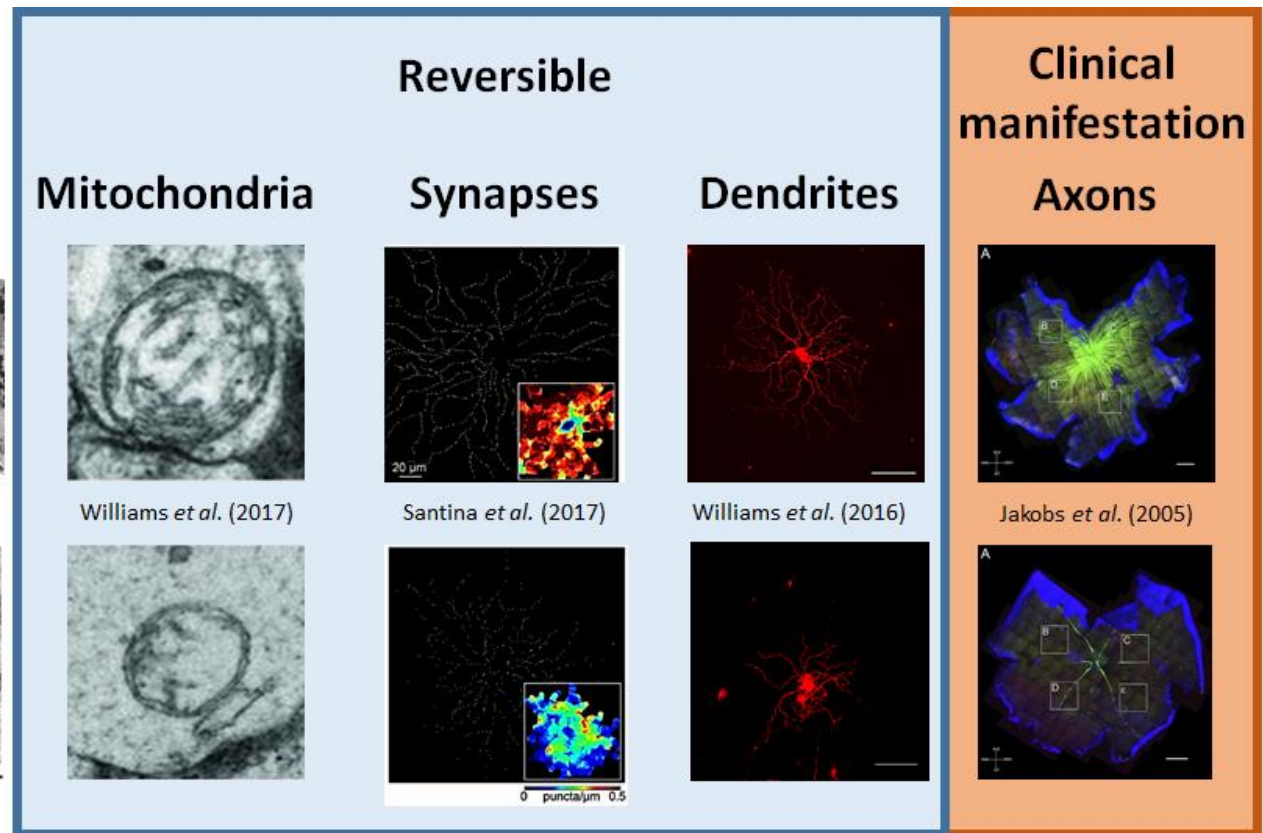
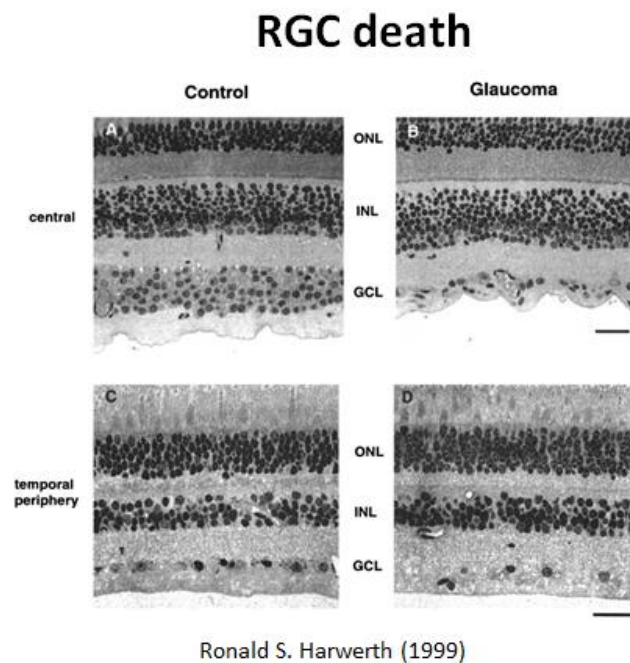


Figure 6.1. The order of morphological changes of the RGC apoptosis. Reversible glaucoma pathogenesis starts from the alteration of morphology and number of mitochondria, which leads to loss of synapses with underlying bipolar cells and loss of dendrites. The constant effect of IOP and progressive degeneration of RGC leads to the loss of axons, which is clinically manifested as vision impairment and have irreversible nature. Images reproduced with permissions from (Harwerth *et al.* 1999; Jakobs *et al.* 2005; Williams *et al.* 2016; Della Santina and Ou 2017; Williams *et al.* 2017)

6.1.1. Hypothesis

The OCT texture of the inner plexiform layer (IPL) may change in glaucoma due to the dendritic neurodegeneration. These subtle optical alterations can be determined using the various supervised machine learning tools: linear and non-linear kernel support vector machines, logistic regression, linear and quadratic discriminant analyses and decision tree classifier. All these classifiers will be assessed with and without principal component analysis.

6.1.2. Aims

- To extract the textural features from the IPL of healthy and glaucomatous OCT images.
- To detect the optical changes of the IPL in glaucoma.
- To evaluate the performance accuracy, precision, recall and F_1 score of each classifier and compare the best in the case of glaucoma classification.

6.2. Methods

6.2.1. OCT dataset, texture analysis and machine learning

I am grateful to Ryan Bartlett (School of Optometry and Vision Sciences, Cardiff University) for OCT image acquisition and processing of raw FD1 file format to .tiff image format from glaucoma patients and healthy controls using OCT-1040 (see Section 2.6).

All further image processing, feature extraction, machine learning classification, coding the programs were conducted by me (Figure 6.2). 40 OCT scans, 20 acquired from the participants with early and moderate glaucoma (diagnosed by a glaucoma specialist) and 20 age-matched controls were investigated. The images were centred on the macula and acquired using 20° scans. Fundus photographs were collected and used to exclude any other retinal diseases.

After the inspection of the OCT images, 10 random volumes of interests (VOIs) were selected manually from the IPL layer of each image using ImageJ. The dimensions of each VOI were 30x30x30 pixels (x, y, z). 400 3D VOIs then underwent the feature extraction procedure, which was achieved using MATLAB (MathWorks) as described in Section 2.6. Apart from GLCM and LBP parameters, grey-level run-length matrix (GLRM) features were also investigated. The data on the related length of a particular pixel in a specific direction can be derived from GLRM features (Connors and Harlow 1980). In this chapter, for the GLRM matrix production, four spatial angles were taken: 0°, 45°, 90° and 135°. All features were imported to the classification tools: linear and non-linear SVMs, logistic regression, linear and non-linear discriminant analyses, and decision tree (Figure 6.2). Then, the performance of classifiers was evaluated using classification accuracy, precision, recall and F_1 score as described in Section 2.8.

Inspection of the OCT scans was carried out and then followed by image processing. Selected VOIs, therefore, were imported to MATLAB for the extraction of 131 features (Table 6.1). After the preparation of the dataset matrix (400x131), the classification algorithms were run. Coding scripts are attached in Appendix 1.

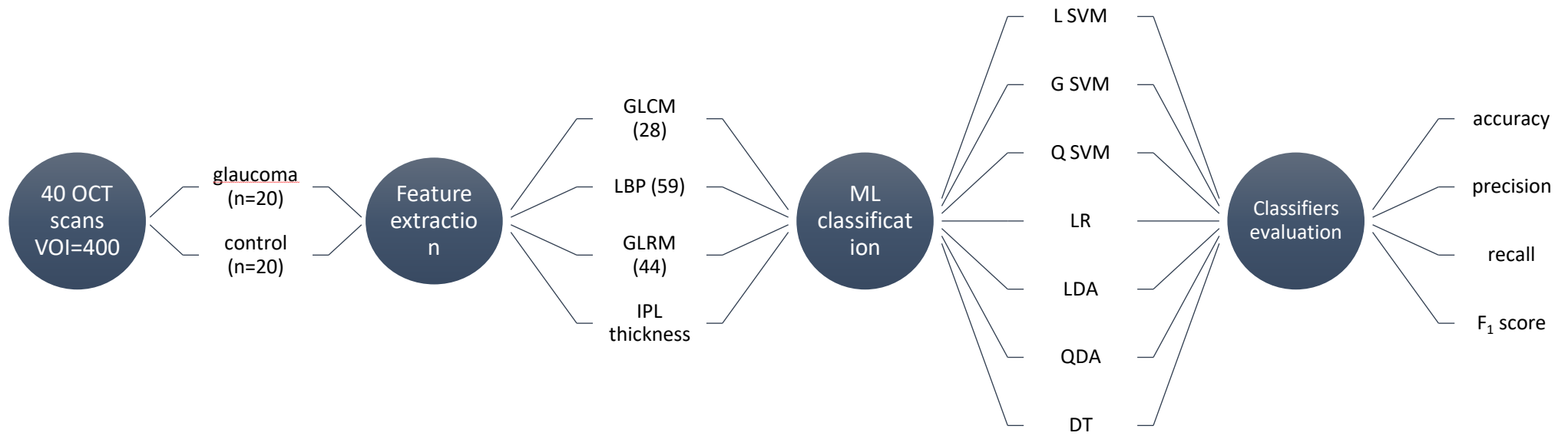


Figure 6.2. Algorithm of the OCT scans analysis process. After the selection of VOIs, textural features (GLCM, GLRM and LBP) and thickness parameters of IPL were extracted for ml-based classification. The performance of algorithms was evaluated using accuracy, precision, recall and F_1 score. Here: GLCM – grey-level co-occurrence matrix; LBP – local binary pattern; GLRM – grey-level run-length matrix; L SVM – linear SVM; G SVM – Gaussian SVM; Q SVM – quadratic SVM, LR – logistic regression; LDA – linear discriminant analysis; QDA – quadratic discriminant analysis; DT – decision tree.

Group of features	Features	Total number
LBP	Uniform Patterns	59
GLCM	Angular Second Moment (ASM) or Energy	$7 \times 4 = 28$
	Correlation	
	Contrast or inertia	
	Entropy	
	Cluster shade	
	Inverse Difference Moment (IDM)	
	Homogeneity	
GLRM	Short Run Emphasis (SRE)	$11 \times 4 = 44$
	Long Run Emphasis (LRE)	
	Grey-Level Nonuniformity (GLN)	
	Run Length Nonuniformity (RLN)	
	Run Percentage (RP)	
	Low Gray-Level Run Emphasis (LGRE)	
	High Gray-Level Run Emphasis (HGRE)	
	Short Run Low Gray-Level Emphasis (SRLGE)	
	Short Run High Gray-Level Emphasis (SRHGE)	
	Long Run Low Gray-Level Emphasis (LRLGE)	
	Long Run High Gray-Level Emphasis (LRHGE)	
Total		131

Table 6.1. List of features used in the classification study

PCA and linear SVM were applied based on relatively high classification accuracy in the cases of phantom, explant and AMD detection and classification. Here, the number of classifiers was increased for the purpose of further larger studies on glaucoma classification. Literature data show that other machine learning techniques may also have a decent efficient performance. For instance, linear and quadratic discriminant analyses (Fleming et al. 2013; Choi et al. 2016), logistic regression (Chen et al. 2006) and decision tree (Sugimoto et al. 2013) were also used in the OCT image classification.

6.2.2. Retinal layer segmentation

For the retinal segmentation, several stages of the image processing software were used (Figure 6.3). Firstly, spectral data from the raw OCT converted to '.tiff' image files in the OCT1_FD1 program. Then, anomalous B scans were removed with image registration and alignment in the ImageJ. Also, noise reduction and removal of the eye movement artefacts were conducted on this program. Then, the OCT *en face* images were orientated using the fundus photographs. The next step was the automated retinal layer segmentation of the macula OCT images in 11 distinct layers, identifying 12 boundaries using the Iowa reference algorithm OCT Explorer 3.1 (The University of Iowa) (Figure 6.4).



Figure 6.3. Algorithm of the OCT image processing with software in brackets

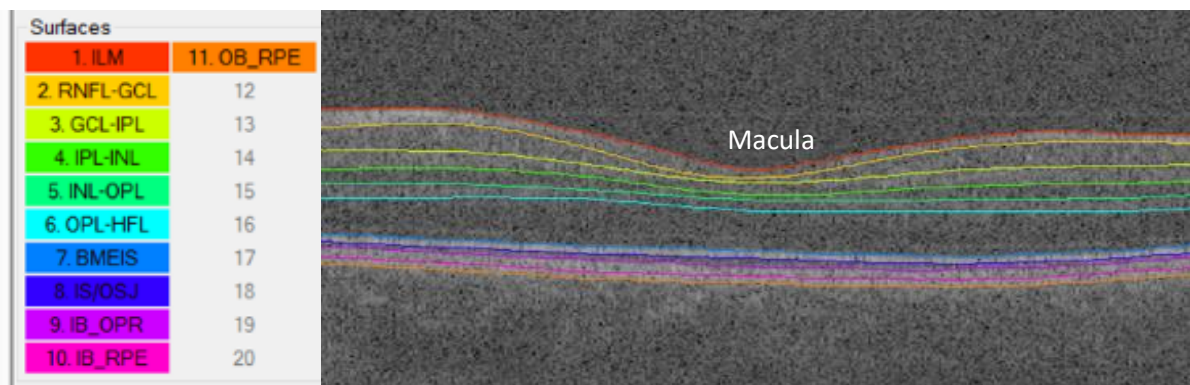


Figure 6.4. The screenshot of the cross-sectional OCT image of the retina cantered at the macula. Retinal layers segmentation was performed using OCT Explorer software. Retinal surfaces (left): 1. ILM; 2. RNFL-GCL; 3. GCL-IPL; 4. IPL-INL; 5. INL-OPL; 6. OPL-HFL (Henle fibre layer); 7. BMEIS (Boundary of myoid and ellipsoid of inner segments); 8. IS/OSJ (IS/OS junction); 9. IB_OPR (Inner boundary of Outer segment PR/RPE complex); 10. IB_RPE (Inner boundary of RPE); 11. OB_RPE (Outer boundary of RPE)

6.3. Results

Segmentation of 3 inner retinal layers of ganglion cell complex, where the axon (RNFL), cell body (RGC) and dendrites of RGC (IPL) are located, was conducted. These layers are important in glaucoma pathogenesis, as the early cellular and molecular alterations occur here.

Moreover, the OCT Explorer software calculated the Early Treatment Diabetic Retinopathy Study (ETDRS) thickness maps for 9 subfields (Figure 6.5). Each of these subfields in the macular thickness map specifies the number of regions: 1 mm (fovea), 3 mm (inner ring), and 6 mm (outer ring) distance from the fovea and shows superior, inferior, nasal and temporal regions of the macula. The mean thickness of IPL was measured using the Iowa Reference Algorithms. The average thickness over grids is calculated in microns.

Then, the thickness values of all 9 regions (Figure 6.5) and 2 rings (inner and outer) corresponding to the dendrites of RGCs were added as the thickness features for the classifier. So, apart from textural features (GLCM, GLRM and LBP), IPL layer thicknesses were considered as a separate group of features (below). The thickness measurements of the inner retinal layers are shown in Table 6.2. It can be noted the decrease of the thickness of all GCC complex in the foveal area for the patients with glaucoma.

b

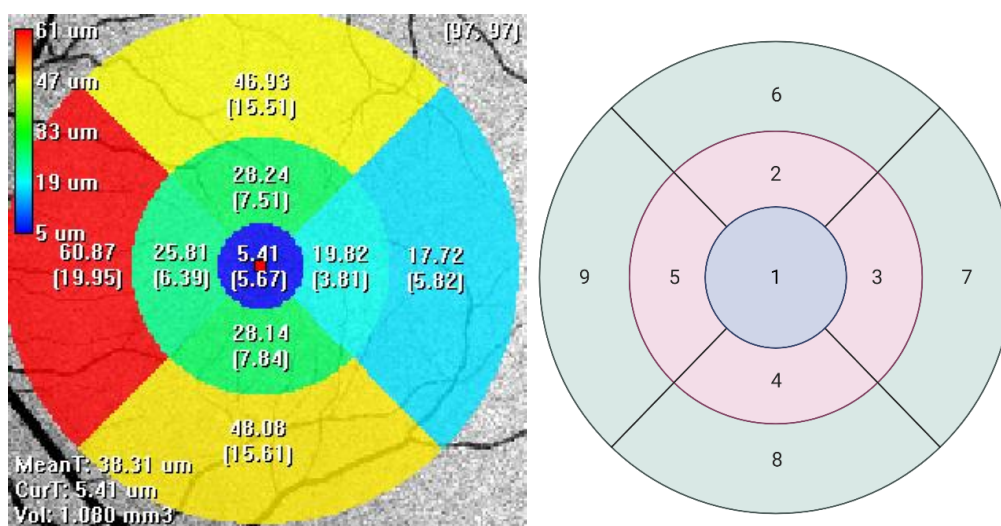


Figure 6.5. a – the screenshot of the thickness of the retinal layers. Macular thickness map using ETDRS circles (1mm, 3mm, and 6mm) demonstrating the mean thickness in each of the 9 grids; b – schematic view of regions 1-9. Created with BioRender.com

Retinal layer	Group	Region 1	Region 2	Region 3	Region 4	Region 5	Region 6	Region 7	Region 8	Region 9	Inner Ring	Outer Ring
RNFL	Control	16.05	20.72	28.18	25.73	27.14	20.85	37.14	43.20	36.16	25.44	34.34
	Glaucoma	7.30	18.92	29.77	24.71	26.94	20.56	44.69	50.94	42.85	25.08	39.76
GCL	Control	15.72	37.42	40.61	41.82	40.77	26.08	22.27	32.01	23.36	40.15	25.93
	Glaucoma	18.06	49.05	51.66	52.80	52.64	33.14	25.91	34.74	27.05	51.54	30.21
IPL	Control	27.87	41.44	42.63	40.47	39.59	38.72	31.64	34.94	30.22	41.03	33.88
	Glaucoma	25.31	39.86	42.96	39.04	40.14	43.31	37.23	40.06	35.78	40.50	39.10
GCC	Control	59.65	99.58	111.53	108.55	104.29	85.65	91.05	104.89	89.75	105.99	92.84
	Glaucoma	50.67	107.83	124.39	116.54	119.71	97.01	107.83	125.74	105.68	117.12	109.06

Table 6.2. Average thickness values (in μm) of inner retinal layers, corresponding to RGC dendrites (IPL), axon (RNFL) and body (GCL). IPL thickness values were used as a separate group of features for glaucoma classification. Regions and rings are stated in Figure 6.5

Firstly, classification algorithms were run only with textural features and all classifiers had similar efficiency. The summary of their performances is provided in Table 6.3. It should be noted that the SVM had higher rates of accuracy, precision, recall and F_1 score without the data dimensionality reduction. Also, QDA has a similar accuracy level. Regardless of the negative influence of PCA for SVMs and quadratic discriminant analysis, the values of logistic regression, linear discriminant analysis and decision tree were slightly increased.

As it was demonstrated in previous chapters, PCA did not increase the classification performance of linear SVM. The same trend occurred in this study, which can be explained that PCA treated the features of a large variance as important features. However, in most cases, the features with a large variance may have nothing to do with the prediction target, which means the production of a lot of useless features and elimination of useful features after PCA application.

Nevertheless, analysis of principal components helped to improve the classification accuracy of logistic regression, LDA and DT. These models operated better with an eigenvalue decomposition, which produced the eigenvalues and eigenvectors for representing the amount of variation of the imported textural data.

Among SVMs, the Gaussian kernel showed the highest accuracy, and it was further used to test the influence of each group of features and the input of the retinal IPL thickness as a classification parameter (Tables 6.4 and 6.5). Among the textural parameters, the major contribution to the classification was provided by the run-length matrix. GLRM also increased the accuracy of GLCM and LBP to 68.5 and 69.3, respectively, when they were imported collectively.

Then, after the measurement of inner retinal layers' thicknesses, they were included as a group of features to test whether they can influence the performance of the SVM classifiers (as they were selected as a suitable and most efficient tool for texture-based glaucoma detection). Interesting to note that thickness measurement of IPL as an individual group of features has higher accuracy, but it decreased the Gaussian SVM accuracy when it was used with the textural properties. Moreover, classifier accuracy with PCA was elevated only with the case of the inner plexiform layer thickness.

Algorithm	Without PCA				With PCA			
	Accuracy	Precision	Recall	F ₁ score	Accuracy	Precision	Recall	F ₁ score
Linear SVM	65.3%	0.651	0.652	0.652	60.3%	0.608	0.602	0.605
Gaussian SVM	70.3%	0.635	0.667	0.650	58.8%	0.686	0.677	0.682
Quadratic SVM	65%	0.650	0.646	0.648	61.8%	0.618	0.615	0.617
Logistic regression	60%	0.600	0.600	0.600	61.3%	0.615	0.615	0.615
Linear discriminant analysis	58.3%	0.582	0.580	0.581	60.8%	0.610	0.606	0.609
Quadratic discriminant analysis	64.8%	0.650	0.646	0.648	54.8%	0.550	0.585	0.567
Decision tree	59.3%	0.592	0.589	0.591	60.8%	0.607	0.607	0.607

Table 6.3. Classification summary for all textural features (GLCM, GLRM and LBP) and all classifiers

	Accuracy, %	
Features	Gaussian SVM	Gaussian SVM+PCA
GLCM	64.8	53.0
GLRM	67.5	60.8
LBP	62.5	57.8
GLCM + GLRM	68.5	62.0
GLCM + LBP	64.8	50.2
GLRM + LBP	69.3	57.0
GLCM + GLRM + LBP	70.3	58.8
IPL thickness	72.5	80.0
GLCM + GLRM + LBP + IPL thickness	54.3	50.5

Table 6.4. Classification summary for Gaussian SVM with a separate group of features and their combinations: the accuracy percentage is for the discrimination of normal and glaucoma cases

Groups	control	glaucoma
control	100%	70.3%
glaucoma	70.3%	100%

Table 6.5. Gaussian SVM classification of GLCM, GLRM and LBP features

6.4. Discussion

In vivo detection of textural differences between healthy and early glaucomatous human retina was the goal of the study. As the early changes of glaucoma characterised by RGC apoptosis, during cell death, some structural changes occur. Consequently, they lead to optical changes that can be detected by OCT. The backscattered light from the tissue generates speckles and may produce specific OCT image patterns.

In this chapter, textural features of glaucomatous OCT images were extracted and then used as discriminative information for machine learning tools. Especially, among feature groups, GLRM was the most valuable and it increased the role of LBP and GLCM parameters. But, the complex use of all 131 features resulted in the higher accuracy of all classifiers (Table 6.4).

Comparison between machine learning tools showed that support vector machines, especially Gaussian SVM, outperformed other methods. The impact of PCA was different for each classification technique. For instance, PCA was lowering the accuracy of SVMs, which can be the result of the elimination of valuable features. Moreover, it can be concluded that SVM is capable of managing the high-dimensional dataset better without prior reduction of dimensions.

Nevertheless, PCA improved the classification performance of logistic regression, linear discriminant analysis and decision tree. In these cases, the first and second principal components served as better variables by separating the correlations between features and eliminating outliers. To sum up, all the implemented tools had similar performance, excluding SVMs.

Retinal layers' thickness measurement is one of the common reasons to use OCT in clinical settings. For this purpose, segmentation of the same dataset was carried out. The thickness values of IPL were used as a group of features separately and together with textural features. It can be noted that isolated thickness values had higher accuracy, but they decreased when was used with GLRM, GLCM and LBP. This needs further study and determination of segmentation role in glaucoma classification.

Although accuracy, precision, recall, F_1 score and confusion matrix are the most common tools for the evaluation of classifier performance, greater analysis for significance and computation

of such parameters as sensitivity and specificity, confidence intervals and error bars are needed.

Future work should be performed with multiple OCT images. This can show the applicability of machine learning classifiers for the detection of glaucoma using optical dendritic degeneration changes. Also, further studies are needed to use the visual field data of patients for the purpose of demonstrating the optical differences in the same retina but different regions. For instance, the regions with already degenerated RGCs against the healthy parts of the retina, which could modify the strategy of VOI selection.

Even though the OCT system that was used in this project does not have a cellular resolution, texture analysis shows promise in being able to quantify the subtle textural shifts in tissue. Since the speckle size is a function of the resolution of the system, it may be possible to perform texture analysis of subcellular components using ultrahigh-resolution OCT systems.

Chapter 7. General Discussion

This chapter provides an overview of the results obtained in the experimental chapters, with a focus on the texture analysis of optical phantoms, murine retinal explants, human AMD and glaucoma OCT images. Also, study progress, limitations and the proposed future direction of investigations are stated.

7.1. OCT resolution and texture analysis

OCT device performance is predominantly determined by its image resolution (axial and transverse). Also, data acquisition sensitivity (dynamic range) and specificity (light speed and digitization resolution) play a major role in the OCT system operation (Drexler and Fujimoto 2008). Among medical *in vivo* imaging techniques, OCT has one of the highest values of axial resolution and it is characterised by the wavelength of the coherent light (Figure 7.1). OCT axial resolution, in comparison to confocal microscopy, is not dependent on the depth of field and numerical aperture (NA). However, light source bandwidth can affect the axial resolution (Swanson et al. 1993): the broader the spectral bandwidth ($\Delta\lambda$) and the lower the wavelength (λ) of the light source, the better the longitudinal resolution (7.1).

$$\Delta z = \frac{2 \ln 2}{\pi} \frac{\lambda^2}{\Delta\lambda} \quad (7.1)$$

In contrast, NA is important for the transverse resolution of OCT (higher NA increases the transverse resolution), as well as the focus spot size (d) and focal length (f) of the objective lens (Equations 7.2 and 7.3). The latter determines the depth of focus b in Figure 7.1, which is the $1/e^2$ beamwidth of a Gaussian beam.

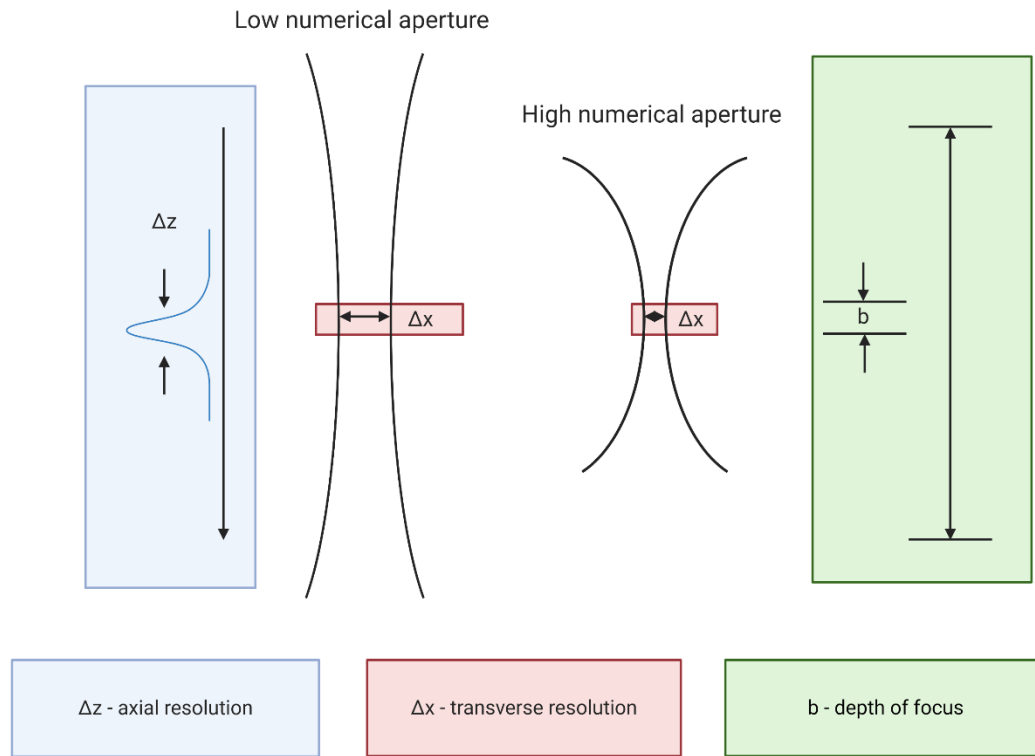


Figure 7.1. OCT system resolution scheme. Created with BioRender.com

$$\Delta x = \frac{4\lambda f}{\pi d} \quad (7.2)$$

$$b = \frac{\pi \Delta x^2}{2\lambda} \quad (7.3)$$

The OCT system that used in these studies is a lab-based custom device with a long-wavelength light source. The central wavelength of the spectrum is 1040nm, which improves the penetration depth. However, the light source bandwidth is ≈ 70 nm. Ideally, broad and ultrabroad-bandwidth sources (c. 150nm and higher) could be used for the acquisition of images with submicron axial resolution (Drexler et al. 2001; Unterhuber et al. 2005), which can provide more valuable information about the cellular and subcellular processes of neurodegeneration. On the positive side, using a 1040nm wavelength light source is a trade-off between axial resolution and penetration of the light, therefore, transverse resolution.

Even though OCT devices may have ultra-broadband light sources with high axial and transversal isotropic resolutions with AO technology, without the development of image processing and extraction of all valuable information from already existing OCT systems, achievements are still small. The texture of OCT images is least investigated and, therefore, is mostly ignoring a vital source of information about the microstructure of tissues. To assess whether the texture of known objects could be discriminated, phantoms were prepared, and their textural features were extracted.

7.2. Phantom study: Feasibility of SVM and PCA to classify phantoms based on OCT-derived GLCM features

Innovations in the field of photonics triggered the rapid development of OCT in the last two decades. Despite the dramatic progress of the OCT systems, there were few advancements in the improvement of standardized test methods to assess the function of OCT technology. Phantoms are artificial models for the evaluation of the imaging devices they can be used to provide quality assurance and calibration to standardised controls to support comparison between OCT devices. Moreover, phantoms can imitate the subcellular structures (mitochondria, endoplasmic reticulum, Golgi apparatus) of the retinal ganglion cell and are essential for the validation of OCT-based texture analysis.

In Chapter 3, the results of the texture analysis of OCT phantoms were provided. Optical differences were shown in terms of various concentration, size and refractive indices of scatterers and volume of matrix material solution. Machine learning classification tools on the basis of support vector machine (SVM) and principal component analysis (PCA) could discriminate various types of phantoms with a high classification accuracy (80-99%). For the purpose of analysis of multidimensional data, the *n-dimensional* PCA (*nD*-PCA) was suggested by (Hongchuan and Bennamoun 2006). *nD*-PCA extends the PCA method to a higher dimensional data set. However, the data cannot be represented efficiently due to transforming the original dataset in terms of eigenvectors.

Light scatterers were chosen as phantoms based on their ability to imitate membranous organelles, which have a high scattering coefficient and play a vital role in cell death. Not only the size (1-5 μ m) but also their refractive indices (1.43-1.57) and density (various volumes) in the cytoplasm were considered. Besides, to ensure the uniform dispersion of beads, their spatial distribution was quantified using nearest neighbour distance measurement. However, polystyrene and silica microbeads are homogenous spheres, whereas the organelles have a more complicated structure. OCT subcellular phantoms should be directed at recreating the structure of a cell in future studies. This may enable the imitation of cellular pathologies and then they can be tested on OCT technologies. Also, OCT with adaptive optics will allow precisely visualising the optical changes in chemical and biological samples.

GLCM features have been extracted for image classification of microscopy (Yogesana et al. 1996), ultrasound (Basset et al. 1993) and OCT images (Gossage et al. 2003) for detection of normal and pathologic tissues. In this study, only GLCM features were extracted, ignoring the other textural properties: grey-level run-length matrices, local binary patterns, wavelet transform and grey-level difference matrices. According to the studies of (Conners and Harlow 1980; Gossage et al. 2003), GLCM texture analysis provides better feature discrimination. Additionally, for better, faster and accurate operation of the classifier, the minimum number of features has to be applied, free from noise, discarded irrelevant and redundant data (Wu et al. 2012).

As this was the first study in this thesis, few numbers of textural features were used. Further studies can be undertaken with the same groups of phantoms, but with more parameters (GLRM and LBP). Although this may increase the accuracy of classification, overfitting issues should also be considered. Nevertheless, the performance of the OCT device and supervised learning classifiers were evaluated showing the ability to visualise the microparticle phantoms and classify them on the basis of their textural differences. Hence, it was determined that both tools could be further applied for the texture-based classification of OCT images in experimental and clinical studies.

7.3. Explant study: Feasibility of using OCT image-derived texture features to detect early retinal neurodegeneration in models of retinal axotomy and Alzheimer's disease

Studies on the early neuronal degeneration of axotomized retinal ganglion cells (RGCs) demonstrated that the subcellular apoptotic changes may start in the dendritic tree of the neurons (Thanos 1988; Morgan et al. 2017; Tribble et al. 2019). Optical detection of these alterations is possible using OCT and, for that reason, mathematical computations of biological processes is provided in Chapter 4.

Following the dissection of the murine eye and transection of the optic nerve, it was possible to monitor the optical signature of the inner plexiform layer (IPL) of tissues within 2 hours of retinal dissections. The explant model is useful in that the onset of RGC degeneration is initiated with the optic nerve section which is performed as part of the explant preparation. The results of the GLCM-based texture analysis suggest that the SVM classifier was able to discriminate the subtle pixel-level optical changes of the early dendritic degeneration of dying RGCs. The dendritic degeneration of the axotomized RGCs was histologically demonstrated in the study of (Tudor et al. 2014).

Retinal neurodegeneration in Alzheimer's disease (AD) was demonstrated in the study of Grimaldi et al. (2018). In a similar way, the optical signature of the IPL of transgenic 3xTg-AD mouse model explants was studied. Our classification algorithm was able to detect textural differences between control and AD mice models. GLCM features, especially contrast and entropy, were chosen by PCA as the most descriptive values. The texture of IPL of all transgenic mice retinae was different than the healthy IPL of C57BL/6 mice.

As we consider the eye as a "mirror to the brain", it will be a huge contribution to neuroscience, whether *in vivo* ligand-free non-invasive techniques may detect AD prior to its clinical manifestation. Whereas the main shortcomings of ligand-based methods, e.g. Annexin V (Aloya et al. 2006), the brain positron emission tomography with the radioactive Pittsburgh Compound B (PitB) (Mathis et al. 2012), are toxic and not applicable for the screening and monitoring of AD. With the clinical application of OCT with detailed textural analysis of the vulnerable high-risk group of patients and the intake of Capsaicin and other neuroprotectors, there will be a chance to prevent the disease.

Among limitations, the study could also be undertaken for *in vivo* investigation of glaucomatous or AD-related IPL dendritic degeneration. Also, cell culture experiments could demonstrate apoptosis of retinal ganglion cells and their textural signature could be studied. Histological observation of dying RGCs could be done to demonstrate the mechanism of cell death. Nevertheless, these questions were outside the scope of this PhD and have been stated in the study of (Tudor et al. 2014), where the transparency of dissected tissue was not investigated. Calculation of spread and modulation transfer functions revealed the absence of secondary opacification in the explants. Transparency of post axotomy eyes was relatively constant over the 2-hours.

These *ex vivo* studies provide useful evidence to support *in vivo* human OCT studies, especially in the investigation of the early diagnosis of diseases associated with retinal destruction. Glaucoma and macular degenerations can be the candidates, in the first instance, due to their irreversible manifestations and absence of radical treatment.

7.4. Human studies: Feasibility of machine learning classification tools for use in early detection of retinal neurodegeneration in AMD and Glaucoma

After the confirmation of the SVM classifier feasibility on *in vitro* and *ex vivo* studies on the artificial retinal samples and animal retinal explants, this algorithm was applied to study the optical changes of *in vivo* human retinal OCT images. Among a huge variety of neuronal degenerative diseases, two most common and causing vision-related socio-economic burden worldwide diseases were chosen: glaucoma and age-related macular degeneration.

On the basis of glaucoma, RGC apoptosis is the key element of disease pathogenesis (Guo et al. 2005; Huang et al. 2019; Zhang et al. 2019). This can be the result of impaired axonal transport, direct and indirect pressure influence from intraocular fluid and vitreous and vascular ischemia of the retina (Quigley et al. 1995; Osborne et al. 2001; Chidlow et al. 2011; Mroczkowska et al. 2012; Fahy et al. 2016; Maddineni et al. 2020). Moreover, RGC death is controlled by specific genes, activated in the apoptotic cell: tumour-suppressor *p53* protein, which enhances pro-apoptotic gene *Bax* and inhibits the antiapoptotic gene *BCL-2* (Nickells 1999).

Several studies showed that programmed cell death has an early onset from the dendritic tree (Morgan et al. 2017; Tribble et al. 2019). Despite the popular theory of the initiation of the RGC axonal damage from the optic nerve head in glaucoma (Johnson et al. 2003), Williams et al. (2013) diolistically demonstrated the evidence of the prolonged atrophy of RGC dendrites preceding the injury of the neuron body and axon. Hence, the primary regions of interest for OCT imaging are IPL and GCL, where the dendrites and bodies of RGC are located.

Even though the described pathogenesis of the programmed cell death can be visualised under microscopy, due to the limited resolution and the noise from back-reflected light, OCT cannot provide the morphology of individual subcellular structures. Individual RGC was imaged *in vivo* in the study of (Rossi et al. 2017) with a custom confocal adaptive optics scanning light ophthalmoscopy (AOSLO).

Textural features of OCT images can distinguish the difference between healthy and glaucomatous tissues (Anantrasirichai et al. 2013). Thus, if apoptosis can be detected by OCT,

this would allow diagnosing the disease in the early stages of the disease (Figure 7.2Figure), which can help to start early treatment avoiding irreversible RGC loss. Hence, the prevention of RGC death and early regenerative treatment (neuroprotection and neuronal rehabilitation) should be the main purposes of future work.

The texture of IPL was already investigated in Chapter 4, but in an animal model and to study the early apoptosis of RGC. Here, the idea remains the same in terms of the mitochondrial and other organelle changes prior to cell death. Subcellular structures may cumulatively generate the optical signature of the disease and the machine learning classification algorithms demonstrated these differences. This optical signature is produced by the summation of subtle textural alterations of pixel intensities (Tudor et al. 2014).

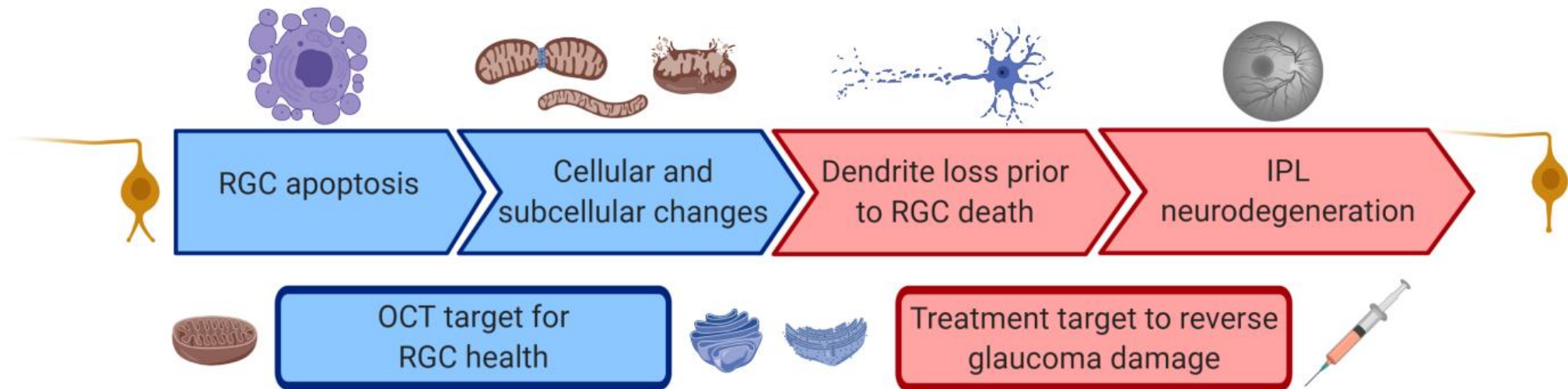


Figure 7.2. Strategy scheme of the early detection of glaucoma and its potential prevention. Cellular and subcellular optical changes of RGC pre-apoptosis can be detected using UHR-OCT in the stage of dendritic degeneration in the IPL layer. This allows monitoring the RGC viability and helps to decide the glaucoma treatment and prevention strategy

Changes in OCT image texture were analysed using GLCM, GLRM and LBP features and various machine learning classifiers techniques. Not only SVMs, but other methods (discriminant analyses, decision tree, logistic regression) were able to classify glaucoma and control group OCT images. Gaussian kernel SVM outperformed linear and quadratic SVMs, as well as other supervised machine learning classifiers. Among the textural features, the grey-level run-length matrix illustrated the highest value for classifiers. Nevertheless, the combined use of all features had higher power for the classification. In the study of Anantrasirichai et al. (2013), linear SVM outperformed non-linear SVM and complex use of all features showed the highest classification accuracy.

Studies on RGC apoptosis was followed by the study of outer retinal layers degeneration. OCT in the detection of AMD signs plays a major role: various types of drusen, RPE degenerations and neovascular exudates can be easily detected and classified using machine learning tools (Do et al. 2012; Leuschen et al. 2013; Stehouwer et al. 2016; Saha et al. 2019). However, there has not been implemented in the current clinical diagnostic guidelines the texture analysis of the OCT images of AMD patients. The latter may help to determine the early subtle optical changes in the structure of the photoreceptors and retinal pigment epithelium cells.

The results of Chapter 5 suggest that the SVM-based classification may distinguish healthy outer retinal layers from early and neovascular AMD. GLCM and LBP features were extracted from the outer nuclear layer, inner and outer segments of the photoreceptor layer corresponding to the body and dendrite of photoreceptors. Moreover, the texture of the RPE was investigated and this layer was the most prominent in terms of the optical alterations. Classifiers' accuracy reached 93-100% for the detection of AMD in the RPE layer, whereas this value was in the range from 60% to 90% for other outer retinal layers. This confirms that the RPE cells are one of the earliest cell classes affected by AMD.

Near-infrared autofluorescence imaging with AOSLO detected the pattern changes of the hexagonal mosaic of RPE in the early preclinical stages of AMD (Vienola et al. 2020). In the study of (Golestaneh et al. 2018), cultured human RPE cells from AMD patients were morphologically and functionally damaged, which can be explained by the cumulation of

products of metabolism (lipids and glycogen) and organelle alterations (fragmentation of mitochondria and increase in autophagosomes). These changes were not presented in the healthy human RPE cultures, which supports the theory of dysfunctional autophagy as a fundamental mechanism contributing to the pathophysiology of AMD. OCT-1040 has been also applied to detect AMD symptoms not only in neural retina and RPE but also in choriocapillaris and choroids interface in the study of Unterhuber et al. (2005).

For the classification of AMD, the combined use of GLCM and LBP features outperformed the separate extraction of each textural property. Well-timed and early detection of AMD cellular and subcellular manifestations open new avenues for the development of novel treatment strategies, which may reverse the flow of the disease and prevent vision impairment.

7.5. Other limitations

OCT is state-of-the-art technology in clinical medicine, especially in ophthalmology. Nevertheless, in the diagnosis of a human eye, there may be shadows and artefacts, limiting the image quality. Also, the axial resolution of the OCT system might be affected by water absorption in the anterior chamber and the vitreous. Hence, contrast and image penetration depth decrease. In general, the absorption coefficient of water (intraocular fluid and vitreous body) equals 0.04mm^{-1} for the spectral range of 950-1130nm. Therefore, with average axial eye length (24-25mm) and due to forward-backwards light travel the loss of signal-to-noise ratio amounts to $\sim 9\text{dB}$ (Hariri et al. 2009). Notwithstanding, this loss in the murine eye is less ($\sim 2\text{dB}$) and can be ignored as a limiting factor in small animal retinal OCT.

Due to the inhomogeneities in the refractive index of the tissue structures, light reflects back at various angles (Schmitt et al. 1994; Schmitt 1999). There are two groups debating sides on the nature of speckle: if one cohort thinks this is a source of optical information about the microscopic structures of the tissue, whereas the other group categorize the speckle as a noise (Schmitt et al. 1999). Hence, in the process of noise filtering, some valuable data can be removed. Consequently, this can lead to the misinterpretation of the OCT results. The strategy of efficient noise reduction is one of the goals of the improvement of image processing.

Moreover, averaging the tissue spatial properties of the scans with the signal-carrying speckle together with signal-degrading one (Schmitt 1999). To avoid this issue, there is a demand for effective speckle reduction techniques. It requires widening the source bandwidth and numerical aperture (NA) of the objective (Schmitt 1999).

The application of machine learning algorithms enhanced recently in medicine, especially in the early diagnosis of pathologies. Especially this trend is progressing faster in ophthalmology due to the highly technological basis of the field (Bajwa et al. 2015). Glaucoma, AMD, diabetic retinopathy and other common socially significant diseases can be detected early with the methods of automatic detection of signs (Abràmoff et al. 2008; Kucur et al. 2018; Zhongyang and Yankui 2019; Bisneto et al. 2020; González-Gonzalo et al. 2020), which also can be served as a screening tool for the tremendous amount of data (Antal and Hajdu 2014; Ting et al. 2017; Grzybowski et al. 2020).

Particularly, supervised machine learning tools demonstrated the effectiveness in the performance of binary classification of diseased and healthy participants (Kucur et al. 2018; Bajwa et al. 2019). This type of learning is based on the training of the system from input data (OCT scans) and iteratively improve its operation for the detection of correct output (accurate diagnosis). In the studies of this thesis, there was performed binary (glaucoma and healthy) and ternary (early AMD, neovascular AMD and healthy) classifications of human OCT images. Moreover, there was conducted the classification of OCT images of early apoptosis of murine retinal explants, where the number of classes was four: time 0, time 30 minutes, time 60 minutes and time 120 minutes after the transection of the optic nerve.

After the repetitive training of the program with the increasing amount of input data, the effectiveness of the classifier improves. When new unseen data is imported into the system, the supervised learning tool can identify the correct diagnosis. Hence, in the studies with the involvement of machine learning techniques, there should be as much data as possible. Consequently, the validity of the technique is dependent on the size and quality of the training dataset (LeCun et al. 2015).

Due to the multi-layered structure of retinal, shadows and artefacts from the adjacent layers, an automatic approach to detect the region and volume of interest is challenging. Hence, the classifier is semi-automatic in this study. The selection of VOIs is needed by a human expert to avoid these issues.

7.6. Conclusions and future work

I have demonstrated the utility of texture analysis methods and their suitability for machine learning approaches in the detection of subcellular changes. With advances in OCT light sources, scanning speeds and the ability to process signals in near real-time there is considerable scope for the application of the techniques described in this thesis. It is likely that the power of this technique will increase with white light lasers and faster acquisition times (less image misalignment).

The trend in medicine is to prioritize the organ-preserving methods of diagnosis and treatment. The emerging opportunities for new technical solutions served as an incentive for the development of non-invasive highly permissive methods for the investigation of the biological tissues' structure. OCT can perform a resolution of 1 – 15 μ m and the coherence length of the light source in OCT determines the spatial resolution of the device.

The progress should not only focus on the technical improvement of OCT scanning but also the enhancement of image post-processing, extraction and understanding of all valuable information of acquired data and application of machine learning algorithms. In the consecutive studies of this PhD, there was demonstrated the possibilities of subtle image speckle-containing information on phantoms, retinal tissues of animals and humans. Texture analysis may be a vital technique for the early detection and prevention of retinal and brain neurodegeneration.

OCT evaluation of mouse retinal explant was performed *ex vivo*. For further studies, there is a demand for the detection of neurodegeneration of murine retinal OCT *in vivo*. Furthermore, the diseases with cellular and subcellular alterations (glaucoma, AD, AMD and others) can be

modelled in animal studies and the texture signature might be calculated using this semi-automated and other types of machine learning techniques.

For the purpose of *in vivo* studies in humans, there should be applied several changes in the OCT device: numerical aperture of lenses would be decreased and complex use of adaptive optics. The latter improves the transverse resolution. However, there are some limitations for the human eye: cataract, vitreal haemorrhage or other media opacities and movement artefacts.

References

- Abadi, E., Segars, W.P., Sturgeon, G.M., Harrawood, B. and Kapadia, A. 2019. Modeling "Textured" Bones in Virtual Human Phantoms. *IEEE transactions on radiation and plasma medical sciences* 3(1), pp. 47-53. doi: 10.1109/TRPMS.2018.2828083
- Abràmoff, M.D., Niemeijer, M., Suttorp-Schulten, M.S.A., Viergever, M.A., Russell, S.R. and Ginneken, B. 2008. Evaluation of a System for Automatic Detection of Diabetic Retinopathy from Color Fundus Photographs in a Large Population of Patients with Diabetes. *Diabetes Care* 31(2), p. 193. doi: 10.2337/dc07-1312
- Adler, R., Curcio, C., Hicks, D., Price, D. and Wong, F. 1999. Cell death in age-related macular degeneration. *Molecular Vision* 3(5), p. 31. PMID: 10562655.
- Ahmad, S.S. 2017. An introduction to DARC technology. *Saudi Journal of Ophthalmology* 31(1), pp. 38-41. doi: <https://doi.org/10.1016/j.sjopt.2016.08.001>
- Albrecht, P., Ringelstein, M., Müller, A.K., Keser, N., Dietlein, T., Lappas, A., Foerster, A., Hartung, H.P., Aktas, O. and Methner, A. 2012. Degeneration of retinal layers in multiple sclerosis subtypes quantified by optical coherence tomography. *Multiple Sclerosis Journal* 18(10), pp. 1422-1429. doi: 10.1177/1352458512439237
- Almasieh, M., Wilson, A.M., Morquette, B., Vargas, J.L.C. and Di Polo, A. 2012. The molecular basis of retinal ganglion cell death in glaucoma. *Progress in Retinal and Eye Research* 31(2), pp. 152-181. doi: 10.1016/j.preteyeres.2011.11.002
- Aloya, R., Shirvan, A., Grimberg, H., Reshef, A., Levin, G., Kidron, D., Cohen, A. and Ziv, I. 2006. Molecular imaging of cell death in vivo by a novel small molecule probe. *Apoptosis* 11(12), p. 2089. doi: 10.1007/s10495-006-0282-7
- Alsbirk, P. H. 1976. Primary angle-closure glaucoma. Oculometry, epidemiology, and genetics in a high risk population. *Acta Ophthalmologica supplements* (127), pp. 5-31. PMID: 179266.
- Ammar, M., Saïd, M. and Stylianos, D. 2018. A Set of Texture-Based Methods for Breast Cancer Response Prediction in Neoadjuvant Chemotherapy Treatment. In: Dey, N., Ashour, A.S., Shi, F. and Balas V.E. eds. *Soft Computing Based Medical Image Analysis*. Academic Press, pp. 137-147. doi: 10.1016/B978-0-12-813087-2.00007-5.
- Anantrasirichai, N., Achim, A., Morgan, J. E., Erchova, I. and Nicholson, L. (2013). SVM-based texture classification in Optical Coherence Tomography. *2013 IEEE 10th International Symposium on Biomedical Imaging*. 7-11 April 2013. pp. 1332-1335, doi: 10.1109/ISBI.2013.6556778.

Antal, B. and Hajdu, A. 2014. An ensemble-based system for automatic screening of diabetic retinopathy. *Knowledge-Based Systems* 60, pp. 20-27. doi: 10.1016/j.knosys.2013.12.023

Armaly, M.F. 1969. Ocular pressure and visual fields: A ten-year follow-up study. *Archives of Ophthalmology* 81(1), pp. 25-40. doi: 10.1001/archopht.1969.00990010027005

Bajwa, A., Aman, R. and Reddy, A.K. 2015. A comprehensive review of diagnostic imaging technologies to evaluate the retina and the optic disk. *International Ophthalmology* 35(5), pp. 733-755. doi: 10.1007/s10792-015-0087-1

Bajwa, M.N., Malik, M.I., Siddiqui, S.A., Dengel, A., Shafait, F., Neumeier, W. and Ahmed, S. 2019. Two-stage framework for optic disc localization and glaucoma classification in retinal fundus images using deep learning. *BMC Medical Informatics and Decision Making* 19(1), p. 136. doi: 10.1186/s12911-019-0842-8

Barer, R. and Tkaczyk, S. 1954. Refractive Index of Concentrated Protein Solutions. *Nature* 173(4409), pp. 821-822. doi: 10.1038/173821b0

Basset, O., Sun, Z., Mestas, J. L. and Gimenez, G. 1993. Texture Analysis of Ultrasonic Images of the Prostate by Means of Co-occurrence Matrices. *Ultrasonic Imaging* 15(3), p. 218-237. doi: 10.1177/016173469301500303

Baumann, B., Gotzinger, E., Pircher, M., Sattmann, H., Schuutze, C., Schlanitz, F., Ahlers, C., Schmidt-Erfurth, U. and Hitzenberger, C.K. 2010. Segmentation and quantification of retinal lesions in age-related macular degeneration using polarization-sensitive optical coherence tomography. *Journal of Biomedical Optics* 15(6), p. 061704. doi: 10.1117/1.3499420

Beatty, S., Koh, H., Phil, M., Henson, D. and Boulton, M. 2000. The Role of Oxidative Stress in the Pathogenesis of Age-Related Macular Degeneration. *Survey of Ophthalmology* 45(2), pp. 115-134. doi: 10.1016/S0039-6257(00)00140-5

Bell, K., Rosignol, I., Sierra-Filardi, E., Rodriguez-Muela, N., Schmelter, C., Cecconi, F., Grus, F. and Boya P. 2020. Age related retinal Ganglion cell susceptibility in context of autophagy deficiency. *Cell Death Discovery* 6(1), p. 21. doi: 10.1038/s41420-020-0257-4

Benedicto, I., Lehmann, G.L., Ginsberg, M., Nolan, D.J., Bareja, R., Elemento, O., Salfati, Z., Alam, N.M., Prusky, G.T., Llanos, P., Rabbany, S.Y., Maminishkis, A., Miller, S.S., Rafii, S. and Rodriguez-Boulan, E. 2017. Concerted regulation of retinal pigment epithelium basement membrane and barrier function by angiocrine factors. *Nature Communications* 8(1), p. 15374. doi: 10.1038/ncomms15374

Bereiter-Hahn, J. 1990. Behavior of Mitochondria in the Living Cell. In: Jeon, K.W. and Friedlander, M. eds. *International Review of Cytology*. Vol. 122. Academic Press, pp. 1-63. doi: 10.1016/s0074-7696(08)61205-x

Berkelaar, M., Clarke, D.B., Wang, Y.-C., Bray, G.M. and Aguayo, A.J. 1994. Axotomy results in delayed death and apoptosis of retinal ganglion cells in adult rats. *The Journal of Neuroscience* 14(7), pp. 4368-4374. doi: 10.1523/jneurosci.14-07-04368.1994

Beuthan, J., Minet, O., Helfmann, J., Herrig, M. and Müller, G. 1996. The spatial variation of the refractive index in biological cells. *Physics in Medicine & Biology* 41(3), p. 369. doi: 10.1088/0031-9155/41/3/002

Bevan, R.J., Hughes, T.R., Williams, P.A., Good, M.A., Morgan, B.P. and Morgan, J.E. 2020. Retinal ganglion cell degeneration correlates with hippocampal spine loss in experimental Alzheimer's disease. *Acta Neuropathologica Communications* 8(1), p. 216. doi: 10.1186/s40478-020-01094-2

Bhattacharjee, M., Ashok, P.C., Rao, K.D., Majumder, S.K., Verma, Y. and Gupta, P.K. 2011. Binary Tissue Classification Studies on Resected Human Breast Tissues Using Optical Coherence Tomography Images. *Journal of Innovative Optical Health Sciences* 04(01), pp. 59-66. doi: 10.1142/s1793545811001083

Bhutto, I. and Lutty, G. 2012. Understanding age-related macular degeneration (AMD): relationships between the photoreceptor/retinal pigment epithelium/Bruch's membrane/choriocapillaris complex. *Molecular aspects of medicine* 33(4), pp. 295-317. doi: 10.1016/j.mam.2012.04.005

Binley, K., Ng, W.S., Barde, Y.A., Song, B. and Morgan, J.E. 2016. Brain-derived neurotrophic factor prevents dendritic retraction of adult mouse retinal ganglion cells. *European Journal of Neuroscience* 44(3), pp. 2028-2039. doi: 10.1111/ejn.13295

Bird, A.C., Bressler, N.M., Bressler, S.B., Chisholm, I.H., Coscas, G., Davis, M.D., de Jong, P.T.V.M., Klaver, C.C.W., Klein, B.E.K., Klein, R., Mitchell, P., Sarks, J.P., Sarks, S.H., Soubrane, G. and Taylor, H.R. 1995. An international classification and grading system for age-related maculopathy and age-related macular degeneration. *Survey of Ophthalmology* 39(5), pp. 367-374. doi: 10.1016/S0039-6257(05)80092-X

Bisneto, T.R.V., Carvalho Filho, A.O. and Magalhães, D.M.V. 2020. Generative adversarial network and texture features applied to automatic glaucoma detection. *Applied Software Computing* 90, p. 106165. doi: 10.1016/j.asoc.2020.106165

Blanks, J.C., Hinton, D.R., Sadun, A.A., Miller, C.A. 1989. Retinal ganglion cell degeneration in Alzheimer's disease. *Brain Research* 501(2), pp. 364-372. doi: 10.1016/0006-8993(89)90653-7

Blennow, K. 2004. Cerebrospinal fluid protein biomarkers for Alzheimer's disease. *NeuroRx: the journal of the American Society for Experimental NeuroTherapeutics* 1(2), pp. 213-225. doi: 10.1602/neurorx.1.2.213

Bonilha, V.L. 2008. Age and disease-related structural changes in the retinal pigment epithelium. *Clinical ophthalmology* 2(2), pp. 413-424. doi: 10.2147/opth.s2151

Boreman, G.D. 2001. *Modulation Transfer Function in Optical and Electro-optical Systems*. Second Edition. Bellingham: Society of Photo Optical. doi: 10.1117/3.419857

Bourne, R.R.A., Stevens, G.A., White, R.A., Smith, J.L., Flaxman, S.R., Price, H., Jonas, J.B., Keeffe, J., Leasher, J., Naidoo, K., Pesudovs, K., Resnikoff, S., Taylor, H.R. and Vision Loss Expert Group. 2013. Causes of vision loss worldwide, 1990–2010: a systematic analysis. *The Lancet Global Health* 1(6), pp. e339-e349. doi: 10.1016/S2214-109X(13)70113-X

Bowes Rickman, C., Farsiu, S., Toth, C.A. and Klingeborn, M. 2013. Dry age-related macular degeneration: mechanisms, therapeutic targets, and imaging. *Investigative ophthalmology & visual science* 54(14), pp. ORSF68-ORSF80. doi: 10.1167/iovs.13-12757

Boycott, B.B., Dowling, J.E., Fisher, S.K., Kolb, H. and Laties, A.M. 1975. Interplexiform cells of the mammalian retina and their comparison with catecholamine-containing retinal cells. *Proceedings of the Royal Society of London. Series B. Biological Sciences* 191(1104), pp. 353-368. doi: 10.1098/rspb.1975.0133

Bressler, N.M., Bressler, S.B. and Fine, S.L. 1988. Age-related macular degeneration. *Survey of Ophthalmology* 32(6), pp. 375-413. doi: 10.1016/0039-6257(88)90052-5

Brown, C.N., Green, B.D., Thompson, R.B., den Hollander, A.I. and Lengyel, I. 2018. Metabolomics and Age-Related Macular Degeneration. *Metabolites* 9(1), p. 4. doi: 10.3390/metabo9010004

Brown, E.E., DeWeerd, A.J., Ildefonso, C.J., Lewin, A.S. and Ash, J.D. 2019. Mitochondrial oxidative stress in the retinal pigment epithelium (RPE) led to metabolic dysfunction in both the RPE and retinal photoreceptors. *Redox Biology* 24, p. 101201. doi: 10.1016/j.redox.2019.101201

Buerger, K., Ewers, M., Pirttilä, T., Zinkowski, R., Alafuzoff, I., Teipel, S.J., DeBernardis, J., Kerkman, D., McCulloch, C., Soininen, H. and Hampel, H. 2006. CSF phosphorylated tau protein correlates with neocortical neurofibrillary pathology in Alzheimer's disease. *Brain* 129(Pt 11), pp. 3035-3041. doi: 10.1093/brain/awl269

Bull, N.D., Johnson, T.V., Welsapar, G., DeKorver, N.W., Tomarev, S.I. and Martin, K.R. 2011. Use of an Adult Rat Retinal Explant Model for Screening of Potential Retinal Ganglion Cell

Neuroprotective Therapies. *Investigative Ophthalmology & Visual Science* 52(6), pp. 3309-3320. doi: 10.1167/iovs.10-6873

Burgoyne, T., O'Connor, M.N, Seabra, M.C., Cutler, D.F. and Futter, C.E. 2015. Regulation of melanosome number, shape and movement in the zebrafish retinal pigment epithelium by OA1 and PMEL. *Journal of cell science* 128(7), pp. 1400-1407. doi: 10.1242/jcs.164400

Cabral, T., Mello, L.G.M, Lima, L.H., Polido, J., Regatieri, C.V., Belfort Jr, R. and Mahajan, V.B. 2017. Retinal and choroidal angiogenesis: a review of new targets. *International journal of retina and vitreous* 3, pp. 31-31. doi: 10.1186/s40942-017-0084-9

Campochiaro, P. A. 2015. Molecular pathogenesis of retinal and choroidal vascular diseases. *Progress in retinal and eye research* 49, pp. 67-81. doi: 10.1016/j.preteyeres.2015.06.002

Catalani, E. and Cervia, D. 2020. Diabetic retinopathy: a matter of retinal ganglion cell homeostasis. *Neural regeneration research* 15(7), pp. 1253-1254. doi: 10.4103/1673-5374.272577

Cedrone, C., Mancino, R., Cerulli, A., Cesareo, M. and Nucci, C. 2008. Epidemiology of primary glaucoma: prevalence, incidence, and blinding effects. In: Nucci, C. et al. eds. *Progress in Brain Research*. Vol. 173. Elsevier, pp. 3-14. doi: 10.1016/S0079-6123(08)01101-1

Chakravarthy, U., Williams, M. and AMD Guidelines Group. 2013. The Royal College of Ophthalmologists Guidelines on AMD: Executive Summary. *Eye* 27(12), pp. 1429-1431. doi: 10.1038/eye.2013.233

Chan, D.C. 2006. Mitochondria: Dynamic Organelles in Disease, Aging, and Development. *Cell* 125(7), pp. 1241-1252. doi: 10.1016/j.cell.2006.06.010

Chauhan, B.C., O'Leary, N., AlMobarak, F.A., Reis, A.S.C., Yang, H., Sharpe, G.P., Hutchison, D.M., Nicoleta, M.T. and Burgoyne, C.F. 2013. Enhanced detection of open-angle glaucoma with an anatomically accurate optical coherence tomography-derived neuroretinal rim parameter. *Ophthalmology* 120(3), pp. 535-543. doi: 10.1016/j.opht.2012.09.055

Chen, H.Y., Huang, M.L. and Hung, P.T. 2006. Logistic regression analysis for glaucoma diagnosis using Stratus Optical Coherence Tomography. *Optometry and Vision Science* 83(7), pp. 527-534. doi: 10.1097/01.opx.0000225893.38212.07

Chen, S., Urban, M.W., Pislaru, C., Kinnick, R., Zheng, Y., Yao, A. and Greenleaf, J.F. 2009. Shearwave dispersion ultrasound vibrometry (SDUV) for measuring tissue elasticity and viscosity. *IEEE Transactions on Ultrasonics, Ferroelectrics, and Frequency Control* 56(1), pp. 55-62. doi: 10.1109/TUFFC.2009.1005

Cherkezyan, L., Subramanian, H., Stoyneva, V., Rogers, J.D., Yang, S., Damania, D., Taflove, A. and Backman, V. 2012. Targeted alteration of real and imaginary refractive index of biological cells by histological staining. *Optics Letters* 37(10), pp. 1601-1603. doi: 10.1364/OL.37.001601

Chiasseu, M., Alarcon-Martinez, L., Belforte, N., Quintero, H., Dotigny, F., Destroismaisons, L., Velde, C.V., Panayi, F., Louis, C. and Di Polo, A. 2017. Tau accumulation in the retina promotes early neuronal dysfunction and precedes brain pathology in a mouse model of Alzheimer's disease. *Molecular Neurodegeneration* 12(1), p. 58. doi: 10.1186/s13024-017-0199-3

Chidlow, G., Ebnetter, A., Wood, J.P.M and Casson, R.J. 2011. The optic nerve head is the site of axonal transport disruption, axonal cytoskeleton damage and putative axonal regeneration failure in a rat model of glaucoma. *Acta Neuropathologica* 121(6), pp. 737-751. doi: 10.1007/s00401-011-0807-1

Choi, Y.J., Jeoung, J.W., Park, K.H. and Kim, D.M. 2016. Clinical Use of an Optical Coherence Tomography Linear Discriminant Function for Differentiating Glaucoma from Normal Eyes. *Journal of Glaucoma* 25(3), pp. e162-169. doi: 10.1097/ijg.0000000000000210

Choma, M.A., Sarunic, M.V., Yang, C. and Izatt, J.A. 2003. Sensitivity advantage of swept source and Fourier domain optical coherence tomography. *Optics Express* 11(18), pp. 2183-2189. doi: 10.1364/OE.11.002183

Coco, R.M. and Sala-Puigdollers, A. 2014. Management of significant reactivation of old disciform scars in wet age-related macular degeneration. *BMC ophthalmology* 14, pp. 82-82. doi: 10.1186/1471-2415-14-82

Coleman, A.L. 1999. Glaucoma. *The Lancet* 354(9192), pp. 1803-1810. doi: 10.1016/S0140-6736(99)04240-3

Connors, R.W. and Harlow, C.A. 1980. A theoretical comparison of texture algorithms. *IEEE Transactions on Pattern Analysis and Machine Intelligence* 2(3), pp. 204-222. doi: 10.1109/TPAMI.1980.4767008.

Cordeiro, M.F. 2007. DARC: a new method for detecting progressive neuronal death. *Eye* 21(1), pp. S15-S17. doi: 10.1038/sj.eye.6702881

Cordeiro, M.F., Guo, L., Coxon, K.M., Duggan, J., Nizari, S., Normando, E.M., Sensi, S.L., Sillito, A.M., Fitzke, F.W., Salt, T.E. and Moss, S.E. 2010. Imaging multiple phases of neurodegeneration: a novel approach to assessing cell death in vivo. *Cell Death and Disease* 1, p. e3. doi: 10.1038/cddis.2009.3

- Costantini, R., Sbaiz, L. and Susstrunk, S. 2008. Higher Order SVD Analysis for Dynamic Texture Synthesis. *IEEE Transactions on Image Processing* 17(1), pp. 42-52. doi: 10.1109/TIP.2007.910956
- Cras, P., Kawai, M., Lowery, D., Gonzalez-DeWhitt, P., Greenberg, B. and Perry, G. 1991. Senile plaque neurites in Alzheimer disease accumulate amyloid precursor protein. *Proceedings of the National Academy of Sciences of the United States of America* 88(17), pp. 7552-7556. doi: 10.1073/pnas.88.17.7552
- Culjat, M.O., Goldenberg, D., Tewari, P. and Singh, R.S. 2010. A Review of Tissue Substitutes for Ultrasound Imaging. *Ultrasound in Medicine & Biology* 36(6), pp. 861-873. doi: 10.1016/j.ultrasmedbio.2010.02.012
- Curcio, C.A., Sloan, K.R., Kalina, R.E. and Hendrickson, A.E. 1990. Human photoreceptor topography. *Journal of Comparative Neurology* 292(4), pp. 497-523. doi: 10.1002/cne.902920402
- Czakó, C., Kovács, T., Ungvari, Z., Csiszar, A., Yabluchanskiy, A., Conley, S., Csipo, T., Lipecz, A., Horváth, H., Sándor, G.L., István, L., Logan, T., Nagy, Z.Z. and Kovács, I. 2020. Retinal biomarkers for Alzheimer's disease and vascular cognitive impairment and dementia (VCID): implication for early diagnosis and prognosis. *GeroScience* 42(6), pp. 1499-1525. doi: 10.1007/s11357-020-00252-7
- Daruich, A., Matet, A., Moulin, A., Kowalczyk, L., Nicolas, M., Sellam, A., Rothschild, P.R., Omri, S., Gélizé, E., Jonet, L., Delaunay, K., De Kozak, Y., Berdugo, M., Zhao, M., Crisanti, P. and Behar-Cohen, F. 2018. Mechanisms of macular edema: Beyond the surface. *Progress in Retinal and Eye Research* 63, pp. 20-68. doi: 10.1016/j.preteyeres.2017.10.006
- Davies, E.R. 2005. Texture. In: Davies, E.R. ed. *Machine Vision* (Third Edition). Burlington: Morgan Kaufmann, pp. 757-779. doi: 10.1016/B978-0-12-206093-9.X5000-X
- Davies, H.G., Wilkins, M.H.F., Chayen, J. and La Cour, L.F. 1954. The Use of the Interference Microscope to Determine Dry Mass in Living Cells and as a Quantitative Cytochemical Method. *Quarterly Journal of Microscopical Science* s3-95(31), pp. 271-304. doi: 10.1242/jcs.s3-95.31.271
- de Amorim Garcia Filho, C.A., Yehoshua, Z., Gregori, G., Farah, M.E., Feuer, W. and Rosenfeld, P.J. 2013. Optical Coherence Tomography A2 - Ryan, Stephen J. In: Wilkinson, C., Hinton, D., Sadda, S., Wiedemann, P. and Ryan, S. eds. *Retina* (Fifth Edition). London: W.B. Saunders, pp. 82-110. doi: 0.1097/IAE.0b013e318285cbd2
- De Robertis, E. and Lasansky, A. 1958. Submicroscopic organization of retinal cones of the rabbit. *The Journal of biophysical and biochemical cytology* 4(6), pp. 743-746. doi: 10.1083/jcb.4.6.743

Della Santina, L. and Ou, Y. 2017. Who's lost first? Susceptibility of retinal ganglion cell types in experimental glaucoma. *Experimental Eye Research* 158, pp. 43-50. doi: 10.1016/j.exer.2016.06.006

den Haan, J., Morrema, T.H.J., Verbraak, F.D., de Boer, J.F., Scheltens, P., Rozemuller, A.J., Bergen, A.A.B., Bouwman, F.H. and Hoozemans J.J. 2018. Amyloid-beta and phosphorylated tau in post-mortem Alzheimer's disease retinas. *Acta Neuropathologica Communications* 6(1), p. 147. doi: 10.1186/s40478-018-0650-x

DePina, A.S. and Langford, G.M. 1999. Vesicle transport: The role of actin filaments and myosin motors. *Microscopy Research and Technique* 47(2), pp. 93-106. doi: 10.1002/(sici)1097-0029(19991015)47:23.0.Co;2-p

Ding, X., Patel, M. and Chan, C.C. 2009. Molecular pathology of age-related macular degeneration. *Progress in retinal and eye research* 28(1), pp. 1-18. doi: 10.1016/j.preteyeres.2008.10.001

Do, D.V., Gower, E.W., Cassard, S.D., Boyer, D., Bressler, N.M., Bressler, S.B., Heier, J.S., Jefferys, J.L., Singerman, L.J. and Solomon, S.D. 2012. Detection of New-Onset Choroidal Neovascularization Using Optical Coherence Tomography: The AMD DOC Study. *Ophthalmology* 119(4), pp. 771-778. doi: 10.1016/j.ophtha.2011.10.019

Dong, Y., Feng, J., Liang, L., Zheng, L. and Wu, Q. 2017. Multiscale Sampling Based Texture Image Classification. *IEEE Signal Processing Letters* 24(5), pp. 614-618. doi: 10.1109/LSP.2017.2670026

Dorey, C.K., Wu, G., Ebenstein, D., Garsd, A. and Weiter, J.J. 1989. Cell loss in the aging retina. Relationship to lipofuscin accumulation and macular degeneration. *Investigative Ophthalmology & Visual Science* 30(8), pp. 1691-1699. PMID: 2759786

Dowling, J.E. 1987. *The retina: an approachable part of the brain*. Cambridge, Mass: Belknap Press of Harvard University Press. doi: 10.1002/ajhb.22305

Drasdo, N. and Fowler, C.W. (1974). Non-linear projection of the retinal image in a wide-angle schematic eye. *The British journal of ophthalmology* 58(8), pp. 709-714. doi: 10.1136/bjo.58.8.709

Drexler, W. 2010. Optical Coherence Tomography. In: Dartt, D.A. *Encyclopedia of the Eye*. Oxford: Academic Press, pp. 194-204. doi: 10.1136/bjo.58.8.709

Drexler, W. and Fujimoto, J.G. 2008. *Optical Coherence Tomography: Technology and Applications*. Berlin, Heidelberg: Springer-Verlag Berlin Heidelberg. doi: 10.1007/978-3-319-06419-2

Drexler, W., Morgner, U., Ghanta, R.K., Kärtner, F.X., Schuman, J.S. and Fujimoto, J.G. 2001. Ultrahigh-resolution ophthalmic optical coherence tomography. *Nature Medicine* 7, p. 502. doi: 10.1038/86589

Dubose, T.B., Cunefare, D., Cole, E., Milanfar, P., Izatt, J.A. and Farsiu, S. 2018. Statistical Models of Signal and Noise and Fundamental Limits of Segmentation Accuracy in Retinal Optical Coherence Tomography. *IEEE Transactions on Medical Imaging* 37(9), pp. 1978-1988. doi: 10.1109/TMI.2017.2772963

Dunaief, J.L., Dentchev, T., Ying, G.S. and Milam, A.H. 2002. The role of apoptosis in age-related macular degeneration. *Archives of Ophthalmology* 120(11), pp. 1435-1442. doi: 10.1001/archophth.120.11.1435

Ebrahimi, K.B. and Handa, J.T. 2011. Lipids, Lipoproteins, and Age-Related Macular Degeneration. *Journal of Lipids* 2011, p. 802059. doi: 10.1155/2011/802059

Edwards, M.M., Rodríguez, J.J., Gutierrez-Lanza, R., Yates, J., Verkhatsky, A. and Lutty, G.A. 2014. Retinal macroglia changes in a triple transgenic mouse model of Alzheimer's disease. *Experimental Eye Research* 127, pp. 252-260. doi: 10.1016/j.exer.2014.08.006

Ejofodomi, O. 2014. Measurement of Optical Scattering Coefficient of the Individual Layers of the Human Urinary Bladder Using Optical Coherence Tomography. *ISRN Biomedical Imaging* 2014, p. 591592. doi: 10.1155/2014/591592

Elkington, A.R., Inman, C.B., Steart, P.V. and Weller, R.O. 1990. The structure of the lamina cribrosa of the human eye: An immunocytochemical and electron microscopical study. *Eye* 4, p. 42. doi: 10.1038/eye.1990.5

Evennett, P.J., McMahon, J., Mahers, E.G., Joyce, S.C., Reed, M.G., Rood, A.P., Brocklehurst, K.G., Julian, K. and Mills, S.L. 1993. Particle characterisation by microscopy and image analysis. *Analytical Proceedings* 30(5), pp. 227-232. doi: 10.1039/AP9933000227

Fahy, E.T., Chrysostomou, V. and Crowston, J.G. 2016. Mini-Review: Impaired Axonal Transport and Glaucoma. *Current Eye Research* 41(3), pp. 273-283. doi: 10.3109/02713683.2015.1037924

Fan, T.-J., Han, L.-H., Cong, R.-S. and Liang, J. 2005. Caspase Family Proteases and Apoptosis. *Acta Biochimica et Biophysica Sinica* 37(11), pp. 719-727. doi: 10.1111/j.1745-7270.2005.00108.x

Fercher, A.F. 1996. Optical coherence tomography. *Journal of Biomedical Optics* 1(2), pp. 157-173, 117. doi: 10.1117/12.231361

Fleming, C.P., Eckert, J., Halpern, E.F., Gardecki, J.A. and Tearney, G.J. 2013. Depth resolved detection of lipid using spectroscopic optical coherence tomography. *Biomedical Optics Express* 4(8), pp. 1269-1284. doi: 10.1364/BOE.4.001269

Foster, P.J. 2001. Advances in the understanding of primary angle-closure as a cause of glaucomatous optic neuropathy. *Community eye health* 14(39), pp. 37-39. PMID: 17491924

Foster, P.J., Buhrmann, R., Quigley, H.A. and Johnson, G.J. 2002. The definition and classification of glaucoma in prevalence surveys. *British Journal of Ophthalmology* 86(2), pp. 238-242. doi: 10.1136/bjo.86.2.238

Frank, S., Gaume, B., Bergmann-Leitner, E.S., Leitner, W.W., Robert, E.G., Catez, F., Smith, C.L. and Youle, R.J. 2001. The Role of Dynamin-Related Protein 1, a Mediator of Mitochondrial Fission, in Apoptosis. *Developmental Cell* 1(4), pp. 515-525. doi: 10.1016/S1534-5807(01)00055-7

Frankfort, B.J., Khan, A.K., Tse, D.Y., Chung, I., Pang, J.-J., Yang, Z., Gross, R.L. and Wu, S.M. 2013. Elevated intraocular pressure causes inner retinal dysfunction before cell loss in a mouse model of experimental glaucoma. *Investigative ophthalmology & visual science* 54(1), pp. 762-770. doi: 10.1167/iovs.12-10581

Fuhrmann, S., Zou, C. and Levine, E.M. 2014. Retinal pigment epithelium development, plasticity, and tissue homeostasis. *Experimental eye research* 123, pp. 141-150. doi: 10.1016/j.exer.2013.09.003

Fujimoto, J.G., Brezinski, M.E., Tearney, G.J., Boppart, S.A., Bouma, B., Hee, M.R., Southern, J.F. and Swanson, E.A. 1995. Optical biopsy and imaging using optical coherence tomography. *Nature Medicine* 1, p. 970. doi: 10.1038/nm0995-970

Gabriele, M.L., Wollstein, G., Ishikawa, H., Kagemann, L., Xu, J., Folio, L.S. and Schuman, J.S. 2011. Optical Coherence Tomography: History, Current Status, and Laboratory Work. *Investigative Ophthalmology & Visual Science* 52(5), pp. 2425-2436. doi: 10.1167/iovs.10-6312

Galloway, M.M. (1975). Texture analysis using gray level run lengths. *Computer Graphics and Image Processing* 4(2), pp. 172-179. doi: 10.1016/S0146-664X(75)80008-6

Galvao, J., Davis, B.M. and Cordeiro, M.F. 2013. In vivo imaging of retinal ganglion cell apoptosis. *Current Opinion in Pharmacology* 13(1), pp. 123-127. doi: 10.1016/j.coph.2012.08.007

Ganesan, R., Das, T.K. and Venkataraman, V. (2004). Wavelet-based multiscale statistical process monitoring: A literature review. *IIE Transactions* 36(9), pp. 787-806. doi: 10.1080/07408170490473060

García-Layana, A., Cabrera-López, F., García-Arumí, J., Arias-Barquet, L. and Ruiz-Moreno, J.M. 2017. Early and intermediate age-related macular degeneration: update and clinical review. *Clinical interventions in aging* 12, pp. 1579-1587. doi: 10.2147/CIA.S142685

Garcia-Valenzulela, E., Gorczyca, W., Darzynkiewicz, Z., Sharma, S.C. 1994. Apoptosis in adult retinal ganglion cells after axotomy. *Journal of Neurobiology* 25(4), pp. 431-438. doi: 10.1002/neu.480250408

Garhart, C. and Lakshminarayanan, V. 2016. Anatomy of the Eye. In: Chen, J. et al. eds. *Handbook of Visual Display Technology*. Cham: Springer International Publishing, pp. 93-104. doi: 10.1007/978-3-319-14346-0_4

Garvin, M.K., Abràmoff, M.D., Wu, X., Russell, S.R., Burns, T.L. and Sonka, M. 2009. Automated 3-D Intraretinal Layer Segmentation of Macular Spectral-Domain Optical Coherence Tomography Images. *IEEE Transactions on Medical Imaging* 28(9), pp. 1436-1447. doi: 10.1109/TMI.2009.2016958

Gavrieli, Y., Sherman, Y. and Ben-Sasson, S.A. 1992. Identification of programmed cell death in situ via specific labeling of nuclear DNA fragmentation. *The Journal of Cell Biology* 119(3), pp. 493-501. doi: 10.1083/jcb.119.3.493

Gazzard, G. 2015. Angle Imaging: Ultrasound Biomicroscopy and Anterior Segment Optical Coherence Tomography. In: Shaarawy, T., Sherwood, M., Hitchings, R., Crowst, J. eds. *Glaucoma* (Second Edition). W.B. Saunders, pp. 191-200. doi: 10.1016/B978-0-7020-5193-7.00033-9

Giannoccaro, M.P., La Morgia, C., Rizzo, G. and Carelli, V. 2017. Mitochondrial DNA and primary mitochondrial dysfunction in Parkinson's disease. *Movement Disorders* 32(3), pp. 346-363. doi: 10.1002/mds.26966

Giorgi, C., Agnoletto, C., Bononi, A., Bonora, M., De Marchi, E., Marchi, S., Missiroli, S., Patergnani, S., Poletti, F., Rimessi, A., Suski, J.M., Wieckowski, M.R. and Pinton, P. 2012. Mitochondrial calcium homeostasis as potential target for mitochondrial medicine. *Mitochondrion* 12(1), pp. 77-85. doi: 10.1016/j.mito.2011.07.004

Golestaneh, N., Chu, Y., Xiao, Y.-Y., Stoleru, G.L. and Theos, A.C. 2018. Dysfunctional autophagy in RPE, a contributing factor in age-related macular degeneration. *Cell Death and Disease* 8(1), pp. e2537-e2537. doi: 10.1038/cddis.2016.453

González-Gonzalo, C., Sánchez-Gutiérrez, V., Hernández-Martínez, P., Contreras, I., Lechanteur, Y.T., Domanian, A., van Ginneken, B. and Sánchez, C.I. 2020. Evaluation of a deep learning system for the joint automated detection of diabetic retinopathy and age-

related macular degeneration. *Acta Ophthalmologica* 98(4), pp. 368-377. doi: 10.1111/aos.14306

González-López, A., Remeseiro, B., Ortega, M., Penedo, M. and Charlón, P. eds. 2015. *A Texture-Based Method for Choroid Segmentation in Retinal EDI-OCT Images*. Cham, Springer International Publishing. doi: 10.1007/978-3-319-27340-2

Gossage, K.W., Cynthia, M.S., Elizabeth, M.K., Lida, P.H., Alice, L.S., Jeffrey, J.R., Williams, S.K., Jennifer, K.B. (2006). Texture analysis of speckle in optical coherence tomography images of tissue phantoms. *Physics in Medicine & Biology* 51(6), pp. 1563-1575. doi: 10.1088/0031-9155/51/6/014

Gossage, K.W., Tkaczyk, T.S., Rodriguez, J.J. and Barton, J.K. (2003). Texture analysis of optical coherence tomography images: feasibility for tissue classification. *Journal of Biomedical Optics* 8(3). doi: 10.1117/1.1577575 .

Gourley, P.L. and Naviaux, R.K. 2005. Optical phenotyping of human mitochondria in a biocavity laser. *IEEE Journal of Selected Topics in Quantum Electronics* 11(4), pp. 818-826. doi: 10.1109/JSTQE.2005.857680

Gourley, P.L., Hendricks, J.K., McDonald, A.E., Copeland, R.G., Barrett, K.E., Gourley, C.R., Singh, K.K. and Naviaux, R.K. 2005. Mitochondrial Correlation Microscopy and Nanolaser Spectroscopy — New Tools for Biophotonic Detection of Cancer in Single Cells. *Technology in Cancer Research & Treatment* 4(6), pp. 585-592. doi: 10.1177/153303460500400602

Granger, C.E., Yang, Q., Song, H., Saito, K., Nozato, K., Latchney, L.R., Leonard, B.T., Chung, M.M., Williams, D.R. and Rossi, E.A. 2018. Human Retinal Pigment Epithelium: In Vivo Cell Morphometry, Multispectral Autofluorescence, and Relationship to Cone Mosaic. *Investigative Ophthalmology & Visual Science* 59(15), pp. 5705-5716. doi: 10.1167/iovs.18-24677

Grafstein, B. and Ingoglia, N.A. 1982. Intracranial transection of the optic nerve in adult mice: Preliminary observations. *Experimental Neurology* 76(2), pp. 318-330. doi: 10.1016/0014-4886(82)90212-6

Greferath, U., Guymer, R.H., Vessey, K.A., Brassington, K. and Fletcher, E.L. 2016. Correlation of Histologic Features with In Vivo Imaging of Reticular Pseudodrusen. *Ophthalmology* 123(6), pp. 1320-1331. doi: 10.1016/j.optha.2016.02.009

Grimaldi, A., Brighi, C., Peruzzi, G., Ragozzino, D., Bonanni, V., Limatola, C., Ruocco, G. and Di Angelantonio, S. 2018. Inflammation, neurodegeneration and protein aggregation in the retina as ocular biomarkers for Alzheimer's disease in the 3xTg-AD mouse model. *Cell Death and Disease* 9(6), p. 685. doi: 10.1038/s41419-018-0740-5

Grzybowski, A., Brona, P., Lim, G., Ruamviboonsuk, P., Tan, G.S.W., Abramoff, M. and Ting, D.S.W. 2020. Artificial intelligence for diabetic retinopathy screening: a review. *Eye* 34(3), pp. 451-460. doi: 10.1038/s41433-019-0566-0

Guo, L., Moss, S.E., Alexander, R.A., Ali, R.S., Fitzke, F.W. and Cordeiro, M.F. 2005. Retinal Ganglion Cell Apoptosis in Glaucoma Is Related to Intraocular Pressure and IOP-Induced Effects on Extracellular Matrix. *Investigative Ophthalmology & Visual Science* 46(1), pp. 175-182. doi: 10.1167/iops.04-0832

Gupta, V., You, Y., Li, J., Gupta, V., Golzan, M., Klistorner, A., van den Buuse, M. and Graham, S. 2014. BDNF impairment is associated with age-related changes in the inner retina and exacerbates experimental glaucoma. *Biochimica et Biophysica Acta (BBA) - Molecular Basis of Disease* 1842(9), pp. 1567-1578. doi: 10.1016/j.bbadis.2014.05.026

Haeker, M., Sonka, M., Kardon, R., Shah, V.A., Wu, X. and Abramoff, M.D. 2007. Automated segmentation of intraretinal layers from macular optical coherence tomography images. *Proc. SPIE 6512, Medical Imaging 2007: Image Processing*, p. 651214. doi: 10.1117/12.710231 .

Handa, J.T., Rickman, C.B., Dick, A.D., Gorin, M.B., Miller, J.W., Toth, C.A., Ueffing, M., Zarbin, M. and Farrer, L.A. 2019. A systems biology approach towards understanding and treating non-neovascular age-related macular degeneration. *Nature Communications* 10(1), p. 3347. doi: 10.1038/s41467-019-11262-1

Haralick, R.M., Shanmugam, K. and Dinstein, I. 1973. Textural Features for Image Classification. *IEEE Transactions on Systems, Man, and Cybernetics* 3(6), pp. 610-621. doi: 10.1109/TSMC.1973.4309314

Hart, N.J., Koronyo, Y., Black, K.L. and Koronyo-Hamaoui, M. 2016. Ocular indicators of Alzheimer's: exploring disease in the retina. *Acta Neuropathologica* 132(6), pp. 767-787. doi: 10.1007/s00401-016-1613-6

Harwerth, R.S., Carter-Dawson, L., Shen, F., Smith 3rd, E.L. and Crawford, M.L. 1999. Ganglion Cell Losses Underlying Visual Field Defects from Experimental Glaucoma. *Investigative Ophthalmology & Visual Science* 40(10), pp. 2242-2250. PMID: 10476789

Haseda, K., Kanematsu, K., Noguchi, K., Saito, H., Umeda, N. and Ohta, Y. 2015. Significant correlation between refractive index and activity of mitochondria: single mitochondrion study. *Biomedical Optics Express* 6(3), pp. 859-869. doi: 10.1364/BOE.6.000859

Hee, M.R., Izatt, J.A., Swanson, E.A., Huang, D., Schuman, J.S., Lin, C.P., Puliafito, C.A. and Fujimoto, J.G. 1995. Optical coherence tomography of the human retina. *Archives of Ophthalmology* 113(3), pp. 325-332. doi: 10.1001/archopht.1995.01100030081025

Heijl, A. 2015. Glaucoma treatment: by the highest level of evidence. *The Lancet* 385(9975), pp. 1264-1266. doi: 10.1016/S0140-6736(14)62347-3

Heijl, A., Leske, M.C., Bengtsson, B., Hyman, L., Bengtsson, B., Hussein, M. and Early Manifest Glaucoma Trial Group. 2002. Reduction of Intraocular Pressure and Glaucoma Progression: Results from the Early Manifest Glaucoma Trial. *Archives of Ophthalmology* 120(10), pp. 1268-1279. doi: 10.1001/archophth.120.10.1268

Herman, K.G. and Steinberg, R.H. 1982. Melanosome metabolism in the retinal pigmented epithelium of the opossum. *Cell and Tissue Research* 227(3), pp. 485-507. doi: 10.1007/BF00204780

Holloway, T.B. and Verhoeff, F.H. 1929. Disc-like degeneration of the macula. *American Journal of Ophthalmology* 12(5), p. 439. doi: 10.5555/uri:pii:S0002939429923564

Hongchuan, Y. and Bennamoun, M. 2006. 1D-PCA, 2D-PCA to nD-PCA. *18th International Conference on Pattern Recognition (ICPR'06)*. Hong Kong; China, 20-24 August 2006. IEEE. doi: 10.1109/ICPR.2006.19

Howell, G.R., Libby, R.T., Jakobs, T.C., Smith, R.S., Phalan, F.C., Barter, J.W., Barbay, J.M., Marchant, J.K., Mahesh, N., Porciatti, V., Whitmore, A.V., Masland, R.H. and John, S.W.M. 2007. Axons of retinal ganglion cells are insulated in the optic nerve early in DBA/2J glaucoma. *The Journal of Cell Biology* 179(7), pp. 1523-1537. doi: 10.1083/jcb.200706181

Huang, D., Swanson, E.A., Lin, C.P. Schuman, J.S., Stinson, W.G., Chang, W., Hee, M.R., Flotte, T., Gregory, K., Puliafito C.A. and Fujimoto J.G. 1991. Optical Coherence Tomography. *Science* 254(5035), pp. 1178-1181. doi: 10.1126/science.1957169

Huang, J. et al. 2019. The effects of endothelium-specific CYP2J2 overexpression on the attenuation of retinal ganglion cell apoptosis in a glaucoma rat model. *The FASEB Journal* 33(10), pp. 11194-11209. doi: <https://doi.org/10.1096/fj.201900756R>

Huang, W.C., Zhao, Q., Li, M., Duan, Q., Zhao, Y. and Zhang, H . 2014. Inner and Outer Retinal Changes in Retinal Degenerations Associated with ABCA4 Mutations. *Investigative Ophthalmology & Visual Science* 55(3), pp. 1810-1822. doi: 10.1167/iovs.13-13768

Humeau-Heurtier, A. 2019. Texture Feature Extraction Methods: A Survey. *IEEE Access* 7, pp. 8975-9000. doi: 10.1109/ACCESS.2018.2890743

Jack, C. R., Bennett, D.A., Blennow, K., Carrillo, M.C., Dunn, B., Haeberlein, S.B., Holtzman, D.M., Jagust, W., Jessen, F., Karlawish, J., Liu, E., Molinuevo, J.L., Montine, T., Phelps, C., Rankin, K.P., Rowe, C.C., Scheltens, P., Siemers, E., Snyder, H.M., Sperling, R., Elliott, C., Masliah, E., Ryan, L. and Silverberg, N. 2018. NIA-AA Research Framework: Toward a

biological definition of Alzheimer's disease. *Alzheimer's & dementia: the journal of the Alzheimer's Association* 14(4), pp. 535-562. doi: 10.1016/j.jalz.2018.02.018

Jadiya, P., Kolmetzky, D.W., Tomar, D., Di Meco, A., Lombardi, A.A., Lambert, J.P., Luongo, T.S., Ludtmann, M.H., Praticò D. and Elrod, J.W. 2019. Impaired mitochondrial calcium efflux contributes to disease progression in models of Alzheimer's disease. *Nature Communications* 10(1), p. 3885. doi: 10.1038/s41467-019-11813-6

Jakobs, T.C., Libby, R.T., Ben, Y., John, S.W.M. and Masland, R.H. 2005. Retinal ganglion cell degeneration is topological but not cell type specific in DBA/2J mice. *Journal of Cell Biology* 171(2), pp. 313-325. doi: 10.1083/jcb.200506099

James, O.G., Doraiswamy, P.M. and Borges-Neto, S. 2015. PET Imaging of Tau Pathology in Alzheimer's Disease and Tauopathies. *Frontiers in Neurology* 6, p. 38. doi: 10.3389/fneur.2015.00038

Jarrett, S.G. and Boulton, M.E. 2012. Consequences of oxidative stress in age-related macular degeneration. *Molecular aspects of medicine* 33(4), pp. 399-417. doi: 10.1016/j.mam.2012.03.009

Jia, J., Sun, B., Guo, Z., Zhang, J., Tian, J., Tang, H. and Wang, L. 2011. Positron emission tomography with Pittsburgh compound B in diagnosis of early stage Alzheimer's disease. *Cell Biochemistry and Biophysics* 59(1), pp. 57-62. doi: 10.1007/s12013-010-9111-2

Jian, W., Sun, X. and Luo, S. (2012). Computer-aided diagnosis of breast microcalcifications based on dual-tree complex wavelet transform. *Biomedical engineering online* 11, pp. 96-96. doi: 10.1186/1475-925X-11-96

Jiang, K., To, E., Cui, J.Z., Cao, S., Gao, J. and Matsubara, J.A. 2012. Drusen and Pro-inflammatory Mediators in the Post-Mortem Human Eye. *Journal of clinical & experimental ophthalmology* 3, pp. 208-208. doi: 10.4172/2155-9570.1000208

Johnson, C.A., Sample, P.A., Zangwill, L.M., Vasile, C.G., Cioffi, G.A., Liebmann, J.R. and Weinreb, R.N. 2003. Structure and function evaluation (SAFE): II. Comparison of optic disk and visual field characteristics. *American Journal of Ophthalmology* 135(2), pp. 148-154. doi: 10.1016/s0002-9394(02)01930-x

Johnson, K.A., Fox, N.C., Sperling, R.A. and Klunk, W.E. 2012. Brain imaging in Alzheimer disease. *Cold Spring Harbor perspectives in medicine* 2(4), pp. a006213-a006213. doi: 10.1101/cshperspect.a006213

Johnson, P.T., Lewis, G.P., Talaga, K.C., Brown, M.N., Kappel, P.J., Fisher, S.K., Anderson, D.H. and Johnson, L.V. 2003. Drusen-Associated Degeneration in the Retina. *Investigative Ophthalmology & Visual Science* 44(10), pp. 4481-4488. doi: 10.1167/iovs.03-0436

Jonas, J.B., Budde, W.M. and Panda-Jonas, S. 1999. Ophthalmoscopic Evaluation of the Optic Nerve Head. *Survey of Ophthalmology* 43(4), pp. 293-320. doi: 10.1016/S0039-6257(98)00049-6

Jonas, J.B., Aung, T., Bourne, R.R., Bron, A.M., Ritch, R. and Panda-Jonas, S. 2017. Glaucoma. *The Lancet* 390(10108), pp. 2183-2193. doi: 10.1016/S0140-6736(17)31469-1

Jones, S.H., King, M.D. and Ward, A.D. 2013. Determining the unique refractive index properties of solid polystyrene aerosol using broadband Mie scattering from optically trapped beads. *Physical Chemistry Chemical Physics* 15(47), pp. 20735-20741. doi: 10.1039/C3CP53498G

Jonnal, R.S., Kocaoglu, O.P., Zawadzki, R.J., Liu, Z., Miller, D.T. and Werner, J.S. 2016. A Review of Adaptive Optics Optical Coherence Tomography: Technical Advances, Scientific Applications, and the Future. *Investigative ophthalmology & visual science* 57(9), pp. OCT51-OCT68. doi: 10.1167/iovs.16-19103

Julien, S., Kreppel, F., Beck, S., Heiduschka, P., Brito, V., Schnichels, S., Kochanek, S. and Schraermeyer, U. 2008. A reproducible and quantifiable model of choroidal neovascularization induced by VEGF A165 after subretinal adenoviral gene transfer in the rabbit. *Molecular vision* 14, pp. 1358-1372. PMID: 18682809

Kafieh, R., Rabbani, H. and Kermani, S. 2013. A review of algorithms for segmentation of optical coherence tomography from retina. *Journal of medical signals and sensors* 3(1), pp. 45-60. PMID: 24083137

Kajić, V., Považay, B., Hermann, B., Hofer, B., Marshall, D., Rosin, P.L. and Drexler, W. 2010. Robust segmentation of intraretinal layers in the normal human fovea using a novel statistical model based on texture and shape analysis. *Optics Express* 18(14), pp. 14730-14744. doi: 10.1364/OE.18.014730

Kanagasingam, Y., Bhuiyan, A., Abramoff, M.D., Smith, R.T., Goldschmidt, L. and Wong, T.Y. 2014. Progress on retinal image analysis for age related macular degeneration. *Progress in Retinal and Eye Research* 38, pp. 20-42. doi: 10.1016/j.preteyeres.2013.10.002

Kanow, M.A., Giarmarco, M.M., Jankowski, C.S.R., Tsantilas, K., Engel, A.L., Du, J., Linton, J.D., Farnsworth, C.C., Sloat, S.R., Rountree, A., Sweet, I.R., Lindsay, K.J., Parker, E.D., Brockerhoff, S.E., Sadilek, M., Chao, J.R. and Hurley, J.B. 2017. Biochemical adaptations of the retina and retinal pigment epithelium support a metabolic ecosystem in the vertebrate eye. *eLife* 6, doi: 10.7554/eLife.28899

Karunadharma, P.P., Nordgaard, C.L., Olsen, T.W. and Ferrington D.A. 2010. Mitochondrial DNA damage as a potential mechanism for age-related macular degeneration. *Investigative ophthalmology & visual science* 51(11), pp. 5470-5479. doi: 10.1167/iovs.10-5429

Katz, M.L., Drea, M., Eldred, G.E., Hess, H.H. and Robison Jr, W.G. 1986. Influence of early photoreceptor degeneration on lipofuscin in the retinal pigment epithelium. *Experimental Eye Research* 43(4), pp. 561-573. doi: 10.1016/s0014-4835(86)80023-9

Kauppinen, A., Paterno, J.J., Blasiak, J., Salminen, A. and Kaarniranta, K. 2016. Inflammation and its role in age-related macular degeneration. *Cellular and molecular life sciences* 73(9), pp. 1765-1786. doi: 10.1007/s00018-016-2147-8

Kayabasi, U.A. and Sergott, R.C. 2015. Retina examination in neurodegenerative diseases. *Alzheimer's & Dementia: The Journal of the Alzheimer's Association* 11(7), p. P159. doi: 10.1016/j.jalz.2015.07.095

Kemal, E.H. and Sankur, B. 2005. Multiresolution face recognition. *Image and Vision Computing* 23(5), pp. 469-477. doi: 10.1016/j.imavis.2004.09.002

Kennedy, C.J., Rakoczy, P.E. and Constable, I.J. 1995. Lipofuscin of the retinal pigment epithelium: A review. *Eye* 9(6), pp. 763-771. doi: 10.1038/eye.1995.192

Kern, T.S. and Barber, A.J. 2008. Retinal ganglion cells in diabetes. *The Journal of physiology* 586(18), pp. 4401-4408. doi: 10.1113/jphysiol.2008.156695

Kerrigan, L.A., Zack, D.J., Quigley, H.A., Smith, S.D. and Pease, M.E. 1997. TUNEL-Positive Ganglion Cells in Human Primary Open-angle Glaucoma. *Archives of Ophthalmology* 115(8), pp. 1031-1035. doi: 10.1001/archophth.1997.01100160201010

Khatun, M., Gray, A. and Marshall, S. 2011. Morphological granulometry for classification of evolving and ordered texture images. *2011 19th European Signal Processing Conference*. Barcelona; Spain, 29 August-2 September 2011, pp. 759-763. doi: 10.5281/zenodo.42446

Kim, N.R., Lee, E.S., Seong, G.J., Kang, S.Y., Kim, J.H., Hong, S. and Kim, C.Y. 2011. Comparing the ganglion cell complex and retinal nerve fibre layer measurements by Fourier domain OCT to detect glaucoma in high myopia. *British Journal of Ophthalmology* 95(8), pp. 1115-1121. doi: 10.1136/bjo.2010.182493

Kingsbury, N. (2001). Complex Wavelets for Shift Invariant Analysis and Filtering of Signals. *Applied and Computational Harmonic Analysis* 10(3), pp. 234-253. doi: 10.1006/acha.2000.0343

Kirkpatrick, J.N.P., Spencer, T., Manivannan, A., Sharp, P.F. and Forrester, J.V. 1995. Quantitative image analysis of macular drusen from fundus photographs and scanning laser ophthalmoscope images. *Eye* 9(1), pp. 48-55. doi: 10.1038/eye.1995.7

Kischkat, J., Peters, S., Gruska, B., Semtsiv, M., Chashnikova, M., Klinkmüller, M., Fedosenko, O., Machulik, S., Aleksandrova, A., Monastyrskyi, G., Flores, Y. and Masselink, W.T. 2012. Mid-infrared optical properties of thin films of aluminum oxide, titanium dioxide, silicon dioxide, aluminum nitride, and silicon nitride. *Applied Optics* 51(28), pp. 6789-6798. doi: 10.1364/ao.51.006789

Klein, R. 1991. Age-Related Eye Disease, Visual Impairment, and Driving in the Elderly. *Human Factors* 33(5), pp. 521-525. doi: 10.1177/001872089103300504

Klistorner, A., Graham, E.C., Yiannikas, C., Barnett, M., Parratt, J., Garrick, R., Wang, C., You, Y and Graham, S.L. 2017. Progression of retinal ganglion cell loss in multiple sclerosis is associated with new lesions in the optic radiations. *European Journal of Neurology* 24(11), pp. 1392-1398. doi: 10.1111/ene.13404

Krauss, J.M. and Puliafito, C.A. 1995. Lasers in ophthalmology. *Lasers in Surgery and Medicine* 17(2), pp. 102-159. doi: 10.1002/lsm.1900170203

Kucur, Ş.S., Holló, G. and Sznitman, R. 2018. A deep learning approach to automatic detection of early glaucoma from visual fields. *PLoS ONE* 13(11), p. e0206081. doi: 10.1371/journal.pone.0206081

Kumar, S. 2006. Caspase function in programmed cell death. *Cell Death and Differentiation* 14, p. 32. doi: 10.1038/sj.cdd.4402060

la Cour, M., Kiilgaard, J.F. and Nissen, M.H. 2002. Age-Related Macular Degeneration. *Drugs & Aging* 19(2), pp. 101-133. doi: 10.2165/00002512-200219020-00003

La Morgia, C., Di Vito, L., Carelli, V. and Carbonelli, M. 2017. Patterns of Retinal Ganglion Cell Damage in Neurodegenerative Disorders: Parvocellular vs Magnocellular Degeneration in Optical Coherence Tomography Studies. *Frontiers in Neurology* 8, p. 710. doi: 10.3389/fneur.2017.00710

Lai, Y.-L., Masuda, K., Hayasaka, S., Suzuyama, Y., Lin, T.C., Chang, T., Lug, R., Wang, S.J. and Liu, Y.P. 1982. Study of subretinal intercellular space. *Experimental Eye Research* 34(1), pp. 7-14. doi: 10.1016/0014-4835(82)90003-3

Lambert, N.G., ElShelmani, H., Singh, M.K., Mansergh, F.C., Wride, M.A., Padilla, M., Keegan, D, Hogg, R.E. and Ambati, B.K. 2016. Risk factors and biomarkers of age-related macular degeneration. *Progress in retinal and eye research* 54, pp. 64-102. doi: 10.1016/j.preteyeres.2016.04.003

LeCun, Y., Bengio, Y. and Hinton, G. 2015. Deep learning. *Nature* 521(7553), pp. 436-444. doi: 10.1038/nature14539

Lee, H., Leamey, C.A. and Sawatari, A. 2012. Perineuronal Nets Play a Role in Regulating Striatal Function in the Mouse. *PLoS ONE* 7(3), p. e32747. doi: 10.1371/journal.pone.0032747

Lee, H., Kang, K.E., Chung, H. and Kim, H.C. 2018. Automated Segmentation of Lesions Including Subretinal Hyperreflective Material in Neovascular Age-related Macular Degeneration. *American Journal of Ophthalmology* 191, pp. 64-75. doi: 10.1016/j.ajo.2018.04.007

Lee, H.-J., Kim, M.-S., Jo, Y.-J. and Kim, J.-Y. 2015. Ganglion Cell–Inner Plexiform Layer Thickness in Retinal Diseases: Repeatability Study of Spectral-Domain Optical Coherence Tomography. *American Journal of Ophthalmology* 160(2), pp. 283-289.e281. doi: 10.1016/j.ajo.2015.05.015

Lei, Y., Garrahan, N., Hermann, B., Fautsch, M.P., Johnson, D.H., Hernandez, M.R., Boulton, M. and Morgan, J.E. (2011). Transretinal degeneration in ageing human retina: a multiphoton microscopy analysis. *British Journal of Ophthalmology* 95(5), pp. 727-730. doi: 10.1136/bjo.2010.180869

Leitgeb, R., Hitzengerger, C.K. and Fercher, A.F. 2003. Performance of fourier domain vs. time domain optical coherence tomography. *Optics Express* 11(8), pp. 889-894. doi: 10.1364/OE.11.000889

Lemaître, G., Rastgoo, M., Massich, J., Cheung, C.Y., Wong, T.Y., Lamoureux, E., Milea, D., Mériaudeau, F. and Sidibé, D. 2016. Classification of SD-OCT Volumes Using Local Binary Patterns: Experimental Validation for DME Detection. *Journal of Ophthalmology* 2016, p. 3298606. doi: 10.1155/2016/3298606

Leuschen, J.N., Schuman, S.G., Winter, K.P., McCall, M.N., Wong, W.T., Chew, E.Y., Hwang, T., Srivastava, S., Sarin, N., Clemons, T., Harrington, M. and Toth, C.A. 2013. Spectral-Domain Optical Coherence Tomography Characteristics of Intermediate Age-related Macular Degeneration. *Ophthalmology* 120(1), pp. 140-150. doi: 10.1016/j.ophtha.2012.07.004

Lim, J.K.H., Li, Q.-X., He, Z., Vingrys, A.J., Wong, V.H.Y., Currier, N., Mullen, J., Bui, B.V. and Nguyen, C.T.O. 2016. The Eye as a Biomarker for Alzheimer's Disease. *Frontiers in neuroscience* 10, pp. 536-536. doi: 10.3389/fnins.2016.00536

Lim, Y., Johnson, L.N., Fernandez, B.M., Santos, C.Y., Maruff, P. and Snyder, P.J. 2015. High-resolution retinal imaging in the identification of preclinical Alzheimer's disease. *Alzheimer's*

& *Dementia: The Journal of the Alzheimer's Association* 11(7), pp. P158-P159. doi: 10.1016/j.jalz.2015.07.093

Ling, E.A., Dahlström, A., Polinsky, R.J., Nee, L.E. and McRae, A. 1992. Studies of activated microglial cells and macrophages using Alzheimer's disease cerebrospinal fluid in adult rats with experimentally induced lesions. *Neuroscience* 51(4), pp. 815-825. doi: 10.1016/0306-4522(92)90522-4

Lingadurai, K. and Shunmugam, M.S. 2006. Metrological characteristics of wavelet filter used for engineering surfaces. *Measurement* 39(7), pp. 575-584. doi: 10.1016/j.measurement.2006.02.003

Liu, Y.Y., Ishikawa, H., Chen, M., Wollstein, G., Duker, J.S., Fujimoto, J.G., Schuman, J.S. and Reh, J.M. 2011. Computerized macular pathology diagnosis in spectral domain optical coherence tomography scans based on multiscale texture and shape features. *Investigative Ophthalmology & Visual Science* 52(11), pp. 8316-8322. doi: 10.1167/iovs.10-7012

Lo, A.C.Y., Woo, T.T.Y., Wong, R.L.M. and Wong, D. 2011. Apoptosis and Other Cell Death Mechanisms after Retinal Detachment: Implications for Photoreceptor Rescue. *Ophthalmologica* 226(suppl 1), pp. 10-17. doi: 10.1159/000328206

Ma, Y., Chen, X., Zhu, W., Cheng, X., Xiang, D. and Shi, F. 2018. Speckle noise reduction in optical coherence tomography images based on edge-sensitive cGAN. *Biomedical Optics Express* 9(11), pp. 5129-5146. doi: 10.1364/BOE.9.005129

Maddineni, P., Kasetti, R.B., Patel, P.D., Millar, J.C. Kiehlbauch, C., Clark, A.F. and Zode, G.S. 2020. CNS axonal degeneration and transport deficits at the optic nerve head precede structural and functional loss of retinal ganglion cells in a mouse model of glaucoma. *Molecular Neurodegeneration* 15(1), p. 48. doi: 10.1186/s13024-020-00400-9

Malhotra, A., Minja, F.J., Crum, A. and Burrowes, D. 2011. Ocular Anatomy and Cross-Sectional Imaging of the Eye. *Seminars in Ultrasound, CT and MRI* 32(1), pp. 2-13. doi: 10.1053/j.sult.2010.10.009

Mallick, J., Devi, L., Malik, P.K. and Mallick, J. 2016. Update on normal tension glaucoma. *Journal of Ophthalmic and Vision Research* 11(2), pp. 204-208. doi: 10.4103/2008-322x.183914

Marchini, G. 2015. Ultrasound Biomicroscopy. In: Shaarawy, T., Sherwood, M., Hitchings, R., Crowston, J. eds. *Glaucoma* (Second Edition). W.B. Saunders, pp. 179-190. doi: 10.1016/B978-0-7020-5193-7.00033-9

Marshall, J. 1987. The ageing retina: Physiology or pathology. *Eye* 1(2), pp. 282-295. doi: 10.1038/eye.1987.47

Mathis, C.A., Mason, N.S., Lopresti, B.J. and Klunk, W.E. 2012. Development of positron emission tomography β -amyloid plaque imaging agents. *Seminars in Nuclear Medicine* 42(6), pp. 423-432. doi: 10.1053/j.semnuclmed.2012.07.001

Mazzoni, F., Müller, C., DeAssis, J., Lew, D., Leevy, W.M. and Finnemann, S.C. 2019. Non-invasive in vivo fluorescence imaging of apoptotic retinal photoreceptors. *Scientific Reports* 9(1), p. 1590. doi: 10.1038/s41598-018-38363-z

Meschede, I.P., Ovenden, N.C, Seabra, M.C., Futter, C.E., Votruba, M., Cheetham, M.E. and Burgoyne, T. 2020. Symmetric arrangement of mitochondria:plasma membrane contacts between adjacent photoreceptor cells regulated by Opa1. *Proceedings of the National Academy of Sciences* 117(27), p. 15684. doi: 10.1073/pnas.2000304117

Milam, A. H., Curcio, C.A., Cideciyan, A.V., Saxena, S., John, S.K., Kruth, H.S., Malek, G., Heckenlively, J.R., Weleber, R.G. and Jacobson, S.G. 2000. Dominant late-onset retinal degeneration with regional variation of sub-retinal pigment epithelium deposits, retinal function, and photoreceptor degeneration. *Ophthalmology* 107(12), pp. 2256-2266. doi: 10.1016/S0161-6420(00)00419-X

Mirmehdi, M., Xie, X., Suri, J. 2009. *Handbook of Texture Analysis*. London: Imperial College Press. url: <http://www.iapr.org/docs/newsletter-2009-04.pdf>

Mishra, P. and Bhatnagar, C. 2020. Automated Hole and Non-hole Screening in Retinal OCT Images Using Local Binary Patterns with Support Vector Machine. *National Academy Science Letters* 43(6), pp. 529-531. doi: 10.1007/s40009-020-00924-0

Mohammad, N., Schloss, R.S., Berjaud, P. and Boustany, N.N. 2018. Label-free dynamic segmentation and morphological analysis of subcellular optical scatterers. *Journal of Biomedical Optics* 23(9), pp. 1-11. doi: 10.1117/1.JBO.23.9.096004

Molina, D., Pérez-Beteta, J., Luque, B., Arregui, E., Calvo, M., Borrás, J. M., López, C., Martino, J., Velasquez, C., Asenjo, B., Benavides, M., Herruzo, I., Martínez-González, A., Pérez-Romasanta, L., Arana, E. and Pérez-García, V. M. (2016). Tumour heterogeneity in glioblastoma assessed by MRI texture analysis: a potential marker of survival. *The British Journal of Radiology* 89(1064), p. 20160242. doi: 10.1259/bjr.20160242

Morgan, J.E. 2004. Circulation and axonal transport in the optic nerve. *Eye* 18(11), pp. 1089-1095. doi: 10.1038/sj.eye.6701574

Morgan, J.E., Tribble, J., Fergusson, J., White N. and Erchova, I. 2017. The optical detection of retinal ganglion cell damage. *Eye* 31, p. 199. doi: 10.1038/eye.2016.290

- Morgan-Davies, J., Taylor, N., Hill, A.R., Aspinall, P., O'Brien, C.J. and Azuara-Blanco, A. 2004. Three dimensional analysis of the lamina cribrosa in glaucoma. *The British Journal of Ophthalmology* 88(10), pp. 1299-1304. doi: 10.1136/bjo.2003.036020
- Morgner, U., Drexler, W., Kärtner, F.X., Li, X.D., Pitris, C., Ippen, E.P. and Fujimoto, J.G. 2000. Spectroscopic optical coherence tomography. *Optics Letters* 25(2), pp. 111-113. doi: 10.1364/OL.25.000111
- Mosconi, L., Berti, V., Glodzik, L., Pupi, A., De Santi, S. and de Leon, M.J. 2010. Pre-clinical detection of Alzheimer's disease using FDG-PET, with or without amyloid imaging. *Journal of Alzheimer's disease* 20(3), pp. 843-854. doi: 10.3233/JAD-2010-091504
- Mourant, J.R., Freyer, J.P., Hielscher, A.H., Eick, A.A., Shen, D. and Johnson, T.M. 1998. Mechanisms of light scattering from biological cells relevant to noninvasive optical-tissue diagnostics. *Applied Optics* 37(16), pp. 3586-3593. doi: 10.1364/AO.37.003586
- Mourant, J.R., Canpolat, M., Brocker, C., Esponda-Ramos, O., Johnson, T.M., Matanock, A., Stetter, K. and Freyer, J.P. 2000. Light scattering from cells: the contribution of the nucleus and the effects of proliferative status. *Journal of Biomedical Optics* 5(2). doi: 10.1117/1.429979
- Mroczkowska, S., Ekart, A., Sung, V., Negi, A., Qin, L., Patel, S.R., Jacob, S., Atkins, C., Benavente-Perez, A. and Gherghel, D. 2012. Coexistence of macro- and micro-vascular abnormalities in newly diagnosed normal tension glaucoma patients. *Acta Ophthalmologica* 90(7), pp. e553-e559. doi: 10.1111/j.1755-3768.2012.02494.x
- Munemasa, Y. and Kitaoka, Y. 2013. Molecular mechanisms of retinal ganglion cell degeneration in glaucoma and future prospects for cell body and axonal protection. *Frontiers in Cellular Neuroscience* 6(60). doi: 10.3389/fncel.2012.00060
- Murakami, Y., Notomi, S., Hisatomi, T., Nakazawa, T., Ishibashi, T., Miller, J.W. and Vavvas, D.G. 2013. Photoreceptor cell death and rescue in retinal detachment and degenerations. *Progress in retinal and eye research* 37, pp. 114-140. doi: 10.1016/j.preteyeres.2013.08.001
- Murphy, M.P. and LeVine 3rd, H. 2010. Alzheimer's disease and the amyloid-beta peptide. *Journal of Alzheimer's disease* 19(1), pp. 311-323. doi: 10.3233/JAD-2010-1221
- Mursch-Edlmayr, A.S., Ng, W.S., Diniz-Filho, A., Sousa, D.C., Arnould, L., Schlenker, M.B., Duenas-Angeles, K., Keane, P.A., Crowston, J.G. and Jayaram, H. 2020. Artificial Intelligence Algorithms to Diagnose Glaucoma and Detect Glaucoma Progression: Translation to Clinical Practice. *Translational vision science & technology* 9(2), pp. 55-55. doi: 10.1167/tvst.9.2.55

Murtagh, P., Greene, G. and O'Brien, C. 2020. Current applications of machine learning in the screening and diagnosis of glaucoma: a systematic review and Meta-analysis. *International journal of ophthalmology* 13(1), pp. 149-162. doi: 10.18240/ijo.2020.01.22

Nadal-Nicolás, F.M., Sobrado-Calvo, P., Jiménez-López, M., Vidal-Sanz, M. and Agudo-Barriuso, M. 2015. Long-Term Effect of Optic Nerve Axotomy on the Retinal Ganglion Cell Layer. *Investigative Ophthalmology & Visual Science* 56(10), pp. 6095-6112. doi: 10.1167/iovs.15-17195

Nafar, Z., Wen, R., Guan, Z., Li, Y. and Jiao, S. 2020. Quantifying lipofuscin in retinal pigment epithelium in vivo by visible-light optical coherence tomography-based multimodal imaging. *Scientific Reports* 10(1), p. 2942. doi: 10.1038/s41598-020-59951-y

Neves, A.C., Chiquita, S., Carecho, R., Campos, E. Moreira, P. Baptista, F. and Ambrósio, F. 2017. Alzheimer's disease: can the retina be a window to the brain? *Acta Ophthalmologica* 95, p. 259. doi: 10.1111/j.1755-3768.2017.01564

Ni Ni, S., Tian, J., Marziliano, P. and Wong, H.-T. 2014. Anterior Chamber Angle Shape Analysis and Classification of Glaucoma in SS-OCT Images. *Journal of Ophthalmology* 2014, p. 12. doi: 10.1155/2014/942367

Nickells, R.W. 1999. Apoptosis of Retinal Ganglion Cells in Glaucoma: An Update of the Molecular Pathways Involved in Cell Death. *Survey of Ophthalmology* 43, pp. S151-S161. doi: 10.1016/S0039-6257(99)00029-6

Nilforushan, N., Yadgari, M. and Jazayeri, A. 2016. Comparison between visual field defect in pigmentary glaucoma and primary open-angle glaucoma. *International Ophthalmology* 36(5), pp. 637-642. doi: 10.1007/s10792-016-0173-z

Obulesu, M. and Lakshmi, M.J. 2014. Apoptosis in Alzheimer's Disease: An Understanding of the Physiology, Pathology and Therapeutic Avenues. *Neurochemical Research* 39(12), pp. 2301-2312. doi: 10.1007/s11064-014-1454-4

Ojala, T., Pietikainen, M. and Maenpaa, T. (2002). Multiresolution gray-scale and rotation invariant texture classification with local binary patterns. *IEEE Transactions on Pattern Analysis and Machine Intelligence* 24(7), pp. 971-987. doi: 10.1109/TPAMI.2002.1017623

Okamoto, K. and Shaw, J.M. 2005. Mitochondrial Morphology and Dynamics in Yeast and Multicellular Eukaryotes. *Annual Review of Genetics* 39(1), pp. 503-536. doi: 10.1146/annurev.genet.38.072902.093019

Okisaka, S., Murakami, A., Mizukawa, A. and Ito, J. 1997. Apoptosis in retinal ganglion cell decrease in human glaucomatous eyes. *Japanese Journal of Ophthalmology* 41(2), pp. 84-88. doi: 10.1016/s0021-5155(97)00013-0

Osborne, N.N., Melena, J., Chidlow, G. and Wood, J.P. 2001. A hypothesis to explain ganglion cell death caused by vascular insults at the optic nerve head: possible implication for the treatment of glaucoma. *British Journal of Ophthalmology* 85(10), p. 1252. doi: 10.1136/bjo.85.10.1252

Ozawa, Y., Kurihara, T., Sasaki, M., Ban, N., Yuki, K., Kubota, S. and Tsubota, K. 2011. Neural Degeneration in the Retina of the Streptozotocin-Induced Type 1 Diabetes Model. *Experimental Diabetes Research* 2011, p. 108328. doi: 10.1155/2011/108328

Paavo, M., Lee, W., Merriam, J., Bearely, S., Tsang, S., Chang, S. and Sparrow, J.R. 2017. Intraretinal Correlates of Reticular Pseudodrusen Revealed by Autofluorescence and En Face OCT. *Investigative ophthalmology & visual science* 58(11), pp. 4769-4777. doi: 10.1167/iovs.17-22338

Pan, Y., Birngruber, R., Rosperich, J. and Engelhardt, R. 1995. Low-coherence optical tomography in turbid tissue: theoretical analysis. *Applied Optics* 34(28), pp. 6564-6574. doi: 10.1364/AO.34.006564

Pascale, A., Dragob, F. and Govonia, S. 2012. Protecting the retinal neurons from glaucoma: Lowering ocular pressure is not enough. *Pharmacological Research* 66(1), pp. 19-32. doi: 10.1016/j.phrs.2012.03.002

Pasternack, R.M., Zheng, J.-Y. and Boustany, N.N. 2010. Optical scatter changes at the onset of apoptosis are spatially associated with mitochondria. *Journal of Biomedical Optics* 15(4), p. 040504. doi: 10.1117/1.3467501

Pasternack, R.M., Zheng, J.-Y. and Boustany, N.N. 2011. Detection of mitochondrial fission with orientation-dependent optical Fourier filters. *Cytometry Part A* 79A(2), pp. 137-148. doi: 10.1002/cyto.a.21011

Pellegrino de Iraldi, A. and Jaim Etcheverry, G. 1967. Granulated vesicles in retinal synapses and neurons. *Zeitschrift für Zellforschung und Mikroskopische Anatomie* 81(2), pp. 283-296. doi: 10.1007/bf02075974

Peng, S., Rahner, C. and Rizzolo, L.J. 2003. Apical and Basal Regulation of the Permeability of the Retinal Pigment Epithelium. *Investigative Ophthalmology & Visual Science* 44(2), pp. 808-817. doi: 10.1167/iovs.02-0473

Pentland, A.P. 1984. Fractal-Based Description of Natural Scenes. *IEEE Transactions on Pattern Analysis and Machine Intelligence* 6(6), pp. 661-674. doi: 10.1109/TPAMI.1984.4767591

Perfettini, J.-L., Roumier, T. and Kroemer, G. 2005. Mitochondrial fusion and fission in the control of apoptosis. *Trends in Cell Biology* 15(4), pp. 179-183. doi: 10.1016/j.tcb.2005.02.005

Perry, V.H. and Cowey, A. 1985. The ganglion cell and cone distributions in the monkey's retina: Implications for central magnification factors. *Vision Research* 25(12), pp. 1795-1810. doi: 10.1016/0042-6989(85)90004-5

Peña, F., Gutiérrez-Lerma, A., Quiroz-Baez, R. and Arias, C. 2006. The role of beta-amyloid protein in synaptic function: implications for Alzheimer's disease therapy. *Current neuropharmacology* 4(2), pp. 149-163. doi: 10.2174/157015906776359531

Pietikainen, M. K. 2000. *Texture Analysis in Machine Vision*. Singapore: World Scientific Publishing Co., Inc. doi: 10.1142/4483

Podda, B. and Giachetti, A. eds. (2005). *Texture Analysis of CT Images for Vascular Segmentation: A Revised Run Length Approach*. Berlin, Heidelberg: Springer Berlin Heidelberg. doi: 10.1007/11553595_111

Prieto, P.M., McLellan, J.S., Burns, S.A. 2005. Investigating the light absorption in a single pass through the photoreceptor layer by means of the lipofuscin fluorescence. *Vision research* 45(15), pp. 1957-1965. doi: 10.1016/j.visres.2005.01.023

Prilloff, S., Fan, J., Henrich-Noack, P. and Sabel, B.A. 2010. In vivo confocal neuroimaging (ICON): non-invasive, functional imaging of the mammalian CNS with cellular resolution. *European Journal of Neuroscience* 31(3), pp. 521-528. doi: 10.1111/j.1460-9568.2010.07078.x

Prince, M.J. 2015. Wimo, A., Guerchet, M.M., Ali, G.C., Wu, Y.-T. and Prina, M. 2015. World Alzheimer Report 2015 - The Global Impact of Dementia: An analysis of prevalence, incidence, cost and trends. *Alzheimer's Disease International*, London. url: <http://www.alz.co.uk/research/world-report-2015>

Prum, B.E., Herndon Jr, L.W., Moroi, S.E., Mansberger, S.L., Stein, J.D., Lim, M.C., Rosenberg, L.F., Gedde, S.J. and Williams, R.D. 2016a. Primary Angle Closure Preferred Practice Pattern® Guidelines. *Ophthalmology* 123(1), pp. P1-P40. doi: <https://doi.org/10.1016/j.ophtha.2015.10.049>

Prum, B.E., Rosenberg, L.F., Gedde, S.J., Mansberger, S.L., Stein, J.D., Moroi, S.E., Herndon Jr, L.W., Lim, M.C. and Williams, R.D. 2016b. Primary Open-Angle Glaucoma Preferred Practice Pattern® Guidelines. *Ophthalmology* 123(1), pp. P41-P111. doi: <https://doi.org/10.1016/j.ophtha.2015.10.053>

Pudil, P., Ferri, F.J., Novovicova, J. and Kittler, J. 1994. Floating search methods for feature selection with nonmonotonic criterion functions. *Proceedings of the 12th IAPR International Conference on Pattern Recognition*, Vol. 3 - Conference C: Signal Processing (Cat. No.94CH3440-5), 9-13 October 1994, pp. 279-283. doi: 10.1109/ICPR.1994.576920

Purnyn, H. 2013. The Mammalian Retina: Structure and Blood Supply. *Neurophysiology* 45(3), pp. 266-276. doi: 10.1007/s11062-013-9365-6

Qiao, X. and Chen, Y.-W. 2011. A Statistical Texture Model of the Liver Based on Generalized N-Dimensional Principal Component Analysis (GND-PCA) and 3D Shape Normalization. *International Journal of Biomedical Imaging* 2011, p. 8. doi: 10.1155/2011/601672

Quigley, H.A. 1993. Open-Angle Glaucoma. *New England Journal of Medicine* 328(15), pp. 1097-1106. doi: 10.1056/nejm199304153281507

Quigley, H.A. 1996. Number of people with glaucoma worldwide. *British Journal of Ophthalmology* 80(5), pp. 389-393. doi: 10.1136/bjo.80.5.389

Quigley, H.A. 2011. Glaucoma. *The Lancet* 377(9774), pp. 1367-1377. doi: 10.1016/S0140-6736(10)61423-7

Quigley, H.A. and Broman, A.T. 2006. The number of people with glaucoma worldwide in 2010 and 2020. *British Journal of Ophthalmology* 90(3), p. 262. doi: 10.1136/bjo.2005.081224

Quigley, H.A., Dunkelberger, G.R. and Green, W.R. 1989. Retinal Ganglion Cell Atrophy Correlated with Automated Perimetry in Human Eyes with Glaucoma. *American Journal of Ophthalmology* 107(5), pp. 453-464. doi: 10.1016/0002-9394(89)90488-1

Quigley, H.A., Nickells, R.W., Kerrigan, L.A., Pease, M.E., Thibault, D.J. and Zack, D.J. 1995. Retinal ganglion cell death in experimental glaucoma and after axotomy occurs by apoptosis. *Investigative Ophthalmology & Visual Science* 36(5), pp. 774-786. PMID: 7706025

Rabiolo, A., Sacconi, R., Cicinelli, M.V., Querques, L., Bandello, F. and Querques, G. 2017. Spotlight on reticular pseudodrusen. *Clinical ophthalmology* 11, pp. 1707-1718. doi: 10.2147/OPTH.S130165

Radius, R.L. 1981. Regional specificity in anatomy at the lamina cribrosa. *Archives of Ophthalmology* 99(3), pp. 478-480. doi: 10.1001/archopht.1981.03930010480020

Rafelski, S.M. and Marshall, W.F. 2008. Building the cell: design principles of cellular architecture. *Nature Reviews Molecular Cell Biology* 9, p. 593. doi: 10.1038/nrm2460

- Ramola, A., Shakya, A.K. and Van Pham, D. 2020. Study of statistical methods for texture analysis and their modern evolutions. *Engineering Reports* 2(4), p. e12149. doi: 10.1002/eng2.12149
- Rapantzikos, K., Zervakis, M. and Balas, K. 2003. Detection and segmentation of drusen deposits on human retina: Potential in the diagnosis of age-related macular degeneration. *Medical Image Analysis* 7(1), pp. 95-108. doi: 10.1016/S1361-8415(02)00093-2
- Ravenscroft, D., Deng, J., Xie, X., Terry, L., Margrain, T.H., North, R.V. and Wood, A. 2017. AMD Classification in Choroidal OCT Using Hierarchical Texton Mining. In: Blanc-Talon, J., Penne, R., Philips, W., Popescu, D. and Scheunders, P. (eds) *Advanced Concepts for Intelligent Vision Systems. ACIVS 2017. Lecture Notes in Computer Science* 10617. Springer, Cham. doi: 10.1007/978-3-319-70353-4_21
- Remé, C.E., Grimm, C., Hafezi, F., Wenzel, A. and Williams, T.P. 2000. Apoptosis in the Retina: The Silent Death of Vision. *Physiology* 15(3), pp. 120-124. doi: 10.1152/physiologyonline.2000.15.3.120
- Riad, R., Jennane, R., Brahim, A., Janvier, T., Toumi, H. and Lespessailles, E. 2018. Texture analysis using complex wavelet decomposition for knee osteoarthritis detection: Data from the osteoarthritis initiative. *Computers & Electrical Engineering* 68, pp. 181-191. doi: 10.1016/j.compeleceng.2018.04.004
- Rossi, E.A., Granger, C.E., Sharma, R., Yang, Q., Saito, K., Schwarz, C., Walters, S., Nozato, K., Zhang, J., Kawakami, T., Fischer, W., Latchney, L.R., Hunter, J.J., Chung, M.M. and Williams, D.R. 2017. Imaging individual neurons in the retinal ganglion cell layer of the living eye. *Proceedings of the National Academy of Sciences* 114(3), p. 586. doi: 10.1073/pnas.1613445114
- Saccà, S.C., Cutolo, C.A., Ferrari, D., Corazza, P. and Traverso, C.E. 2018. The Eye, Oxidative Damage and Polyunsaturated Fatty Acids. *Nutrients* 10(6), p. 668. doi: 10.3390/nu10060668
- Saha, S., Nassisi, M., Wang, M., Lindenberg, S., Kanagasingam, Y., Sadda, S. and Hu, Z.J. 2019. Automated detection and classification of early AMD biomarkers using deep learning. *Scientific Reports* 9(1), p. 10990. doi: 10.1038/s41598-019-47390-3
- Saint-Geniez, M., Kurihara, T., Sekiyama, E., Maldonado, A.E. and D'Amore, P.A. 2009. An essential role for RPE-derived soluble VEGF in the maintenance of the choriocapillaris. *Proceedings of the National Academy of Sciences* 106(44), p. 18751. doi: 10.1073/pnas.0905010106
- Saleh, M., Nagaraju, M. and Porciatti, V. 2007. Longitudinal Evaluation of Retinal Ganglion Cell Function and IOP in the DBA/2J Mouse Model of Glaucoma. *Investigative Ophthalmology & Visual Science* 48(10), pp. 4564-4572. doi: 10.1167/iovs.07-0483

Schmitt, J.M. 1999. Optical coherence tomography (OCT): a review. *IEEE Journal of Selected Topics in Quantum Electronics* 5(4), pp. 1205-1215. doi: 10.1109/2944.796348

Schmitt, J.M., Knüttel, A., Yadlowsky, M. and Eckhaus, M.A. 1994. Optical-coherence tomography of a dense tissue: statistics of attenuation and backscattering. *Physics in Medicine & Biology* 39(10), p. 1705. doi: 10.1088/0031-9155/39/10/013.

Schmitt, J.M., Xiang, S.H. and Yung, K.M. 1999. Speckle in optical coherence tomography. *Journal of Biomedical Optics* 4(1), pp. 95-105. doi: 10.1117/1.429925

Schultze, M. 1866. Zur Anatomie und Physiologie der Retina. *Archiv für mikroskopische Anatomie* 2(1), pp. 175-286. doi: 10.1007/bf02962033

Schuman, J.S., Hee, M.R., Arya, A.V., Pedut-Kloizman, T., Puliafito, C.A., Fujimoto, J.G. and Swanson, E.A. 1995. Optical coherence tomography: a new tool for glaucoma diagnosis. *Current opinion in ophthalmology* 6(2), pp. 89-95. doi: 10.1097/00055735-199504000-00014

Serrano-Pozo, A., Frosch, M.O., Masliah, E. and Hyman, B.T. 2011. Neuropathological alterations in Alzheimer disease. *Cold Spring Harbor perspectives in medicine* 1(1), pp. a006189-a006189. doi: 10.1101/cshperspect.a006189

Shim, M.S., Takihara, Y., Kim, K.-Y., Iwata, T., Yue, B.Y.J.T., Inatani, M., Weinreb, R.N., Perkins, G.A. and Ju, W.-K. 2016. Mitochondrial pathogenic mechanism and degradation in optineurin E50K mutation-mediated retinal ganglion cell degeneration. *Scientific Reports* 6, p. 33830. doi: 10.1038/srep33830

Shirwany, N.A., Payette, D., Xie, J. and Guo, Q. 2007. The amyloid beta ion channel hypothesis of Alzheimer's disease. *Neuropsychiatric disease and treatment* 3(5), pp. 597-612. PMID: 19300589

Singh, C.B., Choudhary, R., Jayas, D.S. and Paliwal, J. 2008. Wavelet Analysis of Signals in Agriculture and Food Quality Inspection. *Food and Bioprocess Technology* 3(1), p. 2. doi: 10.1007/s11947-008-0093-7

Smerdon, D. 2000. Anatomy of the eye and orbit. *Current Anaesthesia & Critical Care* 11(6), pp. 286-292. doi: 10.1054/cacc.2000.0296

Smith, W., Assink, J., Klein, R., Mitchell, P., Klaver, C.C., Klein, B.E., Hofman, A., Jensen, S., Wang, J.J. and de Jong, P.T. 2001. Risk factors for age-related macular degeneration: Pooled findings from three continents. *Ophthalmology* 108(4), pp. 697-704. doi: 10.1016/S0161-6420(00)00580-7

- Sommer, A., Tielsch, J.M., Katz, J., Quigley, H.A., Gottsch, J.D., Javitt, J. and Singh, K. 1991a. Relationship between intraocular pressure and primary open angle glaucoma among white and black americans: The baltimore eye survey. *Archives of Ophthalmology* 109(8), pp. 1090-1095. doi: 10.1001/archopht.1991.01080080050026
- Sommer, A., Tielsch, J.M., Katz, J., Quigley, H.A., Gottsch, J.D., Javitt, J., Martone, J.F., Royall, R.M., Witt, K.A. and Ezrine, S. 1991b. Racial-differences in the cause-specific prevalence of blindness in east Baltimore. *New England Journal of Medicine* 325(20), pp. 1412-1417. doi: 10.1056/nejm199111143252004
- Spaide, R.F. and Curcio, C.A. 2010. Drusen characterization with multimodal imaging. *Retina* 30(9), pp. 1441-1454. doi: 10.1097/IAE.0b013e3181ee5ce8
- Sparrow, J.R., Hicks, D. and Hamel, C.P. 2010. The retinal pigment epithelium in health and disease. *Current molecular medicine* 10(9), pp. 802-823. doi: 10.2174/156652410793937813
- Stefánsson, E., Geirsdóttir, A. and Sigurdsson, H. 2011. Metabolic physiology in age related macular degeneration. *Progress in Retinal and Eye Research* 30(1), pp. 72-80. doi: 10.1016/j.preteyeres.2010.09.003
- Stehouwer, M., Verbraak, F.D., Schlingemann, R.O. and van Leeuwen, T.G. 2016. Detecting signs of retinal leakage in exudative AMD using Cirrus OCT versus SL SCAN-1, a novel integrated FD-OCT into a common slit lamp. *Graefes Archive for Clinical and Experimental Ophthalmology* 254(1), pp. 37-41. doi: 10.1007/s00417-015-2997-z
- Stone, J. and Johnston, E. 1981. The topography of primate retina: A study of the human, bushbaby, and new- and old-world monkeys. *Journal of Comparative Neurology* 196(2), pp. 205-223. doi:10.1002/cne.901960204
- Stone, J., van Driel, D., Valter, K., Rees, S. and Provis, J. 2008. The locations of mitochondria in mammalian photoreceptors: relation to retinal vasculature. *Brain Research* 1189, pp. 58-69. doi: 10.1016/j.brainres.2007.10.083
- Strauss, O. 2005. The Retinal Pigment Epithelium in Visual Function. *Physiological Reviews* 85(3), pp. 845-881. doi: 10.1152/physrev.00021.2004
- Subrahmanyam, M., Maheshwari, R.P. and Balasubramanian, R. 2012. Expert system design using wavelet and color vocabulary trees for image retrieval. *Expert Systems with Applications* 39(5), p. 5104-5114. doi: 10.1016/j.eswa.2011.11.029
- Suciati, N., Anugrah, A.B., Fatichah, C., Tjandrasa, H., Arifin, A.Z., Purwitasari, D. and Navastara, D.A. 2016. Feature extraction using statistical moments of wavelet transform for iris recognition. *2016 International Conference on Information & Communication Technology and Systems* 12 October 2016, pp. 193-198. doi: 10.1109/ICTS.2016.7910297.

- Sugimoto, K., Murata, H., Hirasawa, H., Aihara, M., Mayama, C. and Asaoka, R. 2013. Cross-sectional study: Does combining optical coherence tomography measurements using the 'Random Forest' decision tree classifier improve the prediction of the presence of perimetric deterioration in glaucoma suspects? *BMJ Open* 3(10), p. e003114. doi: 10.1136/bmjopen-2013-003114
- Sun, M., Zhang, H., Chen, X. and Zhang, Q. 2020. Quantitative Analysis of Macular Retina Using Light Reflection Indices Derived from SD-OCT for Pituitary Adenoma. *Journal of Ophthalmology* 2020, p. 8896114. doi: 10.1155/2020/8896114
- Sun, Y. and Smith, L.E.H. 2018. Retinal Vasculature in Development and Diseases. *Annual review of vision science* 4, pp. 101-122. doi: 10.1146/annurev-vision-091517-034018
- Sung, C.-H. and Chuang, J.-Z. 2010. The cell biology of vision. *The Journal of Cell Biology* 190(6), pp. 953-963. doi: 10.1083/jcb.201006020
- Swanson, E.A., Izatt, J.A., Hee, M.R., Huang, D., Lin, C.P., Schuman, J.S., Puliafito, C.A. and Fujimoto, J.G. 1993. In vivo retinal imaging by optical coherence tomography. *Optics Letters* 18(21), pp. 1864-1866. doi: 10.1364/OL.18.001864
- Tan, O., Chopra, V., Lu, A.T.-H., Schuman, J.S., Ishikawa, H., Wollstein, G., Varma, R. and Huang, D. 2009. Detection of Macular Ganglion Cell Loss in Glaucoma by Fourier-Domain Optical Coherence Tomography. *Ophthalmology* 116(12), pp. 2305-2314.e2302. doi: 10.1016/j.ophtha.2009.05.025
- Tang, J., Oliveros, A. and Jang, M.-H. 2019. Dysfunctional Mitochondrial Bioenergetics and Synaptic Degeneration in Alzheimer Disease. *International Neuropsychology Journal* 23(Suppl 1), pp. S5-10. doi: 10.5213/inj.1938036.018
- Tanna, A.P. 2015. Normal-Tension Glaucoma. In: Shaarawy, T., Sherwood, M., Hitchings, R., Crowston, J. eds. *Glaucoma* (Second Edition). W.B. Saunders, pp. 378-386. doi: 10.1016/B978-0-7020-5193-7.00033-9
- Tapiola, T., Alafuzoff, I., Herukka, S.-K., Parkkinen, L., Hartikainen, P., Soininen, H. and Pirttilä, T. 2009. Cerebrospinal fluid {beta}-amyloid 42 and tau proteins as biomarkers of Alzheimer-type pathologic changes in the brain. *Archives of Neurology* 66(3), pp. 382-389. doi: 10.1001/archneurol.2008.596
- Telegina, D.V., Kozhevnikova O.S. and Kolosova, N.G. 2017. Molecular mechanisms of cell death in retina during development of age-related macular degeneration. *Advances in Gerontology* 7(1), pp. 17-24. doi: 10.1134/S2079057017010155

Terluk, M.R., Kapphahn, R.J., Soukup, L.M., Gong, H., Gallardo, C., Montezuma, S.R. and Ferrington, D.A. 2015. Investigating mitochondria as a target for treating age-related macular degeneration. *The Journal of Neuroscience: the official journal of the Society for Neuroscience* 35(18), pp. 7304-7311. doi: 10.1523/JNEUROSCI.0190-15.2015

Tham, Y.-C., Li, X., Wong, T.Y., Quigley, H.A., Aung, T. and Cheng, C.-Y. 2014. Global Prevalence of Glaucoma and Projections of Glaucoma Burden through 2040: A Systematic Review and Meta-Analysis. *Ophthalmology* 121(11), pp. 2081-2090. doi: 10.1016/j.ophtha.2014.05.013

Thanos, S. 1988. Alterations in the morphology of ganglion cell dendrites in the adult rat retina after optic nerve transection and grafting of peripheral nerve segments. *Cell and Tissue Research* 254(3), pp. 599-609. doi: 10.1007/BF00226510

Theurey, P., Connolly, N.M.C, Fortunati, I., Basso, E., Lauwen, S., Ferrante, C., Pinho, C.M., Joselin, A., Gioran, A., Bano, D., Park, D.S., Ankarcrona, M., Pizzo, P. and Prehn, J.H.M. 2019. Systems biology identifies preserved integrity but impaired metabolism of mitochondria due to a glycolytic defect in Alzheimer's disease neurons. *Aging Cell* 18(3), p. e12924. doi: 10.1111/accel.12924

Thomas, C.N., Berry, M., Logan, A., Blanch, R.J. and Ahmed, Z. 2017. Caspases in retinal ganglion cell death and axon regeneration. *Cell Death Discovery* 3, p. 17032. doi: 10.1038/cddiscovery.2017.32

Tian, H., Li, L. and Song, F. 2017. Study on the deformations of the lamina cribrosa during glaucoma. *Acta Biomaterialia* 55, pp. 340-348. doi: 10.1016/j.actbio.2017.03.028

Ting, D.S.W., Cheung, C.Y.-L., Lim, G., Tan, G.S.W., Quang, N.D., Gan, A., Hamzah, H., Garcia-Franco, R., Yeo, I.Y.S., Lee, S.Y., Wong, E.Y.M., Sabanayagam, C., Baskaran, M., Ibrahim, F., Tan, N.C., Finkelstein, E.A., Lamoureux, E.L., Wong, I.Y., Bressler, N.M., Sivaprasad, S., Varma, R., Jonas, J.B., He, M.G., Cheng, C.-Y., Cheung, G.C.M., Aung, T., Hsu, W., Lee, M.L. and Wong, T.Y. 2017. Development and Validation of a Deep Learning System for Diabetic Retinopathy and Related Eye Diseases Using Retinal Images from Multiethnic Populations with Diabetes. *The Journal of the American Medical Association* 318(22), pp. 2211-2223. doi: 10.1001/jama.2017.18152

Tokarz, P., Kaarniranta, K. and Blasiak, J. 2013. Role of antioxidant enzymes and small molecular weight antioxidants in the pathogenesis of age-related macular degeneration (AMD). *Biogerontology* 14(5), pp. 461-482. doi: 10.1007/s10522-013-9463-2

Toth, C.A., Narayan, D.G., Boppart, S.A., Hee, M.R., Fujimoto, J.G., Birngruber, R., Cain, C.P., DiCarlo, C.D. and Roach, W.P. 1997. A comparison of retinal morphology viewed by optical coherence tomography and by light microscopy. *Archives of Ophthalmology* 115(11), pp. 1425-1428. doi: 10.1001/archopht.1997.01100160595012

Travis, G.H. 1998. Mechanisms of cell death in the inherited retinal degenerations. *American journal of human genetics* 62(3), pp. 503-508. doi: 10.1086/301772

Tribble, J.R., Vasalauskaite, A., Redmond, T., Young, R.D., Hassan, S., Fautsch, M.P., Sengpiel, F., Williams, P.A. and Morgan, J.E. 2019. Midget retinal ganglion cell dendritic and mitochondrial degeneration is an early feature of human glaucoma. *Brain Communications* 1(1), p. fcz035. doi: 10.1093/braincomms/fcz035

Tso, M.O., Zhang, C., Abler, A.S., Chang, C.J., Wong, F., Chang, G.Q. and Lam, T.T. 1994. Apoptosis leads to photoreceptor degeneration in inherited retinal dystrophy of RCS rats. *Investigative Ophthalmology & Visual Science* 35(6), pp. 2693-2699. PMID: 8188463.

Tudor, D., Kajić, V., Rey, S., Erchova, I., Považay, B., Hofer, B., Powell, K.A., Marshall, D., Rosin, P.L., Drexler, W. and Morgan, J.E. 2014. Non-Invasive Detection of Early Retinal Neuronal Degeneration by Ultrahigh Resolution Optical Coherence Tomography. *PLoS ONE* 9(4), p. e93916. doi: 10.1371/journal.pone.0093916

Unterhuber, A., Považay, B., Hermann, B., Sattmann, H., Chavez-Pirson, A. and Drexler, W. 2005. In vivo retinal optical coherence tomography at 1040 nm - enhanced penetration into the choroid. *Optics Express* 13(9), pp. 3252-3258. doi: 10.1364/opex.13.003252

Uttam, S. and Liu, Y. 2015. Fourier phase in Fourier-domain optical coherence tomography. *Journal of the Optical Society of America* 32(12), pp. 2286-2306. doi: 10.1364/JOSAA.32.002286

Vajzovic, L., Hendrickson, A.E., O'Connell, R.V., Clark, L.A., Tran-Viet, D., Possin, D., Chiu, S.J. Farsiu, S. and Toth, C.A. 2012. Maturation of the Human Fovea: Correlation of Spectral-Domain Optical Coherence Tomography Findings with Histology. *American Journal of Ophthalmology* 154(5), pp. 779-789.e772. doi: 10.1016/j.ajo.2012.05.004

van der Meer, F.J., Faber, D.J., Aalders, M.C.G., Poot, A.A., Vermes, I. and van Leeuwen, T.G. 2010. Apoptosis- and necrosis-induced changes in light attenuation measured by optical coherence tomography. *Lasers in Medical Science* 25(2), pp. 259-267. doi: 10.1007/s10103-009-0723-y

van Dijk, H.W., Verbraak, F.D., Kok, P.H.B., Stehouwer, M., Garvin, M.K., Sonka, M., DeVries, J.H., Schlingemann, R.O. and Abràmoff, M.D. 2012. Early Neurodegeneration in the Retina of Type 2 Diabetic Patients. *Investigative Ophthalmology & Visual Science* 53(6), pp. 2715-2719. doi: 10.1167/iovs.11-8997

Velez-Montoya, R., Oliver, S.C.N., Olson, J.L., Fine, S.L., Quiroz-Mercado, H. and Mandava, N. 2014. Current knowledge and trends in age-related macular degeneration: genetics,

epidemiology, and prevention. *Retina* 34(3), pp. 423-441. doi: 10.1097/iae.0000000000000036

Vienola, K.V., Zhang, M., Snyder, V.C., Sahel, J.-A., Dansingani K.K. and Rossi, E.A. 2020. Microstructure of the retinal pigment epithelium near-infrared autofluorescence in healthy young eyes and in patients with AMD. *Scientific Reports* 10(1), p. 9561. doi: 10.1038/s41598-020-66581-x

Vulprecht, L., Gerstenberg C. and Rauh, C. 2020. Refractive index matching (RIM) of liquid and semi-solid materials to acrylic glass for optically measuring the mechanics in soft granular matter. *Granular Matter* 22(2), p. 47. doi: 10.1007/s10035-020-01016-y

Wang, R.K. and Tuchin, V.V. 2013. Optical Coherence Tomography: Light Scattering and Imaging Enhancement. In: Tuchin, V.V. ed. *Handbook of Coherent-Domain Optical Methods: Biomedical Diagnostics, Environmental Monitoring, and Materials Science*. New York, NY: Springer New York, pp. 665-742. doi: 10.1007/978-1-4614-5176-1_16

Wang, Y., Shen, D., Wang, V.M., Yu, C.-R., Wang, R.-X., Tuo, J. and Chan, C.-C. 2012. Enhanced apoptosis in retinal pigment epithelium under inflammatory stimuli and oxidative stress. *Apoptosis: an international journal on programmed cell death* 17(11), pp. 1144-1155. doi: 10.1007/s10495-012-0750-1

Wang, Z. and Yong, J. 2008. Texture Analysis and Classification with Linear Regression Model Based on Wavelet Transform. *IEEE Transactions on Image Processing* 17(8), pp. 1421-1430. doi: 10.1109/TIP.2008.926150.

Wert, K.J., Lin, J.H. and Tsang, S.H. 2014. General pathophysiology in retinal degeneration. *Developments in ophthalmology* 53, pp. 33-43. doi: 10.1159/000357294

Westwood, D.A. 2009. Visual Pathways for Perception and Action. In: Binder, M.D. et al. eds. *Encyclopedia of Neuroscience*. Berlin, Heidelberg: Springer Berlin Heidelberg, pp. 4324-4327. doi: 10.1007/978-3-540-29678-2_6362

White, T.L., Lewis, P., Hayes, S., Fergusson, J., Bell, J., Farinha, L., White, N.S., Pereira, L.V. and Meek, K.M. 2017. The Structural Role of Elastic Fibers in the Cornea Investigated Using a Mouse Model for Marfan Syndrome Corneal Elastic Fibers in Marfan's Syndrome. *Investigative Ophthalmology & Visual Science* 58(4), pp. 2106-2116. doi: 10.1167/iovs.16-21358

Wiemerslage, L. and Lee, D. 2016. Quantification of Mitochondrial Morphology in Neurites of Dopaminergic Neurons using Multiple Parameters. *Journal of neuroscience methods* 262, pp. 56-65. doi: 10.1016/j.jneumeth.2016.01.008

- Williams, C.S. and Becklund, O.A. 2002. *Introduction to the optical transfer function*. Bellingham, Washington: SPIE Press.
- Williams, P.A., Howell, G.R., Barbay, J.M., Braine, C.E., Sousa, G.L., John, S.W.M. and Morgan, J.E. 2013. Retinal ganglion cell dendritic atrophy in DBA/2J glaucoma. *PLoS ONE* 8(8), p. e72282. doi: 10.1371/journal.pone.0072282
- Williams, P.A., Thirgood, R.A., Oliphant, H., Frizzati, A., Littlewood, E., Votruba, M., Good, M.A., Williams, J. and Morgan, J.E. 2013a. Retinal ganglion cell dendritic degeneration in a mouse model of Alzheimer's disease. *Neurobiology of Aging* 34(7), pp. 1799-1806. doi: 10.1016/j.neurobiolaging.2013.01.006
- Williams, P.A., Tribble, J.R., Pepper, K.W., Cross, S.D., Morgan, B.P., Morgan, J.E., John, S.W.M. and Howell, G.R. 2016. Inhibition of the classical pathway of the complement cascade prevents early dendritic and synaptic degeneration in glaucoma. *Molecular Neurodegeneration* 11(1), p. 26. doi: 10.1186/s13024-016-0091-6
- Williams, P.A., Harder, J.M., Foxworth, N.E., Cochran, K.E., Philip, V.M., Porciatti, V., Smithies, O. and John, S.W.M. 2017. Vitamin B(3) modulates mitochondrial vulnerability and prevents glaucoma in aged mice. *Science* 355(6326), pp. 756-760. doi: 10.1126/science.aal0092
- Workman, M.J., Serov, A., Halevi, B., Atanasov, P. and Artyushkova, K. 2015. Application of the Discrete Wavelet Transform to SEM and AFM Micrographs for Quantitative Analysis of Complex Surfaces. *Langmuir* 31(17), pp. 4924-4933. doi: 10.1021/acs.langmuir.5b00292
- Wright, C., Tawfik, M.A., Waisbourd, M. and Katz, L.J. 2016. Primary angle-closure glaucoma: an update. *Acta Ophthalmologica* 94(3), pp. 217-225. doi: doi:10.1111/aos.12784
- Wu, W.-J., Lina, S.-W. and Moon, W.K. 2012. Combining support vector machine with genetic algorithm to classify ultrasound breast tumor images. *Computerized Medical Imaging and Graphics* 36(8), pp. 627-633. doi: 10.1016/j.compmedimag.2012.07.004
- Wässle, H. and Boycott, B.B. 1991. Functional architecture of the mammalian retina. *Physiological Reviews* 71(2), pp. 447-480. doi: 10.1152/physrev.1991.71.2.447
- Xavier, J.M., Rodrigues, C.M.P and Solá, S. 2016. Mitochondria: Major Regulators of Neural Development. *The Neuroscientist* 22(4), pp. 346-358. doi: 10.1177/1073858415585472
- Yadav, A.R., Anand, R.S., Dewal, M.L. and Gupta, S. 2015. Performance Analysis of Discrete Wavelet Transform Based First-order Statistical Texture Features for Hardwood Species Classification. *Procedia Computer Science* 57, p. 214-221. doi: 10.1016/j.procs.2015.07.435

- Yang, X., Zou, H., Jung, G., Richard, G., Linke, S.J., Ader, M. and Bartsch, U. 2013. Nonneuronal control of the differential distribution of myelin along retinal ganglion cell axons in the mouse. *Investigative Ophthalmology & Visual Science* 54(13), pp. 7819-7827. doi: 10.1167/iovs.13-12596
- Yap, T.E., Donna, P., Almonte, M.T. and Cordeiro, M.F. 2018. Real-Time Imaging of Retinal Ganglion Cell Apoptosis. *Cells* 7(6), p. 60. doi: 10.3390/cells7060060
- Yasaka, K., Akai, H., Mackin, D., Court, L., Moros, E., Ohtomo, K. and Kiryu, S. 2017. Precision of quantitative computed tomography texture analysis using image filtering: A phantom study for scanner variability. *Medicine* 96(21), p. e6993. doi: 10.1097/md.0000000000006993
- Yeo, N.J.Y., Chan, E.J.J. and Cheung, C. 2019. Choroidal Neovascularization: Mechanisms of Endothelial Dysfunction. *Frontiers in pharmacology* 10, pp. 1363-1363. doi: 10.3389/fphar.2019.01363
- Yi, J., Puyang, Z., Feng, L., Duan, L., Liang, P., Backman, V., Liu, X. and Zhang, H.F. 2016. Optical Detection of Early Damage in Retinal Ganglion Cells in a Mouse Model of Partial Optic Nerve Crush Injury. *Investigative Ophthalmology & Visual Science* 57(13), pp. 5665-5671. doi: 10.1167/iovs.16-19955
- Yip, J.L. and Foster, P.J. 2006. Ethnic differences in primary angle-closure glaucoma. *Current Opinion in Ophthalmology* 17(2), pp. 175-180. doi: 10.1097/01.icu.0000193078.47616.aa
- Yogesana, K., Jørgensen, T., Albrechtsen, F., Tveter, K.J. and Danielsen, H.E. 1996. Entropy-based texture analysis of chromatin structure in advanced prostate cancer. *Cytometry* 24(3), p. 268-276. doi: 10.1002/(SICI)1097-0320(19960701)24:3<268::AID-CYTO10>3.0.CO;2-O
- Youle, R.J. and Karbowski, M. 2005. Mitochondrial fission in apoptosis. *Nature Reviews Molecular Cell Biology* 6, p. 657. doi: 10.1038/nrm1697
- Young, R.W. 1967. The renewal of photoreceptor cell outer segments. *The Journal of cell biology* 33(1), pp. 61-72. doi: 10.1083/jcb.33.1.61
- Zeimer, R.C. and Ogura, Y. 1989. The relation between glaucomatous damage and optic nerve head mechanical compliance. *Archives of Ophthalmology* 107(8), pp. 1232-1234. doi: 10.1001/archophth.1989.01070020298042
- Zhang, L., Lee, K., Niemeijer, M., Mullins, R.F., Sonka, M. and Abramoff, M.D. 2012. Automated segmentation of the choroid from clinical SD-OCT. *Investigative Ophthalmology & Visual Science* 53(12), pp. 7510-7519. doi: 10.1167/iovs.12-10311

Zhang, L.-Q., Cui, H., Yu, Y.-B., Shi, H.-Q., Zhou, Y. and Liu, M.-J. 2019. MicroRNA-141-3p inhibits retinal neovascularization and retinal ganglion cell apoptosis in glaucoma mice through the inactivation of Docking protein 5-dependent mitogen-activated protein kinase signaling pathway. *Journal of Cellular Physiology* 234(6), pp. 8873-8887. doi: 10.1002/jcp.27549

Zhongyang, S. and Yankui, S. 2019. Automatic detection of retinal regions using fully convolutional networks for diagnosis of abnormal maculae in optical coherence tomography images. *Journal of Biomedical Optics* 24(5), pp. 1-9. doi: 10.1117/1.JBO.24.5.056003

Zorov, D.B., Juhaszova, M. and Sollott, S.J. 2014. Mitochondrial reactive oxygen species (ROS) and ROS-induced ROS release. *Physiological reviews* 94(3), pp. 909-950. doi: 10.1152/physrev.00026.2013

Zweifel, S.A., Imamura, Y., Spaide, T.C., Fujiwara, T. and Spaide, R.F. 2010. Prevalence and Significance of Subretinal Drusenoid Deposits (Reticular Pseudodrusen) in Age-Related Macular Degeneration. *Ophthalmology* 117(9), pp. 1775-1781. doi: 10.1016/j.ophtha.2010.01.027

Appendices

Appendix 1. Programming scripts and functions

Find all features features

```
function features = findAllfeatures(cubeImg, bitsperpixel,  
mask, listfeature)  
addpath(genpath(' ./ '));
```

```
if (nargin<3) || (isempty(mask))  
    mask = ones(size(cubeImg));  
end
```

```
if nargin<4  
    listfeature = 1:6; %listfeature = [1 2 5];  
end
```

```
if sum(size(cubeImg)==1)>0  
    addMat = (size(cubeImg)==1)*2 + 1;  
    cubeImg = repmat(cubeImg, addMat);  
end
```

```
% -----  
-----
```

```
% I. Intensity level distribution
```

```
% -----  
-----
```

```
if sum(listfeature==1)
```

```
    % 1) mean
```

```
    meanCube = mean(cubeImg(mask(:)>0));
```

```
    % 2) variance
```

```
    varCube = var(cubeImg(mask(:)>0));
```

```
    % 3) skewness
```

```
    skewCube = skewness(cubeImg(mask(:)>0));
```

```
    % 4) kurtosis
```

```
    kurtCube = kurtosis(cubeImg(mask(:)>0));
```

```
    % 5) entropy
```

```
%    entropyCube = entropy(cubeImg(mask(:)>0));
```

```
else
```

```
    meanCube = [];
```

```
    varCube = [];
```

```
    skewCube = [];
```

```
    kurtCube = [];
```

```
    entropyCube = [];
```

```
end
```

```
% -----  
-----
```

```
% II. Run length measures
```



```

% -----
% -----
if sum(listfeature==2)

    % 1) Short Run Emphasis (SRE)
    % 2) Long Run Emphasis (LRE)
    % 3) Gray-Level Nonuniformity (GLN)
    % 4) Run Length Nonuniformity (RLN)
    % 5) Run Percentage (RP)
    % 6) Low Gray-Level Run Emphasis (LGRE)
    % 7) High Gray-Level Run Emphasis (HGRE)
    % 8) Short Run Low Gray-Level Emphasis (SRLGE)
    % 9) Short Run High Gray-Level Emphasis (SRHGE)
    % 10) Long Run Low Gray-Level Emphasis (LRLGE)
    % 11) Long Run High Gray-Level Emphasis (LRHGE)
    % runLengthStat = findRunLengthProp(cubeImg, bitsperpixel);
else
    runLengthStat = [];
end

% -----
% -----
% III. Co-occurrence matrix
% -----
% -----
if sum(listfeature==3)

    % 1) angular second moment or energy
    % 2) correlation
    % 3) contrast or inertia
    % 4) entropy
    % 5) Cluster Shade
    % 6) inverse difference moment
    % 7) Stat = [];
    glcmStat = findGLCMPProp(cubeImg);
else
    glcmStat = [];
end

% -----
% -----
% IV. Wavelet transform
% -----
% -----
if sum(listfeature==4)

    % 1) mean and variance (2 levels)
    % 2) kurtosis measures (2 levels)
    % 3) fractal dimension

```

```

%      [cwtParameters,cwtglcmStat,cwtrunLengthStat] =
findCWTProp(cubeImg, 2, bitsperpixel, 1);
else
    cwtParameters = [];
    cwtglcmStat = [];
    cwtrunLengthStat = [];
end

% -----
% -----
% V. Local Binary Pattern Histogram
% -----
% -----
if sum(listfeature==5)
    LBPhist = findLBPhist(cubeImg);
else
    LBPhist = [];
end

% -----
% -----
% VI. Granulometry
% -----
% -----
if sum(listfeature==6)
%     Granhist = findGranulometry(cubeImg);
else
    Granhist = [];
end

% -----
% -----
% All features;
% -----
% -----
features = [meanCube varCube skewCube kurtCube entropyCube
runLengthStat glcmStat cwtParameters cwtglcmStat
cwtrunLengthStat LBPhist Granhist];
%features = [LBPhist];

```

GLCM features

```
function glcmStat = findGLCMProp(cubeImg)

% 1) angular second moment or energy
energyCube = [];
% 2) correlation
correlateCube = [];
% 3) contrast or inertia
contrastCube = [];
% 4) entropy
entropyCube = [];
% 5) Cluster Shade
clusterCube = [];
% 6) inverse difference moment
invertDiffMomentCube = [];
% 7) Homogeneity
homoCube = [];

for k = 1:size(cubeImg,3)
    glcm = graycomatrix(cubeImg(:,:,k), 'Offset', [0 1;-1 1;-1
0;-1 -1]);
    out = GLCM_Features1(glcm);
    energyCube = [energyCube out.energ];
    correlateCube = [correlateCube out.corrm];
    contrastCube = [contrastCube out.contr];
    entropyCube = [entropyCube out.entro];
    clusterCube = [clusterCube out.cshad];
    invertDiffMomentCube = [invertDiffMomentCube out.idmnc];
    homoCube = [homoCube out.homom];
end
reCubeImg = permute(cubeImg, [1 3 2]);
for k = 1:size(reCubeImg,3)
    glcm = graycomatrix(reCubeImg(:,:,k), 'Offset', [0 1;-1 1;-1
0;-1 -1]);
    out = GLCM_Features1(glcm);
    energyCube = [energyCube out.energ];
    correlateCube = [correlateCube out.corrm];
    contrastCube = [contrastCube out.contr];
    entropyCube = [entropyCube out.entro];
    clusterCube = [clusterCube out.cshad];
    invertDiffMomentCube = [invertDiffMomentCube out.idmnc];
    homoCube = [homoCube out.homom];
end
reCubeImg = permute(cubeImg, [3 2 1]);
for k = 1:size(reCubeImg,3)
    glcm = graycomatrix(reCubeImg(:,:,k), 'Offset', [0 1;-1 1;-1
0;-1 -1]);
    out = GLCM_Features1(glcm);
    energyCube = [energyCube out.energ];
    correlateCube = [correlateCube out.corrm];
```

```

        contrastCube = [contrastCube out.contr];
        entropyCube = [entropyCube out.entro];
        clusterCube = [clusterCube out.cshad];
        invertDiffMomentCube = [invertDiffMomentCube out.idmnc];
        homoCube = [homoCube out.homom];
end

energyCube(isnan(energyCube)) = [];
correlateCube(isnan(correlateCube)) = [];
contrastCube(isnan(contrastCube)) = [];
entropyCube(isnan(entropyCube)) = [];
clusterCube(isnan(clusterCube)) = [];
invertDiffMomentCube(isnan(invertDiffMomentCube)) = [];
homoCube(isnan(homoCube)) = [];

energyCube = mean(energyCube);
correlateCube = mean(correlateCube);
contrastCube = mean(contrastCube);
entropyCube = mean(entropyCube);
clusterCube = mean(clusterCube);
invertDiffMomentCube = mean(invertDiffMomentCube);
homoCube = mean(homoCube);

% out put
glcmStat = [energyCube correlateCube contrastCube entropyCube
clusterCube invertDiffMomentCube homoCube];

```

LBP features

```
function LBPhist = findLBPhist(cubeImg)

% if cubeImg contains zeros
if sum(cubeImg(:)==0)
    for k = 1:size(cubeImg,2)
        curLine = cubeImg(:,k,:);
        ind = curLine(:,1,1)==0;
        if (ind(1)==1)
            [~,lastindx] = max(ind(1:end-1)-ind(2:end));
            getind = min(length(ind),lastindx + (lastindx:-
1:1));
            cubeImg(1:lastindx,k,:) = curLine(getind,:,:) ;
        end
        if (ind(end)==1)
            [~,firstinx] = max(ind(end:-1:2)-ind(end-1:-
1:1));
            getind = max(1,length(ind)-firstinx:-
1:length(ind)-2*firstinx+1);
            cubeImg(end-firstinx+1:end,k,:) =
curLine(getind,:,:) ;
        end
        % double check
        curLine = cubeImg(:,k,:);
        ind = curLine(:,1,1)==0;
        if (ind(1)==1)
            [~,lastindx] = max(ind(1:end-1)-ind(2:end));
            getind = min(length(ind),lastindx + (lastindx:-
1:1));
            cubeImg(1:lastindx,k,:) = curLine(getind,:,:) ;
        end
        if (ind(end)==1)
            [~,firstinx] = max(ind(end:-1:2)-ind(end-1:-
1:1));
            getind = max(1,length(ind)-firstinx:-
1:length(ind)-2*firstinx+1);
            cubeImg(end-firstinx+1:end,k,:) =
curLine(getind,:,:) ;
        end
    end
end

LBPhist = zeros(1,59);
for k = 1:size(cubeImg,3)
    I = cubeImg(:,:,k);
    LBPhist = LBPhist + extractLBPFeatures(I);
end
LBPhist = LBPhist/numel(cubeImg);
```

Textural feature extraction

```
forflattedimage = 1;

mainfolder = 'C:\Users\mukhi\Desktop\Code_OCT_UoB\';
files = dir([mainfolder, '*.tif']);

mainfoldercube = 'C:\Users\mukhi\Desktop\Code_OCT_UoB\';
% if forflattedimage
    subfolderF = 'flat\';
% else
    subfolder = 'non flat\';
% end
channel1 = ddeinit('excel','original' );
channel2 = ddeinit('excel','despeck' );
channel3 = ddeinit('excel','enhance' );
channel1F = ddeinit('excel','original_flatten' );
channel2F = ddeinit('excel','despeck_flatten' );
channel3F = ddeinit('excel','enhance_flatten' );

diseaseIndex = [1 2 3 8 9 10 14 15 19 20];
controlIndx = [4 5 6 7 11 12 13 16 17 18 21 22 23 24];
row = 1931;
% for fnum = 24:[controlIndx diseaseIndex ]
%
%      % -----
%      % input name
%      % -----
%      fname = [mainfolder,files(fnum).name];
%      if forflattedimage == 0
%      flat = '';
%      else
%      flat = '_flatten2';
%      end
%      % -----
%      % output name
%      % -----
%      flat = '_flatten2';
%      opNameEnhanceF = [files(fnum).name(1:end-
4),flat,'_Enhance_cube2'];
%      opNameOriginalF = [files(fnum).name(1:end-
4),flat,'_cube2'];
%      opNameDespeckF = [files(fnum).name(1:end-
4),flat,'_despeck_cube2'];
%      opNameEnhance = [files(fnum).name(1:end-
4),'_Enhance_cube2'];
```

```

%      opNameOriginal = [files(fnum).name(1:end-4), '_cube2'];
%      opNameDespeck = [files(fnum).name(1:end-
4), '_despeck_cube2'];
%
%      for rad = [1.5 2.5]%1:3
%          for k = 1:(rad*8)
%
%              % original image non flat
%
load([mainfoldercube, subfolder, 'original\', opNameOriginal, '_',
num2str(rad), '_', num2str(k), '.mat']);
%          cubeImg = cubeImg/(2^16);
%          if ~isempty(cubeImg)
%              features = findAllfeatures(cubeImg, 16,
cubeImg>0);
%              rc = ddepoke(channel1,
['r', num2str(row), 'c1'],
[opNameOriginal, '_', num2str(rad), '_', num2str(k)]);
%              rc = ddepoke(channel1,
['r', num2str(row), 'c2:c', num2str(length(features)+1)],
features);
%
%              % despeck image
%
load([mainfoldercube, subfolder, 'despeck\', opNameDespeck, '_', nu
m2str(rad), '_', num2str(k), '.mat']);
%          cubeImg = cubeImg/(2^16);
%          features = findAllfeatures(cubeImg, 16,
cubeImg>0);
%          rc = ddepoke(channel2,
['r', num2str(row), 'c1'],
[opNameDespeck, '_', num2str(rad), '_', num2str(k)]);
%          rc = ddepoke(channel2,
['r', num2str(row), 'c2:c', num2str(length(features)+1)],
features);
%
%          % despeck image
%
load([mainfoldercube, subfolder, 'enhance\', opNameEnhance, '_', nu
m2str(rad), '_', num2str(k), '.mat']);
%          cubeImg = cubeImg/(2^16);
%          features = findAllfeatures(cubeImg, 16,
cubeImg>0);
%          rc = ddepoke(channel3,
['r', num2str(row), 'c1'],
[opNameEnhance, '_', num2str(rad), '_', num2str(k)]);
%          rc = ddepoke(channel3,
['r', num2str(row), 'c2:c', num2str(length(features)+1)],
features);
%
%          % flatted image

```

```

% ----- % -----
% -----
%
load([mainfoldercube,subfolderF,'original\','opNameOriginalF','_','num2str(rad),'_',num2str(k),'.mat']);
%         cubeImg = cubeImg/(2^16);
%         features = findAllfeatures(cubeImg, 16,
ones(size(cubeImg)));
%         rc = ddepoke(channel1F,
['r',num2str(row),'c1'],
[opNameOriginalF,'_',num2str(rad),'_',num2str(k)]);
%         rc = ddepoke(channel1F,
['r',num2str(row),'c2:c',num2str(length(features)+1)],
features);
%
%         % despeck image
%
load([mainfoldercube,subfolderF,'despeck\','opNameDespeckF','_',
num2str(rad),'_',num2str(k),'.mat']);
%         cubeImg = cubeImg/(2^16);
%         features = findAllfeatures(cubeImg, 16,
ones(size(cubeImg)));
%         rc = ddepoke(channel2F,
['r',num2str(row),'c1'],
[opNameDespeckF,'_',num2str(rad),'_',num2str(k)]);
%         rc = ddepoke(channel2F,
['r',num2str(row),'c2:c',num2str(length(features)+1)],
features);
%
%         % despeck image
%
load([mainfoldercube,subfolderF,'enhance\','opNameEnhanceF','_',
num2str(rad),'_',num2str(k),'.mat']);
%         cubeImg = cubeImg/(2^16);
%         features = findAllfeatures(cubeImg, 16,
ones(size(cubeImg)));
%         rc = ddepoke(channel3F,
['r',num2str(row),'c1'],
[opNameEnhanceF,'_',num2str(rad),'_',num2str(k)]);
%         rc = ddepoke(channel3F,
['r',num2str(row),'c2:c',num2str(length(features)+1)],
features);
%         end
%
%         row = row + 1;
%     end
% end

row = row+2;
for fnum = 9:24%[controlIndx diseaseIndex ]

```



```

% -----
% input name
% -----
fname = [mainfolder,files(fnum).name];
% if forflattedimage == 0
%     flat = '';
% else
%     flat = '_flatten2';
% end
% -----
% output name
% -----
flat = '_flatten2';
opNameEnhanceF = [files(fnum).name(1:end-
4),flat,'_Enhance_cube2_60'];
opNameOriginalF = [files(fnum).name(1:end-
4),flat,'_cube2_60'];
opNameDespeckF = [files(fnum).name(1:end-
4),flat,'_despeck_cube2_60'];
opNameEnhance = [files(fnum).name(1:end-
4),'_Enhance_cube2_60'];
opNameOriginal = [files(fnum).name(1:end-4),'_cube2_60'];
opNameDespeck = [files(fnum).name(1:end-
4),'_despeck_cube2_60'];

for rad = [1.5 2.5 3.5]%1:3
    for k = 1:((rad-0.5)*8)

        % original image non flat

load([mainfoldercube,subfolder,'original\ ',opNameOriginal,'_',
num2str(rad),'_',num2str(k),'.mat']);
cubeImg = cubeImg/(2^16);
if ~isempty(cubeImg)
    features = findAllfeatures(cubeImg, 16,
cubeImg>0);
    rc = ddepoke(channel1,
['r',num2str(row),'c1'],
[opNameOriginal,'_',num2str(rad),'_',num2str(k)]);
    rc = ddepoke(channel1,
['r',num2str(row),'c2:c',num2str(length(features)+1)],
features);

    % despeck image

```

```

load([mainfoldercube,subfolder,'despeck\'',opNameDespeck,'_',nu
m2str(rad),'_',num2str(k),'.mat']);
    cubeImg = cubeImg/(2^16);
    features = findAllfeatures(cubeImg, 16,
cubeImg>0);
    rc = ddepoke(channel2,
['r',num2str(row),'c1'],
[opNameDespeck,'_',num2str(rad),'_',num2str(k)]);
    rc = ddepoke(channel2,
['r',num2str(row),'c2:c',num2str(length(features)+1)],
features);

    % despeck image

load([mainfoldercube,subfolder,'enhance\'',opNameEnhance,'_',nu
m2str(rad),'_',num2str(k),'.mat']);
    cubeImg = cubeImg/(2^16);
    features = findAllfeatures(cubeImg, 16,
cubeImg>0);
    rc = ddepoke(channel3,
['r',num2str(row),'c1'],
[opNameEnhance,'_',num2str(rad),'_',num2str(k)]);
    rc = ddepoke(channel3,
['r',num2str(row),'c2:c',num2str(length(features)+1)],
features);

    % flatted image
    % -----
-----

load([mainfoldercube,subfolderF,'original\'',opNameOriginalF,'_
',num2str(rad),'_',num2str(k),'.mat']);
    cubeImg = cubeImg/(2^16);
    features = findAllfeatures(cubeImg, 16,
ones(size(cubeImg)));
    rc = ddepoke(channel1F,
['r',num2str(row),'c1'],
[opNameOriginalF,'_',num2str(rad),'_',num2str(k)]);
    rc = ddepoke(channel1F,
['r',num2str(row),'c2:c',num2str(length(features)+1)],
features);

    % despeck image

load([mainfoldercube,subfolderF,'despeck\'',opNameDespeckF,'_',
num2str(rad),'_',num2str(k),'.mat']);
    cubeImg = cubeImg/(2^16);
    features = findAllfeatures(cubeImg, 16,
ones(size(cubeImg)));

```

```

        rc = ddepoke(channel2F,
['r',num2str(row),'c1'],
[opNameDespeckF,'_',num2str(rad),'_',num2str(k)]);
        rc = ddepoke(channel2F,
['r',num2str(row),'c2:c',num2str(length(features)+1)],
features);

        % despeck image

load([mainfoldercube,subfolderF,'enhance\ ',opNameEnhanceF,'_',
num2str(rad),'_',num2str(k),'.mat']);
        cubeImg = cubeImg/(2^16);
        features = findAllfeatures(cubeImg, 16,
ones(size(cubeImg)));
        rc = ddepoke(channel3F,
['r',num2str(row),'c1'],
[opNameEnhanceF,'_',num2str(rad),'_',num2str(k)]);
        rc = ddepoke(channel3F,
['r',num2str(row),'c2:c',num2str(length(features)+1)],
features);
    end

    row = row + 1;
end
end
end

%% scaling

% data = ddereq(channel3,'r3c128:r1154c148');
% scaling1 = min(data,[],1);
% scaling2 = 1./(max(data,[],1)-min(data,[],1));
% zerosind = (max(data,[],1)==min(data,[],1));
% scaling2(zerosind) = 0;
% data = (data -
repmat(scaling1,size(data,1),1)).*(repmat(scaling2,size(data,1
),1));
% channel1a = ddeinit('excel','enhance_scale');
% rc = ddepoke(channel1a, 'r3c128:r1154c148', data);

```

SVM training

```
clear all

datatype = 2; %1='original_scale', 2='despeck_scale',
3='enhance_scale', 4='original_flatten_scale',
5='despeck_flatten_scale', 6='enhance_flatten_scale'};
numGlaucoma = 10; % number of glaucoma OCT images
numControl = 14; % number of normal OCT images
numPoints1 = 48;
numPoints2 = 32;
numPoints = numPoints1 + numPoints2;
trainingRatio = 1/2;
numIter = 1;% 500;
usePCA = 0;
layerConsider = [1 1 0 0 0]; % RNFL CGG IPL INL OPL
numthickness = sum(layerConsider);

% feature group
rangefeature{1} = 1:147;
rangefeature{2} = 1:5; % intensity level distribution
rangefeature{3} = 6:16; % run length measures
rangefeature{4} = 17:23; % co-occurrence matrix
rangefeature{5} = 24:67; % wavelet
rangefeature{6} = 68:126; % LBP
rangefeature{7} = [127:134 139:142 145:147]; % Granulometry
rangefeature{8} = [rangefeature{5} rangefeature{6}]; % wavelet
+ LBP
rangefeature{9} = [rangefeature{2} rangefeature{6}]; %
intensity + LBP
rangefeature{10} = [rangefeature{2} rangefeature{5}] ; %
intensity + wavelet
rangefeature{11} = [rangefeature{4} rangefeature{6}]; % co-
occurrence matrix + LBP
rangefeature{12} = [rangefeature{4} rangefeature{5}] ; % co-
occurrence matrix + wavelet
rangefeature{13} = [rangefeature{2} rangefeature{6}
rangefeature{5} ]; % intensity + wavelet + LBP
rangefeature{14} = [rangefeature{4} rangefeature{6}
rangefeature{5} ]; % co-occurrence matrix + wavelet + LBP
rangefeature{15} = [1:134 139:142 145:147];
namefeature{1} = 'layer only';
namefeature{2} = 'intensity level';
namefeature{3} = 'run length';
namefeature{4} = 'co-occurrence';
namefeature{5} = 'wavelet';
namefeature{6} = 'LBP';
namefeature{7} = 'Granulometry';
namefeature{8} = 'wavelet + LBP';
namefeature{9} = 'intensity + LBP';
namefeature{10} = 'intensity + wavelet';
```

```

namefeature{11} = 'co-occurrence + LBP';
namefeature{12} = 'co-occurrence + wavelet';
namefeature{13} = 'intensity + wavelet + LBP';
namefeature{14} = 'co-occurrence + wavelet + LBP';
namefeature{15} = 'all texture';

totalFeatureGroup = length(rangefeature);
totalData = numGlucoma+numControl;
diseaseIndex = [1 2 3 8 9 10 14 15 19 20];
controlIndx = [4 5 6 7 11 12 13 16 17 18 21 22 23 24];
indexRe = [controlIndx diseaseIndex];

load datastoreAdd.mat % There are 6 datatypes, each has
1920 samples, each sample has 147 texture features
load thicknessAllLayer.mat % There are 5 retinal layers
(weight by RNFL) of 24 OCT images, each image has 80 values
%load thickness

results = zeros(480,3);
for it = 1:numIter
    it
    row = 1;

    % create random index for choosing which OCT images will
be used for
    % training and the rest for testing. The selection is done
for glaucoma
    % and normal eye separately so that the training and
testing datasets
    % will have both glaucoma and normal
    numTrainControl = round(trainingRatio*numControl);
    inxControl = [];
    while length(inxControl)<numTrainControl
        moreind = numTrainControl - length(inxControl);
        temp = randi(numControl,1,numTrainControl);
        inxControl = unique([inxControl
temp(1:min(length(temp),moreind))]));
    end
    numTrainControl = length(inxControl);
    numTrainGlucoma = round(trainingRatio*numGlucoma);
    inxGlucoma = [];
    while length(inxGlucoma)<numTrainGlucoma
        moreind = numTrainGlucoma - length(inxGlucoma);
        temp = randi(numGlucoma,1,numTrainGlucoma);
        inxGlucoma = unique([inxGlucoma
temp(1:min(length(temp),moreind))]));
    end
    numTrainGlucoma = length(inxGlucoma);
    numTrain = numTrainControl + numTrainGlucoma;

```

```

% run through different features
% -----
-----
% using weights from RNFL layer or not
for useWeight = [1 0]
    % using thickness of NFL or not
    for NFL = [1 0]
        % using thickness of GCC or not
        for GCC = [1 0]
            % using thickness of IPL or not
            for IPL = [1 0]
                % index all thickest that will be used.
                layerConsider = [NFL GCC IPL 0 0];
                numthickness = sum(layerConsider);
                % should apply PCA or not
                for usePCA = [1 0]
                    % test all combinations of texture
features
                    for featuregroupnum =
1:totalFeatureGroup

                                % read feature values
                                % -----
                                -----
                                % Read texture features
                                data = datastore{datatype};
                                % Select only those we want
                                data =
data(:,rangefeature{featuregroupnum});
                                [~, numFeature] = size(data);
                                % control
                                if numFeature>0
                                    dataTemp =
data(1:numControl*numPoints,:);
                                end
                                dataControl = zeros(numControl,
numFeature + numthickness);
                                for k = 1:numControl
                                    if numFeature>0
                                        if useWeight
                                            wtcurl =
weightbyRNFL{controlIndx(k)};
                                            else
                                                wtcurl =
ones(size(weightbyRNFL{controlIndx(k)}));%
                                            end
                                            wtcurl = repmat(wtcurl',[1
numFeature]);
                                            datacurl = dataTemp((k-
1)*numPoints + (1:numPoints),:);

```

```

                                % reorder samples to match
to the position on RNFL to the weights can be applied
correctly
                                datacur = [datacur(1:8,:);
datacur(49:49+11,:); datacur(9:9+15,:); datacur(61:61+19,:);
datacur(25:25+23,:)];

dataControl(k,1:numFeature) = mean(datacur.*wtcur);
                                end
                                temp =
[mean(thickRNFL{controlIndx(k)})
mean(thickGCC{controlIndx(k)}) ...

mean(thickIPL{controlIndx(k)}) mean(thickINL{controlIndx(k)})
mean(thickOPL{controlIndx(k)})];
                                temp(layerConsider==0) = [];

dataControl(k,numFeature+1:end) = temp;
                                end
                                % glaucoma
                                if numFeature>0
                                dataTemp =
data(numControl*numPoints + (1:numGlaucoma*numPoints),:);
                                end
                                dataGlaucoma = zeros(numGlaucoma,
numFeature+numthickness);
                                for k = 1:numGlaucoma
                                if numFeature>0
                                if useWeight
                                wtcur =
weightbyRNFL{diseaseIndex(k)}; %
                                else
                                wtcur =
ones(size(weightbyRNFL{diseaseIndex(k)})); %
                                end
                                wtcur = repmat(wtcur',[1
numFeature]);
                                datacur = dataTemp((k-
1)*numPoints + (1:numPoints),:);
                                % reorder samples to match
to the position on RNFL to the weights can be applied
correctly
                                datacur = [datacur(1:8,:);
datacur(49:49+11,:); datacur(9:9+15,:); datacur(61:61+19,:);
datacur(25:25+23,:)];

dataGlaucoma(k,1:numFeature) = mean(datacur.*wtcur);
                                end
                                temp =
[mean(thickRNFL{diseaseIndex(k)})
mean(thickGCC{diseaseIndex(k)}) ...

```

```

mean(thickIPL{diseaseIndex(k)})
mean(thickINL{diseaseIndex(k)})
mean(thickOPL{diseaseIndex(k)})];
temp(layerConsider==0) = [];

dataGluacoma(k,numFeature+1:end) = temp;
end

% get training and testing data
% -----
-----
Training =
[dataControl(inxControl,:); dataGluacoma(inxGluacoma,:)];
dataControl(inxControl,:) = [];
dataGluacoma(inxGluacoma,:) = [];
Testing = [dataControl;
dataGluacoma];

% labels
Group = ones(numTrain,1);
Group(1:numTrainControl) = -1;
Gtest = ones(totalData-
numTrain,1);
Gtest(1:(numControl-
numTrainControl)) = -1;

if usePCA %usePCA
    shiftdata = mean(Training);
    [coef,score,latent] =
princomp(Training - repmat(shiftdata,[numTrain 1]));
    dimchoose =
(cumsum(latent)./sum(latent))<0.9999;
    Training = score(:,dimchoose);
    % testing
    scoretesting = (Testing -
repmat(shiftdata,[totalData-numTrain 1]))*coef;
    Testing =
scoretesting(:,dimchoose);
end

% perform linear svm
% -----
-----
SVMModel = fitcsvm(Training,Group,
'Standardize',true);

% testing
predict_label =
predict(SVMModel,Testing);

```



```

accTestLin =
mean(predict_label==Gtest);

% perform rbf svm
% -----

SVMModel =
fitcsvm(Training,Group,'KernelFunction','rbf',
'Standardize',true);

% testing
predict_label =
predict(SVMModel,Testing);
accTestRBF =
mean(predict_label==Gtest);

% perform polynomial svm
% -----

SVMModel =
fitcsvm(Training,Group,'KernelFunction','polynomial','Standard
ize',true);

% testing
predict_label =
predict(SVMModel,Testing);
accTestPOLY =
mean(predict_label==Gtest);

results(row,:) = results(row,:) +
[accTestLin accTestRBF accTestPOLY];
row = row + 1;
end
end
end
end
end
end
end
results = results/numIter;

```

FFT for MTF

```
clc
clear

signal_original = load('Image4(40x)_cropped_text.txt');
FO = fft(signal_original);
subplot(2, 1, 1);
plot(abs(FO));
xlabel('Frequency')
ylabel('Magnitude');
title('FFT of the slide without explant');
axis tight;

signal = load('LE_0_cropped_text.txt');
N = length (signal);
fs = 62.5;
fnyquist = fs/2;
F = fft(signal);
subplot(2, 1, 2);
plot(abs(F));
xlabel('Frequency')
ylabel('Magnitude');
title('FFT of the slide with explant');
axis tight
```

FFT for MTF (time series)

```
clc
clear

signal_zero = load('LE_0_cropped_text.txt');
F_zero = fft(signal_zero);
subplot(2, 2, 1);
plot(abs(F_zero));
xlabel('Frequency')
ylabel('Magnitude');
title('FFT of Time 0');
axis tight;

signal_thirty = load('LE_30_cropped_text.txt');
F_thirty = fft(signal_thirty);
subplot(2, 2, 2);
plot(abs(F_thirty));
xlabel('Frequency')
ylabel('Magnitude');
title('FFT of Time 30');
axis tight;

signal_sixty = load('LE_60_cropped_text.txt');
F_sixty = fft(signal_sixty);
subplot(2, 2, 3);
plot(abs(F_sixty));
xlabel('Frequency')
ylabel('Magnitude');
title('FFT of Time 60');
axis tight;

signal_final = load('LE_120_cropped_text.txt');
F_final = fft(signal_final);
subplot(2, 2, 4);
plot(abs(F_final));
xlabel('Frequency')
ylabel('Magnitude');
title('FFT of Time 120');
axis tight;
```